universität wien

DISSERTATION

Titel der Dissertation

"Interferometry of carbon rich AGB stars"

Verfasser

Mag. Claudia Paladini

angestrebter akademischer Grad

Doktor der Naturwissenschaften (Dr.rer.nat.)

Wien, Oktober 2011

Studienkennzahl lt. Studienblatt: A 091 413

Dissertationsgebiet lt. Studienblatt: Astronomie

Betreuer: A.Univ.-Prof. Dr. Franz Kerschbaum

"She sees shooting stars and comet tails
She's got heaven in her eyes
She says I don't need to be an angel
But I'm nothing if I'm not this high..."

(Recovering the satellites, by Counting Crows)

Contents

Abstract

This thesis deals with the comparison of interferometric data of Asymptotic Giant Branch (AGB) stars with hydrostatic and dynamic model atmospheres.
The AGB is the late evolutionary stage of stars with masses below 8 $M_\odot$. These stars are characterised by a C-O degenerated core and 2 shell with ongoing nuclear reactions (He and H shells), a convective envelope and a very extended atmosphere with molecules and dust formation. As a star evolves along the AGB, it becomes subject to photometric variability and mass loss. As it gets older and more luminous the mass loss becomes significant, enriching the interstellar medium with the products of stellar nucleosynthesis.
If the AGB star has enough mass, the convective envelope will extend into the region with nuclear reactions, thereby, bringing processed material to the surface (dredge-up). The "third" dredge-up is responsible for the existence of Carbon Stars. The spectrum of these stars is characterised by features of carbon-bearing molecules (C_2, C_2H_2, C_3, CN, HCN). Dust is mostly present in the outflows as amorphous carbon influencing the spectral energy distribution. Studying AGB stellar atmospheres is essential for a better comprehension of the late stage of stellar evolution, to understand the complicate influence of pulsation on the stellar atmosphere, the dynamic process of dust formation and mass loss. Due to their extended atmospheres and brightness in the red and infrared range, AGB stars are perfect candidates for interferometric investigations. For pulsating, mass-losing carbon stars available atmospheric models are more advanced than for oxygen-rich stars because the dust formation is better understood. Nevertheless, in literature very few interferometric studies were dedicated to this class of objects so far. Therefore, this work is concentrated on carbon stars.

The first part of this thesis is devoted to the interferometric analysis of synthetic intensity profiles and visibility[1] profiles using Johnson JHK broad-band filters, and some narrow filters defined *ad hoc* to sample features of the infrared spectra of C-stars. These profiles are computed for a specified set of hydrodynamic models for stars with different mass-loss rates. Most of the previous studies concerning interferometry of red giant stars used simple approximations for interpreting visibility profiles. Following the same approach used in literature as for M-stars, the computed visibility profiles are fitted with analytical functions (uniform discs) to investigate their dependence on wavelength, pulsation phase and stellar parameters. It was found that the radius predicted by the models increases with wavelength, and the dependence on pulsation phase is not strictly sinusoidal. The $L-$band turned out to be crucial region for parameter determinations.

In the second part of this work newly obtained spectroscopic and interferometric data are presented for a sample of five objects with very limited dynamic effects. The observations are compared with models and the full set of stellar parameters ($T_{\rm eff}$, C/O, mass and $\log(g)$) could be derived. The parameters determined in this way are then compared with evolutionary tracks. The distance determination remains a crucial problem. Never-

[1]The visibility correspond to the Fourier Transform of the source intensity distribution at the spatial frequencies corresponding to the projected baseline on the sky per observing wavelength.

theless, very accurate effective temperature determinations can be obtained from $L-$band spectroscopy, and interferometry is the only tool that can give access to the mass of the object.

In the third and fourth part of the work the radial structure of the atmosphere of the C-rich semiregular variable R Scl and the carbon-Mira R For are investigated with spectro-interferometric observations in the mid-infrared. The $N-$band variability, the stratification of the atmosphere, and the geometry of the circumstellar envelope are presented. The observations are compared with dynamic model atmospheres confirming the interferometric technique as a very powerful tool to constrain our knowledge of dynamic processes (i.e. dust formation and mass-loss process).

Zusammenfassung

Diese Arbeit vergleicht interferometrische Daten von Sternen am Asymptotischen Riesenast (AGB) mit hydrostatischen und dynamischen Modellatmosphären.
Der AGB ist eine der letzten Entwicklungsphasen von Sternen mit Massen kleiner als $8\,M_\odot$. Charakteristisch für diese Sterne sind ein degenerierter C-O Kern, He/H-Schalenbrennen, eine konvektive Hülle und eine pulsierende Atmosphäre mit Molekül- und Staubentstehung. Die Entwicklung des Sterns entlang des AGB ist gekennzeichnet von photometrischer Variabilität und Massenverlust. Je älter und leuchtkräftiger der Stern wird, desto größer wird der Massenverlust welcher das interstellare Medium mit schweren Elementen, entstanden durch Nukleosynthese im Sterninneren, anreichert.
Die konvektive Hülle eines AGB-Sterns mit ausreichend hoher Masse kann bis in die Kernreaktionsregion reichen und prozessiertes Material an die Oberfläche bringen (dredge-up). Der sogenannte "dritte dredge-up" ist für die Existenz von Kohlenstoff-Sternen verantwortlich. Das Spektrum dieser Sterne zeigt charakteristische Features von C-hältigen Molekülen, wie z.B. C_2, C_2H_2, C_3, CN, HCN. Zircumstellarer Staub findet sich hauptsächlich in Form von amorphem Kohlenstoff.

Die Untersuchung der Atmosphären von AGB Sternen ist grundlegend für ein besseres Verständnis der Pulsation und des Massenverlusts sowie des dynamischen Prozesses der Staubentstehung. Aufgrund ihrer ausgedehnten Hüllen und ihrer Helligkeit im roten und infraroten Wellenlängenbereich sind AGB Sterne perfekte Kandidaten für interferometrische Untersuchungen. Die verfügbaren Atmosphärenmodelle für kohlenstoffreiche Sterne sind weiter entwickelt als jene für sauerstoffreiche Objekte. Dies ist auf Unterschiede im Mechanismus der Staubentstehung und des Massenverlusts zurückzuführen. Dennoch gibt es wenige interferometrische Studien, welche sich solchen kohlenstoffreichen Objekten widmen.
Der erste Teil dieser Doktorarbeit widmet sich der interferometrischen Analyse von synthetischen Intensitäts- und Visibilitätsprofilen[2] unter der Verwendung von Johnson JHK Breitbandfiltern und *ad hoc* definierten Schmalbandfiltern, um spezielle Features in den Infrarotspektren der Kohlenstoffsterne zu untersuchen. Diese Profile werden für ein vorgegebenes Set von hydrodynamischen Modellatmosphären berechnet und konzentrieren sich auf Sterne mit starker Variabilität und hohem Massenverlust. In Anlehnung an Studien über sauerstoffreiche Sterne werden die berechneten Visibilitätsprofile mit analytischen Funktionen (Uniform Disk) gefittet. Dies ermöglicht eine genaue Untersuchung der Abhängigkeit des Visibilitätsprofils von der Wellenlänge, der Pulsationsphase sowie von stellaren Parametern. Der auf diesem Weg bestimmte Sternradius variiert mit der Wellenlänge, wobei die Abhängigkeit von der Pulsationsphase nicht sinusförmig ist. Das L-Wellenlängenband ist eine äußerst wichtige Region für die Bestimmung von stellaren Parametern.
Der zweite Teil beschäftigt sich mit neuen spektroskopischen und interferometrischen Daten von fünf Objekten mit geringer Variabilität. In diesem Kapitel werden die Beobachtungen

[2]Visibilität (auch: Interferenzkontrast) ist die Fouriertransformierte der Intensitätsverteilung bei gegebener Raumfrequenz, welche der projizierten Basislinie am Himmel pro Wellenlänge entspricht.

mit Modellrechnungen verglichen und die stellaren Parameter dieser Objekte ($T_{\rm eff}$, C/O, M und $\log(g)$) ermittelt. Diese Parameter werden anschließend mit Sternentwicklungsrechnungen verglichen. Die Entfernungsbestimmung bleibt ein entscheidendes Problem. Die Temperatur der Objekte kann mit Hilfe von L-Band Spektroskopie präzise bestimmt werden.
Im dritten Teil wird die Atmosphärenmorphologie vom semiregulär Veränderlichen R Scl und dem kohlenstoffreichen Mira R For mit Hilfe von Spektro-Interferometrie im mittleren Infraroten genauer unter die Lupe genommen. Die Variabilität im N-Band, die unterschiedlichen Schichten der Atmosphäre und die Geometrie der zirkumstellaren Hülle werden besprochen. Die Beobachtungen werden mit dynamischen Modellatmosphären verglichen.

Chapter 1

Asymptotic Giant Branch Stars

The topic of this thesis is the investigation of a subclass of asymptotic giant branch (AGB) stars: the so-called carbon stars. In this chapter the relevance of studying C-stars will be described first. The evolutionary path of a star becoming a C-star will be followed. The last part of the chapter will be dedicated to illustrate some aspects of the carbon stars, which are particularly relevant for this thesis work. A detailed and extensive introduction to AGB stars can be found in Habing & Olofsson (2004). Parts of the text of this chapter are based on Habing & Olofsson (2004), Salaris & Cassisi (2006), and Huang & Yu (1998).

1.1 The importance of studying AGB Stars

"Where does it all come from? Where do we come from?" These are just a few of the fundamental questions every person asks at least once during their life. If you ask these questions to astronomers, they will probably answer you (with a little emphasis) that "we all come from the stars, and we are all made of star dust". You may smile, you may think we are incurable sentimental, but behind this sentence there is a kind of truth.

Stars play a very important role in the cosmic cycle matter. The human body is made up of 65% of oxygen, 18% of carbon, 10% of hydrogen, and the remaining quantity of heavier elements. Except for hydrogen, which was produced during the first moments after the Big Bang, all the other material is a result of the life cycle of stars. When stars reach the final stages of their evolution, processed material is ejected into the interstellar medium via a stellar wind (this happens for most of the low- to intermediate-mass stars) or through explosive mechanisms (as for Supernovae). This material is observed in the form of dust even in the Early Universe, for example in damped Lyman-alpha systems (Pettini et al. 1994), submillimiter selected galaxies (Smail et al. 1997), and high redshift quasars (Omont

et al. 2001, Isaak et al. 2002).

But what is the role of AGB stars in this global picture? For low- to intermediate-mass stars the bulk of the mass is ejected during the AGB phase. Therefore, this evolutionary stage is crucial for the enrichment of the interstellar medium (ISM) and galaxies with heavy elements. These elements will form molecules and condensate into dust grains, becoming the "bricks" to build new stars, planets, and eventually life.

1.2 Evolution of a star before the AGB phase

A star like the sun, but in general all the stars with masses between $1-8\,M_{\odot}$, spend almost 90% of their life on the **main sequence** (MS) of the Hertzsprung-Russel diagram (Fig. 1.1). Stars on the main sequence are in hydrostatic equilibrium. The energy irradiated is due to reactions which consume hydrogen and produce helium. This process can happen, according to the initial mass of the star, through the p-p chain or the CNO cycle ($M > 2M_{\odot}$). Both have a different sensitivity to the temperature, and only if the star burns H via the CNO cycle it develops a convective core. This is not the case if the H-burning runs through the p-p chain. During the pre-main sequence phase the star is chemically homogeneous because of the convection. While the star evolves through the main sequence it develops a chemical gradient with increasing helium abundance in the centre. The conversion of H into He leads to a pressure decrease in the centre of the star, which is followed by contraction of the inner layers in order to keep the hydrostatic equilibrium. When the hydrogen in the core has been exhausted, the star has a inner helium core surrounded by a shell with hydrogen burning. At this stage the core of the star starts to contract because it is not anymore supported by energy produced through the nuclear reactions. As a consequence, the outer envelope of the star starts to expand. While the radius of the star increases, the temperature decreases and the object moves towards the red part of the HR-diagram, close to the Hayashi line[1]. The timescale of the evolution of the star from the main sequence to the red giant branch is relatively fast. The observed HR-diagram usually is almost empty in this region, that is why this is called the *Hertzsprung Gap*.

The evolution on the **red giant branch** (RGB) proceeds rather quickly. The star has a helium core, a buffer convective shell, and an outer shell with hydrogen burning. During this stage the star may experience a *first dredge-up*: the outer convective shell penetrates the region where nuclear reactions are ongoing, and dredges up freshly processed material. As a result the chemical composition of the atmosphere is enriched with the products of the H-burning. At this stage the star starts to loose mass from its outer boundary through a slow stellar wind (quite low rates, though). The mass of the helium core increases (while the radius contracts) until it reaches the critical mass to start the helium burning. Low mass stars ($M < 2.3\ M_{\odot}$) are characterised by a helium core in a degenerate state. Because of this degeneracy, the core is highly unstable and experiences an explosion -*the helium*

[1]For a given mass and stellar composition the Hayashi line is a boundary on the HR diagram. In fact this line separate the diagram in an "allowed" and a "forbidden" region. The forbidden region, on the right of the Hayashi line, marks a zone where the object is not in hydrostatic equilibrium. A star on the Hayashi line is fully convective and in thermal equilibrium (Kippenhahn & Weigert 1991).

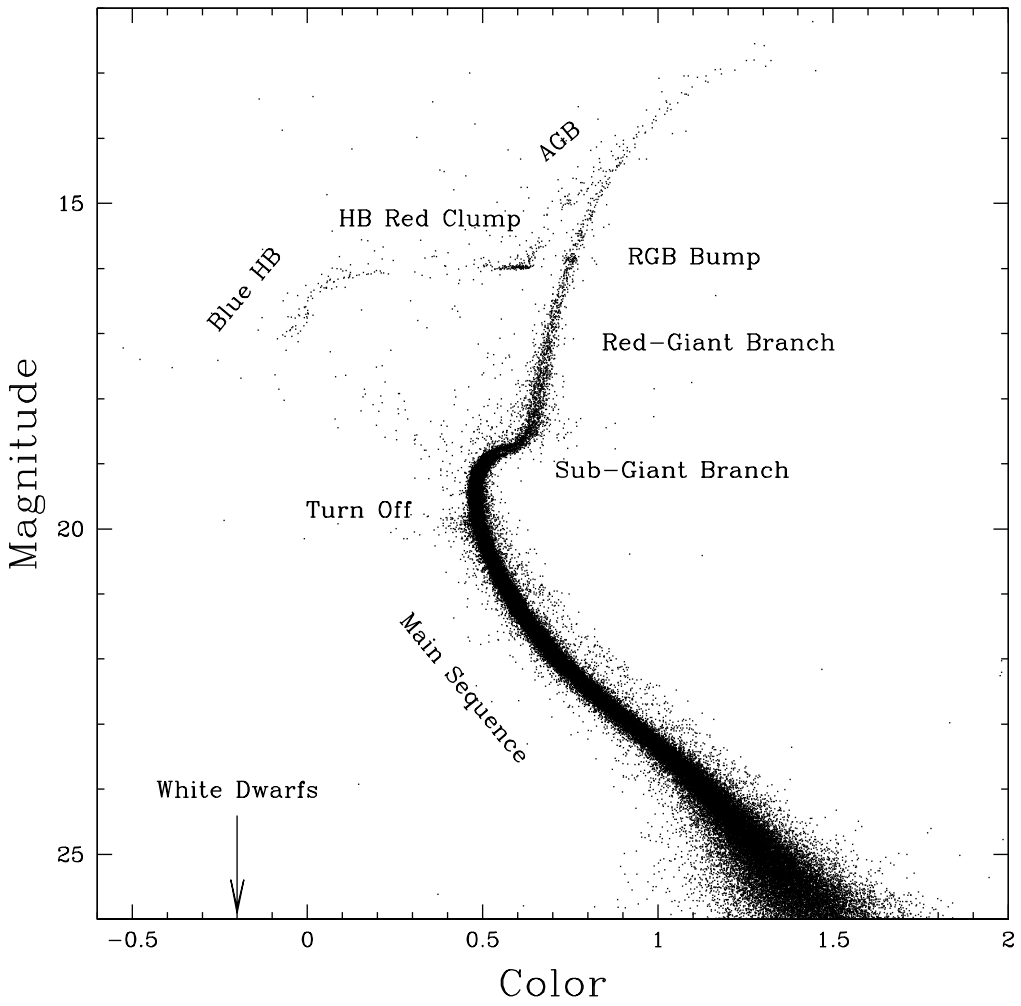

Figure 1.1: Color-Magnitude diagram of a globular cluster. The labels indicate the main steps of the evolution of a low mass star. (Unpublished ACS/WFC data in the F606W e F814W, courtesy of A. Bellini.).

flash- when the mass reaches the critical temperature for the helium burning. The energy produced during the flash is used to remove the degenerate state from the core. After the helium flash the star leaves the RGB and moves towards hotter temperatures on the **horizontal branch** (HB).

The position of the star on the HB depends on different parameters such as the ratio between the core mass and the mass of the envelope. During this evolutionary stage the star burns helium in the core via the triple$-\alpha$ process (the density of the core and the level of degeneracy depends on the total mass of the star). The core is surrounded by a convective buffer layer, and a shell with hydrogen burning. While the helium is consumed

in the inner core, the star moves slowly towards the Hayashi line for a second time, and it starts ascending the **asymptotic giant branch** (AGB).

The AGB evolutionary stage is the topic of this thesis, therefore, it will be discussed extensively in the following sections. While the star evolves along the AGB it develops a stellar wind with increasing intensity.

At the tip of the AGB the star eventually goes through a super-wind phase with very high mass-loss rates. The material of the outer envelope will keep expanding until the outer layers will leave the star merging with the ISM. There are many open issues concerning this transition phase (Renzini & Voli 1981).

Inside the object, the core keeps contracting, and continues the evolution towards lower luminosity and hotter temperature. The photons coming from the inner remnants of the star ionise the ejected material, producing what is called a **planetary nebula**. During this stage the core is still surrounded by a hydrogen burning shell.

When the fuel in this shell is consumed the star descends slowly the cooling sequence of the **white dwarfs**. Here the star will spend the rest of its life, radiating the energy accumulated during the last stages.

1.3 The Asymptotic Giant Branch

The structure of a star when it reaches the AGB is characterised by: (i) a small, very hot and dense core of carbon and oxygen; (ii) He- and H- alternately burning shells; (iii) a large, hot, and less dense stellar envelope; (vi) a warm atmosphere and a very large, diluted and cool circumstellar envelope. The evolution on the AGB can be divided in two stages: the Early AGB (running almost parallel to the RGB in the HR-diagram), and the Thermal Pulse (TP) AGB phase. The typical parameters of the regions of the atmosphere of a TP AGB star are displayed in the Fig. 1.2. The following sections will describe shortly the two phases. The text is based on Lattanzio & Wood (2003).

1.3.1 Early AGB phase

During the Early AGB most of the energy that supports the stellar structure comes from the He-burning shell, while the H-shell is initially quiescent. As the star consumes the He shell, the temperature slowly decreases, the atmosphere extends, and the luminosity of the object increases. During this stage the object starts ascending the asymptotic giant branch. For objects with masses larger than 3.5 $M_{\odot}$ the so-called *second dredge-up* may occur, with the consequence of increasing the abundance of ^{14}N, and decreasing the abundance of ^{16}O. When the star approaches the luminosity of the tip of the RGB, the He-burning stops, and the H-shell is thick enough to start the nuclear burning.

1.3.2 Thermal Pulse phase

During the phase of thermal pulses, the H and He shells ignite alternatively (nuclear burning). Schwarzschild & Härm (1965) and Weigert (1966) demonstrated that thin shells are

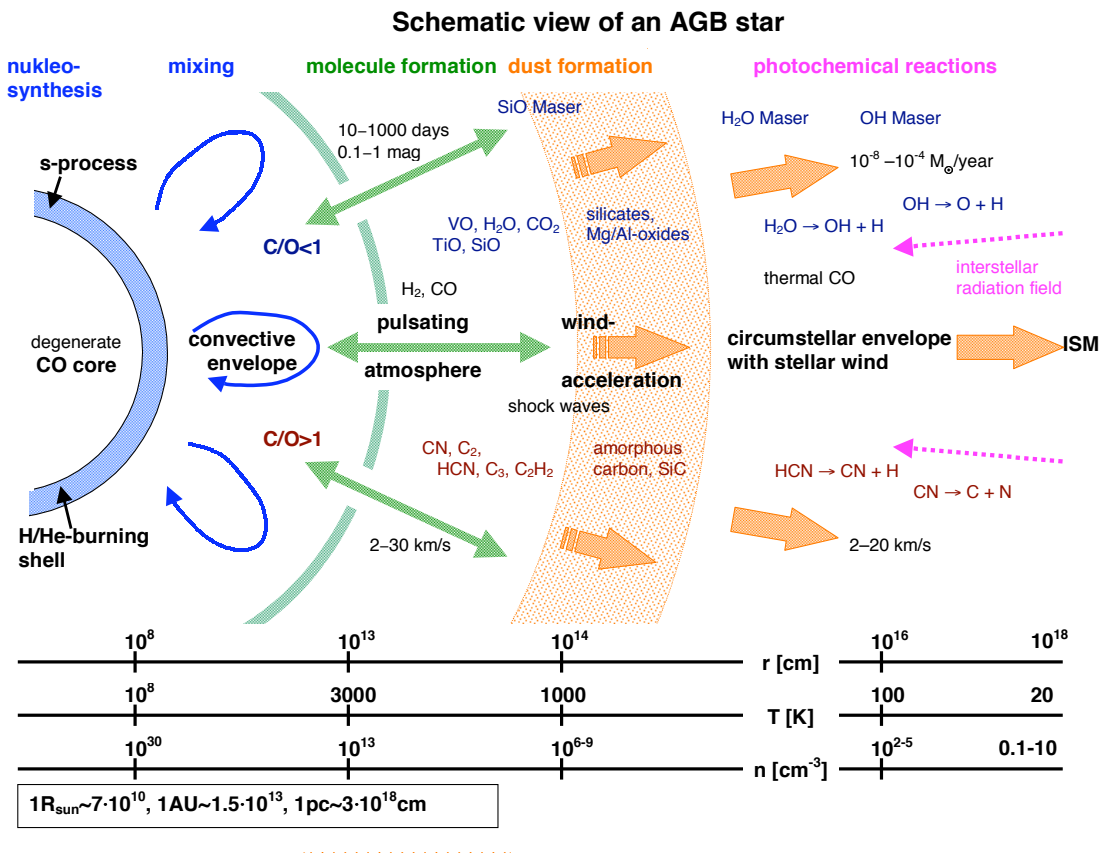

Figure 1.2: Radial structure of a TP-AGB star. The figure shows the different regions of the atmosphere and the typical parameters (radius, temperature, and density). The main processes occurring in the atmosphere are also labelled. The chemical composition of an O-rich star is represented in the upper part of the figure, while in the lower part the main molecules characterising the atmosphere of a C-rich object are shown. (Courtesy of J.Hron. Figure adapted by J. Hron from an original idea of Th. Le Bertre.).

thermally unstable, and they start oscillating due to this instability. When the helium shell becomes too thin, a thermal instability induces a nuclear runaway. As a consequence, the object experiences a sudden increase of luminosity and extension of the atmosphere. A small convective region appears feeding the He-shell with He deposited at the bottom of the H-shell which is above. The He-shell becomes thicker, and it starts producing carbon via nuclear reactions. The carbon increases the mass of the core of the star. The luminosity modulation observed during this phase is called "thermal pulse" or "He-shell flash". Several thermal pulses may occur during the AGB lifetime of a star. In between the thermal pulses the nuclear reactions take place only in the hydrogen shell.

During the thermal pulse another important phenomena may occur: **the third dredge-up**. This time, the atmosphere is enriched with the products of He-burning, mainly carbon. At the beginning of the thermal pulse phase the atmosphere of the star is basically dominated by oxygen-bearing molecules (CO, TiO, SiO, H_2O, VO). CO is the most abundant molecular species (after H_2), and in O-rich objects all the carbon is locked therein. If the

dredge-up is efficient enough, it will turn the C/O of the atmosphere from C/O < 1 to C/O > 1. The atmosphere is carbon-enriched and molecules like CO, C_2, C_3, C_2H_2, CN, HCN will form. This is the typical atmosphere of what is called a **carbon-star**. C-stars are the objects of investigation in this thesis and they will be described in the following Sect. 1.4. The intermediate stage between O-rich and C-rich needs to be mentioned for completeness. When C/O is comprised between 0.5 and 1 and the spectrum is characterised by strong ZrO bands and no TiO, the star is called **S-type star** (Jorissen et al. 1993, Van Eck et al. 2010).

1.4 Carbon stars

This section describes the AGB carbon-stars and it is based on reviews by Wallerstein & Knapp (1998) and Lloyd Evans (2010). The discussion does not cover the R Coronae Borealis stars, Cepheids II, and J-type carbon stars.

1.4.1 The discovery

The carbon stars were recognised as a new spectral type for the first time by Padre Angelo Secchi in 1868. The discovery was reported in the French Academie des Sciences in the following way (but in French):

> *"Stars which do not belong to the three established types are very rare. I have examinated without success many hundreds of faint stars. I have just come across one very extraordinary star*[2] *which is listed in Lalande's catalogue (RA = 4hr 54m 10s and Dec= +0°59′) Its spectrum is very peculiar. The red region is divided into two bands by a very broad dark line. The golden yellow is reduced to a very clear and sharp line. After a broad dark band comes a broad green-yellow band and, after another dark interval, a zone of blue ... Although I have not examined the whole sky I believe that one will find very few of these stars and that they will belong to the family of red stars and of variable stars."*

Later in the same year Padre Secchi introduced the IV type in its classification of stellar spectra. This class included red stars with carbon lines and bands in their spectrum: the carbon stars.

Almost 150 years passed until today and C-stars are not anymore such a rare species as they appeared at the time of Padre Secchi. The third edition of the *General Catalogue of Galactic C-stars* by Alksnis et al. (2001) includes 6,891 stars. The first technique widely used to detect C-stars was prism spectroscopy. C-stars were recognised because of the typical C_2 Swan bands in the blue spectral region, and because of the CN bands in the violet. Starting from the late 1970's many C-stars were detected in the Magellanic Clouds, first through by photometric survey Lloyd Evans (1978, 1980) and then spectroscopically by Lloyd Evans (1980, 1983), Bessel et al. (1983). In the 1950's there was no theory of

[2]The first carbon-star observed by Padre Secchi was W Ori.

evolution able to explain the phenomenon of C-stars, neither a theory about the mass-loss. Only in the 1980's, Iben & Renzini (1983) classified these objects as a subclass of the AGB that evolve through the M-S-C sequence. A huge advance in the knowledge of these objects was achieved with the advent of infrared detectors in the 1970's. In those years the investigation of the mass-loss process started. The low resolution spectrometer on board the IRAS satellite showed that many C-stars were not visible in the $V-$band, but they are extremely bright in the near-IR. Among the other results of this mission was the unexpected discovery of the SiC feature at $11.2\,\mu$m in the spectra of many C-stars (Olnon et al. 1986). Even if these objects were studied for such a long time, many questions are still far from being understood. Thanks to the new ground and space facilities such as Very Large Telescope Interferometer (VLTI), Herschel, and the Atacama Large Millimeter/submillimeter Array (ALMA) available to the scientific community, the field of AGB research is blossoming into a fascinating field at the forefront of science. In the following sections some of the characteristics of C-stars will be described. The focus will be on the topics which are relevant for the research presented in the following chapters.

1.4.2 Stellar Parameters

The **luminosity** of C-stars ranges between a few $\sim 10^3$ and $10^4\,L_\odot$, but precise measurements are very difficult, especially in the case of the galactic objects were **the distance** estimates are uncertain. The situation is better for objects belonging to stellar systems. The Hipparcos parallaxes for C-stars have always very large errors. The most probable reason being that the objects are resolved, and Hipparcos is therefore sensitive to spatial and temporal variation of the surface brightness (Feast 1999). Schwarzschild (1975) suggested for the first time the appearance of large convective cells on the stellar surface as possible explanation to this fluctuation of the surface brightness. These cells are of the order of the astronomical unit. The existence of such cells has been demonstrated theoretically by the 3D models of Freytag et al. (2002). Chiavassa et al. (2011) showed, using the same models, how the fluctuation in surface brightness will affect the astrometric measurements for super-giants from the space mission GAIA (Perryman et al 2001, Lindegren et al. 2007). The situation for the AGB stars might be even worse as it was shown by Sacuto et al. (2011a). The method to correct such an effect is still a matter of research.

The **masses** of C-stars are currently inferred only via stellar population studies, or stellar evolution calculations. High angular resolution will likely change this in the near future. The range of mass accepted at the moment is between 1-4 $M_\odot$, but the lower and upper limit are still uncertain.

The **effective temperature** can be defined through the relation:

$$L = 4\pi R^2 \sigma T_{\rm eff}^4. \tag{1.1}$$

The radius can be measured with lunar occultations or interferometric methods, but for dynamic objects strongly variates with the wavelength, and in the end only a "brightness temperature" can be derived. The measurements of photospheric radius and effective temperature are therefore very uncertain. From model calculations the temperature ranges

between 2 400 up to 3 400 K. In the literature, sometimes values down to 2 000 K are reported. The **stellar radii** estimated from lunar occultation and/or interferometry indicate for C-stars values around a few hundreds solar radii (Dyck et al. 1996, van Belle et al. 1997). An extensive discussion on the problem of the definition of the stellar radii for AGB stars can be found in Scholz (2003).

1.4.3 Photometric variability

C-stars show, in general, long term variability from 80 up to 1000 days. They are classified like the other (M- and S-type) AGB stars in Miras, Semiregulars, and Irregular variables. The Mira stars are the objects with the longest period of pulsation and they are known to pulsate in the fundamental mode. These objects show also a very large amplitude of variability between 2.5 and 7 magnitudes in the visual. The variability exhibited in the infrared has usually smaller amplitudes compared to the visual (Nowotny et al. 2011). The semiregular objects usually show no defined period. The irregular variables are usually not completely distinguishable from the semiregular. They are characterised by a small amplitude of variability (down to 0.2 magnitudes), and a poorly defined period. The light curves of Mira variables are generally described as regular and sinusoidal, but this is not always the case. Some objects show a deviation from sinusoidal pattern within the primary pulsation period (Vardya 1988, Lebzelter 2011). This kind of asymmetry seems to correlate with the chemistry of the object, meaning that they are more frequent among C- and S-stars than in the M-type stars. Other Miras show dramatic long-term variations of both maxima and minima from one cycle to another (Barthes et al. 1996). Among the C-stars there are some Miras (R For, R Lep, and R Vol, Whitelock et al. 1997) showing erratic drops in the brightness, which are likely associated to obscuration events. What causes these events is still discussed among the scientific community.

1.4.4 Mass-loss

Mass-loss process appears to be quite complex. It was studied for over 30 years, and it is still not fully understood. For C-stars the situation is slightly better than for the O-rich objects, because the theory of dust formation is understood.

In the previous sections one of the processes affecting the atmosphere of the AGB stars is highlighted: the pulsation. The basic concept which explains the mass-loss process assumes that the stellar pulsation triggers shock waves in the atmosphere. These waves lift the gas outwards. Dense cool layers are created where microscopic solid particles may form. The radiation pressure coming from the star accelerates these dust particles away transferring momentum through the collisions to the gas dragging it away (Fleischer et al. 1992, Sedlmayr 1994, Höfner & Dorfi 1997, Willson 2000). According to this picture one can deduce that most of the atmosphere of the AGB star is somehow affected and influenced by the mass-loss process. Therefore, from the point of view of the modelling this has to be taken into account.

From the point of view of an observer, many techniques need to be combined in order

to gain a global picture. Photometric observations, in particular time series, are crucial to study the pulsation and eventually the dust-formation process. According to models (e.g. Winters et al. 1994) these two dynamic processes occur on two different time-scales which might explain the long term modulation observed in the light curves. High-resolution spectroscopy and spectral-dispersed interferometry allow to study the atmosphere of the star, and the onset of the stellar wind. Imaging is not yet a routine for optical/infrared interferometry, therefore, it is limited to the outer parts of the envelope where the stellar atmosphere interacts with the ISM. These thesis focuses on two aspects of the mass-loss process: the dependence on stellar parameters, and the structure of the atmosphere.

1.5 Model atmospheres for C-rich AGB stars

This section is based on Gautschy-Loidl et al. (2004) and the reviews of Woitke (2003), Höfner (2005, 2007, 2009).

The observed spectra of AGB stars are characterised by a plethora of atomic lines and molecular bands. C-stars are not an exception. Most of these lines originate in the stellar atmosphere, and in order to interpret the astronomical observables in a more or less consistent way, model atmospheres are needed. The atmospheres of AGB stars are very complex, and this makes the modelling very challenging. Besides atoms, molecules form in the atmosphere of these stars because of low effective temperature. From the point of view of the dynamics the challenges for theoreticians are modelling the pulsation, the dust formation, and driving the wind. As already pointed out in the previous section, for C-stars the situation of the modelling is likely more advanced than the one of the O-rich stars. This is because the theory of dust formation is better understood. Up to now most of the models available are 1-dimensional, i.e. spherically symmetric.

The atmospheric models used in this thesis are the hydrostatic COMARCS models from Aringer et al. (2009) that are described in Chap. 4, and the dynamic model atmospheres (DMA) from Höfner et al. (2003) described in Chap. 3.

The COMARCS hydrostatic model atmosphere are based on a version of the MARCS code (Gustafsson et al. 1975), that was used by Jørgensen et al. (1992) and Aringer et al. (1997). The models adopt local thermal and chemical equilibrium (LTE), they are dust-free, and the molecular absorption is treated using the opacity sampling approximation.

The dynamic model atmospheres from Höfner et al. (2003) are 1-D models and spherically symmetric like the COMARCS models. The coupled system of equations for hydrodynamics, frequency-dependent radiative transfer, and time-dependent treatment dust formation (Gail & Sedlmayr 1988, Gauger et al. 1990) is solved. The models include pulsation which is simulated by a piston at the inner boundary.

Both set of models just described are self-consistent and were compared successfully with photometric, and spectroscopic observations (Gautschy-Loidl et al. 2004, Nowotny et al. 2005a,b, 2010, 2011).

Interferometry, and speckle observations showed that deviations from spherical or even central symmetry are quite frequent among AGB stars. An attempt to move from 1- to 2-D

was made by Woitke (2006). The author showed how deviations from symmetric structure can be reproduced using axisymmetric modes of dust-driven winds. These models were not pulsating, meaning that the inner boundary condition is fixed. The hydrodynamics with radiation pressure on dust is included, LTE and time-dependent dust formation is coupled with grey Monte Carlo radiative transfer.

The only 3-D attempt was made by Freytag & Höfner (2008). The authors combined the 3D radiation hydrodynamic code named CO5BOLD (Freytag et al. 2002, 2004) used to model the outer convective layers of the atmosphere of giant stars, with the code to account for dust formation also implemented in Höfner et al. (2003). With their simulations the authors showed that the convective cells are so large that the associated shock fronts are in first approximation spherical. Nevertheless, the simulations predict also the presence of deviation from symmetric structures deep inside the atmosphere. The layers were such asymmetries appear are currently detectable only applying interferometric techniques via closure and differential phase. These last two set of models were never compared with observations.

1.6 Outline

The motivation and the outline of the thesis will be summarised here.

Carbon-stars are frequent in external galaxies, especially in the ones with low metallicity, but the fact we see them as point source does not mean that we can ignore the physics going on in their interior. They are among the main sources of carbon in the Universe (Mattsson 2009). Understanding C-stars is crucial for the correct implementation of this evolutionary stage in the models of galaxies. The C-stars have been the topic of investigation over the last 150 years, but still there are many open questions. Carbon stars are very bright in the infrared, relatively frequent in the neighbourhood of the sun (within 1 kpc), and their atmosphere is very extended and optically thin. For all the reasons listed above these objects are a natural perfect target for investigations with infrared interferometry. Nevertheless, for some reasons, they were neglected up to now as most of the data available in the archives, and most of published studies, were devoted to M-type stars. This work aims to start filling the gap, taking advantage of the advanced status of the model atmosphere for C-rich stars. The main goals of this thesis can be summarised as follows:

- Link the models with interferometric observables.
  This is done first identifying the representative features in the spectra of C-stars that can be used to probe the atmosphere of this class of giants. The interferometric observables are then computed for a set of model atmospheres in these selected wavelength regions. Through a morphological study of the observables we try to link the stellar parameters and the properties of the atmosphere. This part of the work is presented in Chap. 3.

- Derive stellar parameters by comparing models and interferometric observations.
  This is presented in Chap. 4 and Chap. 5. In the first of the two chapters spectra and

interferometric observations for a set of low amplitude variables are compared with COMARCS hydrostatic model atmospheres. The stellar parameters are derived for all objects, and the difficulties and limitations of such kind of studies are discussed. In Chap. 5 the spectroscopic and interferometric observations of the semiregular variable R Scl are compared with the DMAs of Höfner et al. (2003), and stellar parameters are derived.

- Assess the effect of asymmetries.
  In Chap. 6 the capabilities of MIDI to study the geometry of the mass-loss process are shown. The observations map the outer layers of the carbon Mira R For between 1.5 and 13 stellar radii. Evidence of asymmetries is detected deep inside the atmosphere. This might be related (among other reasons) to an asymmetric mass-loss process. Since the object does not show any asymmetry in the outer parts, the observations are compared with the DMA. These observations are once again a unique testbed for the theory of the mass-loss process.

Chap. 1 and Chap. 2 give a general introduction to the topic, while in Chap. 6 the main results and future outlook are described.

Chapter 2

Interferometry

The intent of this chapter is to briefly present the terminology and the basic concepts of optical/infrared long baseline interferometry. A detailed introduction to the topic is given in the books by Lawson (2000), Laberyrie et al. (2007), and Glindemann (2011) or in the proceedings of the VLTI Euro interferometric summer schools (Malbet & Perrin 2007, Delplancke 2009). The long baseline interferometers available around the world will be shortly described, and in the final part of this chapter the main results concerning the topic of C-rich AGB stars will be listed.

2.1 Principles of interferometry

Most of the stellar objects in the sky can not be spatially resolved with the single-dish telescopes available nowadays. The smallest detail one can resolve on the image is indirectly proportional to the size of the telescope, according to the Rayleigh criterion:

$$\theta \simeq \frac{\lambda}{D} \tag{2.1}$$

where θ is what is called angular resolution (in radians), D is the diameter of the telescope (in meters), and λ is the wavelength of observations (in meters). With a 10-m-class telescope (like Keck, Mauna Kea Hawaii) the resolution is around 20 milli-arcseconds (hereafter mas) in the visible and 250 mas in the mid-infrared. Giant AGB stars for example (cf. Chap. 1) are very bright in the infrared, therefore, near- or mid-IR wavelength are suited to observe them. If the typical size of the dust shell at 11 μm is $\sim$ 50 mas, a telescope of 45 m would be needed to spatially resolve the object. This is more than the size of the E-ELT (European Extremely Large Telescope) that ESO plans to build in the coming years. In order to resolve the nucleus of an AGN (Active Galactic Nuclei) in the mid-IR ($\sim$ 5 μm and

a size < 1 mas) a telescope of 100 m is needed. Such kind of instruments are too expensive, therefore, the astronomers adopted a special technique in order to resolve their preferred objects: interferometry.

In interferometry the light is collected through two (or more) spatially separated apertures and is then combined coherently. The result is not an image but an interference pattern called *fringes* (shown on the right side of Fig. 2.1). This technique allows to gain angular resolution but the price is poorer sensitivity and no direct imaging (not as routine at least). The interferometric observable derived from the fringes is the *complex visibility*. The link between the intensity distribution of the object and the complex visibility is given by the fundamental Van-Cittert-Zernicke theorem:

> *"The complex visibility is the Fourier transform of the source intensity distribution on the sky at the spatial frequencies corresponding to the projected baseline on the sky per observing wavelength."*

The *baseline* is defined as the distance between the two apertures, and corresponds to the diameter of a corresponding virtual telescope. The Van-Cittert-Zernicke theorem is expressed by the following formula:

$$I(\alpha,\beta) = \int_{-\infty}^{+\infty}\int_{-\infty}^{+\infty} V(u,v)\ e^{\ 2\pi i\ (\alpha u+\beta u)}\mathrm{d}u\mathrm{d}v \tag{2.2}$$

where I is the intensity distribution of the object, (α,β) are the angular coordinates of the object on the sky (in radians), V is the complex visibility, and (u,v) are the spatial frequencies that describe the brightness distribution. The spatial frequencies are related to the baseline (B) through the following expressions:

$$u = \frac{B_x}{\lambda};\quad v = \frac{B_y}{\lambda}. \tag{2.3}$$

The term $u-v$ *plane* is used in interferometry very frequently. This indicates the plane sampled with the interferometric observations. A two-aperture telescope configuration will give one point in the $u-v$ plane, meaning one visibility. Ideally, in order to reconstruct an image of the object, one should fill the $u-v$ plane with interferometric observations. Knowing the visibility, it would be possible to perform an inverse Fourier Transform in order to retrieve the image of the object. Unfortunately life is not (yet) so easy at optical/infrared wavelength (contrary to submm-radio). Interferometric observations are expensive in terms of time because of the limited number of apertures available. Three points of visibility at VLTI/AMBER (cf. Sect. 2.2) require 90 minutes of observing time (including calibrators). What is done in practise is to wisely sample the $u-v$ plane, in order to have very sparse observations and still constrain the object (more details in Ségransan 2007). The data alone are not sufficient for reconstructing realistic images. Additional constraints, known as *regularisations*, are needed in order to have a unique solution. The requirements for image reconstruction in optical interferometry, with a special emphasis to the regularisation term, are presented in the recent paper from Renard et al. (2011). Image reconstruction is not yet a routine in optical/infrared interferometry, but this will likely change in the (near) future. Commonly the interferometric observations are compared with synthetic observations derived on the basis of geometric or atmospheric models.

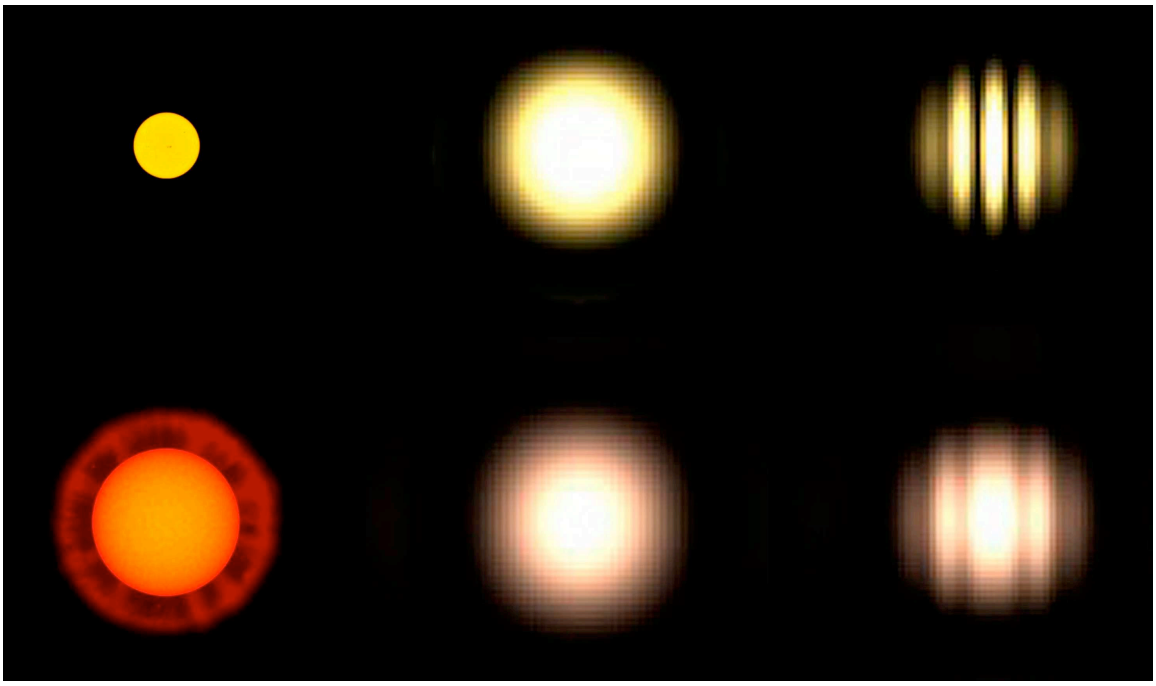

Figure 2.1: Comparison between single-dish and interferometric observables for two objects with different size. *Left:* two simulated stars of different size. *Centre:*two previous objects seen by a single-dish telescope. The difference in size is barely detectable. *Right:* the interferometric observables (fringes) for the two objects. The fringe pattern is clearly different. The contrast between the fringes is smaller for large objects. (Image credit: ESO.)

2.1.1 The visibility

As every complex number, the visibility consists of two parts: the amplitude (often called just visibility), and the phase. The amplitude is a measurement of the contrast between the fringes. In interferometry it is usual to deal with the *normalised visibility*, meaning the amplitude scaled to a factor that depends on the brightness of the object (such that $V(0) = 1$). Hereafter the term visibility will be used for the normalised visibility. This quantity carries information about the size of the object (Fig. 2.1).

2.1.2 The phase

The phase is related to the fringe location and it is very sensitive to the turbulence of the atmosphere. The available optical/IR interferometers are not able to measure directly the phase. This quantity is crucial for image reconstruction as it carries information about the geometry, i.e. symmetry of the object. Usually an object is denoted asymmetric when the shape is not centrally-symmetric. For example an ellipse is a symmetric shape, but an ellipse plus a spot is not. A binary with the two objects having the same brightness is symmetric, if the brightness differs it is not. The current technique of observations that uses only two apertures is able to preserve only the so-called *differential phase*. The differential phase is one of the MIDI (MID-infrared Interferometric instrument; Leinert et al. 2003)

Table 2.1: List of the instruments currently offered to the community. In col. 1 is reported the acronym of the instrument; in col. 2 the facility where the instrument is mounted; in col. 3 the number of apertures; in col. 4 the baseline range; in col. 5 the wavelength band of observation, and in col. 6 the spectral resolution.

Instrument	Facility	Apertures	Baselines range [m]	Wavelength	Resolution
PIONIER	VLTI	4	8-130	H-band	30
AMBER	VLTI	2-3	8-130	HK-bands	35, 1500, 12 000
MIDI	VLTI	2	8-130	N-band	30, 230
CLASSIC	CHARA	2	30-300	HK-bands	< 10
CLIMB	CHARA	3	30-300	HK-bands	< 10
VEGA	CHARA	2-3	30-300	V-band	6 000, 30 000
MIRC	CHARA	6	30-300	HK-bands	30

observables, and it will be discussed in Chap.6. This quantity cannot be used for image reconstruction. Three (or more) aperture telescopes (such as AMBER, Astronomical Multi-BEam combineR; Petrov et al. 2007) provide a quantity called *closure phase*. This quantity is the sum of the phases measured simultaneously between the different apertures. It is free from spurious effects (mainly atmospheric), and it can be used for image reconstruction.

2.2 Interferometric facilities around the world

The intent of this section is to give a short overview of the instruments presently available around the world for optical/infrared interferometric observations (Table 2.1). More emphasis is given to the two "big" interferometers that are currently offered to the international community: VLTI (Very Large Telescope Interferometer) and CHARA (Center for High Angular Resolution). Unfortunately, the Keck Interferometer will cease operations within 2012. Most of the information have been adopted from links listed in the OLBIN (Optical Long Baseline Interferometry News) website[1]. Since VINCI (VLT INterferometer Commissioning Instrument; Kervella et al. 2000), PTI (Palomar Testbed Interferometer; Colavita et al. 1999) and MIDI were used to retrieve the data for this thesis, they will be described in more detail in Sects. 2.2.1, 2.2.2, and 2.2.3, respectively. The sources for the description of MIDI are Tubbs et al. (2004), Chesneau (2007), Wittkowski (2007), and the dedicated website[2] of ESO. The sources for PTI are Colavita et al. (1999) and the PTI website[3].

VLTI is the ESO interferometer located on Cerro Paranal (Chile). It is equipped with 4 Unit Telescopes (UTs) with 8 m aperture and 4 Auxiliary Telescopes (ATs) with 1.8 m aperture. It allows the combination of 2 up to 4 apertures. The instruments routinely offered to the community are AMBER and MIDI. AMBER (Petrov et al. 2007) is a 3-way beam combiner observing in the near-IR (H- and K-bands) with different spectral reso-

[1] `http://olbin.jpl.nasa.gov/`
[2] `http://www.eso.org/sci/facilities/paranal/instruments/midi/`
[3] `http://nexsci.caltech.edu/missions/Palomar/`

lutions ($R = \lambda/\Delta\lambda = 35, 1\,500, 12\,000$). Currently it is offered with 12 different telescope configurations (triplets) with baselines ranging between 11 and 130 m. MIDI will be discussed in more detail in Sect. 2.2.3 and in Chap. 5. PIONIER (Precision Integrated-Optics Near-infrared Imaging ExpeRiment, Le Bouquin et al. 2011) was commissioned at VLTI in Fall 2010. It is offered only in visitor mode and is property of the Institut de Planétology et d'Astrophysique de Grenoble (IPAG) and partners. The instrument is optimised for imaging with its 4-way beam combiner working in the $H-$band at low resolution. At the time of finishing this thesis (September 2011) PIONIER is available only via collaboration with the IPAG. Currently there are three ESO instruments under development: the PRIMA instrument (Phase Referenced Imaging and Microarcsecond Astrometry, Delplancke 2008, van Belle et al. 2008) is designed to perform narrow-angle astrometry in the K-band, or to work as external fringe-tracking in order to produce images of faint objects. Two second generation instruments are under development for VLTI: GRAVITY (Eisenhauer et al. 2008), and MATISSE (Multi-AperTure mid-Infrared SpectroScopic Experiment; Lopez et al. 2006). GRAVITY will combine 4 beams in the near-infrared and it will offer imaging and astrometric mode. The spectral resolution will be $R = 22, 500, 4000$. MATISSE will observe in the $LMNQ$-bands with 4 telescopes and at low- to mid-spectral resolutions ($R = 30, 500, 1500 - 2000$).

CHARA (Center for High Angular Resolution Astronomy) is an array of six 1-meter-telescopes for optical and infrared interferometry on Mount Wilson, California. It offers 15 different baselines with lengths ranging from 30 to 300 m. The instruments operating on CHARA are: CLASSIC, CLIMB, MIRC (Michigan Infrared Beam Combiner; Monnier 2006), VEGA (Mourard et al. 2009, Visible spEctroGraph and polArimeter;). The first two instruments observe in H- or K-broad band and combine 2 and 3 apertures, respectively. VEGA observes in the optical (480-850 nm) with very high resolution (the highest to my knowledge) $R = 30\,000$ or $6\,000$. It combines 2 to 3 telescopes. MIRC is the CHARA imager and it combines all the 6 telescopes. The observations are carried out in H- (K-) band with low resolution ($R = 40$). CHARA is currently offered to the scientific community with a call once per year in September.

SUSI (Sydney University Stellar Interferometer) is the Australian long baseline interferometer. It offers only one baseline direction ranging between 5 and 80 m (160 m foreseen). The beam-combination system was recently upgraded to PAVO (Precision Astronomical Visible Observations, Ireland et al. 2008) with a spectral range between 400 and 900 nm.

NPOI (Navy Prototype Optical Interferometer, recently renamed Navy Optical Interferometer in recognition of its long-term operational status) is located at the Lowell Observatory near Flagstaff (Arizona), and it is undergoing an upgrade. Currently it operates in the wavelength range 550 - 850 nm with low resolution (30 or 50). The baselines have Y-shape with lengths between 2 and 60 m.

At the LBT (Large Binocular Telescope) the instrument LINC/NIRVANA (Near InfraRed and Visible Adaptive iNterferometer for Astronomy, Herbst et al. 2002, Ragazzoni et al. 2002) recently produced the first fringes. This instrument will use the two fixed 8.3 m mirrors as apertures to collect the light. The fixed baseline offered is 23 m long. The wavelength range of observation is $0.6 - 2.4$ μm.

The Magdalena Ridge Observatory Interferometer[4] (MROI) is the upgrade of CHARA and is currently being build in Soccoro, New Mexico. The ambitious project foresees ten-element imaging interferometer that will operate in the wavelength range $0.6 - 2.4$ μm.

2.2.1 PTI

The PTI was a long baseline interferometer installed at Palomar Observatory, San Diego County (California). The instrument was developed by the Jet Propulsion Laboratory for NASA as a testbed for the Keck Interferometer, and it was implementing a dual-star architecture for astrometric measurements (this kind of architecture is also implemented at VLTI for the PRIMA project).

PTI saw the first fringes in July 1995, and it was decommissioned in December 2008. The instrument combines the light of two out of the three 40 cm fixed apertures. The range of baselines available was 85 to 110 m, and the instrument offered H- and K-broad band observations. Observations carried with this instrument are used for this thesis work, and are described in Chap. 4.

2.2.2 VINCI

VINCI was mounted at ESO/VLTI Paranal. It was intended as testbed and alignment instrument for the commission of VLTI. VINCI was a 2-way beam combiner able to produce H- and K-broad bands visibilities. The design of the instrument was based on the FLUOR (Coude du Foresto et al. 1998) instrument. The first fringes were obtained in March 2001 with the ATs, and later in October 2001 with the UTs. A detailed description of the instrument can be found in Kervella et al. (2000). Data retrieved with this instrument are described in Chap. 5.

2.2.3 MIDI

MIDI is mounted at ESO/VLTI Paranal (Chile). The conceptual design started in 1997. This instrument is the result of the efforts of several European institutions, and it detected the first fringes with the UTs on December 12, 2002.

MIDI combines the light coming from two apertures (UTs or ATs) using a two pupil-plane beam splitter. In order to measure the visibility it implements the same method as SUSI, COAST and IOTA (this last two are commissioned interferometers used as testbed for the new generation): temporal scanning of the fringes. The optical layout of the instrument consist of two parts: the warm optics and the cold optics. The latter is enclosed in a cryostat in order to keep them at cryogenic temperature. This is needed to shield the instrument from the thermal emission of the environment that dominates at IR wavelengths. A sketch of the instrument including the cold optics is shown in Fig. 2.2.

The wavelength range of observation is the $N-$band $(8, 13$ μm). Sixteen configurations are offered at the moment with a range in baselines between 11 and 130 m. The observations

[4] `http://www.mro.nmt.edu/Home/index.htm`

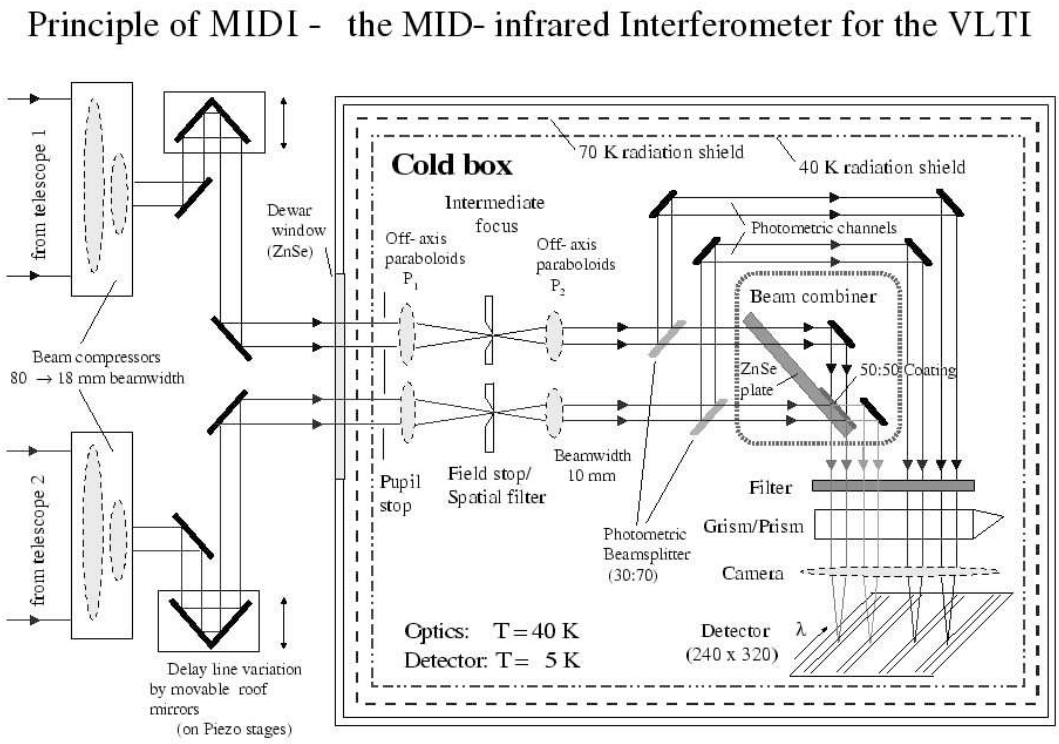

Figure 2.2: Layout of the MIDI instrument. (Image credit: ESO/MIDI website.)

are dispersed in wavelength and two spectral resolutions are available: PRISM ($R = 30$), and GRISM ($R = 230$). The instrument is currently (as of Sept. 2011) offered in three modes: high-sensitivity (HIGH_SENS), science and photometry (SCI_PHOT), and correlated flux (CORR_FLUX). In HIGH_SENS mode the photometry is recorded few minutes after (or before) the fringes. This allows to observe fainter objects but is less accurate (cf. Sect. 6.3.5). In SCI_PHOT mode the photometric channels are recorded simultaneously during the scanning of the fringes. The gain in accuracy of this mode is possible only for target brighter than 200 Jy[5]. The CORR_FLUX mode was implemented only recently. This is optimised for very faint (at the limit of the fringe tracking, i.e., 0.2 Jy for the UTs) objects where accurate photometry cannot be retrieved and can therefore not be used to calibrate the data. The primary observable of MIDI is the visibility, but the instrument provides also differential phases and correlated fluxes. Data observed with this instrument are discussed in Chap. 5 and Chap. 6.

2.3 Interferometric observations of C-stars

Most of the interferometric studies dedicated to AGB stars are focused on oxygen-rich targets, as can be noted also in the results of the statistic of the CHARM2 catalogue (Fig. 2.3). Earlier studies on carbon stars were mainly devoted to the determination of

[5]This value is not the simple 12 μm flux, but (Flux × Visibility)!

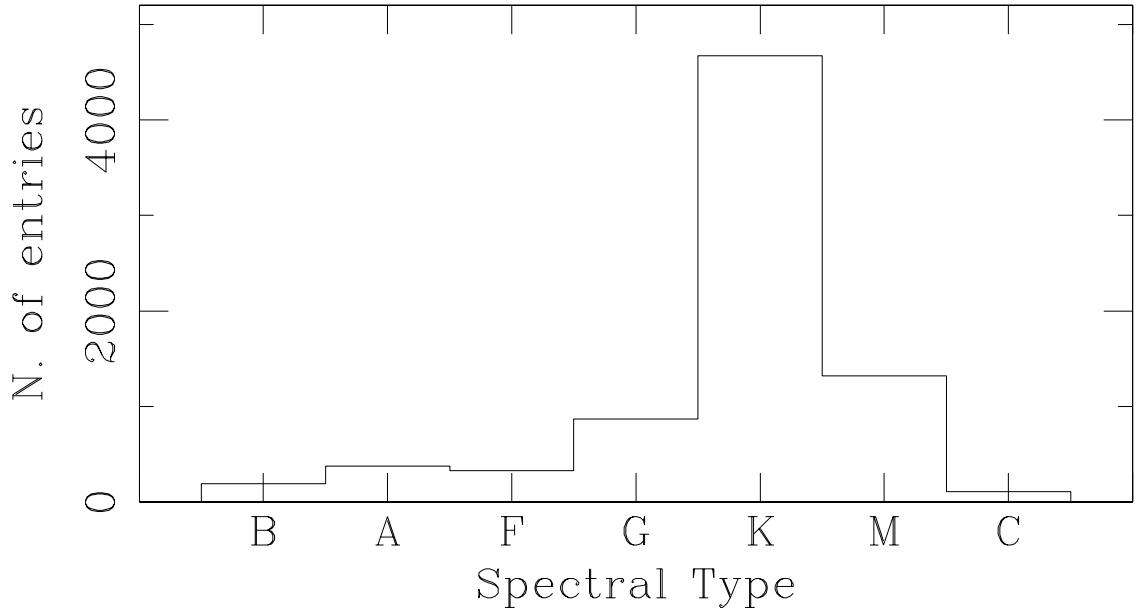

Figure 2.3: Distribution of the entries in the CHARM2 interferometric catalogue as a function of the spectral type. (Adopted from Richichi et al. 2005, Fig. 5).

stellar parameters such as diameter and effective temperature.

Quirrenbach et al. (1994) measured the diameters of the C-stars UU Aur, Y CVn, and TX Psc using the MarkIII[6] interferometer. The bands of measurements were $\lambda = 0.712, 0.754$, and 0.800 μm. The authors claim that in the band of investigation the C-stars show a weaker dependence of the radius with wavelength if compared with the O-rich stars. The nature of this difference is attributed to the different molecules present in the used wavelength ranges. While this region in O-rich stars is dominated by TiO, the CN and C_2 molecules mainly appear in spectra of C-stars. Evidence of temporal variability on the size of TX Psc was also found: the object seems to be larger when the star is brighter. Quirrenbach et al. (1994) combined these interferometric observations with stellar radii derived by lunar occultations of 6 other objects, and the effective temperatures for a set of 9 stars were determined. The effective temperatures were derived using bolometric fluxes from the literature.

Dyck et al. (1996) enlarged the sample of objects to 22. The measurements of radii were carried out with the IOTA interferometer in the near-IR (K-broad band). The authors tried to find a correlation between the effective temperatures determined in this way and Yamashita's spectral classification for C-stars (Yamashita 1972, 1975). Unfortunately, the error bars for the effective temperatures were so large ($\sim$ 300 K) that no clear correlation could be found.

Van Belle et al. (1997) observed five carbon Miras plus a few other M-type and S-

[6]The MarkIII Optical Interferometer was located on Mt. Wilson near Los Angeles, CA. The instrument was operated by the Remote Sensing Division of the Naval Research Laboratory, and it was decommissioned in 1992.

type Miras with the IOTA interferometer in the K-broad band. The error bars on the effective temperature are again rather large. Among the sources of uncertainty for the radii measurement the authors listed variability and possible departures from central symmetry.

Thompson et al. (2002) used this last instrument to monitor another carbon Mira, namely RZ Peg. The study was carried out using five narrow-band filters in the K-band wavelength range 2.0-2.4 μm. The goal of this work was to compare diameter changes of a Mira (pronounced variability) with the corresponding ones of a mildly-pulsating star of the same chemical type, DR Ser. The size of RZ Peg seems to increase with wavelength, the same is true for DR Ser, but the increase is 2.5 times less pronounced in the last case. In analogy to the O-rich objects, the authors used 2.2 μm as reference wavelength for the photospheric radius. But the investigated wavelength range is contaminated by molecular opacity (see Fig. 3.2), therefore it should not be used for the C-stars (unless the star is hydrostatic).

Chagnon et al (2002) presented L'-band interferometric measurements of eighteen evolved stars. The UD-diameter of a carbon-rich Mira is among the results of this work. The same object was also studied in van Belle et al. (1997). The UD size in the K-band from the latter work is 3 times smaller than the one obtained in the L'-band.

A milestone of the interferometric studies on AGB stars is the paper of Ragland et al. (2006). The authors used the closure phase of IOTA in the H-band in order to investigate asymmetries on the surface of a sample of 56 giants of different chemical and variability type. Asymmetries were already detected in previous studies in terms of deviation from circular symmetry (i.e. elliptical shape), or compact structures localised on the top of the photosphere. Around 30% of the total sample of objects showed a non zero closure phase. The signature was found much more frequently among the Miras and irregular variables than for the semiregular variables. In terms of chemistry the percentage of objects with non-zero closure phase was almost equally distributed between carbon- and oxygen-rich stars. The authors also investigated the distribution of the asymmetries geometrically speaking: it appears that the structures were either on the surface of the objects, or right in front of it (in the direction of the line-of-sight). The possible interpretations are various: asymmetries driven by large convective cells (Schwarzschild 1975), discrete dust cloud formation like in R Coronae Borealis stars or interaction with a companion (a star or even a planet). It is interesting that the asymmetries were detected always in the range of 1.5-2 stellar radii, and they are more prevalent among the Mira variables.

The first work on C-stars with the latest generation of interferometers was carried out by Ohnaka et al. (2007). The authors observed the carbon Mira V Oph in the mid-IR with VLTI/MIDI. The aims of the work were to study the variability of the circumstellar envelope where C_2H_2+HCN and dust emission are the main contributors to the opacity. One of the main results of this work is that a small variability effect is detected at the scales of 2-3 stellar radii. The object appears smaller around the minimum light (visual phase of ~ 0.49) than at other visual phases (e.g., 0.18 or 0.65). During the last year two theses including works with MIDI and C-stars were published: Zhao-Geisler (2010) and Ladjal (2011). Zhao-Geisler (2010) analysed the MIDI data of V Hya and used geometric models for the interpretation. Ladjal (2011) presented main parameters of the dusty shells of 5

targets (AQ Sgr, TW Hor, U Ant, V Pav, and W Pic). One of the aims was to confine the region where dust condensates. The authors identified a wide region, between 5 and 18 stellar radii, where grains of amorphous carbon and SiC can condensate.

Chapter 3

Synthetic intensity and visibility profiles for pulsating C-stars

This chapter is based on the paper:

Interferometric properties of pulsating C-rich AGB stars.
Intensity profiles and uniform disc diameters of dynamic model atmospheres.

C. Paladini, B. Aringer, J. Hron, W. Nowotny, S. Sacuto, S. Höfner, 2009, A&A 501, 1073

Abstract: On the basis of a set of dynamic model atmospheres of C-rich AGB stars, we present the first theoretical study of centre-to-limb variation (CLV) properties and relative radius interpretation on narrow and broad-band filters. We computed visibility profiles and the equivalent uniform disc (UD) radii to investigate the dependence of these quantities on the wavelength and pulsation phase. After an accurate morphological analysis of the visibility and intensity profiles determined in narrow and broad-band filters, we fitted our visibility profiles with a UD function simulating the observational approach. The UD-radii were computed using three different fitting-methods to investigate the influence of the visibility sampling profile: single point, two points and a least squares method. The intensity and visibility profiles of models characterises by mass loss show a behaviour very different from a UD. We found that UD-radii are wavelength dependent and that this dependence is stronger if mass loss is present. Strong opacity contributions from C_2H_2 affect all radius measurements at 3 μm and in the N-band, resulting in higher values for the UD-radii. In the case of models with mass loss the predicted behaviour of UD-radii versus phase is complicated, while the radial changes are almost sinusoidal for models without mass loss. Compared to the M-type stars, for the C-stars no windows are available for measuring the pure continuum.

3.1 Introduction

The Asymptotic Giant Branch (AGB) is a late evolutionary stage of stars with masses lower than about $8\,M_{\odot}$. The objects on the AGB are characterised by a degenerate C-O core and He/H-burning shells, a convective envelope, and a very extended atmosphere containing molecules and in many cases even dust grains. The atmospheres are affected by the pulsation of the interior creating shocks in the outer layers. Because of the third dredge-up, the AGB stars may have $C/O > 1$ (Iben & Renzini 1983) and therefore their spectra maybe dominated by features of carbon species such as C_2, C_2H_2, C_3, CN, and HCN (Goebel et al. 1981, Joyce 1998, Lançon et al. 2000, Loidl et al. 2001, Yamamura & de Jong 2000). These are the classical carbon stars. In these objects, dust is mainly present in the form of amorphous carbon grains.

Studying stellar atmospheres is essential to a clearer comprehension of this late stage of stellar evolution, the complicated interaction of pulsation and atmospheric structure, and the processes of dust formation and mass loss. The atmospheres of C-rich AGB stars with no pronounced pulsation can be described by hydrostatic models (Jørgensen et al. 2000, Loidl et al. 2001). As the stars evolve, the effective temperatures decrease and the atmospheres become more extended. At the same time, the effects of time-dependent phenomena (dynamic processes) become important and static models are no longer a good approximation. More sophisticated tools are needed to describe these objects i.e., dynamic model atmospheres. The status of modelling atmospheres of cool AGB stars is summarised in different reviews by Willson (2000), Woitke (2003), and Höfner (2005, 2007, 2009). Comparison of dynamic models with spectroscopy for C-rich stars can be found in Hron et al. (1998), Loidl et al. (2001), Gautschy-Loidl et al. (2004, henceforth GL04), Nowotny et al. (2005a,b), Nowotny (2005), and Nowotny et al. (2010).

Because of their large atmospheric extension and their high brightness in the red and infrared, AGB stars are perfect candidates for interferometric investigations. Moreover, since most observed AGB stars are very far away (at distances larger than 100 pc), only the resolution reached by optical interferometry allows a study of the close circumstellar environment of these objects.

The complex nature of their atmospheres raises the question of how a unique radius can be defined for these stars. Several radius definitions have been used, as summarised in the reviews of Baschek et al. (1991) and Scholz (2003, henceforth S03). This is not an important problem when dealing with objects that have a less extended and almost hydrostatic atmosphere, because in most cases the different definitions of radius converge to a similar final result. However, one can find large differences when the envelope of the star is affected by the phenomena of pulsation and mass loss. Baschek et al. (1991) proposed the use of the intensity radius, which is "a monochromatic (or filter-integrated) quantity depending on wavelength or on the position and width of a specific filter". This radius is determined from the centre-to-limb variation (CLV) as the point of inflection of the CLV curve, in other words as the point where the second derivative of the intensity profile equals zero. To determine this value, a very accurate knowledge of the CLV must, however, be available. For AGB stars, this can be difficult because the intensity profile of

an evolved object can exhibit a quite complicated behaviour and only a few data points are generally measured. In the case of a poorly measured CLV, the standard procedure is to use analytical functions such as the uniform disc (UD), a fully darkened disc (FDD), or a Gaussian fit to the profile. The result of this fit is the so-called fitting radius (S03).

Various theoretical and observational studies have been completed of the different properties of the CLV and radius interpretations for M-type stars, which are summarised in the review of S03. According to this review paper, the CLV shapes can be classified into four types:

- *small to moderate limb-darkening*, when the behaviour of the profile is well fitted by a UD;
- the *Gaussian-type CLV* is typical of extended atmospheres, where there is a large difference in temperature between the cool upper atmosphere layers and the deep layers where the continuum is formed;
- the *CLV with tail or protrusion-type extension* consists of two components, a central part described by the CLV of a near-continuum layer, and a tail shape given by the CLV of an outer shell;
- the *uncommon CLVs*, which are profiles exhibiting strange behaviour that is characteristic of complex extended and cool atmospheres.

The fitting radius is usually converted into a monochromatic optical depth radius R_λ, defined as the distance between the centre of the object and a layer with $\tau_\lambda = 1$ at a given wavelength. However this conversion must be confirmed very carefully: even in the case of near-continuum bandpasses, spectral features can contaminate the measurement of the fitting radius, as demonstrated by Jacob & Scholz (2002) or Aringer et al. (2008), which will then no longer represent a good approximation to the radius of the continuum layer.

Following the definition given by Scholz & Takeda (1987), a filter radius

$$R_{filt} = \frac{\int R_\lambda I^c_\lambda f_\lambda d\lambda}{\int I^c_\lambda f_\lambda d\lambda} \tag{3.1}$$

requires a good knowledge of the filter transmission curve, and the filter itself must be chosen carefully to avoid impure-filter-like effects (see Sect. 5 of S03 for more details). A very common definition of radius is the Rosseland radius, which corresponds to the distance between the stellar centre and the layer with Rosseland optical depth $\tau_{\rm Ross} = 1$. As in the case of the monochromatic optical depth radius, this quantity is not an observable, but is model dependent, and molecular contaminations are the main effect that has to be taken in account.

A suitable window at 1.04 μm for determining the continuum radius of M-type stars was discussed by Scholz & Takeda (1987), Hofmann et al. (1998), Jacob & Scholz (2002), and Tej et al. (2003a,b). These authors defined a narrow-bandpass located in this part of the spectrum, mostly free from contamination by molecules and lines. They indicated that this

radius is the most appropriate for studying the geometric pulsation. Unfortunately, such a window does not exist for C-rich AGB stars (cf. Sect. 3.5), and model assumptions must be made in defining a continuum radius. On the other hand, available dynamic atmospheric models for carbon-stars (Höfner et al. 2003) are more advanced than for M-type stars, the main reason being a clearer understanding of the dust formation.

Following the same approach adopted for M-stars by Scholz and collaborators, we started investigating the CLV characteristics of a set of dynamic models of pulsating C-stars (Hron et al. 2008). We summarise the main properties of the intensity and visibility profiles in narrow and broad-band filters for dynamic model atmospheres with and without mass loss (Sect. 3.2.2). We then use the UD function to determine the UD-radius of the models, and investigate the dependence of the latter upon wavelength and pulsation phase. We also discuss a new definition of a continuum radius for the carbon stars (Sect. 3.5).

3.2 Dynamic models and interferometry

The dynamic models used in this work are described in detail in Höfner et al. (2003), GL04, and Nowotny et al. (2005a).

3.2.1 Overview of the dynamic models

The models are spherically symmetric and characterised by time-dependent dynamics and frequency-dependent radiative transfer. Assuming LTE for both gas and dust, the radiative energy transport in the atmosphere and wind is computed using opacity sampling in typically 50-60 wavelength points. For the gas component, an energy equation is solved together with the dynamics, defining the gas temperature stratification (and allowing, in principle, for deviations from radiative equilibrium, e.g., in strong shocks). For the dust, on the other hand, the corresponding grain temperature is derived by assuming radiative equilibrium. Dust formation (in this sample only amorphous carbon dust is considered) is treated by the "moment method" (Gail & Sedlmayr 1988, Gauger et al. 1990), while the stellar pulsation is simulated by a piston at the inner boundary. Assuming a constant flux there, this leads to a sinusoidal bolometric light curve, which can be used to assign bolometric phases to each 'snapshot' of the model with $\varphi = 0$ corresponding to phases of maximum light.

In Table 3.1, the main parameters of the models used are summarised (see also GL04). Luminosity $L_\star$, effective temperature $T_\star$, and C/O ratio refer to the initial hydrostatic model used to start the dynamic computation. This model can be compared with classical model atmospheres such as MARCS (Gustafsson et al. 2008). The stellar radius $R_\star$ of the initial hydrostatic model is derived from $L_\star$ and $T_\star$ and corresponds to the Rosseland radius. The piston-velocity amplitude Δu_p and the period P are also input parameters that control the pulsation, while the mass-loss rate $\dot{\mathrm{M}}$ and the mean degree of condensation $\langle f_\mathrm{c} \rangle$ are the result of the dynamic computations. The free parameter f_L is introduced to adjust the amplitude of the luminosity variation at the inner boundary such that $L_\mathrm{in}(t) \propto f_\mathrm{L} \cdot R_\mathrm{in}^2(t)$ (GL04). All the initial models have a mass $M_\star = 1\,M_\odot$ and solar metallicity.

Table 3.1: Parameters of the dynamic model atmospheres used in this work.

Model	$L_\star$ [$L_\odot$]	$T_\star$ [K]	$R_\star$ [$R_\odot$]	C/O	Δu_p [km s^{-1}]	P [d]	f_L	$\Delta \mathrm{M_{bol}}$ [mag]	$\langle f_\mathrm{c} \rangle$	$\dot{M}$ [M$_\odot$ yr^{-1}]
D1	**10 000**	**2600**	492	**1.4**	**4.0**	**490**	**2.0**	**0.86**	**0.28**	$\mathbf{4.3 \cdot 10^{-6}}$
D2	10 000	2600	492	1.4	4.0	525	1.0	0.42	0.37	$5.9 \cdot 10^{-6}$
D3	7000	2600	412	1.4	6.0	490	1.5	1.07	0.40	$2.5 \cdot 10^{-6}$
D4	7000	2800	355	1.4	4.0	390	1.0	0.42	0.28	$2.4 \cdot 10^{-6}$
D5	7000	2800	355	1.4	5.0	390	1.0	0.53	0.33	$3.5 \cdot 10^{-6}$
N1	**5200**	**3200**	**234**	**1.1**	**2.0**	**295**	**1.0**	**0.13**	–	–
N2	7000	3000	309	1.1	2.0	390	1.0	0.23	–	–
N3	7000	3000	309	1.4	2.0	390	1.0	0.24	–	–
N4	7000	3000	309	1.4	4.0	390	1.0	0.48	–	–
N5	7000	2800	355	1.1	4.0	390	1.0	0.42	–	–

The models used in this work were chosen to investigate the effects of the different parameters on radius measurements, mass-loss, primarily, but also effective temperature, C/O and piston amplitude. Keeping this purpose in mind, the sample can be divided into two main groups: models with and without mass-loss (in Table 3.1, series D and N, respectively).

It was already mentioned that the pulsation of the inner layers can influence the outer atmosphere of the star. The propagation of the shock waves causes a levitation of the outer layers and in certain cases formation of dust grains can take place. The radiation pressure on the dust grains may drive a stellar wind characterised by terminal velocities V_∞ and mass-loss rates $\dot{\mathrm{M}}$. In Fig. 3.1, an example of the radial structure of the dynamic model atmosphere D1 (scaled to $R_\star$) is plotted for different phases. For comparison, the area covered by the model N1 is also shown grey-shaded. In particular, we show the effect of the dust-driven wind that appears on the model structure D1. The different atmospheric extensions of the two models are clearly evident.

In the series D of Table 3.1, two models, D1 and D2, differ from the others in having a higher luminosity ($L_\star$). The only distinction between these two models are different values of the period P and the parameter f_L. The effect on the structure of the atmosphere is that dust shells observed at a few $R/R_\star$ are more pronounced in the case of D2. The models D4 and D5 have the same luminosity, temperature, and period but different piston velocities and different resulting degrees of dust condensation. In the structure of D4, compared with D5, there is a smoother transition between the region dominated by pulsation and the one dominated by the dust-driven wind (see Fig. 2 of Nowotny et al. 2005a).

In the N set of models, we can identify N1 on the basis of its higher temperature and lower luminosity. All the other models have the same luminosity but differ in terms of other parameters. Both N3 and N4 are examples of studying the effect of different piston velocities on models without mass-loss. The atmospheric structure of N4 is more extended but the outer layers are not yet cool and dense enough for dust formation. N2 and N3 have different C/O ratios causing differences in their spectral features and in the estimation of the diameter at certain wavelengths (Sect. 3.5).

We use model D1 as a reference for models with mass-loss. GL04 compared this model with observed spectra of the star S Cep and demonstrated that different phases of D1 can reproduce the S Cep spectra shortward of $\approx 4\,\mu$m. The same model is in qualitative agreement with the observed CO and CN line-profile variations of S Cep and other Miras (Nowotny et al. 2005a,b). Concerning models without mass-loss, we use model N1 as a reference, which provides the best-fit solution of spectra and colour measurements for TX Psc in GL04. Each of these reference models also represents the most extreme case of its sub-group.

3.2.2 Deriving the synthetic intensity and visibility profiles

To compute the intensity and visibility profiles for each model we proceeded in the following way. For a given atmospheric structure (where temperature and density stratifications were both taken directly from the dynamical simulation), opacities were computed using the COMA code, originally developed by Aringer (2000): all important species, i.e., CO, CH, C_2, C_3, C_2H_2, HCN, and CN were included. The data sources used for the continuous opacity were presented in Lederer & Aringer (2009). Voigt profiles were used for atomic lines, while Doppler profiles were computed for the molecules. Conditions of LTE and a microturbulence value of $\xi = 2.5\,\mathrm{km\,s^{-1}}$ were assumed. All references to the molecular data are listed in Table 2 of Lederer & Aringer (2009). The source for the amorphous carbon opacity is Rouleau & Martin (1991). These input data agree with the previous works (Nowotny 2005, Lederer & Aringer 2009, Aringer et al. 2009), and with the opacities used in computing the dynamic models. Information about recent updates to the COMA code and opacity data can be found in Nowotny (2005), Lederer & Aringer (2009), Aringer et al. (2009), and Nowotny et al. (2010). The resolution of the opacity sampling adopted in our computations is 18 000. The resulting opacities were used as input to a spherical radiative transfer code that computes the spectrum at a selected resolution for a chosen wavelength range. In addition, the code computes the spatial intensity profiles for every frequency point of the calculation. Velocity effects were not taken into account in the radiative transfer.

The monochromatic spatial intensity profiles were subsequently convolved with different filter curves (narrow and broad-band) in the near- to mid-IR range to obtain averaged intensity profiles. The narrow-band filters were rectangular (transmission 1), while the broad-band filters are the standard filters from Bessel & Brett (1988). The visibility profiles were the two-dimensional Fourier transform of the intensity distribution of the object, but under the condition of spherical symmetry (as for our 1D models), this reduces to the more simple Hankel transform of the intensity profiles (e.g., Bracewell 1965).

The intensity and visibility profiles in the case of the broad-band filters were computed with the following procedure. Each broad-band filter was divided into a set of 10 narrow-band subfilters[1] and the squared broad-band visibility was computed as

[1]In principle, this should be done monochromatically but for computational reasons the usual number of narrow-band subfilters was limited to 10. However, we compared the resulting broad-band filters computed with a set of 10 narrow-band subfilters with the one computed with a set of 100 and 200 subfilters without finding any significant difference in the resulting broad-band visibility profile. We also emphasise that the

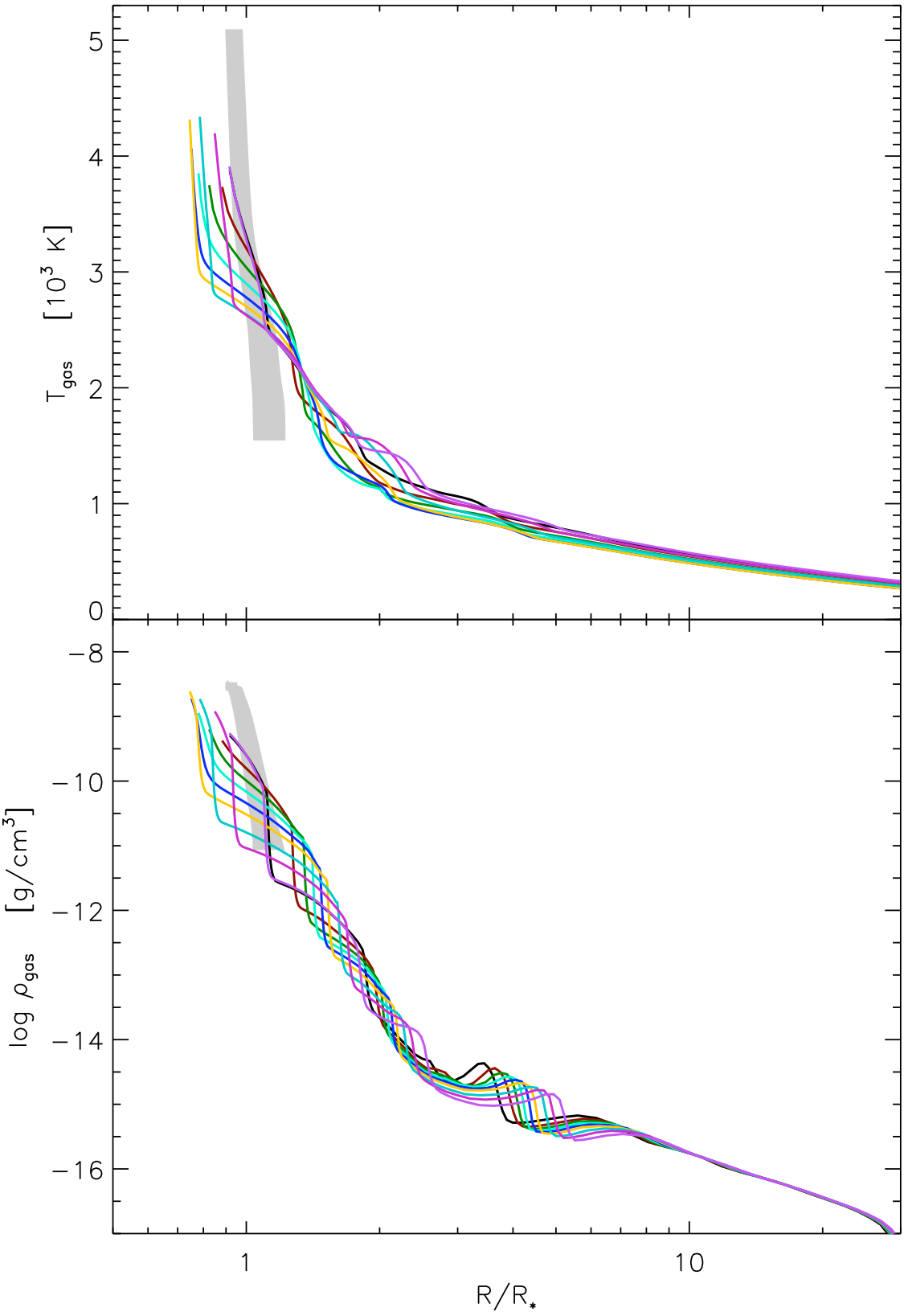

Figure 3.1: Radial structure of the dynamic model D1. Gas temperature (upper panel) and density (lower panel) are plotted for different phases during the pulsation period. For comparison, the grey-shaded area marks the range where the structure of the model N1 at different phases can be found. More details about the structure of the models can be found in the text and in Nowotny et al. (2005a,b).

Table 3.2: Definitions of the narrow- and broad-band filters.

Filter	Features	λ_c [μm]	$\Delta\lambda$ [μm]	Class
1.01	C_2, CN	1.01	0.02	I
1.09	CN	1.09	0.02	I
1.11	"cont"	1.11	0.02	I
1.51	CN+	1.51	0.02	I
1.53	C_2H_2, HCN, CN	1.53	0.02	**I**
1.575	CN	1.575	0.05	I
1.625	CN, CO	1.625	0.05	I
1.675	"cont"	1.675	0.05	I
1.775	C_2	1.775	0.05	I
2.175	CN	2.175	0.05	I
2.375	CO	2.375	0.05	I
3.175	C_2H_2, HCN, CN	3.175	0.05	**III**
3.525	"cont"	3.525	0.05	II
3.775	C_2H_2	3.775	0.05	II
3.825	C_2H_2	3.825	0.05	II
3.975	"cont"	3.975	0.05	II
9.975	"cont"	9.975	0.05	**II**
11.025	"cont"	11.025	0.05	II
12.025	C_2H_2	12.025	0.05	III
12.475	C_2H_2	12.475	0.05	III
12.775	C_2H_2	12.775	0.05	III
J		1.26	0.44	
H		1.65	0.38	
K		2.21	0.54	
L'		3.81	0.74	

$$V^2_{\rm broad} = \frac{\sum\limits_i (S_i^2 F_i^2 V_i^2)}{\sum\limits_i (S_i^2 F_i^2)}\,, \tag{3.2}$$

where the sum was calculated over all the narrow subfilters, $S_{\rm i}$ is the transfer function of the broad-band filter within the corresponding narrow-band subfilter, F_i is the flux integrated over the corresponding narrow-band subfilter, and V_i is the visibility of the narrow-band subfilter computed from the average intensity profile of the corresponding filters.

In the following two sections, we discuss the characteristics of the intensity and visibility profiles for different models and the effects of using different filters. In the case of broad-band filter we also discuss the so-called *band-width smearing effect* (Verhoelst 2005, Kervella et al. 2003).

maximum resolution for the computation of the broad-band filter is given by the opacity-sampling resolution.

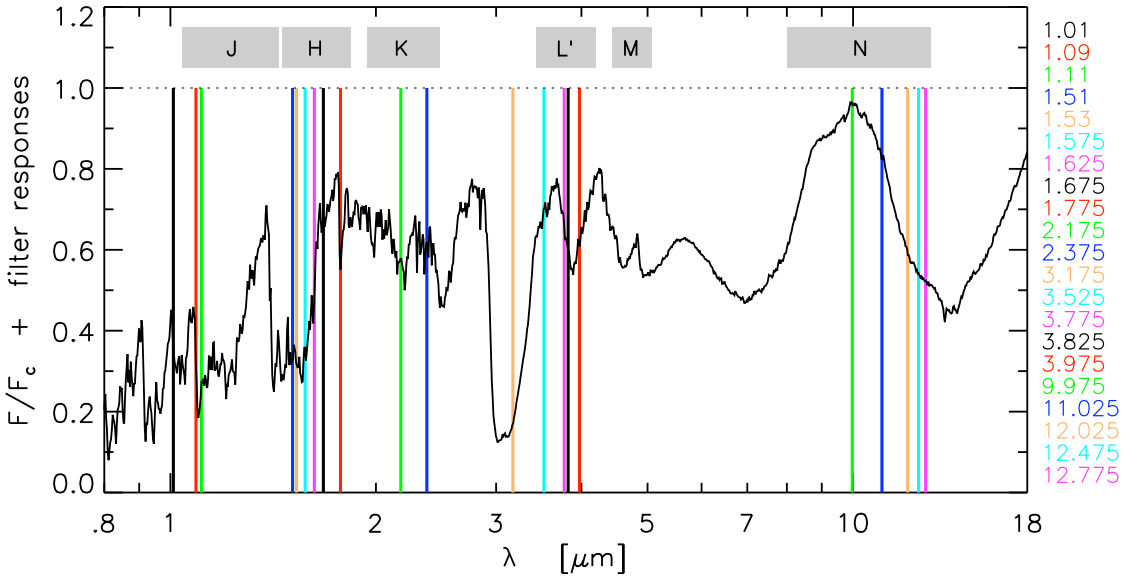

Figure 3.2: Synthetic spectrum ($R = 360$) calculated on the basis of the hydrostatic initial atmospheric structure of model D1. All necessary opacity sources (continuous, atoms, molecules, dust) are included for the spectral synthesis, (see Fig. 4 of Aringer et al. (2009) for the individual contributions of the different molecular species). The flux is normalised to a calculation for which only the continuous opacities were taken into account. Overplotted are the narrow-band filters as defined in Table 2, for which the central wavelengths in [μm] are given in the legend. In addition, the ranges of the broad-band filters are marked grey-shaded.

3.3 Synthetic profiles for narrow-band filters

Twenty-one narrow-band filters were defined in the near-to mid-IR range with a "resolution" ranging from 50 to 200 to study effects of different molecular features characteristic for C-star spectra, following the approach described in Bessel et al. (1989, 1996). Figure 3.2 shows the location of the filters on top of a typical synthetic (continuum-normalised) spectrum of a C-type star for illustration. Table 3.2 gives an overview of our complete set of filters with name of the bands, characteristic features (for narrow-bands), central wavelengths, band widths, and morphological class. A few of these filters are labelled "cont" meaning that the contamination by molecular features is comparably low in this spectral region, but this does not necessarily represent the true continuum. At extremely high spectral resolutions, it may be possible to identify very narrow windows in the spectrum of a C-star, where no molecular lines are located (e.g., Fig. 6 in Nowotny et al. 2005b). However, in general and at the resolutions available nowadays, the observed spectra of evolved C-type stars in the visual and IR are crowded with absorption features. Because of this blending, the continuum level F/F_c=1 is never reached as in Fig. 3.2. This effect is more and more pronounced with lower effective temperatures and decreasing spectral resolutions (cf. Nowotny et al. 2010).

As a first step, we study the morphology of different intensity and visibility profiles. We then proceed to investigate the main opacity contributors to the features that appear in the profiles. For this purpose, we compute three different sets of intensity and visibility

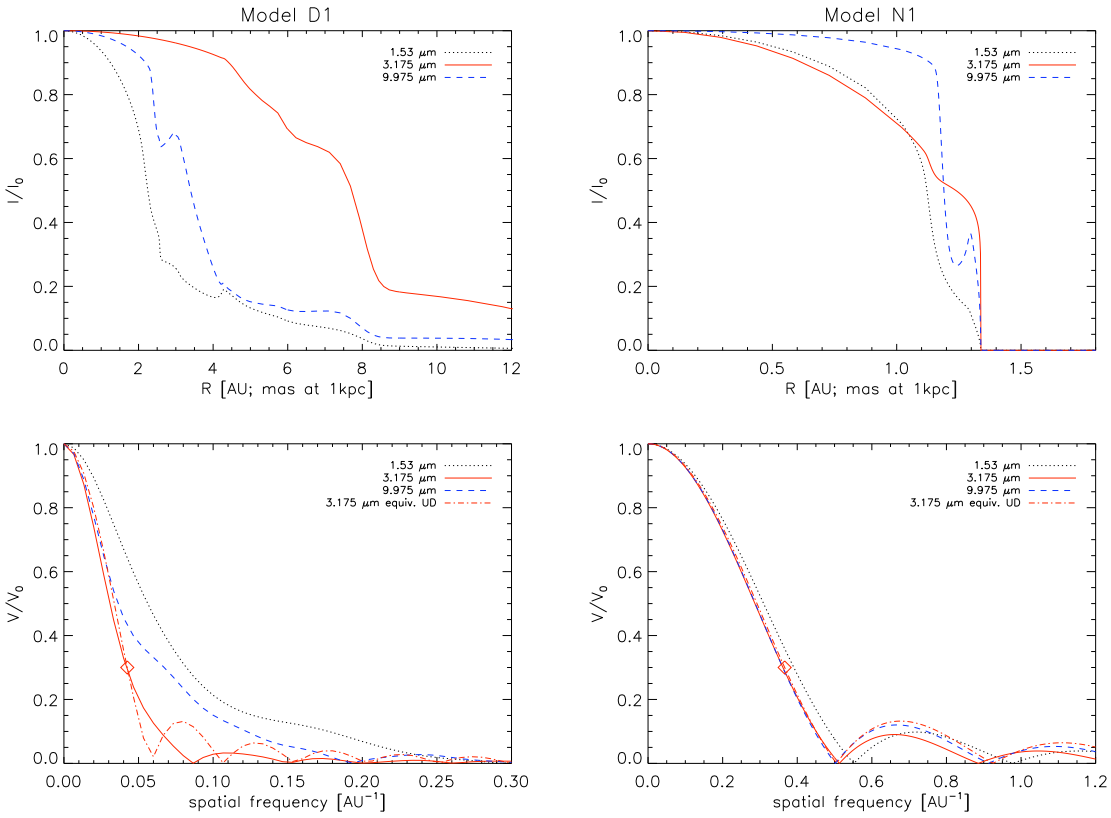

Figure 3.3: Intensity and visibility profiles for the narrow-band filters at the maximum phase of the mass-loss model D1 on the left side, and the model without mass-loss N1 on the right side. All the opacities are included in the computations. Profiles for three representative filters are shown together with the equivalent UD function for the 3.175 μm filter. The UD is fitted to the visibility point $V = 0.3$ marked with the diamond (details in Sect. 3.5).

profiles for the two reference models: (i) profiles including all necessary opacity sources, i.e., continuous, atomic, molecular, and dust opacities; (ii) profiles where the opacities of dust were neglected, to analyse only molecular and atomic contributions; and (iii) profiles for which only the continuous gas opacity is considered, to derive theoretical continuum profiles.

For the narrow-band filters, the intensity profiles of models with mass-loss can be divided into three morphological classes listed in the last column of Table 3.2. It turns out that this classification is related mainly to the wavelength region with the exception of the filter 3.175 μm, which belongs to the third class (that contains filters centred around 12 μm) instead of the second (that contains all the other filters in the 3 μm region, plus the 9 and 11 μm filters). In Fig. 3.3, the intensity and visibility profiles for the representative filters of each class are illustrated. Models with mass-loss (left panels) are more extended than models without mass-loss (right), and their intensity profiles fit into the category of "uncommon profiles" of S03.

The first class of profiles contains the filters in the near IR from 1.01 μm to 2.375 μm.

It can be well represented by filter 1.53 (C_2H_2, HCN, CN). Its morphology is characterised first by a limb-darkened disc, followed by a bump caused by molecular contributions, and a peak indicating the inner radius of the dust shell. At 1.53 μm, a feature due to the molecular species of C_2H_2 and HCN is predicted by some of the cool dynamic models with a wind (GL04). This feature was observed in the spectra of cool C-rich Miras, such as R Lep (Lançon et al. 2000), V Cyg, cya 41 (faint Cygnus field star), and some other faint high-Galactic-latitude carbon stars (Joyce 1998).

The third class of profiles is represented by filter 3.175 (C_2H_2, HCN), which is placed right in the centre of an extremely strong absorption feature characteristic of C-star spectra (Fig. 3.2). Observations in this spectral region are a very powerful tool in understanding the upper photosphere. Here, the inner central part of the intensity profile can be described by an extended plateau due to the strong molecular opacity. All the filters defined around 12 μm – where C_2H_2 has an enhanced absorption – also belong to this class.

The second class of profiles has a behaviour in-between that of the two illustrated before with an indication of an outer dust shell around 8 AU. It is represented by filter 9.975 ("cont") and covers the behaviour of the filter at 11.025 μm plus those defined in the 3 μm region (except 3.175 μm).

In Fourier space, the three representative visibility profiles also differ markedly (lower left panel of Fig. 3.3). The UD function, computed by fitting the point at visibility[2] $V = 0.3$ of the 3.175 μm profile (for details, see Sect. 3.5), is shown for comparison in Fig. 3.3. The visibility profiles from the model and the UD differ at visibility < 0.2, and in this region the model profile is less steep and has a less pronounced second lobe compared with the UD.

In the right panel of Fig. 3.3 we present the intensity and visibility profiles for the phase of maximum luminosity of the reference model without mass-loss. As expected from the model structures, the intensity profiles are more compact than those for models with mass-loss. In the intensity profile corresponding to the filter 9.975 around 1.3 AU, a peak related to the molecular opacity of C_3 is visible. Jørgensen et al. (2000) showed that C_3 is particularly sensitive to the temperature-pressure structure and, hence, tends to be found in narrower regions than other molecules. The peak visible at 3 AU of the profile of the model D1 is produced mainly by C_3 but also produce other molecular and dust opacity contributions. These 9.975 μm peaks in the intensity profiles mean a marginally "ring"-type appearance of the disc. The shape of the intensity profiles for the models without mass-loss can be classified as having small to moderate limb-darkening (S03). In the Fourier space, the visibility profiles of the three filters for the series N look very similar, apart from tiny differences especially in the second lobe. In all cases, they can be approximated well by a UD in the first lobe.

Plots of theoretical continuum profiles for both reference models are very similar to UDs. The classification of filters is also valid for all other models in our sample listed in Table 3.1.

[2]All the visibility values V have to be interpreted as normalised visibilities V/V_0.

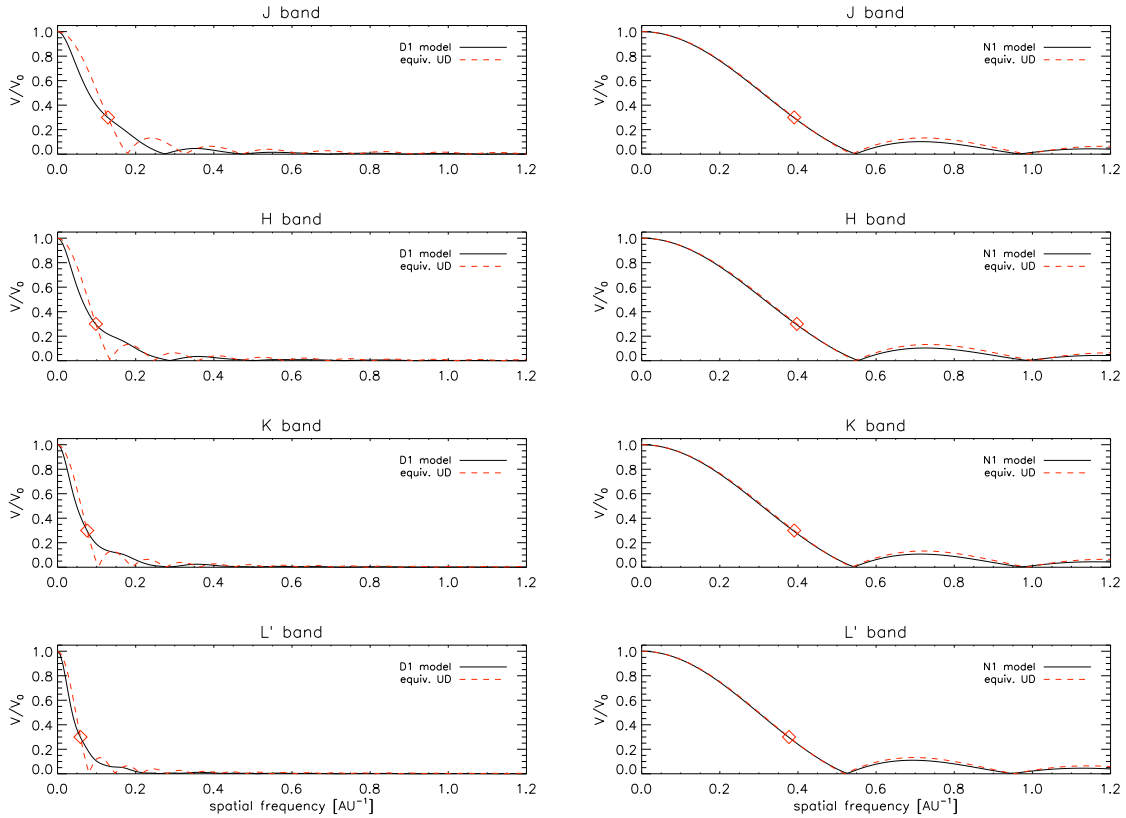

Figure 3.4: Visibility profiles computed in broad-band filters for the maximum phase of the model D1 with mass-loss on the left side, and the model N1 without mass-loss on the right side. The solid line corresponds to the model, while the dashed line is the equivalent UD computed by fitting one point at visibility $V = 0.3$.

3.4 Synthetic profiles for broad-band filters

We also investigated intensity and visibility profiles for the broad-band filters J, H, K, and L′, because several observations of C-stars exist in these filters.

In Fig. 3.4, the resulting broad-band visibility profiles computed for the maximum phase of the reference models are shown together with the corresponding UD visibility, which was calculated with the one-point-fit method at $V = 0.3$. In the case of model D1 (with mass-loss), the broad-band profiles exhibit a completely different behaviour from that of the UD. The slopes of the model profiles are always less steep than the corresponding UD at $V \lesssim 0.2$. The synthetic visibility profile shows a characteristic tail-shape instead of the clearly pronounced second lobe in the UD. The broad-band visibilities for the model N1 are represented well by a UD and, as in the case of the narrow-bands, the major (but small) differences occur in the second lobe of the profiles.

When comparing observations with in a broad-band filter, particular attention must be paid to the smearing effect (also known as bandwidth smearing) affecting the measurements (Davis et al. 2000, Kervella et al. 2003, Verhoelst 2005). This is the chromatic aberration caused by observations never being monochromatic but integrated over a certain wavelength

range defined by the broad-band filter curve. Furthermore, each physical baseline, B, corresponds to a different spatial frequency u with $u = \frac{B}{\lambda}$. Calculated at a given projected baseline, a broad-band visibility will result in a superposition of all the monochromatic profiles over the width of the band.

According to Kervella et al. (2003) and Wittkowski et al. (2004b), the bandwidth smearing is stronger at low visibilities close to the first zero of the visibility profile. We demonstrated that the shape of the profile also plays an important role in the smearing effect.

We investigated this effect with the help of our reference models in the J, H, K, and L' filters. As explained in Sect. 3.2.2, the broad-band profile was computed by dividing the broad-band interval into ten narrow-band subfilters and then averaging the resulting profiles. To take into account the bandwidth smearing, we again divided the broad-band interval into the same set of 10 narrow-band subfilters. The spatial frequencies were then converted from AU^{-1} to baselines in meters, fixing the distance for an hypothetical object (500 pc) and using as corresponding "monochromatic wavelength" the respective central wavelength of the narrow-band filter. The resulting broad-band profile was then obtained using the above Eq. (4.1).

Figure 3.5 illustrates the bandwidth-smearing effect in the K band for the two reference model atmospheres (D1 on the left and N1 on the right). In the upper panels, it is clearly visible in the upper panels that the profiles of the narrow-band subfilters reach the first zero at different baselines. The bandwidth-smearing causes the broad-band profile to never reach zero, as noted in Kervella et al. (2003). We compared the resulting visibility curve with a corresponding one obtained without taking into account the bandwidth effect. The result of this experiment can be seen in the lower panels of Fig. 3.5, where we plot the difference (in percentage) between the visibility with and without taking into account the bandwidth smearing (BW and NBW respectively). For both types of models – with and without mass-loss – the smearing accounts for the differences in the profiles, which at certain baselines reaches more than 70%. For model N1, the major difference occurs close to the first and the second zero and is negligible elsewhere (as already shown in Kervella et al. 2003, Wittkowski et al. 2004b), while in the case of the model D1 the behaviour of the relative difference is less obvious. This result is also confirmed for the other broad-band profiles. However, it obviously depends on the shape of the visibility profile and hence on the model.

In all the cases, we conclude it is important to compute accurate profiles by taking into account the bandwidth smearing.

3.5 Uniform disc (UD) radii

For all models in the sample and all considered filters, we computed the equivalent UD-radii using three different methods: (i) a single-point fit at visibility $V = 0.3$, (ii) a two-point fit at visibilities $V = 0.1$ and 0.4, and (iii) finally a non-linear least squares fit using a Levenberg-Marquardt algorithm method, and taking into account all the points with visibility $V > 0.1$. As emphasised in Sect. 5 of Ireland et al. (2004a), none of these procedures are fully

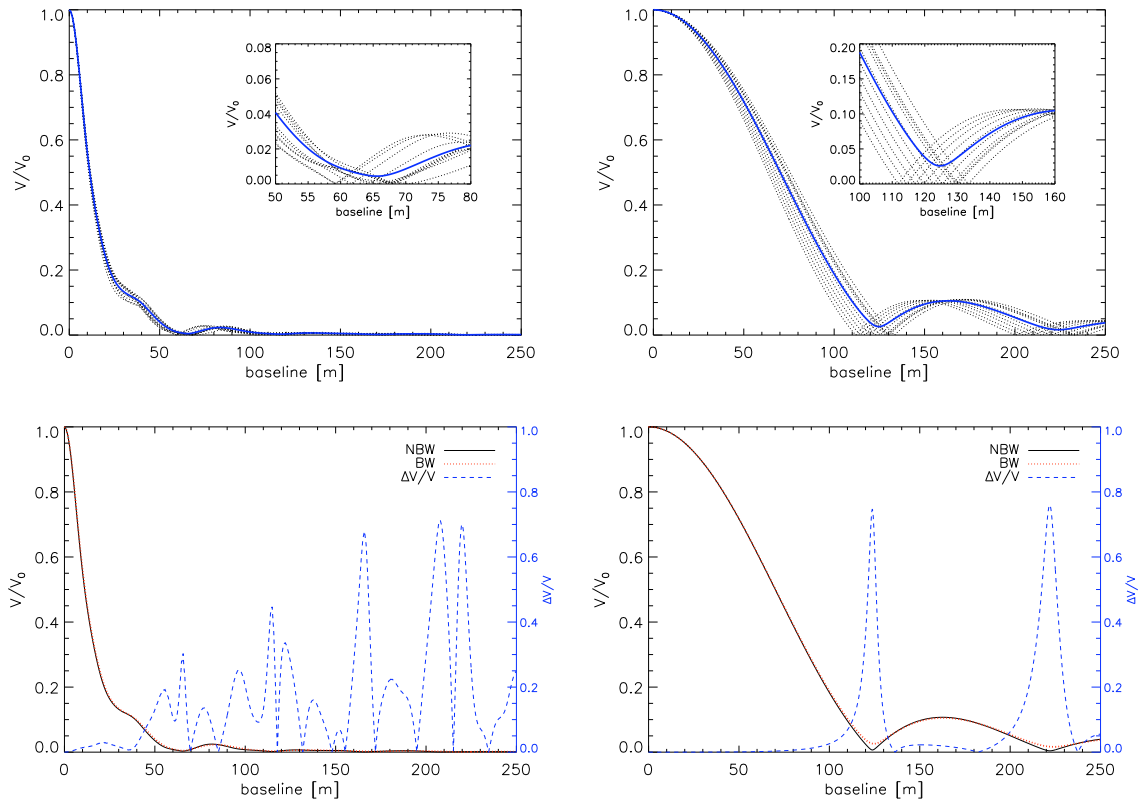

Figure 3.5: Representation of the bandwidth smearing effect for the phase maximum of the model D1 (left panels) and N1 (right panels) in the K-band. In the upper panels, visibility profiles are shown as a function of baseline for the individual narrow-band subfilters (dotted lines) and for the resulting broad-band filter (solid line), computed by taking into account the bandwidth smearing. In the inset, a zoom of the region around the first zero is represented. The lower panels show the visibility profiles computed with bandwidth smearing (BW, solid line), and profiles computed neglecting the effect (NBW, dotted line). The dashed lines present the difference between the two profiles (scale on the right y-axis).

consistent because the UD does not represent the true shape of the profile (especially in the case of models with mass-loss). However, the UD is often chosen to interpret interferometric data with a small sampling of the visibility curve. Thus, the three different methods were used in this work to investigate the influence of the visibility profile sampling, in particular when only a few visibility measurements are available.

We used the visibility $V = 0.3$ for the one-point-fit following Ireland et al. (2004a,b), who identified this point as a good estimator of the object size. While this is true for the M-type models presented in Ireland et al. (2004a,b), it is not obvious for our C-rich models with mass-loss, which are very far from exhibiting a UD behaviour (Sect. 3.3). However, keeping in mind that a UD is a first approximation, we also used this value for our computations of the one-point fit.

The aim of this section is to study the behaviour of the UD-radius versus both wavelength and phase, as well as the dependence on the different parameters of the models.

As we pointed out previously, while for the M-type stars the continuum radius can be measured around 1.04 μm (e.g. Jacob & Scholz 2002), our calculations show that the C-star spectra do not contain any suitable window for this determination. However, the continuum radius is a relevant quantity to modelling the stellar interior and pulsation. Therefore, we computed for our sample of dynamic model atmospheres a set of profiles by taking into account only the continuous gas opacity. The resulting profiles correspond to the pure theoretical continuum absorption of the models. An equivalent UD-continuum radius was computed for this theoretical "pure-continuum" profile. This allows us to study how the UD-continuum radius depends upon wavelength and phase and may provide a possibility of converting observed radii into the continuum radius.

3.5.1 Uniform disc radii as a function of wavelength

The UD-radii resulting from least square fits at the maximum phase of all models are plotted versus wavelength in Fig. 3.6. They are scaled to $R_\star$ to minimise the effects of the initial stellar parameters and enhance the effects of the dynamics and dust formation. The UD-continuum radii are represented with the cross symbols for D1 (upper panel) and N1 (lower panel). The major difference is found between models with and without mass-loss. In both cases, the UD-radius generally increases with wavelength, but this behaviour is more pronounced for mass-loss models. At 3.175 μm, there is a notable "discontinuity" (value significantly higher than its surroundings) in the UD-radius due to the high C_2H_2 opacity. The UD-continuum radius is almost completely independent of wavelength and can thus be adopted as a good reference radius (although it is not observable for C-stars!). In fact, a small increase in its size can hardly be noted at longer wavelengths (see Fig. 3.6), and at 1.6 μm the minimum opacity of H^- is visible. The ratio of the apparent size of the continuum radius at 11 μm to that at 2.2 μm is 1.14 in the case of the model with mass-loss D1 and 1.06 for the model without mass-loss N1. This change in apparent size can be explained by the electron-hydrogen continuum, according to Tatebe & Townes (2006). All the models show a value of UD-continuum radius that is lower than the stellar radius $R_\star$. This is a consequence of the definition of $R_\star$.

Comparing the effect of the different model parameters, we can say that model extensions increase with decreasing effective temperature and higher mass-loss values. The models D1 and D2 for example are identifiable as having a higher mass-loss rate for D2 because of the different period and f_L value. The resulting UD-radii for D2 are systematically higher than that for D1. D5 has a higher piston velocity, and consequently a higher mass-loss, compared to D4, and the UD-radii obtained are larger. A comparison between D1-D2 and D4-D5 in Fig. 3.6 shows that the effect of the mass-loss rate on the UD-radius is larger beyond 3 μm. The model D3 has a systematically larger UD-radii than the one in the model D4 for the region between 1 and 2 μm and at 9 μm. At 3.175 μm, the trend is inverted, while for the other filters at 3 μm and at the longer wavelengths, the resulting UD-radii is the same for the two models. D3 and D4 differ in terms of temperature (2 600 K for D3 and 2 800 K for D4), piston velocity, period, and f_L, while the resulting mass-loss rate is quite similar.

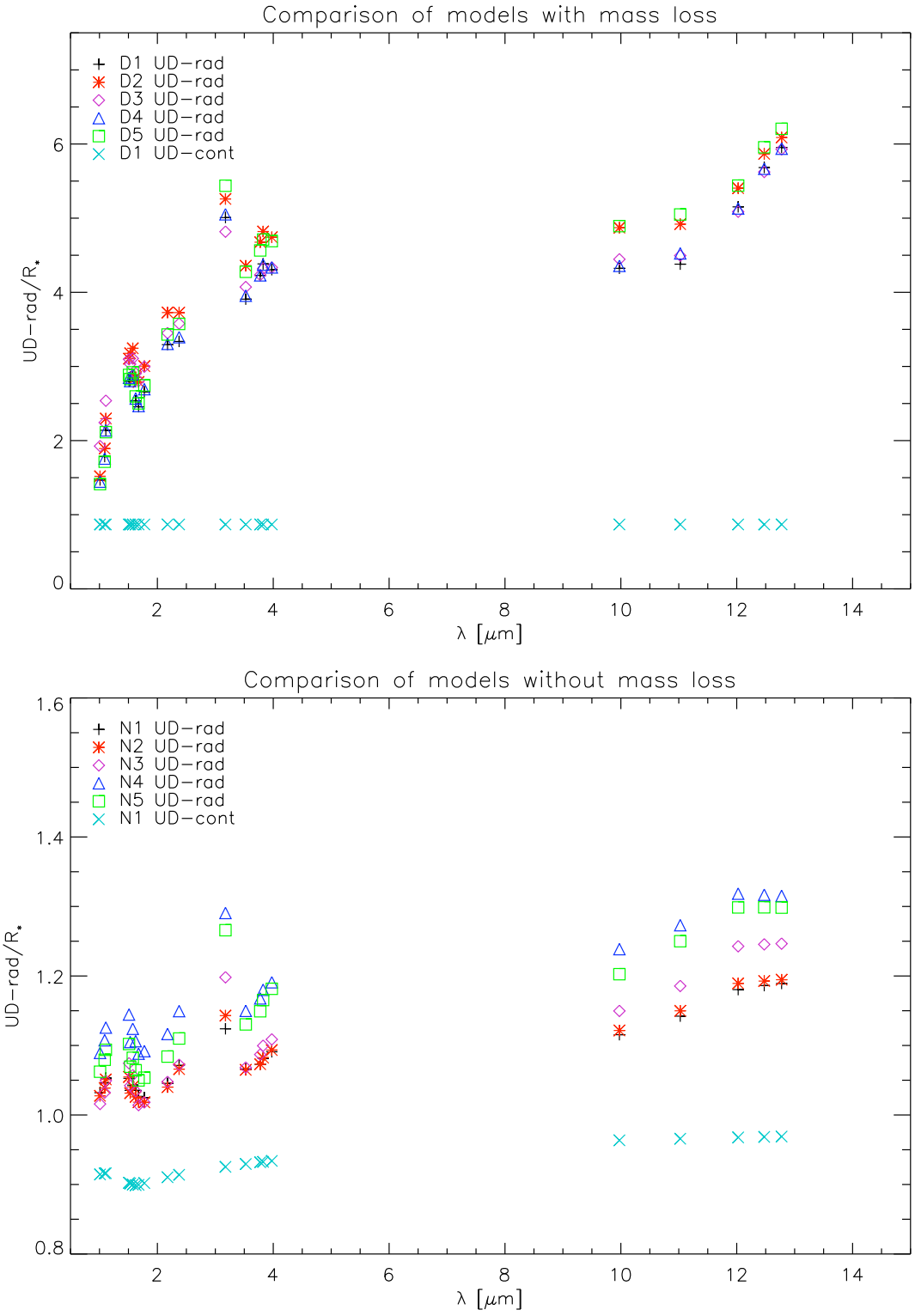

Figure 3.6: UD-radii versus wavelength for the maximum phase of different models with (upper panel) and without (lower panel) mass-loss. The cross symbol represents the UD-continuum radius computed for the two reference models (D1, N1). The method used for the UD determination is a least squares fit using all the points of the synthetic profile with visibility > 0.1.

On the other hand, in the absence of dusty winds the models with the same parameters except for C/O (N2 versus N3) have very similar radii. The difference is barely detectable at 3 μm and at longer wavelengths. If, besides different C/O ratios, the temperature of the model also changes (e.g., as between N4 and N5), the resulting UD-radii show more pronounced differences. The UD-radii of N1 always overlap with that of N2, even if the models have different temperatures (higher for N1), luminosity (higher for N2), and period (longer for N2). N3 and N4 have all the same parameters except for the piston velocity, and the resulting UD-radii is larger for the second model, which has a higher value of $\Delta u_{\rm p}$. Model N4 is also the most extended among its subgroup.

3.5.2 Separating models observationally

Compared with classical hydrostatic models, the dynamic model atmospheres provide, a self-consistent treatment of time-dependent phenomena (shock propagation, stellar wind, dust formation). It is thus of course highly interesting if observed UD-radii at different wavelengths can be used to distinguish between the different models and then assign a given model to a given star.

If the model UD-radii are *not* scaled to their respective $R_\star$, the D models differ between 30% and 50%. These differences should be detectable given the typical distance uncertainties of 20%. However, as discussed above, this would mostly separate the effects of the fundamental stellar parameters (initial radius, luminosity) and allows to differentiate between N and D models, but dynamic effects within each series are only of the order of between 10% and 25%. This can be seen in Fig. 3.6 or if one scales each model to e.g., its UD-radius in the K-band. The latter approach would be the most sensitive since it eliminates errors in the distance (provided the measurements were completed at the same pulsating phase, better within the same pulsation cycle). Assuming that individual UD-radii can be determined with an accuracy between 5% and 10%, the dynamic effects are (barely) identifiable in the D models. The most sensitive wavelengths in this respect would be filters in the K- and L-band. The N-band shows a similar sensitivity to dynamic effects, although at a reduced observational accuracy. For the N models, these effects are less then 10%, the largest difference again occurring redward of the K-band. Nevertheless, the optimal strategy for choosing the correct dynamic model is to combine spectroscopic and interferometric observations.

Finally, we note, that for a larger grid of models (e.g., Mattsson et al. 2010), a wider separation of models might become evident. This will however be the subject of a future paper.

3.5.3 UD-radii as a function of time

The behaviour of the UD-radius as a function of phase predicted by the models is rather complex, especially in the case of mass-losing models. In Fig. 3.7, the UD-radius at a given wavelength/filter versus phase is plotted for the two reference models. The presence of molecular and dust opacities increases the UD-radius significantly compared to the UD-

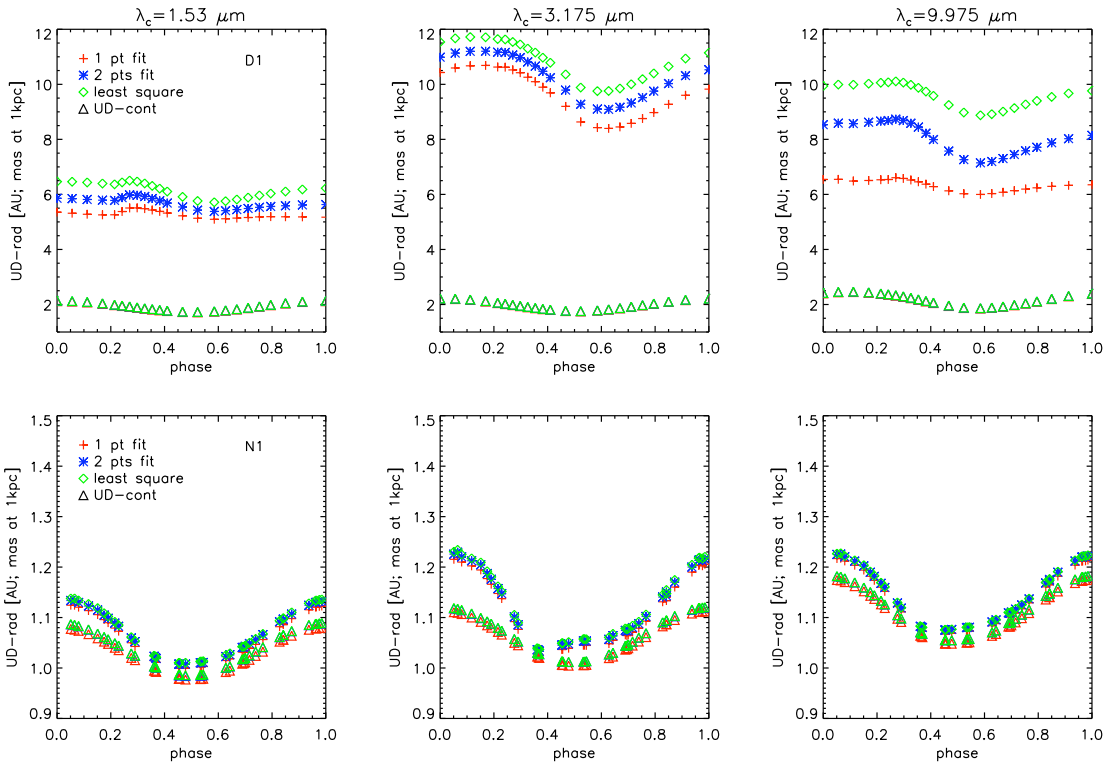

Figure 3.7: UD-radii versus phase are shown for three different narrow-band filters. The three upper panels represent results for the dynamic model D1 with mass-loss, the three panels at the bottom being for the model N1 without mass-loss. Triangles are for UD-radius computed by taking into account only continuum opacity. For the continuum, the same symbol is used for the different methods because there is no appreciable difference between the results. Crosses, stars, and diamonds represent the different methods (one point, two points, least squares, respectively) used for fitting the visibility profiles of models with UDs.

continuum radius. In both types of models, we can observe the periodic movement in the stellar interior, which is pronounced to a different degree for different models of Table 3.1. The periodic variation in the UD-radius in all the models without mass-loss reflects how the movement of the complete atmosphere closely follows the pulsation. The time scales introduced by dust formation in the atmosphere of the models with mass-loss may deform the sinusoidal pattern, a behaviour that can be reproduced by outer layers that do not move parallel to the inner ones. This is represented well in Fig. 2 of Höfner et al. (2003), but one should keep in mind that the movement of theoretical mass shells should not be directly compared to the changes in the atmospheric radius-density structure that we observe by interferometric measurements.

From the lower three panels of Fig. 3.7 (no mass-loss), it is obvious that there is no significant difference between the UD-radius and UD-continuum radius for the model N1, especially for the 1.53 μm and 9.975 μm filter close to minimum luminosity. We find the largest difference for the maximum luminosity ($\varphi = 0$), where the ratio of the UD-radius to the UD-continuum radius is 1.09 for the filter 3.175 μm and 1.04 for the other two filters.

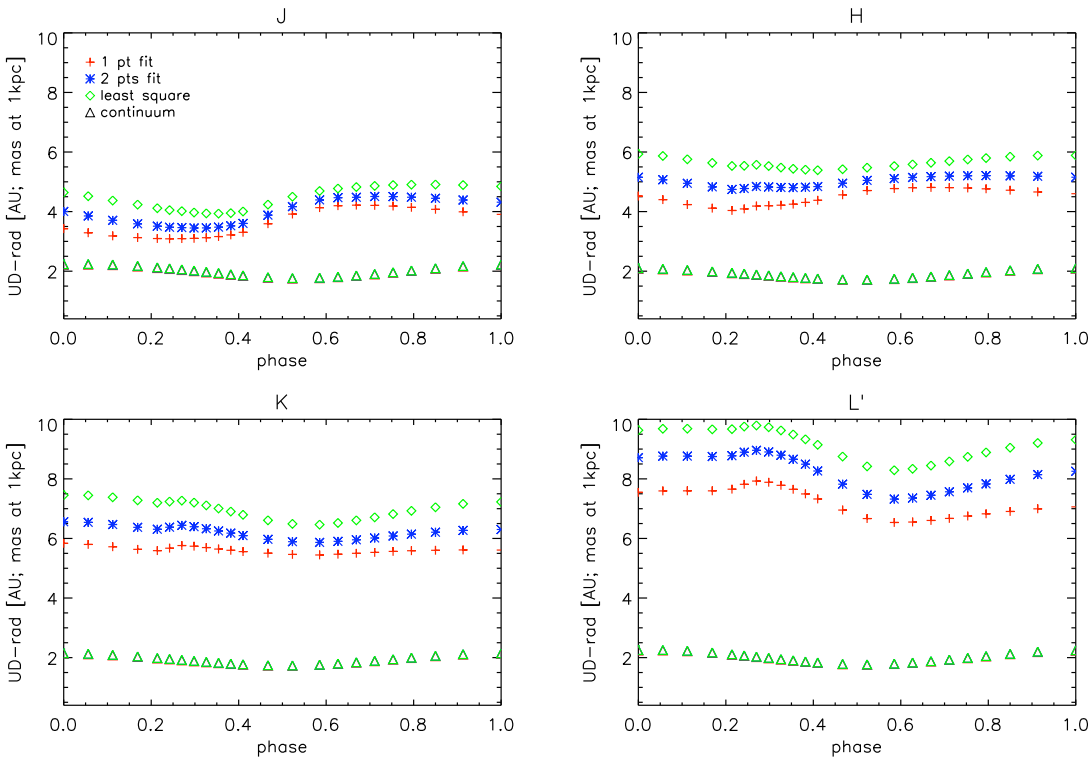

Figure 3.8: UD-Radius versus phase for $JHKL'$ broad-band filters. The four panels show the results for the model D1 with mass-loss.Plot symbols are the same as in Fig. 3.7.

For the model D1 (upper panels), the value of the same ratio is 3.03 for the filter 1.53 μm, 4.29 for 3.175 μm, and 4.12 for 9.975 μm, much higher than the values found for the models without mass-loss.

The three different fitting methods provide mostly the same result in the case of the model without mass-loss, while in the case of models with mass-loss, the UD-radius is smaller for the first 2 methods (one- and two-points fit) than for the least squares result. This last result can be explained by going back to our initial classification of profiles (Sect. 3.3). The first and third class of profiles belong to the "uncommon" profiles of S03, which cannot be approximated by UD functions. The third class of profiles (9.975 μm) in particular deviates the most from a UD (see Fig. 3.3).

Even after increasing the number of fitting points, the resulting UD-radius cannot be considered reliable because of the particular shape of the profiles. From Fig. 3.7, for the narrow-filter it is also clear that it is impossible to define a single, phase-independent scaling factor that enables the UD-radii to be converted to the UD-continuum radii.

We also computed the equivalent UD-radii and UD-continuum radii for the broad-band filters. The results are shown in Fig. 3.8. The broad-band has the effect of smoothing the visibility profile as can be inferred in the UD-radii behaviour versus phase from the smaller amplitude of the radius variation. As for the narrow-band, in the case of broad-band filters the UD-radius versus phase for the set of models D also shows a behaviour that is not

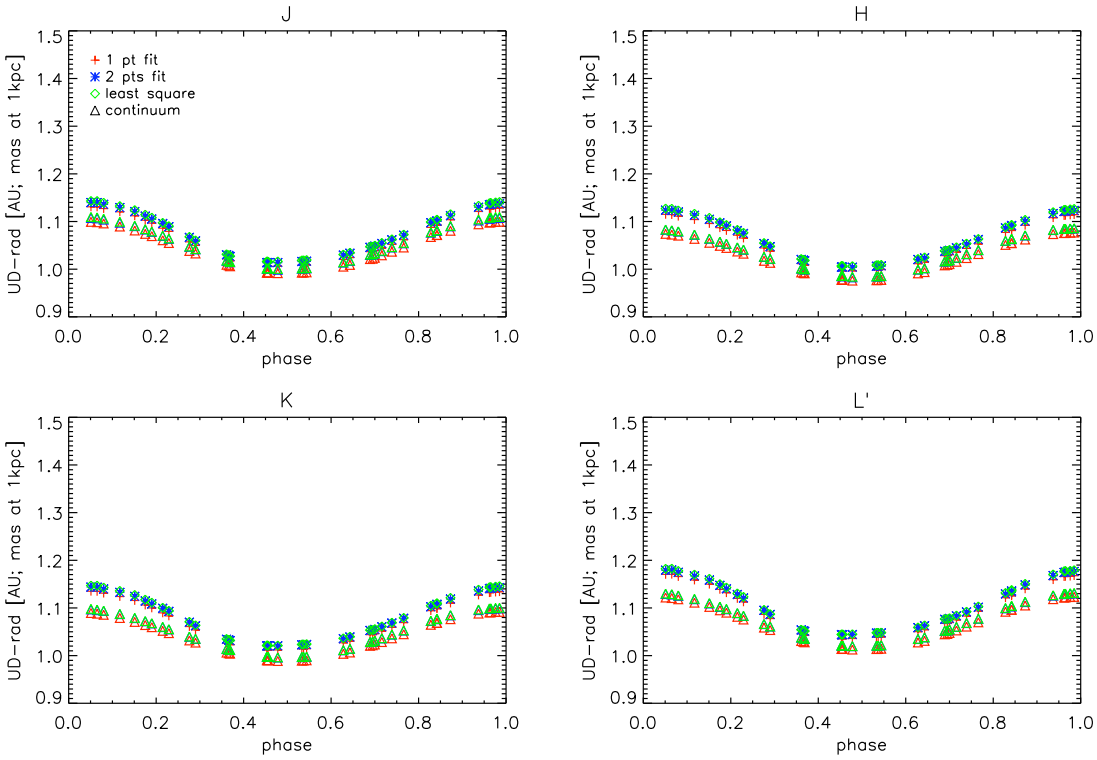

Figure 3.9: UD-Radius versus phase for $JHKL'$ broad-band filters. The four panels show the results for the model N1 without mass-loss. Plot symbols the same as in Fig. 3.7.

synchronised with the pulsation. The ratio of the UD-radius to UD-continuum radius is not constant with phase and/or with wavelength. For the phase zero, it corresponds to 2.08 in J, 2.83 in H, 2.14 in K, and 2.54 in L' band. In the lower panels of Fig. 3.8, where the model N1 is represented, the resulting UD-radius is always closer to the UD-continuum radius. The ratio of the UD-radius to the UD-continuum radius for the phase zero is almost constant: 1.03 for J and H, 1.04 for K and L'. Again, the amplitudes of variation in the radius for the N models are smaller than for the narrow-band filters, and the variation follows the near-sinusoidal behaviour of the inner layers.

For the broad-band filters, the difference in the fitting methods confirms the trend found for the narrow-band case. For the models with mass-loss, the one-point and two-points fit methods produce smaller UD-radii than those produced by the least squares method. The UD-radii, resulting from different methods, agree closely in the case of models without mass-loss and the same result is also obtained for all the UD-continuum measurements.

The dependence of UD-radius on the pulsation cycle is not covered by this contribution, and it will be topic of a future contribution.

3.5.4 Comparison with M-type stars

Compared to the M-type stars, for the C-stars we emphasise the lack of a spectral window for measuring a pure continuum radius. A model-dependent definition of the continuum radius

is thus needed for the cool carbon stars. In Ireland et al. (2004a), the phase variation in filter radii in units of the parent star radius R_p[3] is represented for different near-continuum narrow and broad-band filters. They demonstrate how measurements of radii in near-continuum band passes are affected by molecular contaminations that mask the geometrical pulsation. This contamination is negligible only close to the visual maximum. Other suitable band passes for measuring the pulsation of the continuum layers for M-type stars are the broad-band filters J and H, or the sub-bandpasses of H and K.

It is difficult to complete a consistent comparison between the UD-radii computed in this work for C-stars and the resulting UD-radii of Jacob & Scholz (2002) for M-type stars because of the intrinsic differences between the modelling approaches, and because of the different stellar parameters. However as a general statement we can say that the ratios of UD-radii to UD-continuum that we obtain are systematically larger for our models with mass-loss than those presented for M-type stars in Figs. 4 and 5 of Ireland et al. (2004a). More comparable are the resulting ratios for models without mass-loss. The largest difference is caused by the strong molecular (first of all C_2H_2) and dust opacities that characterise the C-star spectra. The UD-radius increases with wavelength and in the case of carbon-rich model atmospheres with mass-loss, this increase is larger than that found by Jacob & Scholz (2002) for M-type stars. In particular, the ratio of the UD-radius in J to the UD-radius in L' for our model D1 at phase zero is 2.07, while for the M-type models presented in Fig. 4 and Fig. 5 of Jacob & Scholz (2002), it is 1.4 in the case of largest discrepancy (phase 1.5). The same ratio for our N1 model is 1.03, meaning that this model without mass-loss shows an increase in the UD-radius with wavelength lower than that of the M-type stars.

3.6 Summary and Prospects

We have presented, for the first time, a theoretical study of the intensity and visibility profiles computed for a set of dynamic model atmospheres of C-rich AGB stars. The main results of our investigation can be summarised as follows:

- The profiles computed in the narrow-band filters for our set of models can be divided into 3 morphological classes mainly according to wavelength region, with the exception of the filter located at 3.175 μm in the middle of a strong absorption feature characteristic of C-star spectra. This filter shows a behaviour more closely related to one of the narrow-band filters in the region around 12 μm than to the surrounding wavelength range. We have chosen three filters to represent the morphology of intensity and visibility profiles: 1.53, 9.975, and 3.175 μm, for the first, second, and third class, respectively. The intensity profile of the first class is characterised by a limb-darkened disc followed by a tail-shape with a bump and a peak. The 3.175-like profiles show an extended plateau due to strong molecular opacity. The second class is intermediate between the other two.

[3] R_p is defined as the Rosseland radius that "the Mira variable would assume if the pulsation stopped and the stratification of the star becomes static" (Jacob & Scholz 2002).

- The morphology of the profiles (narrow and broad-band) of models with mass-loss is very far from the UD shape. Models without mass-loss, and all theoretical continuum profiles can be approximated quite well by a UD.

- Bandwidth smearing affects the resulting broad-band profiles with an error of about 70% for certain baselines. For models with mass-loss, the difference is notable not only close to the first zero but also on the flank of the first lobe of the visibility profile. When comparing models with observations in broad-band, it is important to take this effect properly into account.

- C-star UD-radii are wavelength-dependent. The dependency is stronger in the case of models with mass-loss, in this case the UD-radii also exhibit significant large phase dependence. Around 3 μm and in the N-band, the star appears more extended because of C_2H_2 opacity. The UD-continuum radius is mostly independent of the wavelength and phase.

- The extensions of the models increase for higher mass-loss rates and lower temperatures.

- Models with mass-loss show a complicated behaviour of the UD-radius versus phase compared to models without mass-loss. This behaviour is not dependent on the pulsation of the interior.

- Using only one or two points of visibility to determine the UD-radii of objects characterised by strong pulsation and mass-loss,it is shown that the radius of the star is smaller than the one measured using more points (least squares method). In the case of models without mass-loss, the different methods of fitting yield the same UD-radii.

- The UD-radius is very close to the UD-continuum radius in the case of models without mass-loss.

- The trend of the UD-radii versus phase in broad-band is smoother than in the case of the narrow-band filters.

- In contrast to O-rich stars, for C-rich stars no spectral windows for observing the continuum radius are available in the case of C-stars, and some assumptions based on models are necessary. A useful replacement for a measured continuum radius is the UD-continuum radius defined in Sect. 3.5, which is basically independent of wavelength and pulsation phase.

- The difference in the UD-radii between the models should be detectable observationally, in particular in the L-band where MATISSE (Lopez et al. 2006) will provide new observational opportunities.

- The radius computed with the UD function must be considered only as a first guess of the true size of the star. The intensity and visibility profiles of a C-star, especially in the case of models producing mass-loss, are very far from being UD-like.

A comparison of the dynamic models with available sets of observations is under way, and the intensity and visibility profiles of specific models can be provided upon request.

Chapter 4

Spectro-interferometric study of a sample of mildly pulsating C-stars

This chapter is based on the paper:

Determination of the stellar parameters of C-rich hydrostatic stars from spectro-interferometric observations

C. Paladini, G. T. van Belle, B. Aringer, J.Hron, P. Reegen, C. J. Davis, T. Lebzelter
2011, A&A, 533, 27

Abstract: Giant stars, and especially C-rich giants, contribute significantly to the chemical enrichment of galaxies. The determination of precise parameters for these stars is a necessary prerequisite for a proper implementation of this evolutionary phase in the models of galaxies. Infrared interferometry opened new horizons in the study of the stellar parameters of giant stars, and provided new important constraints for the atmospheric and evolutionary models. We aim to determine which stellar parameters can be constrained by using infrared interferometry and spectroscopy; for C-stars in particular we aim to determine the precision that can be achieved as well as its limitations. For this purpose we obtained new infrared spectra and combined them with unpublished interferometric measurements for five mildly variable carbon-rich asymptotic giant branch stars. The observations were compared with a large grid of hydrostatic model atmospheres and with new isochrones that include the predictions of the thermally pulsing phase. For the very first time we are able to reproduce spectra in the range between 0.9 and 4 μm, and K broad band interferometry with hydrostatic model atmospheres. Temperature, mass, $\log(g)$, C/O and a reasonable range for the distance were derived for all objects of our study. All our targets have at least one combination of best-fitting parameters that lies in the region of the HR-diagram where C-stars are predicted. We confirm that

low-resolution spectroscopy is not sensitive to the mass and $\log(g)$ determination. For hydrostatic objects the 3 μm feature is very sensitive to temperature variations, therefore it is a very powerful tool for accurate temperature determinations. Interferometry can constrain mass, radius, and $\log(g)$, but a distance has to be assumed. The large uncertainty in the distance measurements available for C-rich stars remains a major problem.

4.1 Introduction

The basic properties and evolutionary status of a star can be determined knowing its mass, luminosity, radius, and chemical composition. Nowadays we are reaching a point where mass estimates are available not only for binary, but also for single objects (see the recent review by Aufdenberg et al. 2009). This major advance has been mainly achieved by establishing interferometry as a standard tool for investigating stars (Wittkowski 2004a). The combination of high angular and spectral resolution gives the possibility to study the spatial structure of single stellar objects, which were treated before as point sources only. Red giant stars are very good targets for interferometric investigations because of their extended atmosphere and their brightness in the infrared. These stars are the main contributors to the infrared light and to the chemical enrichment of galaxies. Therefore, an accurate determination of their fundamental parameters is mandatory for a proper implementation in the models of galaxies.

Wittkowski et al. (2001) made a first attempt at deriving the parameters of a sample of asymptotic giant branch (AGB) stars by comparing the spectro-interferometric observations with Kurucz model atmospheres. The uncertainty in parallax and bolometric flux dominate the errors. Recently, Neilson & Lester (2008) determined the fundamental parameters of three M-type stars. They combined infrared interferometry with spectro-photometric observations. The interferometric data were obtained with the VLTI/VINCI instrument and were previously interpreted by using PHOENIX and ATLAS atmospheric models (Hauschildt et al. 1999, Kurucz 1993, respectively) in the work of Wittkowski et al. (2004b, 2006a,b). Neilson & Lester (2008) used the new generation of SATLAS models (Lester & Neilson 2008) for the interpretation of the data: in this way the authors were able not only to determine the fundamental parameters, but also to constrain the atmospheric models they used. The typical approach followed in these works to determine the stellar parameters is: (i) determination of the limb darkened radius by fitting the interferometric observations, the resulting radius is converted into a Rosseland radius; (ii) a linear radius is derived by assuming a distance; (iii) an effective temperature is derived by fitting the SED; (iv) the luminosity is obtained through the radius and $T_{\rm eff}$; (v) the gravity and the mass of the star are constrained by comparison with the theoretical models.

The targets of our study are an important subclass of the AGB objects: the carbon-rich AGB stars. According to theory, only stars with a range of mass between 1 and 4 $M_{\odot}$ undergo the third dredge-up during their AGB phase, with the result of increasing their C/O ratio (Iben & Renzini 1983). The spectra of these giants are consequently dominated by the absorption features of carbonaceous molecular species such as CO, CN, HCN, C_2,

C_3, and C_2H_2 (Tsuji 1986, Jørgensen et al. 2000, Loidl et al. 2001). As a result, these objects are the main contributors to the C-enrichment of the ISM.

The state-of-the-art model atmospheres for C-stars are very promising, because they are able to produce large grids of models (Aringer et al. 2009, Mattsson 2009) that describe the observed properties of these objects reasonably well. The hydrostatic model atmospheres for C-stars were compared with optical and infrared spectroscopy in Jørgensen et al. (2000), Loidl et al. (2001), and Abia et al. (2010) and references therein. The major difference between an earlier generation of models as used by Jørgensen et al. (2000), and Loidl et al. (2001), and the hydrostatic atmospheres applied in our work (Aringer et al. 2009) is the inclusion of atomic opacities and an update to new and more accurate molecular opacities.

The stellar evolutionary calculations reached a highly sophisticated level as well, being able to include a detailed thermally pulsing phase with third dredge-up, hot-bottom burning and variable molecular opacity (Marigo et al. 2008).

The purpose of this work is to find out which stellar parameters can be determined for weakly variable C-stars (visual amplitude $\leq$ 2 mag) by using spectroscopy, infrared interferometry, and hydrostatic model atmospheres; and to asses their the accuracy. We aim to test the stellar atmospheric models with different techniques and a multiwavelength approach. This is a very important step because errors in the model structure limit quantitative checks of stellar evolution. Our approach in the parameter determination is slightly different from the one adopted by Neilson & Lester (2008) for a few simple reasons: (1) the Rosseland radius is not a direct observable, and in the C-stars (in contrast to M-type AGB stars) there are no windows in the near-infrared where to measure a "continuum" radius (Paladini et al. 2009); (2) it is very rare to obtain simultaneous multiwavelength photometric observations, which is mandatory when dealing with variable stars. Nevertheless, the parameters determined in this work will be compared in a follow-up paper (van Belle et al., in prep.) with that obtained by combining photometric and interferometric observations.

A short description of the acquired observations and of the data reduction for both spectroscopy and interferometry will be given in Sect. 6.2. The hydrostatic model atmospheres and the methods for determining the observables will be presented in Sect. 4.3. The approach used to determine the stellar parameters (temperature, C/O, mass, $\log(g)$) is presented in Sect. 4.4, while in Sect. 4.5 we summarise the comparison with the evolutionary tracks. We present a detailed discussion of the single objects studied in this work in Sect. 4.6, followed by a more general discussion of the obtained results (Sect. 4.7) and the conclusions (Sect. 4.8).

4.2 Observations and data reduction

Five mildly variable stars were selected for this investigation: CR Gem, HK Lyr, RV Mon, Z Psc, DR Ser. In Table 4.1 the coordinates of the objects, near-infrared photometry, and the 12 μm IRAS flux are presented together with period (P) and amplitude (A) of variability. Unless otherwise stated, A and P are derived from the General Catalogue of Variable Stars (GCVS; Samus+ 2007-2009). The amplitude values list the maximum amplitude recorded,

and might be based only on few data points, sometimes recorded on photographic plates. More recent observations from the public surveys such as ASAS (Pojmanski 2002) and the Hipparcos Variability Annex (Beichman et al. 1988) show the smaller V amplitude variations, often quite stable over a long period. These more recent values are listed in the discussion of the individual targets (Sect. 4.6). The objects selected are semiregular or irregular variables. The variability amplitude and the period indicate that the atmospheres of our targets can be represented with hydrostatic models. The literature values of A and P are low compared to dynamic objects such as Mira stars (P longer than one year, and A of several V magnitudes). In the recent grid of dynamic models for C-stars from Mattsson (2009) almost all models with a period lower than 250 days do not develop a stellar wind. The few exceptions are models with extremely low temperature or a very high C/O value. The same applies to the predictions of the previous generations of dynamic models (i.e. Table 1 Gautschy-Loidl et al. 2004). The temperature-density structure of these windless models varies only slightly around the hydrostatic configuration. These small variations of the atmospheric structure are also reflected in the resulting spectra, but as can be seen in Fig. A.1 of Nowotny et al. (2010), the spectra of objects with very mild pulsations and no mass loss do not differ significantly from the corresponding one based on a hydrostatic model. The hydrostatic spherical symmetric approximation will also be checked with interferometric observations (where possible) in Sect. 4.2.2. We collected for all the targets $IJHKL$ infrared spectroscopy and K broad band interferometric observations.

Table 4.1: Target list, available photometry, and variability information. The amplitude and the period (unless otherwise stated) are derived from the General Catalogue of Variable Stars (GCVS; Samus+ 2007-2009). The band used for amplitude of variability measurement is also reported; 'p' denotes photographic plates.[(a)]Kerschbaum et al. (1996a); [(b)]Kerschbaum et al. (1996b);[(c)]Epchtein et al. (1990); [(d)]Bagnulo (1996); [(e)]Beichman et al. (1988); [(f)]Pojmanski (2002).

ID	RA	DEC	J [mag]	H [mag]	K [mag]	L [mag]	$f_{[12\,\mu m]}$ [Jy]
CR Gem	06:34:23.92	+16:04:30.30	3.36	2.07	1.46	0.88[(a)]	39.31
HK Lyr	18:42:50.00	+36:57:30.89	3.23	2.15	1.62	0.99[(b)]	22.74
RV Mon	06:58:21.49	+06:10:01.50	3.06	1.96	1.43	0.85[(c)]	31.13
Z Psc	01:16:05.03	+06:10:01.50	2.11	1.10	0.70	0.41[(d)]	33.42
DR Ser	18 47 21.02	+05 27 18.60	4.12	2.79	2.08	1.38[(a)]	15.9

ID	Var. Type	Amplitude [mag]	Period [days]
CR Gem	Lb	1.20 B	250
HK Lyr	Lb	0.40 V[e]	186[e]
RV Mon	SRb	2.19 B	131
Z Psc	SRb	1.30 p	144
DR Ser	Lb	0.50 V[f]	196[f]

4.2.1 Spectroscopy

The spectra for our targets were obtained with the UIST instrument (Ramsay et al. 2004) on the United Kingdom InfraRed Telescope (UKIRT) as part of the UKIRT Service Programme: `u/serv/1790` and `u/serv/1810`. The first run of observations was on 29 June 2008; the second one on 20, 23, 25, and 26 January 2009. Four grism spectra were collected for every target, covering the following spectral ranges: IJ with wavelengths in the interval[1] $[0.862, 1.418]$ μm; HK with wavelengths in the interval $[1.395, 2.506]$ μm; short$L$, and long$L$ bands covering $[2.905, 3.638]$ and $[3.620, 4.232]$ μm, respectively. We also obtained spectra for three standard stars to be used for the calibration procedure. The spectral type, photometry, and effective temperature of the standard stars are listed in Table 4.2. Because our objects were bright, we observed with a 2-pixel (0.24 arcsec) wide slit. Targets

Table 4.2: Spectral type, photometry, and effective temperature of the standard stars used for the spectroscopic calibration. The photometry is from the 2MASS All Sky catalogue (Cutri et al. 2003); [a]Erspamer & North (2003); [b]Masana et al. (2006); [c]Solano & Fernley (1997).

ID	Sp. Type	V [mag]	J [mag]	H [mag]	K [mag]	$T_{\rm eff}$ [K]
HIP 92946	A5V	4.62	4.160	4.163	4.085	7 880[a]
HIP 33024	F0V	5.753	5.308	5.232	5.088	7 400[b]
HIP 5544	F0V	5.160	4.764	4.545	4.393	7 500[c]

and standard stars were nodded along the slit, with spectra being taken in an A-B-B-A sequence to facilitate first-order sky subtraction. Exposure times of 2-coadds $\times$ 2 seconds or 1-coadd $\times$ 4 seconds were used with each grism, depending on the brightness of the source. The nodding sequence was executed twice, resulting in a total integration time of 32 seconds per source in each grism. The resolution of the spectra ranges between 400 (IJ) and 1800 (long$L$). HIP 92946 was used to remove telluric features for targets observed in 2008 (HK Lyr, DR Ser), while HIP 33024 and HIP 5544 were used for the 2009 observations (CR Gem, RV Mon and Z Psc, respectively).

Data reduction was performed using the ORAC-DR UIST pipeline (Cavanagh et al. 2003). The subtraction of the sky removes the OH lines and the thermal background emission. At this stage the spectrum is made of a positive and a negative part, which can be extracted. An Argon lamp is used for the calibration of the object in wavelength. Before every target observation a telluric standard was observed. The observations of target and reference star are always carried out in a range of airmass between 1.0 and 1.3. Only in one case we had airmass 1.5. The airmass difference between target and standard is usually of the order of 0.1, which produces a negligible error in the flux calibration. Once object and standard were calibrated in wavelength, the telluric correction was performed. For this purpose we used the routine `IRFLUX` from the Starlink[2] software package. `IRFLUX`

[1]Although the wavelengths range of the IJ grism starts at 0.86 μm, only the part beyond 0.9 μm is usable because the spectral blocking filter blocks emission (essentially has zero transmission) below this wavelength and, in any case, the instrumental throughput drops considerably towards the I band.

[2]Starlink software is available for downloading on the webpage `http://starlink.jach.hawaii.edu/`.

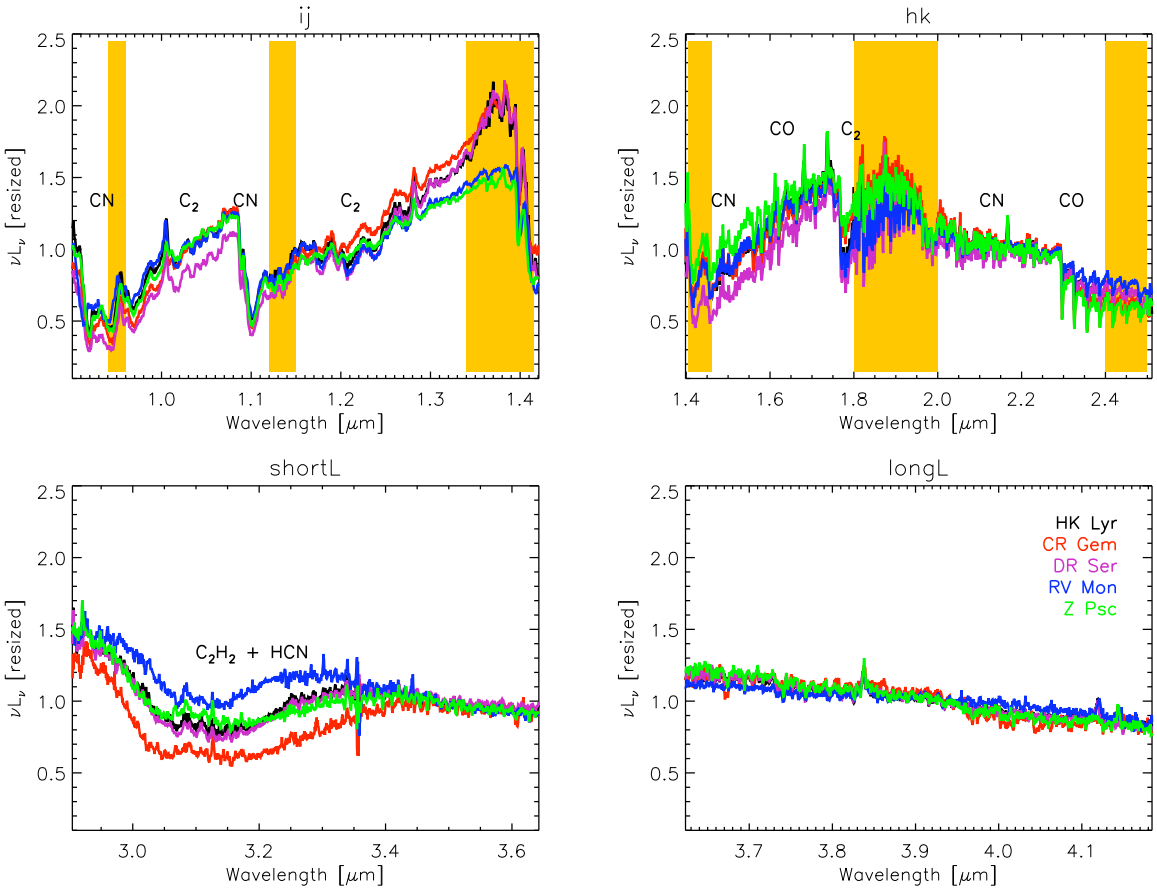

Figure 4.1: Comparison between all the spectra of our targets. The main molecular features are indicated. The shaded (yellow) regions are affected by absorption of the Earth's atmosphere.

divides the standard spectrum by a black body with assigned temperature (the one of the standard). The outcome of this operation is a spectrum that only includes the telluric features and atmospheric and instrumental effects. Finally, the target is divided by this last determined spectrum and the telluric calibration is performed. The standard stars are hot enough to be approximated with a black body in the covered wavelength range.

Once the telluric correction was performed, a few emission lines appeared in the spectrum of the targets. Those are the residual of the atmosphere of the standards, which in this part of the spectrum does not contribute to the continuum (this is flat), but it shows few hydrogen lines. We identified those lines by comparing the spectrum of the standards with the corresponding hydrostatic models from Shulyak et al. (2004). The region where the lines are located was not taken into account in the fitting procedure, neither were the data at the edge of the atmospheric windows (shaded region in Fig. 4.1).

The reddening correction is always a very delicate task in spectroscopy. Every spectrum was dereddened using the `EXTIN.PRO` IDL procedure (Amôres & Lepíne 2005). The code computes the visible extinction (A_V) along a path from the Sun to any point in the Galaxy, specified by galactic coordinates and distance. Unfortunately, the distance measurements associated with our objects are very uncertain. We selected three reference distances for

each target from the literature: the distance measured by the Hipparcos satellite (Perryman et al. 1997), a distance estimated assuming a constant K magnitude (Claussen et al. 1987), and a distance estimated by Bergeat & Chevallier (2005), which is based on Hipparcos measurements but takes into account three distinct biases (see Sect. 2.3 of Bergeat et al. 2002). Hereafter, the different distances will be indicated with the abbreviation $d_{\rm Ber}$, $d_{\rm Cla}$, $d_{\rm Hipp}$.

The distances for each object are listed in Table 4.4. The values are in most of the cases very different, but no trend or systematic behaviour can be identified. For the Hipparcos measurements the errors associated to the distances are also given. No error estimation was found in the literature for $d_{\rm Berg}$ and $d_{\rm Clau}$, therefore we assume at least 20% of uncertainty. This corresponds to 40% error on the luminosity.

Although the distances have very different values, the resulting reddening correction is very similar (as expected because these are nearby objects). We tested the effect of the different reddening correction on the estimation of the parameters (in particular the temperature). The typical shift for the temperature determinations is of the order of 10 K, which is low compared to the error bar. Except for DR Ser, where no correction was applied (see detailed discussion in Sect. 4.6.5), we used for our computation the reddening correction estimated for the Hipparcos distance.

4.2.2 Interferometry

Observations for this investigation were primarily taken with the Palomar Testbed Interferometer (PTI). The PTI was an 85 to 110 m baselines H and K band (1.6 μm and 2.2 μm) interferometer located at the Palomar Observatory in San Diego County, California, and is described in detail in Colavita et al. (1999). It had three 40-cm apertures used in pairwise combination for measurements of stellar fringe visibility on sources that range in angular size from 0.05 to 5.0 milliarcseconds, being able to resolve individual sources $\vartheta > 1.0$ mas in size. The PTI had been in nightly operation since 1997 and was decommissioned in 2009, with minimum downtime during the intervening years. In addition to the carbon stars observed as part of this investigation, appropriate calibration sources were observed as well and can be found in van Belle et al. (2008a).

The calibration of the squared visibility (V^2) data is performed by estimating the interferometer system visibility ($V^2_{\rm SYS}$) using the calibration sources with model angular diameters and then normalising the raw carbon star visibility by $V^2_{\rm SYS}$ to estimate the V^2 measured by an ideal interferometer at that epoch (Mozurkewich et al. 1991, Boden et al. 1998, van Belle & van Belle 2005). Uncertainties in the system visibility and the calibrated target visibility are inferred from internal scatter among the data in an observation using standard error-propagation calculations (Boden et al. 1999). Calibrating our point-like calibration objects against each other produced no evidence of systematics, with all objects delivering reduced $V^2 = 1$.

The PTI's limiting night-to-night measurement error is $\sigma_{V^2_{\rm SYS}} \approx 1.5 - 1.8\%$, the source of which is most likely a combination of effects: uncharacterised atmospheric seeing (in particular, scintillation), detector noise, and other instrumental effects. This measurement

error limit is empirically established from the previous study of Boden et al. (1999).

In our sample there is one star, Z Psc, without PTI observations. One visibility measurement taken with IOTA (Infrared Optical Telescope Array) is available in the literature for this object. The visibility point value was obtained in the $K-$filter ($\lambda = 2.2$ μm, $\Delta\lambda = 0.4$ μm) and is published in Table 1 of Dyck et al. (1996). We will use this value for our investigation.

Table 4.5 gives an overview of the observational parameters of the interferometric observations used, namely UT date, baseline, position angle, and the calibrated visibility with associated error.

From the relationship between visibility and uniform disk (UD) angular size, $V^2 = [2J_1(x)/x]^2$, where $x = \pi B \vartheta_{UD} \lambda^{-1}$, we may establish uniform disk angular sizes for the carbon stars observed by the PTI because the accompanying parameters (projected telescope-to-telescope separation, or baseline, B and wavelength of observation λ) are well-characterised during the observation. This uniform disk angular size will be connected to a more physical limb-darkened angular size in Sect. 4.4. By plotting the UD diameter versus time, we were able to check the reliability of our approximation with hydrostatic models. From the UD diameter versus position angle the assumption of spherical symmetry is checked. In Fig. 4.2 we present the interferometric observations for three of our five targets. The missing objects (CR Gem, Z Psc) have only one available measurement. The panels in the first row, identified with the letter 'a', represent the measurements for DR Ser. In the row 'b' the points for HK Lyr are plotted, and in the row 'c' there are the points for RV Mon. In column '1' we present the uv coverage. In column '2' the visibility points are presented versus the baseline. HK Lyr and RV Mon are observed always with the same baseline setup. The variation in the projected baseline is caused by the Earth's rotation. The UD diameter is plotted versus position angle in column '3'. In column '4' the UD diameter are presented versus the visual phase to investigate eventual variations in the angular size that might be caused among other reason by the pulsation of the stars. The phase estimation for RV Mon and DR Ser is based on the visual light curve from the ASAS database (Pojmanski 2002); while for HK Lyr it is based on the light curve from the Hipparcos Variability Annex (Beichman et al. 1988). Small trends can be identified in the case of RV Mon and HK Lyr, they may be caused by cycle-to-cycle variation, but we can neither completely exclude an instrumental problem (see detailed discussion in Sect. 4.6.3).

4.3 Hydrostatic models and synthetic observables

For the determination of the parameters we used the new grid of hydrostatic and spherically symmetric model atmospheres of Aringer et al. (2009). They are computed with COMARCS, a programme based on the MARCS code (Gustafsson et al. 1975, 2008) in the version used by Jørgensen et al. (1992) and Aringer et al. (1997). The models are generated assuming hydrostatic local thermal and chemical equilibrium. The molecular and atomic opacity is treated in the opacity sampling (OS) approximation. The parameters that characterise a model are effective temperature, metallicity, $\log(g)$, mass, and C/O.

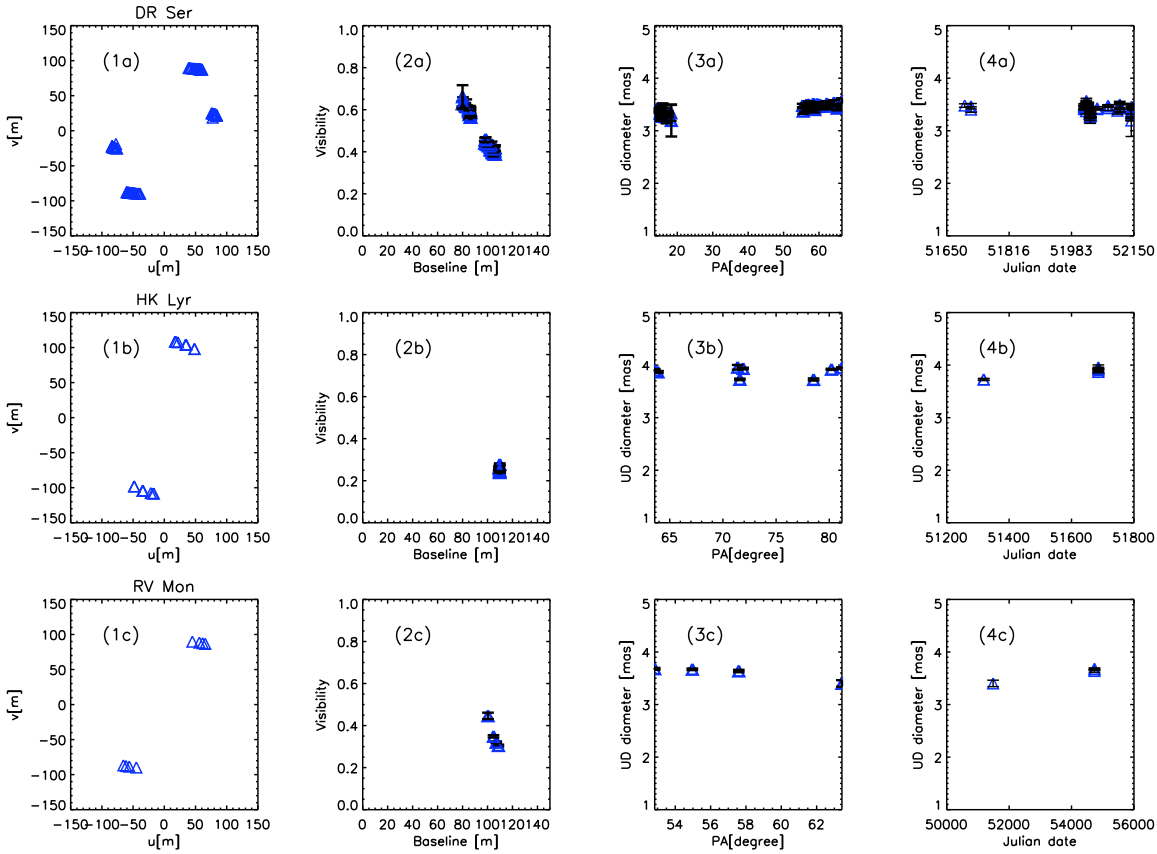

Figure 4.2: Checking of the hydrostatic and spherical symmetric approximation for the interferometric data. The series of panels 'a' refers to DR Ser data, panels 'b' to HK Lyr, and panels 'c' to RV Mon. The plots in column '1' represents the *uv*-coverage of the observations, in column '2' the visibility points acquired are plotted versus the baselines. In column '3' the correspondent UD diameter is plotted versus position angle. In column '4' the UD diameter is plotted versus the visual phase.

4.3.1 Synthetic spectra

Our observed spectra have higher resolution than those of the grid published in Aringer et al. (2009), therefore new synthetic spectra were computed for a subset of the initial grid of hydrostatic models.

We assumed solar metallicity for our targets. The subset of new spectra covers the following parameters [3]: $2\,400 \leq T_{\rm eff} \leq 4\,000$ K with steps of 100 K; $Z/Z_{\odot} = 1$; $-1.0 \leq \log(g) \leq +0.0$; $M = 1\,{\rm or}\,2\,M_{\odot}$; C/O= 1.05, 1.10, 1.40. The COMA code (Aringer 2000) was used to compute the opacities for the different layers of a given temperature-density atmospheric structure. The opacity sources included in the calculations for the continuum are listed in Table 1 of Lederer & Aringer (2009). Voigt profiles were used for atomic lines and Doppler profiles for the molecules. All main molecular opacities typical for C-stars were included: CO (Goorvitch & Chackerian 1994), C_2 (Querci et al. 1974), HCN (Harris et al. 2006), CN

[3] In the model grid the lower limit of $\log(g)$ varies according to the temperature. For more details see Table 1 in Aringer et al. (2009).

(Jørgensen 1997) in the form of line lists, while C_2H_2 and C_3 (Jørgensen et al. 1989) as OS data. This agrees with previous works (Loidl et al. 2001, Aringer et al. 2009, Lederer & Aringer 2009) with the exception of the C_2 linelist, which was not scaled in the infrared range.

The scaling of the gf values for C_2 was suggested for the first time by Jørgensen (1997) and afterwards introduced by Loidl et al. (2001) for fitting spectra of C-rich stars in the range of $0.5 - 2.5$ μm. The authors keep the original linelist up to $1.15\,\mu$m, they scale it by a factor of 0.1 beyond $1.5\,\mu$m, and use a linear extrapolation in the transition region. Different authors already pointed out the need of new C_2 line data. Aringer et al. (2009) showed that the C_2 scaling does not affect the model structure so much, but it introduces a variation in the spectral range between 1.3 and $2.1\,\mu$m. In the same work a discrepancy was observed when comparing synthetic and observed $(H - K)$ colours. This discrepancy was investigated in terms of C_2 opacity. The authors show in their Fig. 15 how the photometry obtained for unscaled models better agrees with observations. Aringer et al. (2009) conclude that this could be an indication that the use of the linelist in its original version is more appropriate, as long as there are no other more precise sources available.

In order to check this conclusion further, we performed the χ^2 test as explained in García-Hernandez et al. (2007) and Uttenthaler & Lebzelter (2010). In most of the cases we obtained a lower result of the χ^2 test for the C_2-unscaled linelist of Querci et al. (1974). This result was also judged by eye in order to test the method. In Fig. 4.3 the effect of the C_2-scaling in the HK-band is shown. The full line is the spectrum of the star Z Psc (upper panel) and HK Lyr (lower panel) convolved to a resolution of 200. The dotted line is the synthetic spectrum corresponding to a model with scaled C_2 opacity, while the dashed line is the same model with the original C_2 list. The result of the χ^2 test, the check by eye and the arguments of previous work of Aringer et al. (2009) led us to opt for the original C_2-unscaled linelist.

The resulting opacities are used as input for a spherically symmetric radiative transfer code that gives the synthetic spectra with a resolution of 18 000 in the wavelength range $0.8 - 25\,\mu$m. We convolved these spectra to obtain same resolution as the observed data.

4.3.2 Synthetic visibility profiles

The spherical radiative transfer code produces an additional output besides the total spectrum: a monochromatic spatial intensity profile. Synthetic visibility profiles for the K-broad band PTI setup were computed for a subset of the grid of hydrostatic models. The metallicity, the temperature range and the C/O ratio were fixed (more details in Sect. 4.4.1). To compute the visibility profiles, i.e. the interferometric observables, we proceeded as follows.

We defined a set of narrow-band filters centred on the sampled wavelength of the transfer function for the PTI $K-$broad band setup. Then the monochromatic intensity profiles were convolved with the filters so defined. The visibility profiles were computed as Hankel transform of the narrow-band intensity profiles. The spatial frequencies were converted from AU^{-1} to baselines in meters for a given distance. The squared visibility broad band

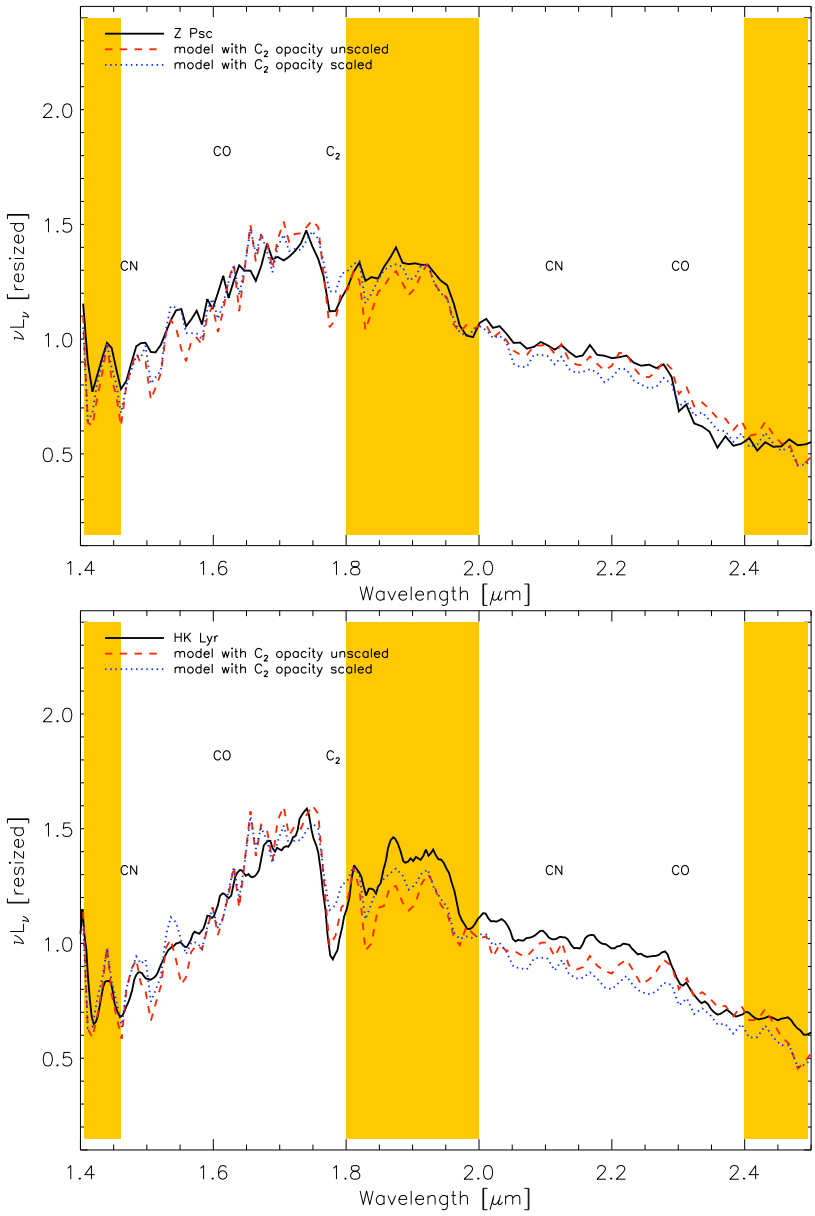

Figure 4.3: Comparison between the observed spectrum of two targets (black full line, Z Psc in the upper panel and HK Lyr in the lower), a spectrum computed assuming scaled C_2 opacity (dotted line) and the spectrum with unscaled C_2 (dashed line). Shaded bands mark regions of poor atmospheric transmission.

profile finally is obtained as

$$V^2_{\rm broad} = \frac{\sum\limits_i (S_i^2 F_i^2 V_i^2)}{\sum\limits_i (S_i^2 F_i^2)}\,, \tag{4.1}$$

were the sum was calculated over the $'i'$ narrow band filters; S_i is the transfer function of PTI in the K broad band setup; F_i is the flux integrated over the narrow band filter, and finally V_i is the visibility corresponding to the narrow band filters. Following this approach

for the computation of the broad band visibility profile, the bandwidth smearing effect is properly taken into account (Kervella et al. 2003, Verhoelst 2005, Paladini et al. 2009).

4.4 Parameter determination

All spectra of the targets appear to be very similar (Fig. 4.1). They are dominated by the CN, C_2 and CO bands between 0.9 and 2.5 μm, while the main absorption feature at 3 μm in the $L-$band is due to HCN and C_2H_2. In Fig. 4.1 the regions affected by telluric absorption are shaded. These regions were of course not considered in our fitting procedure. Loidl et al. (2001) computed the flux ratio of various hydrostatic models (e.g. Fig. 3 of their paper) to investigate the effect of changes in the stellar parameters. They demonstrated that spectral features are mainly sensible to $T_{\rm eff}$ and C/O. Moreover, Aringer et al. (2009) showed that the synthetic spectrum below 2.5 μm of stars with $T_{\rm eff} \geq 3\,000$ K mildly changes for different values of $\log(g)$ and mass.

Therefore, we determined $T_{\rm eff}$ and C/O from spectroscopy and turn to the PTI interferometric observations to determine the remaining characteristic parameters of the models: mass and $\log(g)$.

4.4.1 Temperature and C/O ratio

The ratio between the 3 μm (C_2H_2) and the 5.1 μm (C_3) features is the most powerful tool for determining temperature and C/O ratio for hydrostatic C-stars (Jørgensen et al. 2000). Unfortunately, our spectral coverage does not reach the C_3 feature at 5.1 μm.

Following the approach of Loidl et al. (2001), we used the energy distribution of the available spectra as main temperature indicator. The observed spectrum was convolved to a lower resolution of $R = 200$. Every target of our list was compared with a grid of synthetic spectra with the same resolution. The grid of models is dense enough in temperature to allow an accurate statistic approach, which is described in detail in Appendix. The $T_{\rm eff}$ value was separately estimated for every wavelength range, except for the long$L$ band. This range of the spectrum is mostly flat and free from features, therefore not very sensitive for the temperature estimation. We also computed a temperature taking into account all four parts of the spectrum. The resulting temperatures are presented in Table 4.3. Figure 4.4 shows the mean-squares deviation[4] derived by first fitting single pieces of the spectrum ("IJ", "HK", "short$L$") and then by fitting all pieces of the spectrum at once ("the entire 'wavelength range") for HK Lyr. Our intention is to look for possible minima in the temperature distribution.

The temperature values obtained from the different ranges of wavelength show a trend: by using the IJH bands as indicators, cooler temperatures are obtained. This trend can hardly be explained with problems during the calibration. The data reduction procedure

[4]One root mean square value (rms) was derived by fitting each model. The models were divided into bins of temperature; the single rms values were squared (mean square deviation) to be summed to obtain one value for every bin. The number of models in every bin is not constant, therefore, the final mean-squares deviation was normalised by the number of models in every bin.

(see Sect. 4.2.1) was accurate enough that we do not expect systematic errors in the overall flux distribution, which are large enough to explain the systematic variations in the temperature. The temperature difference might be explained as the effect of an optically thin dust shell surrounding the star. The effect of a dusty shell on the energy distribution of a star is shown in Fig. 3 and 4 of Nowotny et al. (2011). The model used for this simulation corresponds to a very dynamic star. Our objects are fairly static, but we speculate that a thin dust shell would affect the spectrum in the same way with scaled-down intensity. This shell would absorb the light in the IJH band and emit it at longer wavelength. As a direct consequence, a temperature determination based on IJH band is systematically lower, as can be seen in the upper panels of Fig. 4.4. If the shell is thin enough, the effect on the short edge of the L band is negligible. This makes the short$L$ band temperature determination quite robust, as can be seen in the lower left panel of Fig. 4.4.

Table 4.3: Summary of temperature, C/O determination, and rms values corresponding to the different C/O. The boldface corresponds to the best values of temperature and C/O. More details in Sect. 4.4.1. † indicate that the reddening correction was not applied to the spectrum.

ID	$T_{\rm eff}(IJ)$ [K]	$T_{\rm eff}(HK)$ [K]	$T_{\rm eff}$(short$L$) [K]	$T_{\rm eff}$ (all spec) [K]	$\rm rms_{1.05}$	$\rm rms_{1.10}$	$\rm rms_{1.40}$
CR Gem	$2\,700 \pm 200$	$2\,860 \pm 200$	$\mathbf{3\,070 \pm 50}$	$2\,920 \pm 190$	**0.021**	0.027	0.038
HK Lyr	$2\,740 \pm 220$	$2\,920 \pm 210$	$\mathbf{3\,090 \pm 50}$	$3\,080 \pm 120$	0.015	0.016	**0.013**
RV Mon	$2\,950 \pm 300$	$2\,930 \pm 230$	$\mathbf{3\,170 \pm 50}$	$3\,210 \pm 140$	**0.006**	0.008	0.009
Z Psc	$3\,000 \pm 330$	$3\,080 \pm 210$	$\mathbf{3\,130 \pm 60}$	$3\,170 \pm 130$	**0.014**	0.017	0.016
DR Ser†	$2\,790 \pm 250$	$2\,820 \pm 200$	$\mathbf{3\,080 \pm 40}$	$3\,030 \pm 170$	**0.011**	0.013	0.014

We note that this is not the case if the star is a strongly pulsating variable (such as a Mira). In this case the profile of the $3\,\mu$m feature, which is the result of the superposition of molecular opacity and dust continuous emission (Gautschy-Loidl et al. 2004), will be sensitive to the dynamic processes of the atmosphere. The respective temperature derived for every star by fitting the short$L$ band will be assumed below.

The second quantity that mainly modifies the appearance of a C-rich spectrum is the C/O ratio. Unfortunately, the relatively low resolution of the spectra available limits the precision of this measurement. The CO band at $2.29\,\mu$m, the C_2 bands at 1.02 and $1.20\,\mu$m, and the C_2H_2+HCN at $3\,\mu$m were considered as indicators for the C/O ratio. Following to Loidl et al. (2001), the C_2 features longward of $1.20\,\mu$m were not used because of the uncertainty in the C_2 opacity. Two reference wavelengths were chosen to indicate start and end of every selected band. In low-resolution spectroscopy no continuum window is available for C-stars (Paladini et al. 2009), therefore a *pseudo-continuum* was obtained by linear interpolation of the points at the edge of the chosen band. The selected portion of spectrum was normalised to this pseudocontinuum. Following this approach, we derived the equivalent width for the observed spectrum and for all models with the temperature determined from the previous step. Grouping the models in sets according to the C/O (i.e. every "C/O group" includes models with same temperature, but different $\log(g)$ and mass), a root mean-squares value was obtained for every C/O by comparing the observed

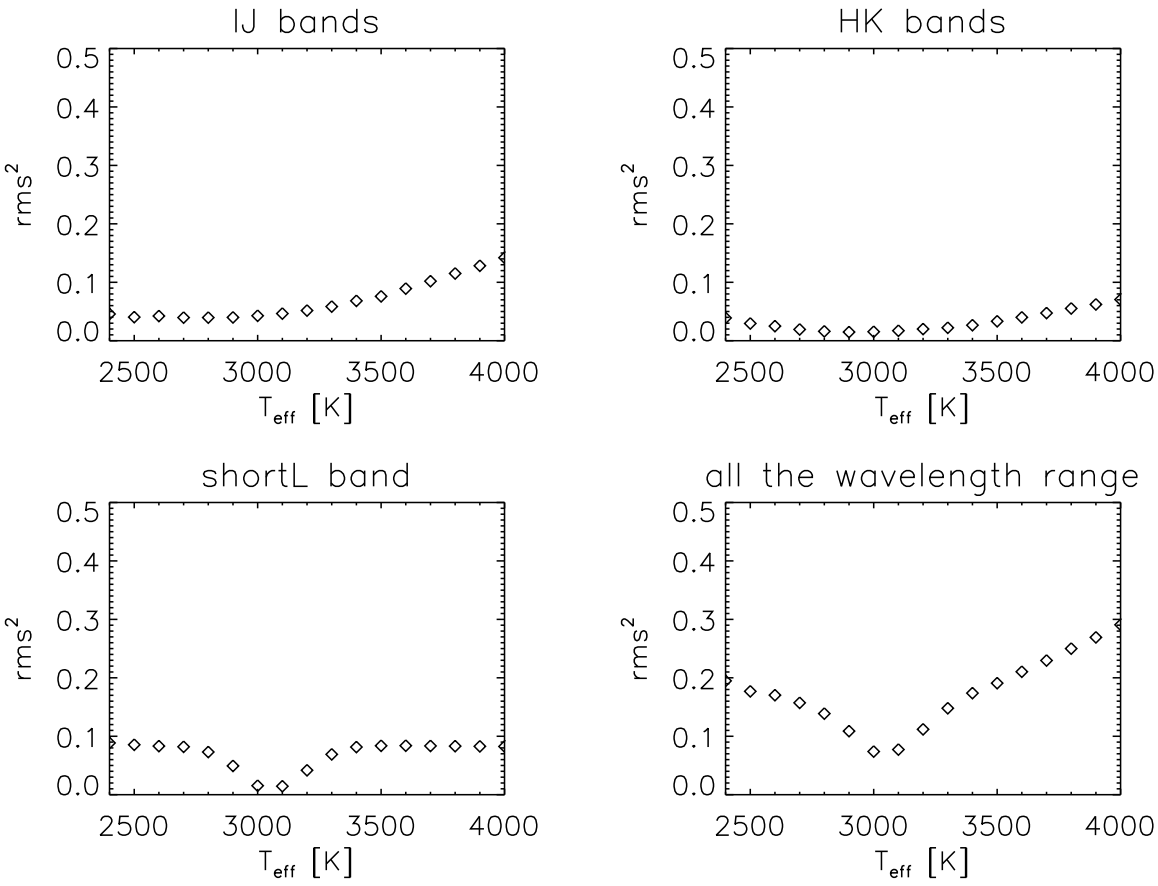

Figure 4.4: Four plots show the mean squared deviation obtained by fitting single portions of the spectra (IJ, HK, short$L$), and by fitting all the portions of spectra at once (all the wavelength range) for HK Lyr. These plots demonstrate the accuracy of the short$L$ measurement.

equivalent width and the synthetic one.

In cols. 6, 7, and 8 of Table 4.3 the resulting rms for the three C/O values (1.05, 1.10, and 1.40) is given. The minimum rms is shown in bold. All stars of the sample have a low value of C/O ratio, which corresponds to 1.05, except for HK Lyr, where the C/O = 1.4.

4.4.2 Mass, log(g), and distance

As already pointed out by other authors, it is hard to detect the effect of mass and log(g) from low-resolution spectroscopy of C-rich stars. This is confirmed in our series of plots in Fig. 4.6-4.10, where models with the same parameters except mass and log(g) are compared with the spectra of the targets. The temperature and C/O ratio of the models were determined following the procedure described above.

Owing to these considerations, we decided to treat the observables of interferometry as completely independent quantities. Because interferometry aims to measure the radius of the target, the distance becomes an important parameter. Unfortunately, the distance measurements available for these objects are quite imprecise (typical error of the order of

20%) and often contradict each other with differences between measurement relative to the same objects that are larger than errors. The problem we face is degenerate because we have to deal with radius, distance, mass, and all these quantities are related to each other.

We handled the problem in the following way. Three distances obtained with different methods were chosen from the literature for every object (see Sect. 4.2.1 and Table 4.4), and a set of synthetic visibility profiles was scaled to every distance. The set has a fixed temperature and C/O ratio. We obtained for every distance the combination of stellar parameters (M, $\log(g)$) from the best-fitting profile.

Table 4.4: Distance measurements and stellar parameters of the model that best fits spectroscopic and interferometric measurements. The boldface distances correspond to the most likely values found by our stellar parameter analysis.

Distance	CR Gem	HK Lyr	RV Mon	Z Psc	DR Ser
$d_{\rm Berg}$	920 pc	**730 pc**	**670 pc**	465 pc	1295 pc
	$L = 11\,000\ L_\odot$	$L = 7\,186\ L_\odot$	$L = 6\,400\ L_\odot$	$L = 4\,534\ L_\odot$	$L = 18\,050\ L_\odot$
	$T_{\rm eff} = 3\,100$ K	$T_{\rm eff} = 3\,100$ K	$T_{\rm eff} = 3\,200$ K	$T_{\rm eff} = 3\,100$ K	$T_{\rm eff} = 3\,100$ K
	C/O = 1.05	C/O = 1.4	C/O = 1.05	C/O = 1.05	C/O = 1.05
	$M = 2M_\odot$	$M = 2M_\odot$	$M = 1M_\odot$	$M = 2M_\odot$	$M = 2M_\odot$
	$\log(g) = -0.40$	$\log(g) = -0.20$	$\log(g) = -0.40$	$\log(g) = +0.0$	$\log(g) = -0.60$
$d_{\rm Clau}$	**780 pc**	**900 pc**	**1000 pc**	**600 pc**	**990 pc**
	$L = 9\,025\ L_\odot$	$L = 11\,389\ L_\odot$	$L = 12\,932\ L_\odot$	$L = 7\,170\ L_\odot$	$L = 11\,390\ L_\odot$
	$T_{\rm eff} = 3\,100$ K	$T_{\rm eff} = 3\,100$ K	$T_{\rm eff} = 3\,200$K	$T_{\rm eff} = 3\,100$ K	$T_{\rm eff} = 3\,100$ K
	C/O = 1.05	C/O = 1.40	C/O = 1.05	C/O = 1.05	C/O = 1.05
	$M = 1M_\odot$	$M = 2M_\odot$	$M = 2M_\odot$	$M = 1M_\odot$	$M = 2M_\odot$
	$\log(g) = -0.60$	$\log(g) = -0.40$	$\log(g) = -0.40$	$\log(g) = -0.50$	$\log(g) = -0.40$
$d_{\rm Hipp}$	323^{+357}_{-111} pc	$1\,369^{+671}_{-NN}$ pc	450^{+369}_{-140} pc	323^{+119}_{-68} pc	$1\,690^{+2810}_{-1120}$
	-	-	$L = 2\,574\ L_\odot$	$L = 2\,267\ L_\odot$	-
	-	-	$T_{\rm eff} = 3\,200$ K	$T_{\rm eff} = 3\,100$ K	-
			C/O = 1.05	C/O = 1.05	
			$M = 1M_\odot$	$M = 1M_\odot$	
			$\log(g) = +0.0$	$\log(g) = +0.0$	

4.5 Comparison with evolutionary tracks

At this point of our investigation, we have one combination of stellar parameters for every object and every distance. To constrain the choice of the parameters even more, we compare them with the recent isochrones for thermally pulsing AGB stars from Marigo et al. (2008). The selection of the isochrones follows the same criteria as Marigo et al. (2008): ages $\log(t/yr)$ between 7.8 and 10.2, and the spacing in $\log(t)$ is 0.1 dex.

Fig. 4.5 shows a zoom into the region of the H-R diagram where AGB stars are located. The shaded area identify the region where C-stars are expected. Owing to the discrete sampling of the points in the isochrones (small square), the transition region from M- to C-stars is not very well defined. According to the stellar evolution calculations (P. Marigo, private communications), all stars on the cool side of the "hook" of the isochrones are C-

stars. Some values of the present mass are marked on the isochrones: they will be compared with the mass of the best-fitting hydrostatic models (see Sect. 4.7).

We overplot on the isochrones the points corresponding to the parameters we determined. Every star is indicated with a different symbol centred on the temperature and luminosity associated to the model: a plus for CR Gem, an asterisk for HK Lyr, diamond for RV Mon, triangle for Z Psc, and square for DR Ser. The error bars of the temperature are the ones associated to the short$L$ band $T_{\rm eff}$ determination, therefore, they are centred on the $T_{\rm eff}$(short$L$) values given in col. 3 of Table 4.3. The errors on the luminosity are not plotted here to avoid confusion but they are of the order of 40% (corresponding to the uncertainty on the distance measurements $d_{\rm Berg}$, $d_{\rm Clau}$).

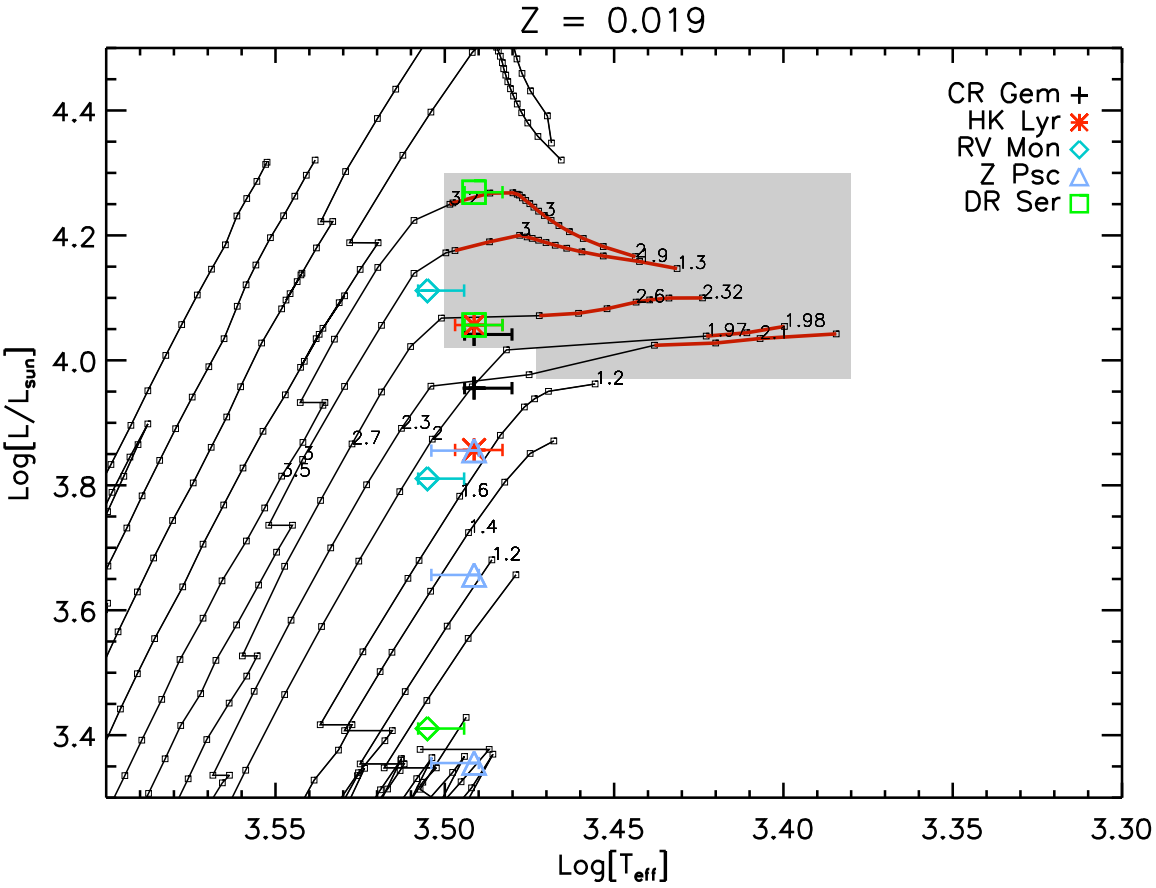

Figure 4.5: Zoom into the H-R diagram where C-stars are located. The solar metallicity isochrones (Marigo et al. 2008) are plotted in grey and the small numbers indicate the predicted present mass. The sampling of points in the isochrones is shown with tiny squares. The position of the C-stars is indicated by a shaded area, the uncertainty about this area is discussed in Sect. 4.5. The different symbols plotted correspond to the parameters determined for every star and distance assumed: plus for CR Gem, asterisk for HK Lyr, diamond for RV Mon, triangle for Z Psc, and square for DR Ser.

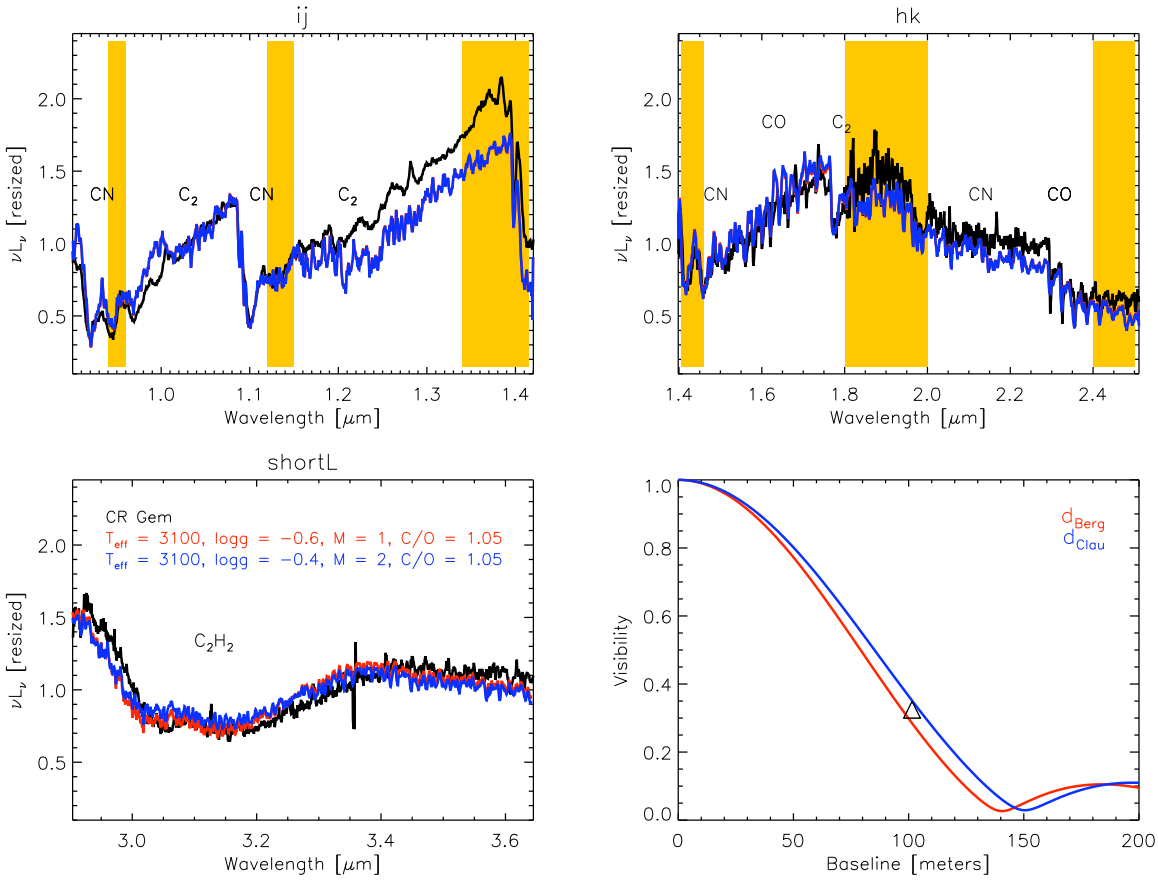

Figure 4.6: Comparison of the UKIRT/UIST spectra (black line) and PTI interferometric measurements (black triangle) of CR Gem with hydrostatic model predictions. The upper left panel illustrates the IJ range of the spectrum, the upper right panel shows the HK wavelength range. The lower left panel shows the short$L$ range. The shaded bands mark the region with poor atmospheric transmission. The molecules that contribute to the spectrum are also indicated. The synthetic spectra are overplotted in grey (blue, and red in colour version). The lower right panel shows the interferometric data point with the models which best fit the data for different distances overplotted.

4.6 Discussion of individual targets

4.6.1 CR Gem

CR Gem is classified as an irregular Lb variable with a variability amplitude in the B-band of 1.20 mag in the General Catalogue of Variable stars (GCVS; Samus+ 2007-2009). Nevertheless, Whitelock et al. (2008) classify this star as SRb with a period of 250^d and the ASAS V band light curve shows an amplitude of 0.5 mag (Pojmanski 2002). The spectral classification given in the GCVS is C8,3e(N).

The 3 μm short$L$ temperature we determine is around 100 K higher than the 2 960 K measured by Bergeat & Chevallier (2005). . The C/O we get is 1.05, we could not find other estimates for this value in the literature. The observed spectrum is presented in Fig. 4.6. It

is in general well reproduced with a few exceptions: the range $1.2-1.4\,\mu$m and the K-band between 2.1 and 2.3 μm, where the real data show an excess compared to the models (see general discussion in Sect. 4.7).

For this star we collected only one point of PTI visibility (Fig. 4.6 lower right panel), therefore it is not possible to check for asymmetries. All visibility profiles corresponding to the Hipparcos distance are not extended enough to fit the visibility point, therefore this distance can be excluded. For the Claussen distance the best-fitting model has mass $1\,M_{\odot}$ and $\log(g) = -0.60$, the luminosity is $9\,000\,L_{\odot}$ and the radius of the star $330\,R_{\odot}$. For the Bergeat distance, the highest value of distance estimated for this star, the best-fitting model has $2\,M_{\odot}$ and $\log(g) = -0.4$, the luminosity is $11\,000\,L_{\odot}$, and the radius $370\,R_{\odot}$.

4.6.2 HK Lyr

According to the GCVS, the visual amplitude of HK Lyr is 1.80 mag, the spectral classification C6,4(N4), and the star is classified as irregular Lb. The Hipparcos Variability Annex (Beichman et al. 1988) reports for this star a period of 196^{d} and an amplitude of variability of 0.4 in the Hipparcos magnitude. From optical spectroscopic analysis, this star is enriched in lithium and technetium (Abia et al. 2002, Boffin et al. 1993).

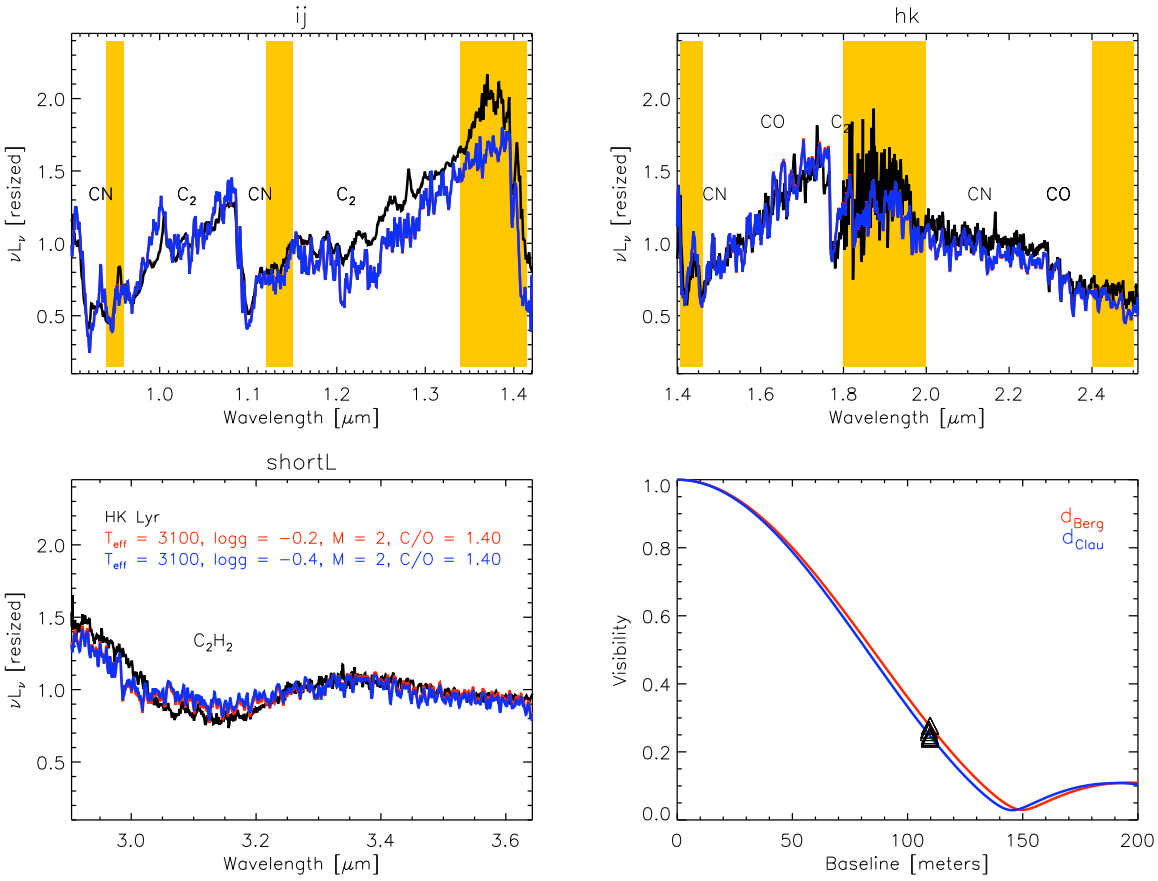

Figure 4.7: Same as in Fig. 4.6 for HK Lyr.

From our spectroscopic investigation the temperature and C/O ratio, obtained are higher than the ones estimated in literature (Table 4.3). While our temperature is 3 080 K, Ohnaka & Tsuji (1996) give 2 866 K and Bergeat & Chevallier (2005) estimate 2 945 K. Concerning the C/O ratio we obtain 1.4, while Abia et al. (2002) estimate 1.02. The fit of the spectroscopic data is quite successful except for the region between 1.2 and 1.45 μm (Fig. 4.7 upper left panel).

Eight visibility points are available from PTI observations. The UD diameters computed by fitting the single points do not differ. Over the time interval and position angle of the observations, the star does show no notable variation nor evidence of asymmetries (Fig. 4.2, row 'b'). We fitted all visibility points with synthetic profiles scaled for different distances (Fig.4.7 lower right panel) .

None of the models corresponding to the Hipparcos distance can fit the points, therefore we excluded this distance. The best-fitting parameters corresponding to $d_{\rm Berg}$ are 2 $M_{\odot}$ and $\log(g) = -0.2$. This model has a luminosity of $L = 7\,200\ L_{\odot}$ and a radius $R = 300\ R_{\odot}$. The best-fitting model corresponding to $d_{\rm Clau}$ has again mass 2 $M_{\odot}$ but $\log(g) = -0.4$. This model has a luminosity of $L = 11\,400 L_{\odot}$ and a radius $R = 370\ R_{\odot}$. In Fig. 4.5 the resulting parameters for HK Lyr are plotted with asterisks.

4.6.3 RV Mon

RV Mon is a C4,4-C6,2(NB/R9) star, its variability class is SRb with a primary pulsation period of 131^d and a long secondary period detected by Houk (1963) of 1047^d. The amplitude of variability given in the GCVS is 2.19 mag in the B-band, while the ASAS light curve suggests a V amplitude of 0.3 mag.

The temperature obtained with our fitting procedure is between the values given in the literature. Ohnaka & Tsuji (1996) get $T_{\rm eff} = 3\,330$ K, we obtained 3 170 K while Bergeat & Chevallier (2005) give 2 910 K. No estimation of C/O was found in the literature to be compared with our 1.05. The model we adopted for RV Mon matches the spectroscopic observations in all ranges quite well except for the region of the CO bands (longward 2.29 μm), where the observations show an IR excess compared to the synthetic spectra. The intensity of the C_2 feature at 1.77 μm is not well reproduced but this is at the border of an atmospheric window.

For this star we collected four visibility points. The first one is in 1999, the other three in 2008. Although the observations were carried out at very similar baseline, the visibility jumps by 0.1 between the two epochs of observation. This jump is visible also in the UD-diameter where it amounts to $\sim$ 0.16 mas, which is larger than the estimated error on the UD diameters ($\sim$ 0.06 in the worst case). This difference is also noted in the plot of the UD-versus-position angle. A careful check was performed to exclude any problem coming from the calibration procedure, but still we cannot completely exclude that the fluctuation in the visibility is caused by an instrument problem. From the astrophysical point of view, the observed trend could be explained in different ways: (i) it could be an asymmetry plus a temporal variation (for example a large convective shell), (ii) or an effect of the pulsation (panel '4c'). The temporal variation caused by the primary short period

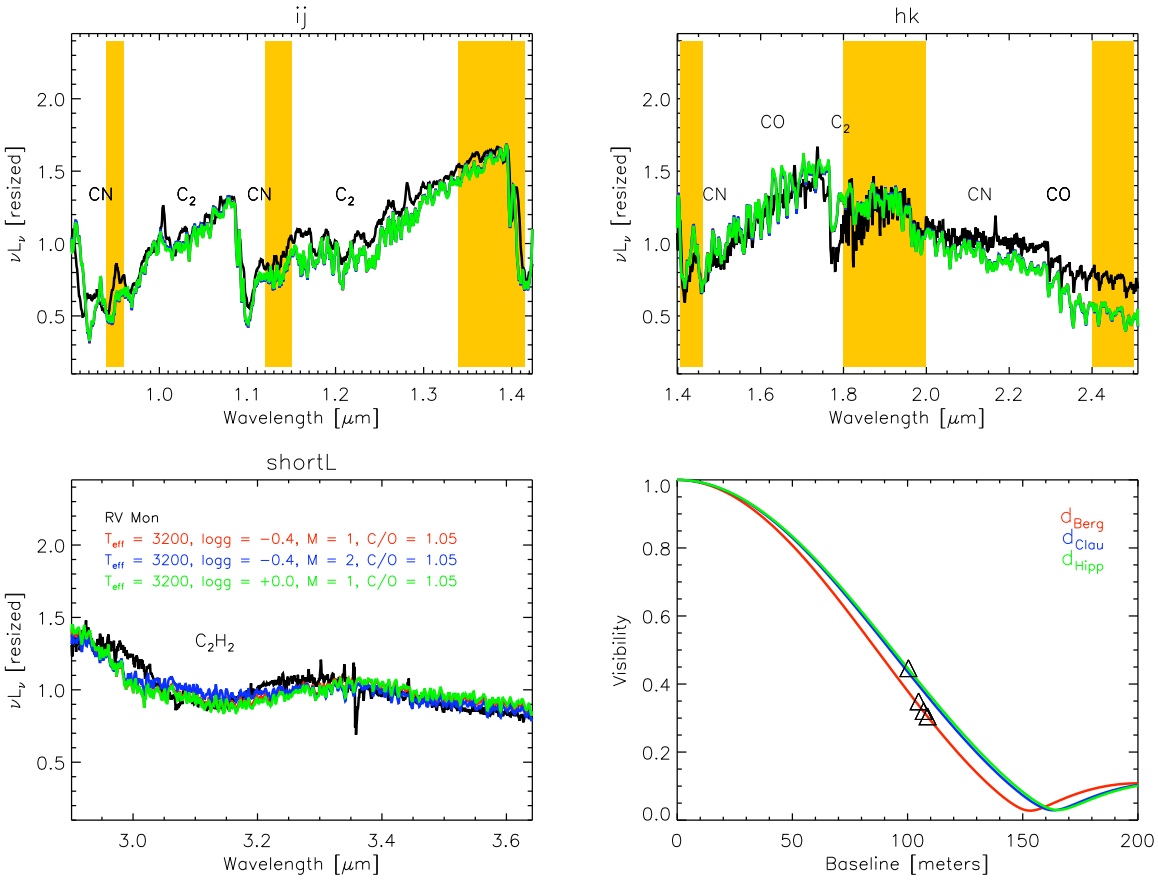

Figure 4.8: Same as in Fig. 4.6 for RV Mon.

of variability is not enough to explain the jump in the visibility. We derived from the light curve a difference in phase for the primary period of 0.16 between the two sets of observations. According to the predictions of the dynamic model atmospheres (Paladini et al. 2009, see Fig. 7 and Fig. 9), a hot C-star should show a difference in UD-diam of 0.06 mas, definitely smaller than 0.16. The two sets of observations have been obtained with a time difference of 3.5 times the length of the long secondary period. This longterm variation may, therefore, be responsible for the observed variation in size. Additional observations are necessary to reach a conclusive interpretation. Keeping this in mind, we performed a fit of the interferometric points with a hydrostatic model atmosphere as a first step. This might be followed by more investigations. From the lower right panel of Fig. 4.8 it is immediately obvious that no synthetic visibility profile can fit all observations at the same time. The best-fitting model obtained for the Hipparcos or Claussen distances can only fit the single point observed in 1999. The other models are either too extended or not extended enough to fit the other observations. The best-fitting model for d_{Hipp} has $M = 1M_{\odot}$, $\log(g) = +0.0$, $L = 2\,600\ L_{\odot}$ and $R = 170\ R_{\odot}$. For the distance determined by Claussen et al. (1987) the single data point is fitted by the model with $2M_{\odot}$, $\log(g) = +0.4$, $L = 13\,000\ L_{\odot}$ and a radius $R = 370\ R_{\odot}$. On the other hand, for the distance determined by Bergeat & Chevallier (2005) the three points observed in 2008 are fitted by the model with $M = 1M_{\odot}$,

$\log(g) = -0.4$, $L = 6\,400\,L_{\odot}$, and $R = 260\ R_{\odot}$. Nevertheless, the effect of variability or possible asymmetries needs to be investigated in more detail, and the parameters derived for this object should be considered with caution.

4.6.4 Z Psc

Z Psc is an SRb variable with amplitude derived from photographic plates of 1.3 mag. The period in the GCVS is 144^{d}. The ASAS light curve has an amplitude of 0.52mag in V band. The spectral classification from the GCVS (Samus+ 2007-2009) is C7,2(N0). Abia et al. (2002), and Boffin et al. (1993) determined a $^{12}C/^{13}C$= 55, moreover, they found enhancement of Tc, and no trace of Li in the spectrum. This implies that Z Psc is a standard low-mass TP-AGB star, and an intrinsic C-rich star.

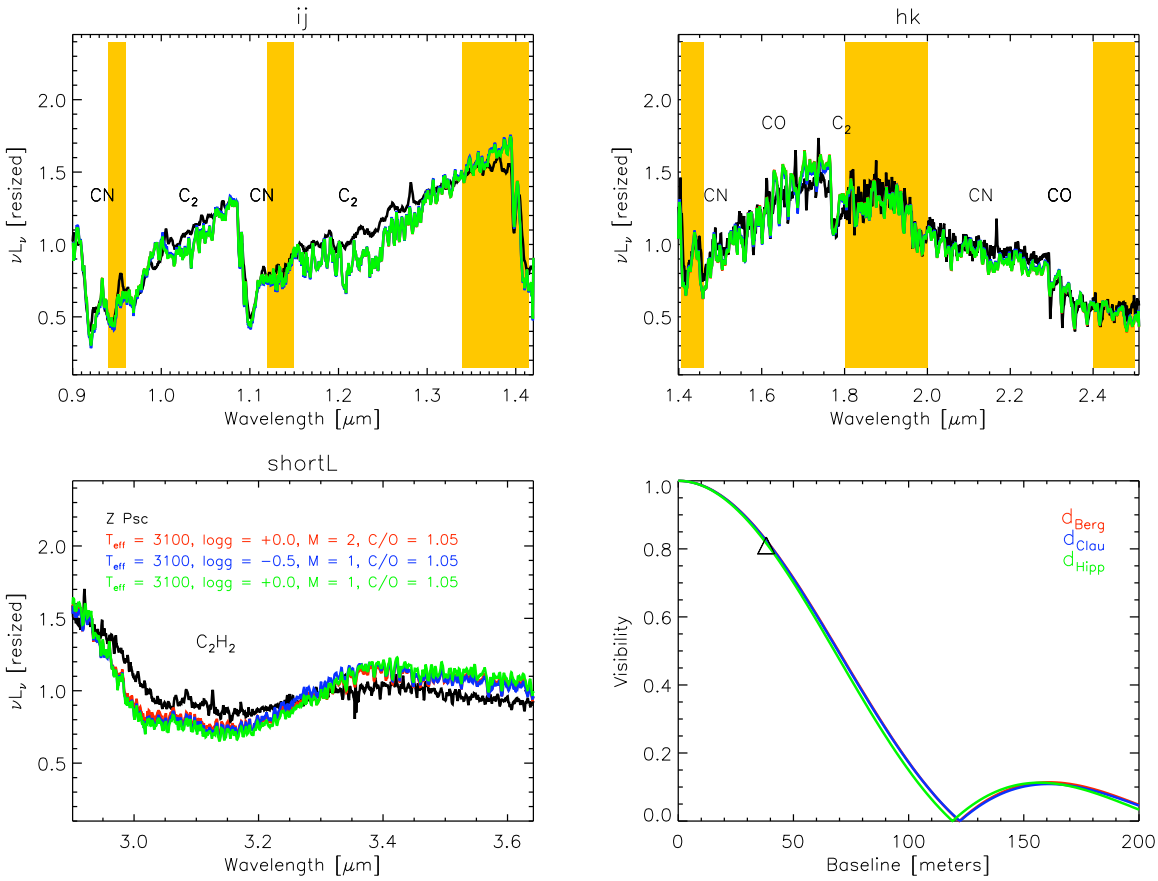

Figure 4.9: Same as in Fig. 4.6 for Z Psc.

Many temperature estimates were given for this star in the literature: Lambert et al. (1986) obtained 2870 K, Dyck et al. (1996) 3240 K, Ohnaka & Tsuji (1996) 3150 K, Bergeat & Chevallier (2005) 3095 K. All these values were obtained with different methods. Our measurement (see Table 4.3) is very close to the one given by Ohnaka & Tsuji (1996). The C/O = 1.05 we estimated agrees with the 1.014 of Lambert et al. (1986) and with the more recent 1.01 value of Abia et al. (2010). The match between models and observations is

shown in Fig. 4.9. From spectroscopy a small disagreement is barely detectable in the C_2 band at 1.20 μm, while the 3 μm feature of the model is too deep to fit the data (the star is hotter than the model).

Z Psc is the only one among our targets with no PTI data. For this star we used an observation available from the literature (Dyck et al. 1996) taken in the K-broad band with IOTA (2.2 μm) as already described in Sect. 4.2.2. The fit of the interferometric IOTA data is presented in the lower right panel of Fig. 4.9. The best-fitting model for the Hipparcos distance has a mass $M = 1 M_{\odot}$, $\log(g) = +0.0$, $L = 2\,300\,L_{\odot}$, and $R = 165\,R_{\odot}$. The distance determined by Bergeat & Chevallier (2005) gives a best-fitting model with the same $\log(g)$ obtained for Hipparcos distance fit but $M = 2\,M_{\odot}$, $L = 4\,500\,L_{\odot}$ and a radius $R = 230\,R_{\odot}$. In the case of the Claussen distance we have the best-fitting, which is the model with mass $1\,M_{\odot}$, $\log(g) = -0.5$, $L = 7\,150\,L_{\odot}$, and $R = 300\,R_{\odot}$.

4.6.5 DR Ser

According to the GCVS, DR Ser is an irregular variable Lb with an amplitude in the B-band of 2.99 mag. The ASAS light curve of this object is quite stable over the last 2000 days, it has a period of 196^d, and a V band amplitude of 0.3 mag. The spectral class is C6,4(N).

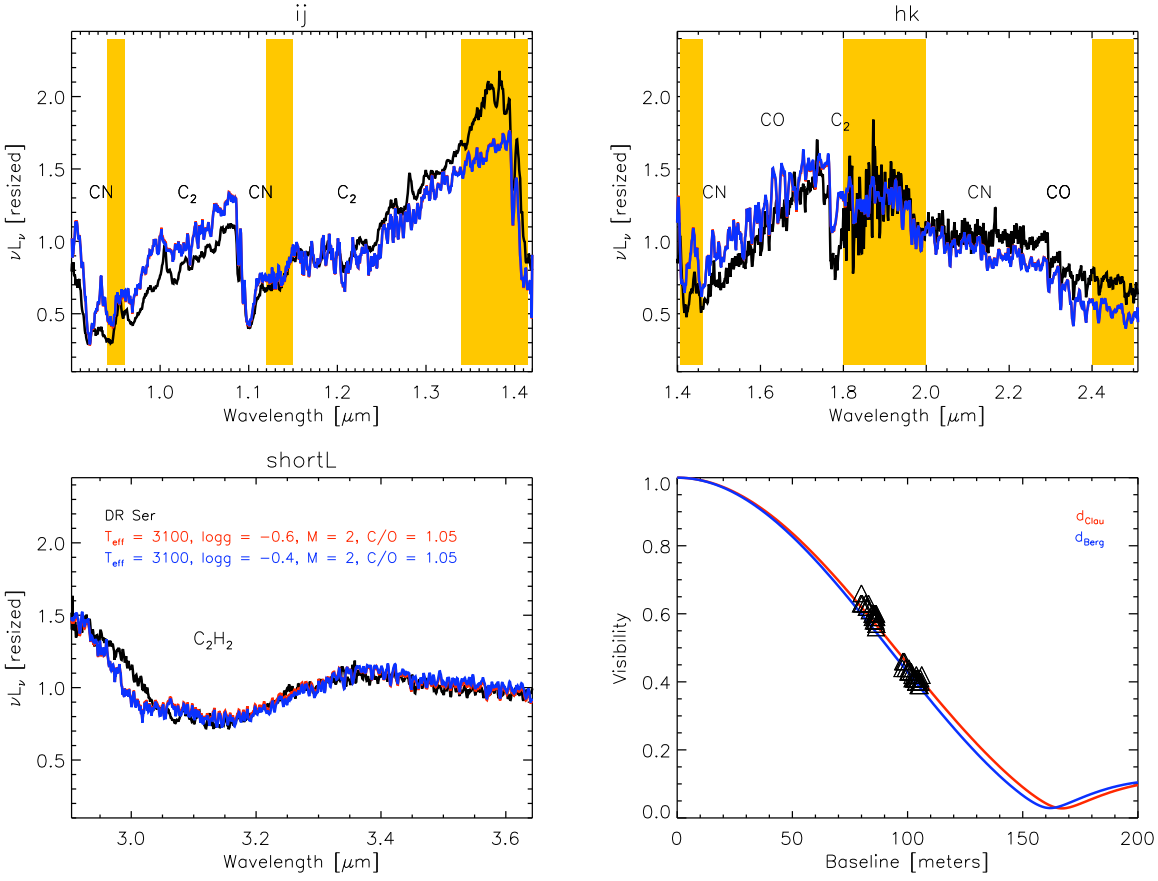

Figure 4.10: Same as in Fig. 4.6 for DR Ser.

This object is the one in our sample with the highest value of interstellar reddening. Applying the reddening correction, we noted that the observed spectrum looks completely unrealistic. Remembering that reddening correction for single objects is always very uncertain, we decided to skip the step of the reddening correction for DR Ser. Further investigation and a detailed map of the ISM in the region of this star are needed.

We determined a temperature of 3080 K. In the literature the $T_{\rm eff}$ values associated to this object are usually lower (see Sect. 4.7): 2500 K (Abia & Isern 1997), 2570 K (Thompson et al. 2002), 2650 K (Schöier et al. 2005, Bergeat & Chevallier 2005). Abia & Isern (1997) estimated the isotopic ratio ^{12}C/^{13}C= 6, which is also surprisingly low! The C/O we found, 1.05 is lower than the C/O = 1.26 obtained in literature by Eglitis & Eglite (1995).

There are 54 PTI points available for this object in the period between June 2000 and August 2001. The UD diameters determined agree with each other within a range of $\pm$0.02 mas, therefore we considered for the model fitting all points together (Fig. 4.10). None of the profiles computed at the Hipparcos distance could fit the data points. The best-fitting models have a mass $M = 2\,M_{\odot}$, and $\log(g) = -0.4$ or -0.6 for d_{Clau} and d_{Berg} respectively. The first model has $L = 11\,400\,L_{\odot}$ and a radius of $370\,R_{\odot}$; the second one $L = 18\,000\,L_{\odot}$ and $R = 470\,R_{\odot}$. It is impressive to note how all the visibility points observed at different epochs and position angles fit the hydrostatic synthetic profile.

4.7 Discussion

Based on the fitting procedure described above, we can identify a sequence in effective temperature for our targets. The temperature increases, starting from CR Gem, DR Ser, HK Lyr, Z Psc, RV Mon. Our temperature determination is very precise thanks to the large grid of models available and to the use of the short$L$ band spectrum. The $T_{\rm eff}$ here determined are always compatible within the error given in the literature.

The C/O ratio determination is not as accurate as the one of the temperature because of the very coarse spacing in the model grid, but mainly because of the low resolution of the spectra. Although the C/O values we determine have to be considered as indicative, they agree quite well with the ones estimated in the literature. We obtained the same C/O= 1.05 for all the stars except HK Lyr, which has C/O= 1.4. Those values agree with the range [1.01, 1.4] reported in the literature for classical C-stars (see Fig. 42 of Lambert et al. (1986), and Table 2 of Bergeat & Chevallier (2005)).

In general there is a good agreement between synthetic and observed spectra. Small discrepancies are observed mainly in the region between 1.2 and 1.4 μm, between 2.1 and 2.3 μm and on the left edge of the 3 μm feature. They can be attributed to small calibration problems, but also to a small amount of dust. This last point is supported by the fact that the differences detected in the IJ band between 1.2 and 1.4 μm are larger for the lower temperature stars (CR Gem, HK Lyr, DR Ser). We simulated the effect on the spectrum of a small amount of dust by using the DUSTY code (Ivezić & Eliztur 1997). Indeed, the IJ band of the spectrum fits slightly better for stars that have a high $J-K$ value (CR Gem, DR Ser). We also checked the effect of this small amount of dust on the

stellar parameter determination. The effect on the temperature and on the interferometric observable was within the error bar we already took into account, therefore we proceed with the hydrostatic models. A detailed analysis of spectro-interferometric observations with a hydrostatic+dusty model atmosphere will be presented in a follow-up work.

From the fit of the interferometric observations with models at different distances we note that in three of five cases no model can fit the observations at the distance estimated from Hipparcos. This is not such a surprise considering the error associated to these distance measurements. Further consideration about the distance can be made by studying the position of the best-fitting models in the H-R diagram (Fig 4.5).

Some of our hydrostatic models lie in a region of the H-R where larger masses are expected. If we consider the agreement between the two masses (from hydrostatic models and evolutionary calculations) as a criterion to select the correct distance of the objects, we have

- CR Gem. The point with lower luminosity is the one fitting the range of mass, therefore the distance determined by Claussen can be retained, and the one of Bergeat discarded.
- HK Lyr. Both models have the same mass and lie in a region in between 1 and 2.6 $M_{\odot}$. Considering an error on both distances of 20% (i.e. a factor 1.44 in luminosity), none of the values can be excluded.
- RV Mon. The Hipparcos distance is in the correct region of mass, but too far from the C-stars region, therefore it can be discarded. Both the other two distances correspond to a model that fits the region of masses, therefore they can be both retained.
- Z Psc. In this case the Bergeat distance can be discarded because the best-fitting model has 2 $M_{\odot}$, but falls in the range of 1 $M_{\odot}$. Considering the error on the luminosity, both the distances from Hipparcos and Claussen can be retained. Nevertheless, the position of the model at the Claussen distance is more probable because this is closer to the C-stars region.
- DR Ser. The distance estimated from Bergeat can be discarded because the model lies in the region of the stars with 3 $M_{\odot}$.

The parameters with the most probable distances, with associated errors in temperature and luminosity are shown in Fig. 4.11.

Taking into account the uncertainty associated to the transition phase M-C stars (see Sect. 4.5), all stars have at least one combination of parameters that lie in the region where the C-stars sequence starts. This agrees with the hydrostatic scenario for our targets: the objects are supposed to be hot C-stars, with relatively low mass-loss and low C/O. They "recently" turned into C-stars, and while moving on the evolutionary track, they will increase the production of carbon and will lose more and more mass because of the stellar wind. Our work is partially limited because that only model atmospheres with mass 1 and 2 are available.

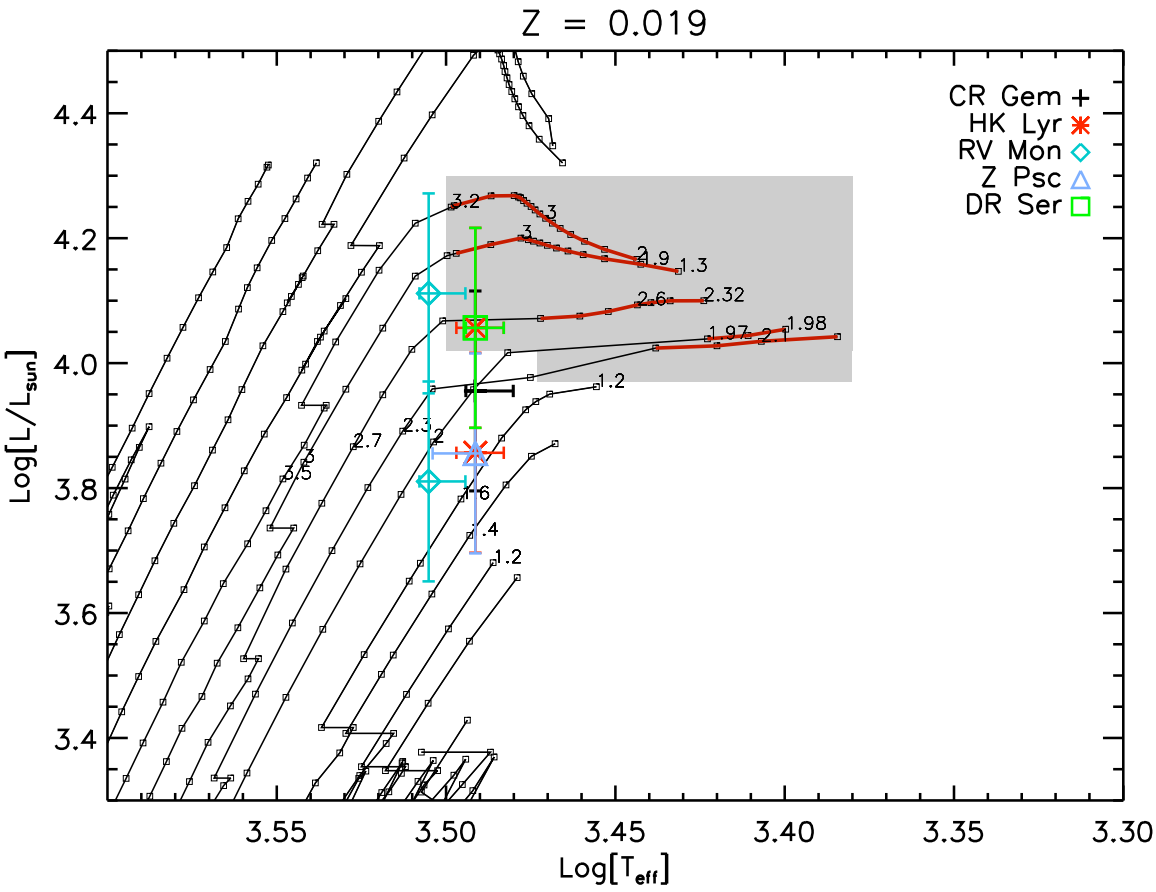

Figure 4.11: Same as in Fig. 4.5, but this time only the parameters with most probable distances are plotted.

Two objects of our sample show some peculiarity that deserves additional investigations. The interferometric observations of RV Mon show a possible non-hydrostatic nature. All visibility points acquired with PTI cannot be fitted with the same model. This might be caused by some instrumental effect, while the physical explanation would be an evidence of an asymmetry or (more probably) of a variability effect. According to the interferometric measurements, the star DR Ser is a hydrostatic object. We were able to fit with the same model 54 visibility points observed in different epochs and position angles. On the other hand, the fit of the IJ and HK band is not very good, and the reddening correction of the spectrum makes the fit even worse. A detailed ISM map for this region of the sky is needed.

4.8 Conclusions

More than a simple parameters determination, this work aims to identify which of the stellar parameters of C-stars can be constrained by using different techniques like spectroscopy and interferometry. Which limits appear by investigating only with one tool? Infrared interferometry is a relatively young field of research, but it can already give a significant

contribution to the stellar parameter determinations.

We confirm that low-resolution infrared spectroscopy is not sensitive to $\log(g)$ and mass determinations of C-stars. We clearly show that a highly precise determination of the temperature can be achieved for C-stars with no significant dust contribution thanks to the use of the $3\,\mu$m feature (C_2H_2 + HCN). The determinations based only on the IJH bands tend to underestimate the temperature.

The hydrostatic model atmospheres adopted in this work were able for the first time to fit simultaneously spectroscopic and interferometric observations. This is a very important achievement considering that inaccuracies in model atmospheres reflect negatively on the check of the stellar evolution calculations. On the other hand, the inaccuracy in the distance determination for this class of objects reflects negatively on the parameter determination, as already noted in Wittkowski et al. (2001). We considered a criterion to select the distance on the agreement between mass of the hydrostatic models and mass predicted by the isochrones. According to this, the distance estimated by Claussen et al. (1987) is the most probable among the three distances we used for this work. Taking into account the uncertainty in the transition phase from O-rich to C-rich star in the evolution models as well, we obtained that all the objects of our sample have at least one combination of observationally determined parameters that fits the C-stars region. We were able to associate temperature, C/O, mass, $\log(g)$ and a range of reasonable distances for all objects of our sample.

A grid of models with larger coverage of the mass range (at least from 1 to $4\,M_{\odot}$) as well as a more dense grid of points for the isochrones would significantly improve our estimations. The advent of a new dedicated mission (Gaia) might improve the distance problem for C-stars.

The synergy between different techniques of investigation and realistic theoretical atmospheric and stellar evolutionary models will be the key to determine precise characteristics for this class of objects, and to be able to understand clearly the physical processes that drive their evolution.

Table 4.5: Interferometric observations.

ID	UT Date	B [m]	PA [deg]	$V \pm \sigma_V$	Additional information
CR Gem	11/03/1999 Nov 3	101.49	80	0.324 ± 0.004	
HK Lyr	1999 May 20	109.79	71	0.277 ± 0.004	
	1999 May 21	109.78	78	0.277 ± 0.005	
	2000 May 22	109.29	63	0.258 ± 0.005	
	2000 May 22	109.33	64	0.265 ± 0.004	
	2000 May 22	109.76	71	0.238 ± 0.010	
	2000 May 22	109.77	72	0.244 ± 0.003	
	2000 May 22	109.73	80	0.249 ± 0.003	
	2000 May 22	109.72	81	0.242 ± 0.003	
RV Mon	1999 Nov 04	100.37	63	0.446 ± 0.015	
	2008 Sep 25	108.68	52	0.305 ± 0.005	
	2008 Sep 25	106.98	55	0.320 ± 0.004	
	2008 Sep 25	104.79	57	0.349 ± 0.006	
Z Psc	1995 Oct 08	38.21	–	0.810 ± 0.123	Dyck et al. (1996)
DR Ser	2000 Jun 03	106.29	55	0.387 ± 0.008	
	2000 Jun 19	107.05	54	0.535 ± 0.024	discarded from interpretation
	2000 Jun 19	106.01	56	0.497 ± 0.035	discarded from interpretation
	2000 Jun 19	105.45	56	0.487 ± 0.032	discarded from interpretation
	2000 Jun 19	104.83	57	0.515 ± 0.024	discarded from interpretation
	2000 Jun 20	103.33	59	0.435 ± 0.013	
	2000 Jun 20	102.19	60	0.429 ± 0.013	
	2001 Apr 18	104.41	57	0.407 ± 0.010	
	2001 Apr 18	104.20	58	0.415 ± 0.004	
	2001 Apr 18	103.23	59	0.407 ± 0.003	
	2001 Apr 18	103.06	59	0.413 ± 0.007	
	2001 Apr 18	102.13	60	0.410 ± 0.005	
	2001 Apr 23	106.14	55	0.418 ± 0.013	
	2001 Apr 23	103.56	58	0.410 ± 0.012	
	2001 Apr 23	100.63	62	0.429 ± 0.011	
	2001 Apr 23	99.18	64	0.435 ± 0.011	
	2001 Apr 23	97.73	66	0.440 ± 0.012	
	2001 Apr 29	105.27	56	0.389 ± 0.006	
	2001 Apr 29	105.01	57	0.391 ± 0.005	
	2001 Apr 29	103.67	58	0.396 ± 0.005	
	2001 Apr 29	102.84	59	0.406 ± 0.005	
	2001 Apr 29	102.68	59	0.407 ± 0.008	
	2001 May 03	86.43	15	0.587 ± 0.014	
	2001 May 03	86.40	15	0.597 ± 0.015	
	2001 May 03	85.92	15	0.591 ± 0.019	
	2001 May 03	84.84	16	0.593 ± 0.018	

Table 4.5: continued.

ID	UT Date	B [m]	PA [deg]	$V \pm \sigma_V$	Additional informations
	2001 May 03	83.03	17	0.626 ± 0.023	
	2001 May 04	86.07	15	0.583 ± 0.009	
	2001 May 04	85.98	15	0.580 ± 0.009	
	2001 May 04	84.76	16	0.599 ± 0.010	
	2001 May 04	82.50	17	0.615 ± 0.007	
	2001 May 04	82.24	17	0.621 ± 0.011	
	2001 May 05	86.31	15	0.589 ± 0.006	
	2001 May 05	85.79	15	0.598 ± 0.007	
	2001 May 05	84.85	16	0.605 ± 0.005	
	2001 May 05	83.54	17	0.613 ± 0.008	
	2001 May 05	81.86	17	0.626 ± 0.006	
	2001 May 23	104.92	57	0.402 ± 0.007	
	2001 May 23	103.80	58	0.416 ± 0.004	
	2001 Jun 21	103.71	58	0.404 ± 0.006	
	2001 Jun 21	102.06	60	0.420 ± 0.005	
	2001 Jun 21	100.30	63	0.433 ± 0.005	
	2001 Jun 21	98.60	65	0.460 ± 0.009	
	2001 Jul 16	79.72	14	0.627 ± 0.012	
	2001 Jul 22	105.69	56	0.402 ± 0.019	
	2001 Jul 22	105.55	56	0.405 ± 0.019	
	2001 Jul 22	104.73	57	0.393 ± 0.015	
	2001 Jul 22	104.59	57	0.413 ± 0.016	
	2001 Jul 22	101.55	61	0.427 ± 0.016	
	2001 Jul 22	100.54	62	0.438 ± 0.014	
	2001 Aug 22	86.22	15	0.586 ± 0.022	
	2001 Aug 22	86.04	15	0.581 ± 0.020	
	2001 Aug 22	85.95	15	0.596 ± 0.022	
	2001 Aug 22	85.41	16	0.586 ± 0.026	
	2001 Aug 22	85.29	16	0.576 ± 0.020	
	2001 Aug 22	80.33	18	0.631 ± 0.028	
	2001 Aug 22	79.97	18	0.661 ± 0.055	
	2001 Aug 23	98.03	66	0.456 ± 0.011	
	2001 Aug 27	86.28	14	0.564 ± 0.005	
	2001 Aug 27	86.45	14	0.565 ± 0.003	
	2001 Aug 27	86.46	15	0.566 ± 0.004	

Chapter 5

Spectro-interferometric study of the semiregular variable R Scl

This chapter is based on the A&A publication by Sacuto et al. (2011). My contribution to this work was: calibrating the VINCI data, choosing the dynamic model atmospheres suitable for the comparison with spectro-interferometric data, computing synthetic spectro-interferometric observables, testing the different options in order to include the SiC. Moreover, I reduced a ESO/SOFI spectrum of the investigated star observed under the program 074.D-0601. Unfortunately the spectrum was saturated and was therefore not usable for the current work. The VLTI/MIDI data presented here are based on observations under programs IDs 60.A-9220, 074.D-0601, 077.D-0294 (French Guaranteed Time Observation), 078.D-0112 (Belgian Guaranteed Time Observation), and 078.D-0122 (French Guaranteed Time Observation).

Observing and modeling the dynamic atmosphere of the low mass-loss C-star R Sculptoris at high angular resolution

S. Sacuto, B. Aringer, J. Hron, W. Nowotny, C. Paladini, T. Verhoelst, and S. Höfner
2011, A&A, 525, 42

Abstract: We study the circumstellar environment of the carbon-rich star R Sculptoris using the near- and mid-infrared high spatial resolution observations from the ESO-VLTI focal instruments VINCI and MIDI, respectively. These observations aim at increasing our knowledge of the dynamic processes in play within the very close circumstellar environment where the mass loss of AGB stars is initiated. We first compare the spectro-interferometric measurements of the star at different epochs to detect the dynamic signatures of the circumstellar structures at different spatial and spectral

scales. We then interpret these data using a self-consistent dynamic model atmosphere to discuss the dynamic picture deduced from the observations. Since the hydrodynamic computation needs stellar parameters as input, a considerable effort is first applied to determining these parameters. Interferometric observations do not show any significant variability effect at the 16 m baseline between phases 0.17 and 0.23 in the K band, and for both the 15 m baseline between phases 0.66 and 0.97 and the 31 m baseline between phases 0.90 and 0.97 in the N band. We find fairly good agreement between the dynamic model and the spectrophotometric data from 0.4 to 25 μm. The model agrees well with the time-dependent flux data at 8.5 μm, whereas it is too faint at 11.3 and 12.5 μm. The VINCI visibility measurements are reproduced well, meaning that the extension of the model is suitable in the K-band. In the mid-infrared, the model has the proper extension to reveal molecular structures of C_2H_2 and HCN located above the stellar photosphere. However, the windless model used is not able to reproduce the more extended and dense dusty environment. Among the different explanations for the discrepancy between the model and the measurements, the strong nonequilibrium process of dust formation is one of the most probable. The transition from windless atmospheres to models with considerable mass-loss rates occurs in a very narrow range of stellar parameters, especially for the effective temperature, the C/O ratio, and the pulsation amplitude. A denser sampling of such critical regions of the parameter space with additional models might lead to a better representation of the extended structures of low mass-loss carbon stars like R Sculptoris. The complete dynamic coupling of gas and dust and the approximation of grain opacities with the small-particle limit in the dynamic calculation could also contribute to the difference between the model and the data.

5.1 Introduction

AGB stars are complex objects where several physical processes are in play (nucleosynthesis, convective effects, stellar pulsation, shock waves, mass-loss, molecular and dust formation, etc.). Among these mechanisms, the mass loss is particularly important for the AGB phase by limiting the maximum luminosity of the object and controlling the overall stellar evolution. The general picture of the mass-loss process of carbon-rich AGB stars is quite well understood nowadays. The pulsation of the star creates shock waves pushing the matter to conditions where both temperature and pressure allow formation of dust grains. As the opacity of amorphous carbon dust is high, grains receive enough momentum through radiative pressure to be accelerated and to drag along the gas by collisions, causing a slow outflow from the star (e.g. Fleischer et al. 1992, Höfner & Dorfi 1997).
To investigate this dynamic process, it is necessary to compare predictions of hydrodynamic atmospheric models with observations. The code described by Höfner et al. (2003) solves the coupled equations of hydrodynamics, together with frequency-dependent radiative transfer, taking the time-dependent formation, growth, and evaporation of dust grains into account. Dynamic model atmospheres coming from this code have successfully reproduced line profile variations (Nowotny et al. 2005a,b) and time-dependent spectrometric data (Gautschy-Loidl et al. 2004) of carbon-rich stars.
Because of the large distance of the closest AGB stars (typically 100 to 1000 parsec), only the high angular resolution technique of long-baseline optical interferometry allows probing

the regions where the mass-loss process develops. Interferometric predictions based on the dynamic atmospheric models with and without mass loss are described in detail by Paladini et al. (2009). The aim of this paper is to extend the work comparing the dynamic models with near- and mid-infrared high angular resolution interferometric observations of a carbon-rich star.

R Sculptoris (R Scl) is a carbon-rich, semi-regular (SRa) variable star having a low mass-loss rate (1-5$\times10^{-7}$ $M_\odot\,yr^{-1}$: Le Bertre 1997, Gustafsson et al. 1997, Wong et al. 2004). The mid-infrared emission between 10 and 12 μm observed in the ISO/SWS data indicates that the star is surrounded by a warm, carbon-rich dusty shell composed of amorphous carbon (AmC) and silicon carbide (SiC) (Hron et al. 1998). The pulsation period of the star is 374 days (Whitelock et al. 1997), and the cycle-to-cycle averaged visual magnitudes vary from 6.7 to 8.1. A second period of 1 804 days ($\sim$5 times the stellar pulsation period) has also been detected by Whitelock et al. (1997); however, its origin is not yet understood.

Until now, all the interferometric studies of temporal evolution of carbon-rich stars have been based on sequences of geometric and hydrostatic models with varying stellar parameters (van Belle et al. 1997, Thompson et al. 2002, Ohnaka et al. 2007). However, as argued by Höfner et al. (2003), the only way to understand how the dynamic processes influence the atmospheric structure at different spatial scales is the use of time-dependent, self-consistent dynamic models.

In this paper, we thus present the first interpretation of spectrophotometric and interferometric data of a carbon-rich star in terms of a self-consistent dynamic model atmosphere. Near- and mid-infrared interferometric data at different baselines (15, 30, and 60 m) will allow probes of regions ranging from the stellar photosphere to the innermost region of its dusty environment where the dynamic processes of shock waves, stellar winds, and mass loss are all at work.

The outline of this paper is as follows. In Sect. 5.2, we present the VINCI and MIDI observations of R Scl and describe the calibration performed with the corresponding data-reduction software packages developed for these instruments. Section 5.3 is dedicated to the variability of the star obtained from previous visual photometric and polarimetric data. We investigate the mid-infrared spectrometric and near- and mid-infrared interferometric variability of the star by comparing measurements from cycle-to-cycle and phase-to-phase. In Sect. 5.4, we investigate the hydrodynamic modeling of R Scl. Since the hydrodynamic computation needs stellar parameters as input, a considerable effort is first applied to the determination of the corresponding stellar parameters. The last part of this section presents the results of the self-consistent hydrodynamic modeling of the spectrophotometric and of near- and mid-infrared interferometric data of the star. Finally, we conclude and give perspectives for future work in Sect. 5.5.

5.2 Observations

The Very Large Telescope Interferometer (VLTI) of ESO's Paranal Observatory was used with VINCI, the near-infrared (λ=2.0-2.4 μm) interferometric recombiner (Kervella et al.

2000), and MIDI, the mid-infrared (λ=8.0-13 μm) interferometric recombiner (Leinert et al. 2003). VINCI operates around 2 μm (K band), using single spatial mode interference by employing optical fibers for spatial filtering and beam combination. MIDI combines the light of two telescopes and provides spectrally resolved visibilities in the N band atmospheric window.
Observations of R Scl were conducted in 2001, 2005, and 2006 with the VLT unit telescopes (UTs) UT2-UT4, and auxiliary telescopes (ATs) E0-G0, D0-G0, A0-G0, G0-K0, G0-H0, and D0-H0. This provides projected baselines and projected angles in the range of 11 to 64 m and 34° to 117°, respectively (see Tables 5.1, 5.2, and Fig. 5.1). The seeing of all the VINCI observations is below 0.9″, whereas it is below 2.4″ in the case of the MIDI observations (see Tables 5.2).
Tables 5.1, 5.2 present the journals of interferometric observations of R Scl with the VINCI and MIDI focal instruments. The calibrators, β Cet (G9II-III, angular diameter: $\theta = 5.18 \pm 0.06$ mas), α CMa (A1V, $\theta = 5.94 \pm 0.02$ mas) for VINCI and HD12524 (K5III, $\theta = 2.53 \pm 0.07$ mas), β Gru (M5III, $\theta = 26.8 \pm 1.3$ mas), τ^4 Eri (M3/M4III, $\theta = 10.6 \pm 1.0$ mas), HD4128 (G9II-III, $\theta = 5.04 \pm 0.07$ mas) for MIDI, were observed before or after the science target. Diameters of the VINCI calibrators were adopted from the `CHARM2` catalog (Richichi et al. 2005). Diameters of the MIDI calibrators HD12524 and HD4128 were taken from the ESO website through the `CalVin` database[1]. The diameter of the MIDI calibrator τ^4 Eri was taken from the `CHARM2` catalog (Richichi et al. 2005). Finally, the diameter of the MIDI calibrator β Gru was defined from the work of Sacuto et al. (2008).

The VINCI data (program 60.A-9220) were processed with the pipeline of data reduction based on the wavelet transform described in Kervella et al. (2004). After checking the stability of the transfer function (T_i) over the two nights of observations, the raw visibility measurements were calibrated using the weighted average of the estimated T_i^2.
The VINCI instrument has a bandpass corresponding to the K-band filter (2.0-2.4 μm) without spectral dispersion. It is thus necessary to compute an effective wavelength to determine the spatial frequency of the observation (Kervella et al. 2007). The effective wavelength of our observations was calculated from the relation given by Wittkowski et al. (2004b) using the best-fitting hydrostatic model spectrum of R Scl described in Sect. 5.4.1. We obtained an effective wavelength of 2.253 μm.
Among the VINCI data, one observation (2001-12-08 01:03:54; see Table 5.1) led to an outlier showing an abnormally low level of amplitude as compared to the other visibility data at close base, PA, and phase. The corresponding visibility measurement was discarded.
In the case of MIDI, chopped acquisition images were recorded (f=2 Hz, 2000 frames, 4 ms per frame) to ensure the accurate acquisition of the target. Photometry from the UT observations (program 074.D-0601) was obtained before and after the interferometric observations with the HIGH-SENS mode of MIDI, using the GRISM that provides a spectral resolution of about 230. Photometry from the AT observations were obtained with the HIGH-SENS mode (program 078.D-0112), and simultaneously with the interferometric observations with the SCI-PHOT mode of MIDI (programs 077.D-294 and 078.D-0122), using the PRISM that provides a spectral resolution of about 30. The acquisition images enabled us to confirm that the mid-IR source was unresolved by the single-dish UT. This

[1] `http://www.eso.org/observing/etc/`

Table 5.1: Journal of all available VINCI observations of R Scl. The calibrators used to calibrate the visibilities are given before or after the science target. The visual phase of the star during the observations is calculated from Eq. 5.1. The configuration used for the observations is given. The length and position angle of the projected baseline are also indicated. Same for Tables 5.2.† means that the data were not exploitable (see text). Same for Tables 5.2.

Star	UT date & Time	Phase	Config.	Base [m]	PA [deg]
β Cet	2001-11-15 01:30:15	...	-	...	...
β Cet	2001-11-15 01:54:23	...	-	...	...
β Cet	2001-11-15 02:01:16	...	-	...	...
R Scl	2001-11-15 02:15:27	0.17	E0-G0	16	69
R Scl	2001-11-15 02:29:56	0.17	E0-G0	16	71
R Scl	2001-11-15 02:35:41	0.17	E0-G0	16	71
R Scl	2001-11-15 02:40:42	0.17	E0-G0	16	72
β Cet	2001-11-15 03:50:07	...	-	...	...
β Cet	2001-11-15 03:58:02	...	-	...	...
β Cet	2001-11-15 04:05:08	...	-	...	...
R Scl	2001-11-15 04:18:11	0.17	E0-G0	15	84
R Scl	2001-11-15 04:34:41	0.17	E0-G0	14	86
R Scl	2001-11-15 04:39:59	0.17	E0-G0	14	87
β Cet	2001-11-15 05:32:55	...	-	...	...
β Cet	2001-11-15 05:39:46	...	-	...	...
β Cet	2001-11-15 05:46:41	...	-	...	...
R Scl	2001-11-15 06:03:45	0.17	E0-G0	11	99
R Scl	2001-11-15 06:09:24	0.17	E0-G0	11	100
R Scl	2001-11-15 06:14:57	0.17	E0-G0	11	101
α Cma	2001-11-15 06:30:06	...	-	...	...
α Cma	2001-11-15 06:34:52	...	-	...	...
α Cma	2001-11-15 06:46:09	...	-	...	...
α Cma	2001-11-15 06:52:23	...	-	...	...
R Scl	2001-12-08 00:57:37	0.23	E0-G0	16	70
R Scl†	2001-12-08 01:03:54	0.23	E0-G0	16	72
R Scl	2001-12-08 01:13:17	0.23	E0-G0	16	72
R Scl	2001-12-08 01:18:42	0.23	E0-G0	16	73
R Scl	2001-12-08 01:25:45	0.23	E0-G0	16	74
β Cet	2001-12-08 01:38:37	...	-	...	...
β Cet	2001-12-08 01:45:31	...	-	...	...
β Cet	2001-12-08 01:50:26	...	-	...	...
R Scl	2001-12-08 02:09:03	0.23	E0-G0	15	79
R Scl	2001-12-08 02:13:53	0.23	E0-G0	15	80
β Cet	2001-12-08 02:26:18	...	-	...	...
β Cet	2001-12-08 02:33:18	...	-	...	...

implies that most of the mid-infrared flux originates in the inner 300 mas of the source, corresponding to the Airy pattern of the UTs and defining the Field Of View (FOV) of the interferometric observations. This also means that the flux detected within the 1.1″ FOV of the single-dish AT originates in this inner region. Therefore, measurements extracted

from the ATs and the UTs are fully consistent with each other.
The data reduction software packages[2] MIA and EWS (Jaffe 2004) were used to derive the calibrated spectra and visibilities (Chesneau et al. 2005, Ratzka et al. 2007). MIA is based on a power spectrum analysis and uses a fast Fourier transformation (FFT) to calculate the Fourier amplitude of the fringe packets, while EWS uses a shift-and-add algorithm in the complex plane, averaging appropriately modified individual exposures (dispersed channeled spectra) to obtain the complex visibility.
To calibrate the MIDI visibility measurements of R Scl, we used the transfer functions derived from the closest calibrators in time from the source (see Tables 5.2). This allows a decrease in the bias due to the air mass difference between the source observation at a given sky location and the calibrator observation at another location. The main source of uncertainties on the calibrated visibility measurements comes from the time-dependent atmospheric transmission between the observation of the calibrator and the source and from the dimension and uncertainty on the calibrator angular diameter (Bordé et al. 2002, Cruzalèbes et al. 2010). The rms of the transfer function deduced from all the calibrators of the night gives an upper estimate of the calibrated visibility error bar due the time-dependent atmospheric condition between the observations of the source and the calibrator. We assume a standard error bar of 10% on the calibrated visibilities corresponding to the upper limit on the error budget previously assigned. However, in the case of the HIGH-SENS mode, the photometry is performed about 5 to 10 minutes after the record of the fringe, i.e. correlated flux. As the atmospheric conditions change between both recordings, an additional error bar on the calibrated visibilities must be considered. Taking a similar error into account for both the SCI-PHOT and HIGH-SENS modes implicitly assumes that the variation in the transfer functions is *much* greater than the intrinsic error of one measurement due to the changing weather conditions. During good atmospheric conditions, this assumption is reasonable. During bad atmospheric conditions (i.e. up to a certain seeing threshold), the large fluctuation of the positions of the two beams reduces the beam overlap leading to strong variations in the fringe amplitude and the photometry. A solution to quantify the influence of the seeing on an individual measurement is to use the SCI-PHOT mode data with additional photometry (*pseudo HIGH-SENS* mode) taken under similar atmospheric conditions. Comparing calibrated visibilities reduced with the pure SCI-PHOT mode with those reduced with the pseudo HIGH-SENS mode gives a direct handle on the midterm (i.e. time span from fringe tracking to the photometry) influence of the seeing. Under bad conditions (i.e. seeing$\geq$1.5″), the pseudo HIGH-SENS mode gives systematic lower visibilities, up to a level of 4%, when comparing them to the ones deduced from the pure SCI-PHOT mode, while the difference falls to zero when the seeing is smaller than 1.1″. This is reasonable considering that the overlap of two beams is statistically reduced leading to systematically lower visibilities. We therefore consider an additional positive deviation of 4% (i.e. up to the 5% SCI-PHOT positive error) on the error bars associated to the calibrated visibilities recorded in HIGH-SENS mode under bad atmospheric conditions (i.e. seeing$\geq$1.5″). Finally, the error bar on the calibrated visibilities recorded in HIGH-SENS mode under better atmospheric conditions (i.e. seeing$\leq$1.1″) is similar to the standard 10% error bar assigned to the SCI-PHOT mode measurements.
The data quality has been checked using the *MIA Graphical User Interface*, and the software developed by Paris Observatory for MIDI[3]. Among the MIDI measurements, data sets #2, #5, #8, #15, and #25 (see Tables 5.2) led to outliers. Data sets #2, #15, and #25 show

[2] `http://www.mpia-hd.mpg.de/MIDISOFT/, http://www.strw.leidenuniv.nl/~nevec/MIDI/`
[3] Software is available through the JMMC website:
`http://mariotti.ujf-grenoble.fr/`

calibrated visibilities greater than unity, data set #5 shows an unusual spectral signature of the dispersed visibility, whereas data set #8 shows an abnormally high level of visibility amplitude compared to the other visibility data at close base, PA, and phase. Finally data sets #9, #10, #11, #12, #13, #14, and #16 show very broad dispersed power spectral densities (PSD) and/or fringe histograms (FH), especially from 8 to 10 μm since shorter wavelengths are more affected by the atmospheric conditions. If the PSD and FH are very broad, a very significant fraction of the fringe power is distributed outside the integration range, leading to a systematic underestimation of visibility. All the corresponding visibility measurements were discarded.

Table 5.2: Journal of all available MIDI observations of R Scl. H stays for HIGH-SENS mode, while S for SCI-PHOT.

#	Star	UT date & Time	Phase	Config.	Base [m]	PA [deg]	Seeing [arcsec]	Mode	R
1	R Scl	2005-01-03 03:01:23	0.23	U2-U4	61	117	1.7	H	230
Cal	HD12524	2005-01-03 03:27:24	...	-	...	...	1.0	-	-
2	R Scl†	2005-01-03 04:05:54	0.23	U2-U4	47	136	0.9	H	230
Cal	HD12524	2005-01-03 04:45:32	...	-	...	...	0.8	-	-
3	R Scl	2006-06-16 09:38:09	0.64	E0-G0	14	42	0.7	S	30
Cal	β Gru	2006-06-16 10:23:60	...	-	...	...	0.6	-	-
4	R Scl	2006-06-22 09:29:58	0.66	D0-G0	29	46	0.8	S	30
Cal	τ^4 Eri	2006-06-22 09:49:48	...	-	...	...	0.9	-	-
5	R Scl†	2006-06-23 09:23:50	0.66	E0-G0	14	45	1.0	S	30
6	R Scl	2006-06-23 09:46:04	0.66	E0-G0	15	50	1.4	S	30
Cal	τ^4 Eri	2006-06-23 10:04:33	...	-	...	...	1.1	-	-
7	R Scl	2006-08-08 09:52:10	0.79	A0-G0	62	77	1.1	S	30
Cal	τ^4 Eri	2006-08-08 10:09:22	...	-	...	...	1.4	-	-
Cal	HD4128	2006-09-17 04:56:51	...	-	...	...	2.0	-	-
8	R Scl†	2006-09-17 05:26:12	0.89	A0-G0	63	63	1.8	H	30
Cal	HD4128	2006-09-17 05:51:43	...	-	...	...	1.7	-	-
9	R Scl†	2006-09-17 06:20:53	0.89	A0-G0	64	71	2.4	H	30
Cal	HD4128	2006-09-17 06:42:41	...	-	...	...	2.0	-	-
10	R Scl†	2006-09-17 07:06:01	0.89	A0-G0	63	77	1.9	H	30
Cal	HD4128	2006-09-18 03:13:16	...	-	...	...	1.5	-	-
11	R Scl†	2006-09-18 03:55:48	0.89	A0-G0	59	48	1.6	H	30
12	R Scl†	2006-09-18 04:19:15	0.89	A0-G0	60	53	1.5	H	30
Cal	HD4128	2006-09-18 04:39:39	...	-	...	...	1.7	-	-
13	R Scl†	2006-09-18 05:02:08	0.89	A0-G0	62	60	1.6	H	30
Cal	HD4128	2006-09-18 05:25:49	...	-	...	...	1.6	-	-
Cal	HD4128	2006-09-18 07:05:14	...	-	...	...	1.5	-	-
14	R Scl†	2006-09-18 07:34:30	0.89	A0-G0	61	80	2.1	H	30
Cal	HD4128	2006-09-19 07:07:06	...	-	...	...	1.2	-	-
15	R Scl†	2006-09-19 07:32:00	0.90	D0-G0	30	81	1.3	H	30
Cal	HD4128	2006-09-19 07:56:01	...	-	...	...	1.2	-	-
16	R Scl†	2006-09-19 08:19:20	0.90	D0-G0	28	87	1.5	H	30
Cal	HD4128	2006-09-20 04:12:27	...	-	...	...	1.3	-	-
17	R Scl	2006-09-20 04:36:30	0.90	D0-G0	31	57	1.6	H	30

Table 5.2: continued.

#	Star	UT date & Time	Phase	Config.	Base [m]	PA [deg]	Seeing [arcsec]	Mode	R
18	R Scl	2006-09-21 02:40:17	0.90	G0-K0	54	34	1.7	H	30
Cal	HD4128	2006-09-21 03:03:59	...	-	...	...	1.1	-	-
19	R Scl	2006-10-16 03:05:26	0.97	G0-H0	31	59	0.6	S	30
Cal	τ^4 Eri	2006-10-16 03:28:25	...	-	...	...	0.5	-	-
20	R Scl	2006-10-16 07:00:03	0.97	D0-H0	53	90	0.6	S	30
Cal	τ^4 Eri	2006-10-16 07:24:05	...	-	...	...	0.5	-	-
21	R Scl	2006-10-17 02:05:02	0.97	D0-H0	59	49	1.4	S	30
Cal	τ^4 Eri	2006-10-17 02:26:29	...	-	...	...	1.0	-	-
22	R Scl	2006-10-18 01:51:25	0.97	E0-G0	15	47	0.8	H	30
Cal	HD4128	2006-10-18 02:13:41	...	-	...	...	0.9	-	-
23	R Scl	2006-10-18 02:34:58	0.97	E0-G0	15	55	0.9	S	30
Cal	τ^4 Eri	2006-10-18 02:59:24	...	-	...	...	0.8	-	-
24	R Scl	2006-10-18 04:51:15	0.97	E0-G0	16	75	1.0	H	30
Cal	HD4128	2006-10-18 05:22:11	...	-	...	...	1.1	-	-
25	R Scl†	2006-10-19 03:28:15	0.98	E0-G0	16	64	1.0	H	30
Cal	HD4128	2006-10-19 03:52:03	...	-	...	...	0.4	-	-
26	R Scl	2006-10-19 04:15:04	0.98	E0-G0	16	71	0.7	H	30
Cal	HD4128	2006-10-19 04:37:45	...	-	...	...	0.7	-	-
27	R Scl	2006-10-19 05:23:42	0.98	E0-G0	15	79	0.5	S	30
Cal	τ^4 Eri	2006-10-19 05:49:48	...	-	...	...	0.4	-	-
Cal	τ^4 Eri	2006-12-16 02:57:16	...	-	...	...	1.7	-	-
28	R Scl	2006-12-16 03:19:24	0.13	G0-H0	25	93	1.4	S	30
Cal	τ^4 Eri	2006-12-18 00:57:42	...	-	...	...	1.2	-	-
29	R Scl	2006-12-18 01:21:29	0.14	G0-H0	31	79	1.2	S	30
Cal	τ^4 Eri	2006-12-21 01:27:43	...	-	...	...	0.9	-	-
30	R Scl	2006-12-21 02:06:31	0.15	G0-H0	29	86	1.7	S	30

Figure 5.1 shows the K-band *uv* coverage of the VINCI observations (see Table 5.1) and the N-band spectrally-dispersed *uv* coverage of the MIDI observations (see Tables 5.2). The spatial coverage spreads over a large scale (from 15 to 60 m baselines), whereas the angular coverage is limited to 90°.

Figure 5.2 presents the VINCI calibrated visibilities observed over 2 nights between November and December 2001 (see Table 5.1). The angular diameters of the equivalent uniform disk are computed from each visibility measurement and show a stability from phase-to-phase at different position angles. Figure 5.3 shows the MIDI calibrated visibilities observed over 14 nights between January 2005 and December 2006 (see Table 5.2). The diameters of the equivalent uniform disk were computed from the visibilities at each spectral channel. The dimension of those diameters regularly increases from 9 to 13 μm, indicating an extended circumstellar environment (Ohnaka et al. 2005).

The phase shifts or differential phases correspond to the information extracted from the difference between the phase at a given wavelength and the mean phase determined in the full N-band region. It provides information about possible asymmetry of the source in

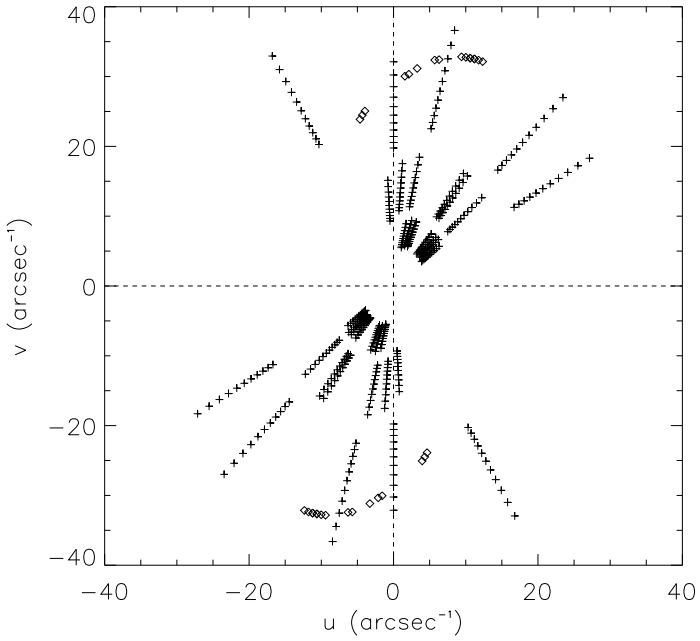

Figure 5.1: K-band *uv* coverage of the VINCI observations (diamonds) and N-band spectrally-dispersed (from 8 to 13 μm) *uv* coverage of the MIDI observations (plus) (see Tables 5.1, and 5.2).

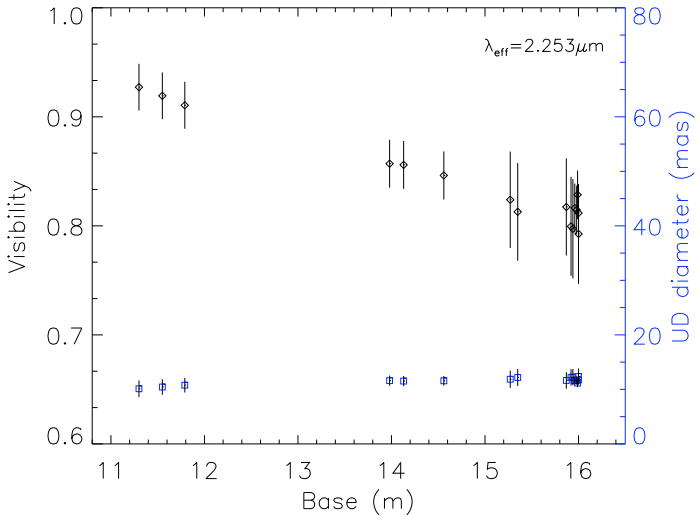

Figure 5.2: Broadband VINCI visibilities of R Scl (black diamonds) as a function of the projected baselines observed over 2 nights between November and December 2001 (see Table 5.1). Uniform disk diameters (blue squares to be read from the scale on the right axis) are computed from each visibility measurement.

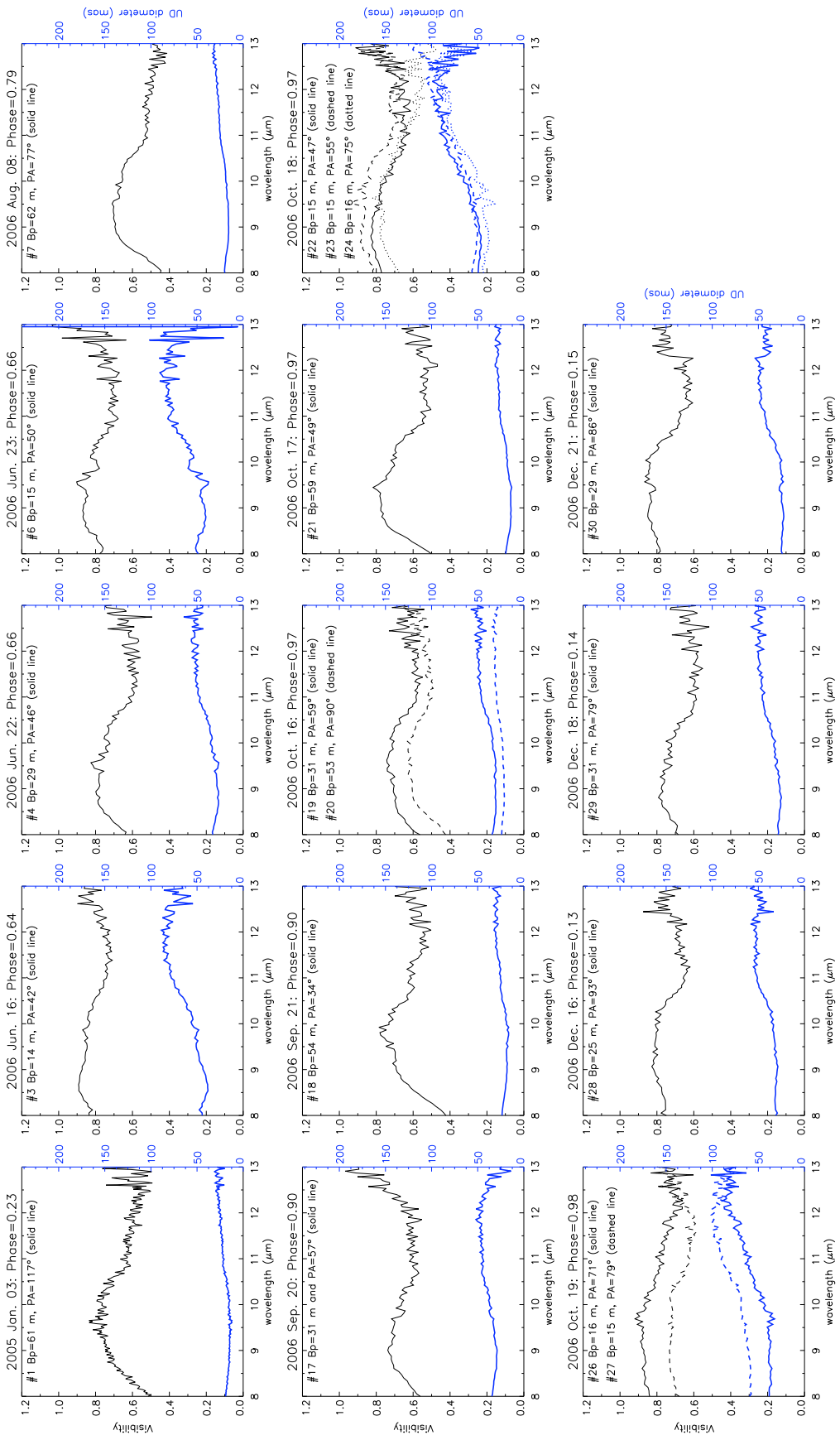

Figure 5.3: Spectrally-dispersed MIDI visibilities of R Scl (black thin lines to be read from the scale on the left axis) observed over 14 nights between January 2005 and December 2006 (see Table 5.2). Uniform disk diameters (blue thick lines to be read from the scale on the right axis) are computed from the visibilities at each spectral channel. Error bars are not included for clarity. The data set numbers are defined in Table 5.2.

the region covered by the different interferometric measurements. As an example, strong phase signals were detected in sources harboring dusty disks (Deroo 2007, Ohnaka et al. 2008). Due to the low values ($< \pm 5°$) of the calibrated differential phases for each projected baseline, the global centrosymmetry of the close circumstellar environment of the object is confirmed in the mid-infrared for the corresponding angular coverage.

5.3 Observed variability of R Scl

Sections 5.3.1, 5.3.2, and 5.3.3 discuss the variability of the star derived from photometry, polarimetry, and spectroscopy. Finally, Sect. 5.3.4 is dedicated to the interferometric variability giving constraints on the dynamic process at work in the close circumstellar environment of R Scl.

5.3.1 Photometric variability

The K-band light curve of R Scl was discussed by Whitelock et al. (1997). The authors distinguish two main periods of 374 and 1 804 days. The shorter period is identified to be the pulsation period of the star, whereas the longer one might be a beat period between two similar pulsation periods (Houk 1963). More recent polarimetric measurements (Yudin & Evans 2002, see Sect. 5.3.2) reveal a clumpy medium surrounding R Scl where orbiting dusty clump structures could also be the origin of the long period.

In the following, the phase of the star is established from the light curve according to

$$\varphi = \frac{(t - T_0) \bmod \mathrm{P}}{\mathrm{P}}, \tag{5.1}$$

where t corresponds to the observing time in Julian day, T_0=2 451 044 is the Julian date of the selected phase-zero point corresponding to the maximum light of the star (φ_0=0; see Fig. 5.4), and P=374 days is the pulsation period of the star.

Besides the VINCI interferometric and MIDI spectro-interferometric observations of R Scl, polarimetric (Yudin & Evans 2002) and additional ISO/SWS spectrometric (Sloan et al. 2003) data of the star are available.
Figure 5.4 represents the visual lightcurve of R Scl where the polarimetric (Pola.), spectroscopic (ISO and MIDI), and interferometric (VINCI and MIDI) observing periods are marked.

5.3.2 Polarimetric variability

Wherever there is appreciable asymmetry in an astronomical situation, emitted light is likely to be polarized at some level. Yudin & Evans (2002) show that R Scl displays polarimetric variability in the VR_CI_C bands on different time scales from hours to one year. The authors argue that the polarimetric variations of the star are most probably not related to

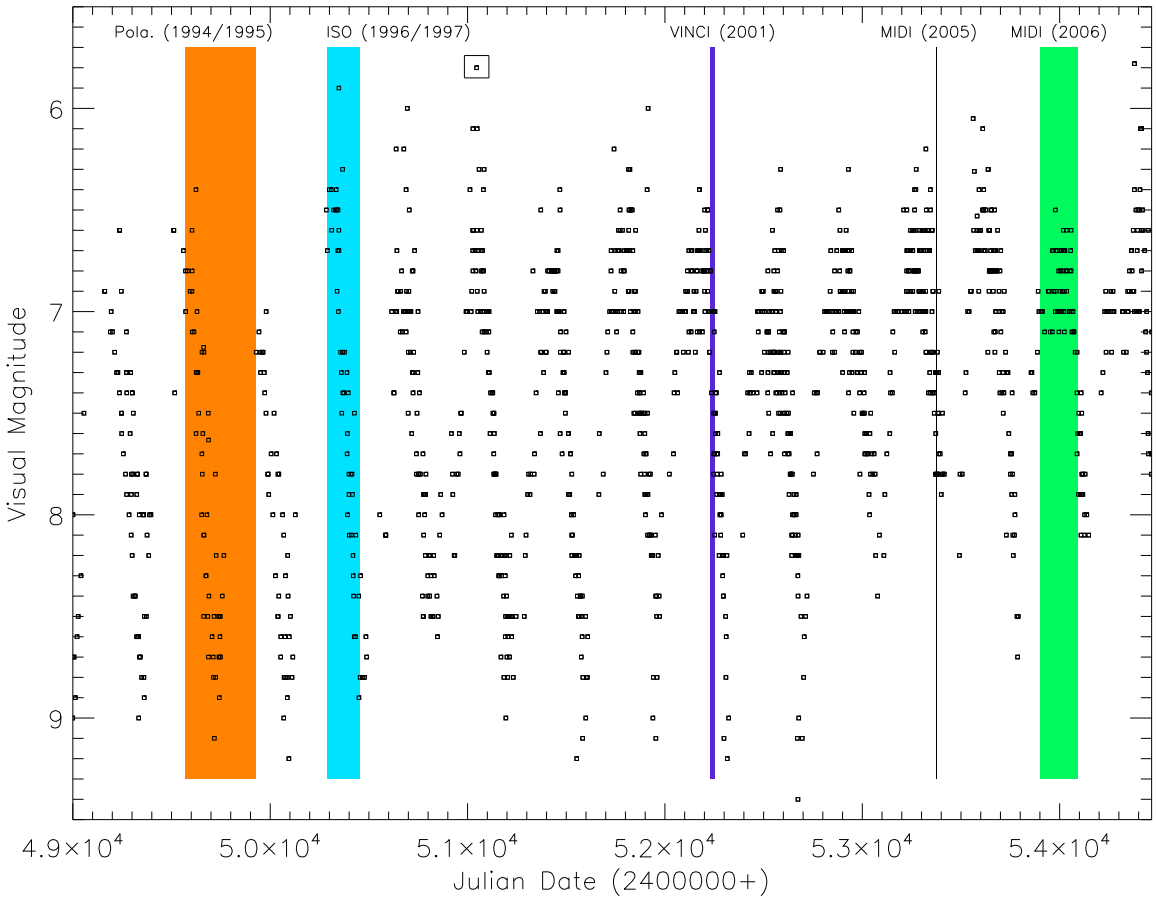

Figure 5.4: AAVSO visual lightcurve of R Scl (Henden 2009). Colored zones indicate the observing period of Polarimetric measurements (orange) (Yudin & Evans 2002), ISO/SWS measurements (blue) (Sloan et al. 2003), VINCI measurements (violet), MIDI UT measurement (black), and MIDI AT measurements (green). The point surrounded by the open rectangle represents the chosen phase-zero point (φ_0=0).

binarity, since these variations occur on timescales that are inferior to one pulsation period (∼374 days). With a wavelength-dependence of polarization close to P∝λ^4, consistent with Rayleigh scattering by small (≈0.01 μm) amorphous grains, the authors suggest that the polarimetric variation would be related to dusty clumps located in the inner zone of the warm dusty shell (i.e. from 2 to 4 $R_\star$) with a quasi-period of rotation in the range 470 to 1600 days.
The constraints provided by the MIDI differential phases (see Sect. 5.2), which do not exhibit any asymmetries in the close vicinity of the source (from 2 to 10 $R_\star$), contradict the conclusions of Yudin & Evans (2002). Therefore, we are left with three possibilities.

(i) **The MIDI interfererometric angular coverage is outside the dusty clumps region.**
It is difficult to determine the position of the clumps because of the large uncertainty on their rotational period found by Yudin & Evans (2002). As it is not possible to locate the clumps at the time of the MIDI observations, we cannot exclude that the clumpy region is situated out of the interferometric coverage, which only spreads over an angle of 90° (see Fig. 5.1).

(ii) **The dynamic range of MIDI is not high enough to separate the emission of the dusty clumps from the one coming from the circumstellar material.**
We can investigate this point by an estimation of the constraints provided by the MIDI differential phase measurements. For that, we performed a perturbation of the intensity distribution of the best-fitting model (see Sect. 5.4.2) by a Gaussian-like dust cloud of 1.8 mas width (defined from the density structure found by Yudin & Evans 2002) varying its flux contrast, its distance (from 2 to 4 $R_\star$), and its position angle. Our tests allow any mid-IR dusty clump source representing more than about 4% of the total flux of the object (i.e. 4 to 8 Jy between 8 μm and 13 μm) to be discarded. Taking the condensation density ρ_c and the condensation mass derived by Yudin & Evans (2002) into account, and describing the dusty clump as a blackbody of 1000 to 1500 K at a distance ranging from 2 to 4 $R_\star$, we obtain a flux range between 2.0 and 3.5 Jy in the N-band. As these values are below 4% of the total flux of the object, this solution can be retained.

(iii) **The dusty clumps emission vanished from the N-band spectral window during the 10 years separation from the polarimetric to the MIDI interferometric observations.**
Shock waves could push the dusty clumps observed by polarimetry to regions where its emission peak is outside the mid-infrared window. However, taking a shell expansion velocity from 10.5 to 16.5 km s^{-1} into account for R Scl (Schöier & Olofsson 2001, Wong et al. 2004), the dusty clump would be located around 14.4 to 23.4 $R_\star$ (within the FOV of both AT and UT telescopes) at the end of the 10-year separation from the polarimetric to the MIDI observations. Assuming a Planckian radiation field geometrically diluted with distance from the star, the temperature of the clump reaches about 400 K corresponding to an emission peak well inside the mid-infrared window. Therefore this solution can be

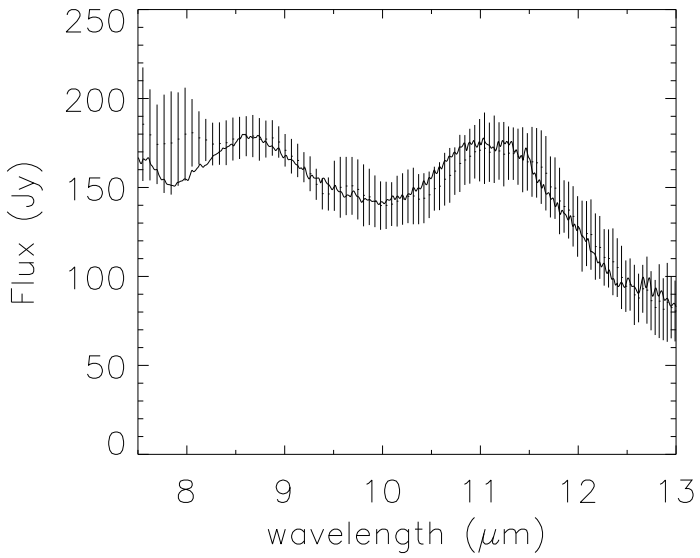

Figure 5.5: Comparison of the ISO/SWS spectrum of R Scl at phase 0.97 (thick line), and the MIDI spectrum of R Scl at phase 0.98 (error bars).

discarded.

5.3.3 Spectrometric variability

As discussed in Sect. 5.2, most of the mid-infrared flux originates in the inner 300 mas of the source. Therefore, the mid-infrared spectra obtained from the AT and UT single dishes are directly comparable to the ones produced by the ISO telescope (FOV=$33'' \times 20''$). To keep consistency in the comparison to the measurements, only ISO/SWS spectra using the AOT 1 template (Leech et al. 2003) are considered in the following. Figure 5.5 compares both calibrated MIDI and ISO/SWS spectra (Sloan et al. 2003) of R Scl around the maximum visual light ($\varphi \sim 0$).
Figure 5.6 presents the calibrated MIDI and ISO/SWS flux of R Scl as a function of the phase at 8.5 μm (*pseudo-continuum*: defined where the blackbody continuum fits to the ISO/SWS spectrum of the star), 11.3 μm (SiC feature), and 12.5 μm (C_2H_2+HCN) spectral bands (Hron et al. 1998, Gautschy-Loidl et al. 2004, Zijlstra et al. 2006). Each monochromatic flux is determined by integration of the narrow-band filter fluxes over a bandwidth of $\Delta\lambda$=0.2 μm. The MIDI error bars are estimated from the standard deviation of the N-band flux-calibrated spectra determined from each night and each telescope, i.e. typically 3 to 10 spectra, except at phases 0.23 and 0.79 where only one spectrum is available (see Tables 5.2).

From Figs. 5.5 and 5.6, we can argue that the level of flux received by MIDI is equivalent to the one of ISO. It means that the cycle-dependent flux level of the object in the N-band has probably not changed significantly from the ISO/SWS (1996/1997) to the MIDI (2005/2006) observations. From Fig. 5.6, it is rather difficult to determine a real trend in variability, keeping in mind typical errors in the absolute ISO/SWS flux level ranging from 10 to 12% (van der Bliek et al. 1998) and an error of about 20% for the MIDI flux.

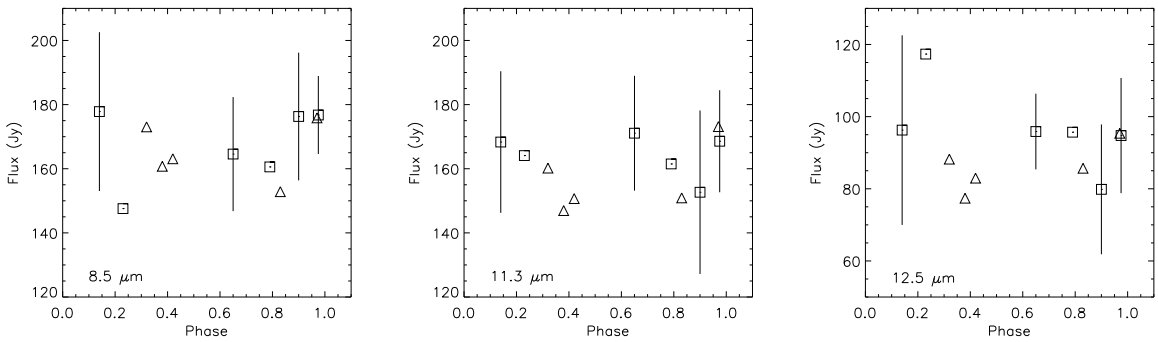

Figure 5.6: MIDI (squares) and ISO/SWS (triangles) flux of R Scl as a function of the visual phase in the 8.5 (left), 11.3 (middle), and 12.5 μm (right) spectral band corresponding to the *pseudo-continuum*, the SiC feature, and the C_2H_2+HCN feature, respectively.

5.3.4 Interferometric variability

To study the interferometric variability of the star, we compare visibility measurements observed at the same projected baseline lengths for very close position angles (few degree differences) from one epoch to another one. The same projected baselines need to be used to probe the same spatial regions of the object, whereas very close projected angles are needed to avoid effect coming from potential deviation in the geometry of the object from spherical symmetry.

We first compare both sets of VINCI visibility measurements at φ=0.17 and φ=0.23 for the given 16 m projected baseline length through a range of 5° in position angle. This comparison does not display any significant (larger than 2σ) temporal variation. This fact is, however, not surprising given the short time interval at post-maximum brightness of the star and because the broadband measurements will average out the possible short term effects of shock fronts in CO or CN lines (e.g. Nowotny et al. 2005a, Paladini et al. 2009). As the VINCI data only probe the very low spatial frequency, what remains are thus only the slow variations due to stellar pulsation (P=374 days).

In the case of the MIDI measurements, the lowest spectral resolution (R=30) is high enough to resolve the broad features contained in the N-band spectral window (i.e. C_2H_2, HCN, C_3, and SiC). Therefore, we do not expect any effect that could possibly smear out the temporal variation coming from emission or absorption bands in that region. Figure 5.7 shows comparisons between the MIDI spectrally-dispersed visibilities from phase-to-phase at a given projected baseline length for very close position angles. The measurements do not show any significant variability effect for both 15 and 31 m baselines. Because those baselines probe the region located from ∼17.5 to 100 mas (3.4 to 19.6 $R_\star$), this means that the stellar radiative pressure is not strong enough to reveal a significant movement of the warm mass dust shells detectable at the spatial resolution of the interferometer (from ∼8 to 12 mas: 2.9 to 4.3 AU at 360 pc). Such behavior agrees with the amplitude of the mass shell of theoretical carbon-rich dynamic models, which does not exceed 3 AU over a full

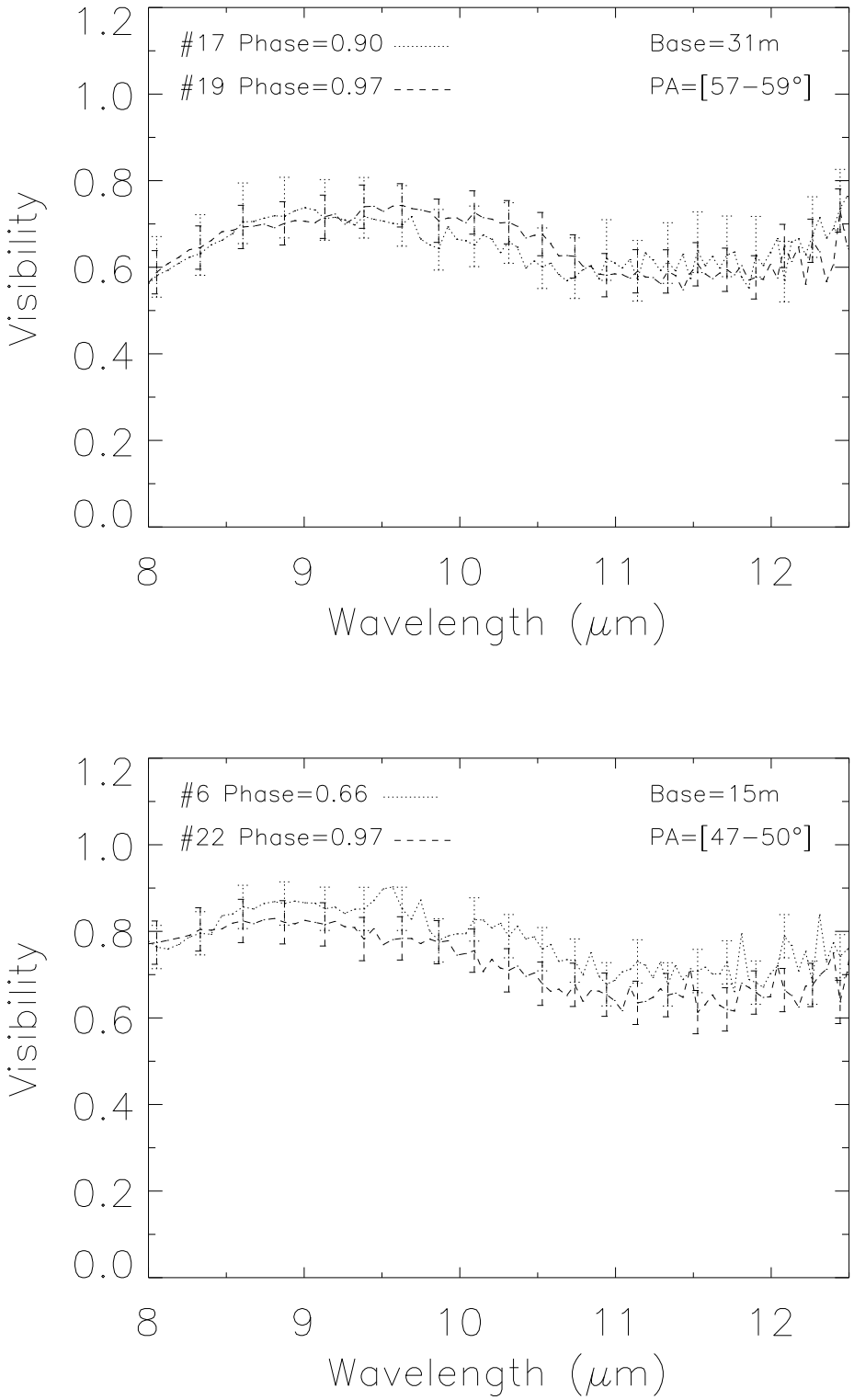

Figure 5.7: Comparison between spectrally-dispersed MIDI visibilities from phase-to-phase (black thin dashed and dotted lines) at a given projected baseline length for very close position angles. The data set numbers are defined in Table 5.2.

cycle in the mid-infrared (see Paladini et al. 2009).

5.4 Modeling the dynamic atmosphere of R Scl

The strategy of determining the best-fitting parameters for the dynamic model atmosphere of the C-rich star R Scl is the following:

Step 1: The hydrodynamic computation (see Sect. 5.4.3) starts with an initial hydrostatic structure mainly characterized by the following parameters (Höfner et al. 2003): luminosity, mass, effective temperature, metallicity, C/O ratio, and micro-turbulent velocity (for line opacities). In order to derive these parameters, we first perform a hydrostatic modeling of the stellar atmosphere (Sect. 5.4.1) using a grid of COMARCS models (Aringer et al. 2009). By fitting synthetic spectra and visibilities based on such models to observed near-infrared spectro-interferometric measurements of R Scl, we find the best set of stellar atmospheric parameters for the initial hydrostatic structure of the dynamic model.

Step 2: The mid-infrared excess of R Scl shows an SiC feature around 11.2 μm (see Fig. 5.5). This component must therefore be considered in the spectral synthesis for the comparison with observational data. Since only AmC dust is treated in the hydrodynamic calculation (Höfner et al. 2003), opacities of SiC dust are added in the a posteriori radiative transfer computation (see Sect. 5.4.3). Those opacities are determined by finding the proper SiC optical constants, and the fractional abundance of SiC to AmC dust that has condensed. These two characteristics are determined in Sect. 5.4.2 by comparing observed mid-infrared spectro-interferometric measurements of R Scl with synthetic spectra and visibilities derived from the DUSTY numerical code (Ivezić & Eliztur 1997, Ivezić et al. 1999), which solves the radiative transfer equation through a dusty envelope.
In Sect. 5.4.2 we present the disagreement of the best-fitting model created by the combination of the hydrostatic COMARCS atmosphere and DUSTY circumstellar envelope (COMARCS+DUSTY model) with the observational data. This shows the necessity of using a self-consistent hydrodynamic model to understand how the time-dependent processes influence the atmospheric structures of the star.

Step 3: Finally, the self-consistent dynamic model used in Sect. 5.4.3 is chosen by the parameters deduced from the best hydrostatic fit of the stellar atmosphere (see Sect. 5.4.1) together with the SiC dust parameters derived from the DUSTY modeling (see Sect. 5.4.2). We then interpret the spectro-interferometric data of R Scl using this model to discuss the dynamic picture deduced from the observations.

5.4.1 Determination of the stellar parameters of R Scl with hydrostatic model atmospheres

Besides the ISO/SWS spectra (see Sect.5.3.3), ground-based photometric measurements (Bagnulo et al. 1998, Whitelock et al. 2006) are available for R Scl (see Table 5.3). Using

the relation of Milne & Aller (1980), also used by Bagnulo et al. (1998), a visual interstellar extinction value of 0.18 was derived. The ratio of total-to-selective extinction at V, 3.1, on average, allowed us to correct the other magnitudes using the absorption curve of Fitzpatrick (1999). The data of Whitelock et al. (2006) are dispersed over a wide range of 26.3 pulsation periods of the star, whereas the data of Bagnulo et al. (1998) are measured at post-maximum light of the object.

Table 5.3: Broadband photometry of R Scl. ⋆Uncertainties calculated from the measurements given in the `Simbad` database.

Band	Extinction coefficient	Dereddened magnitude	Phase	Reference
B	0.25	$11.03 \pm 0.30^{\star}$	0.17	Bagnulo et al. (1998)
V	0.18	$4.55 \pm 0.70^{\star}$	0.17	-
J	0.05	1.56 ± 0.05	0.12	-
H	0.03	0.46 ± 0.05	0.12	-
K	0.02	-0.24 ± 0.06	0.12	-
L'	0.01	-0.84 ± 0.28	0.12	-
J	0.05	1.97 ± 0.86	Whole cycle	Whitelock et al. (2006)
H	0.03	0.63 ± 0.64	-	
K	0.02	-0.10 ± 0.36	-	
L	0.01	-0.74 ± 0.28	-	

Because of all the absorption lines coming from strong molecular opacity sources (mainly species containing C, H, N, O; see Gautschy-Loidl et al. 2004), spectra of cool stars differ a lot from a blackbody continuum spectra as is highlighted in Fig. 5.8. The use of a more realistic synthetic carbon-rich spectrum is then required. The COMA code, developed by Aringer (2000), solves for the ionization and chemical equilibrium (using the method of Tsuji 1973) at a given temperature and density (or pressure) combination for a set of atomic abundances assuming LTE. Based on these results, atomic and molecular opacities are calculated. Details of computation and information on recent updates on the COMA code can be found in Lederer & Aringer (2009), and Aringer et al. (2009). These opacities are then introduced in a spherically symmetric radiative transfer code to calculate the emergent intensity distribution. This intensity distribution is then used to derive the synthetic spectrum and visibility profile, which are compared with observational data of the star.

The determination of the stellar parameters is done by comparing hydrostatic COMARCS models to the spectrophotometric data up to 5 μm. This limit is fixed because of the contribution of the dust becoming non negligible at longer wavelengths for optically thin, *warm dusty objects* like R Scl (Kraemer et al. 2002). This will be confirmed by the DUSTY modeling in Sect. 5.4.2. The hydrostatic model was chosen as best-fitting of the broadband photometric data (see Table 5.3) and the various features in the ISO/SWS spectra (see Fig. 5.8) averaged over all the phases. Furthermore, the best-fitting model should also agree with the K-broadband VINCI interferometric measurements (see Sect. 5.2).
A least-square fitting minimization was completed from the grid of models included in **?**,

varying the parameter values of effective temperature of the star from 2600 to 3000 K (ΔT_{eff}=100 K), the luminosity from 6000 to 8000 $L_\odot$ (ΔL=200 $L_\odot$), the distance from 300 to 500 pc (Δd=50 pc), the mass for values of 1 and 2 $M_\odot$, the metallicity for values of 1, 0.33, and 0.1 $Z_\odot$, and the C/O ratio for values of 1.1, 1.4, and 2.0. Finally, a value of 2.5 km s^{-1} for the microturbulent velocity (ζ), coming from the fit of very high spectral resolution data of carbon stars, is taken into account.
We obtained the best-fitting model to the ISO/SWS spectrometric data from 2.4 to 5 μm with a reduced χ^2 of 3.5 (see Table 5.4).

Figure 5.8 shows the best-fitting hydrostatic model on the spectrophotometric data of the star. As the VINCI data are integrated over the K-band (2.0-2.4 μm) defined by the corresponding filter curve, the synthetic broadband visibility results in a superposition of all the monochromatic profiles over the width of the band (Kervella et al. 2003). Figure 5.11 presents the best-fitting hydrostatic model superimposed on the VINCI visibility measurements.

Table 5.4 summarizes the stellar atmospheric parameters of R Scl deduced from the best-fitting hydrostatic model of the spectrophotometric and near-infrared interferometric measurements.

Table 5.4: Stellar atmospheric parameters of R Scl deduced from best-fitting hydrostatic model of the spectrophotometric and near-infrared interferometric measurements.

Parameter	Value
Effective temperature: T_{eff} (K)	2700
Luminosity: L ($L_\odot$)	7000
Distance: D (pc)	350
Central star diameter: $\theta_\star$ (mas)	10.2
Surface gravity: log g	-0.7
Micro-turbulent velocity: ζ (km s^{-1})	2.5
Stellar mass: M ($M_\odot$)	1
Metallicity: Z ($Z_\odot$)	1
Carbon over oxygen ratio: C/O	1.4

The values found agree well with the ones found in the literature. The distance of 350 pc is relatively far from the Hipparcos distance of 474 pc but in very good agreement with the distance of 360 pc derived from the period-luminosity relation for carbon stars (Groenewegen & Whitelock 1996, Whitelock et al. 2008). The angular diameter of the central star is relatively close to the one coming from the bolometric luminosity of R Scl (from 11.8 to 13.8 mas; Yudin & Evans 2002). The C/O ratio of 1.34 derived by Lambert et al. (1986) agrees with the value that we found. The surface gravity, mass, metallicity, and C/O ratio are also in good agreement with those used by Hron et al. (1998) (log g=-0.5/-0.6, M=1 $M_\odot$, Z=1 $Z_\odot$, and C/O=1.4, respectively).

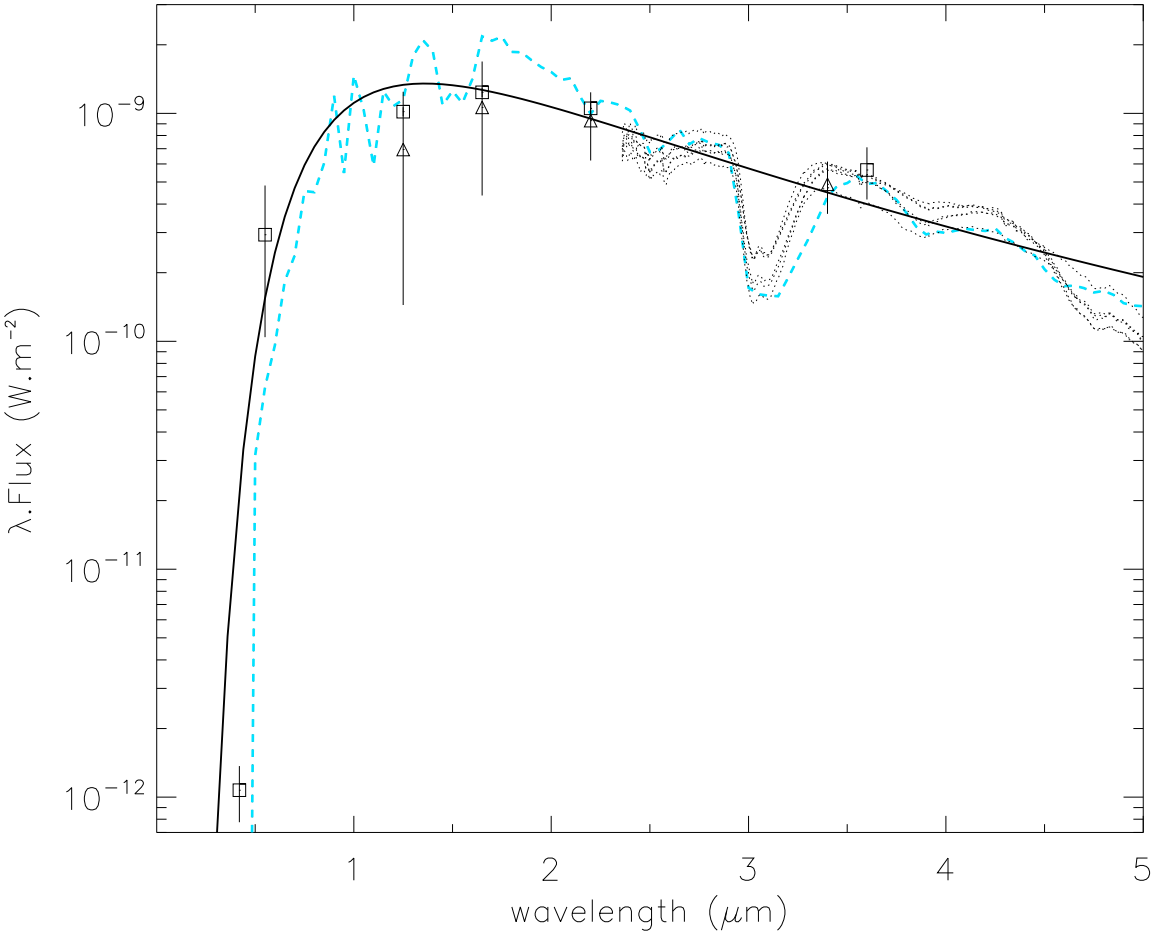

Figure 5.8: Best-fitting hydrostatic model (blue dashed line) on the spectrophotometric measurements. Photometric measurements (squares: Bagnulo et al. 1998 + triangles: Whitelock et al. 2006; see Table 5.3) and ISO/SWS spectra of R Scl at different epochs (dotted lines) are shown. A blackbody continuum having the same temperature ($T_{\rm eff}$=2700 K) and angular diameter ($\oslash_\star$=10.2 mas) as the synthetic COMARCS spectrum is superimposed (black solid line).

5.4.2 Including of a dusty environment

Determination of the SiC dust parameters

The DUSTY code (Ivezić & Eliztur 1997, Ivezić et al. 1999) solves the problem of radiation transport in a circumstellar dusty environment by calculating the radiative transfer equation in plane-parallel or spherical geometry. The radiation from the star is scattered, absorbed, and re-emitted by dust grains. DUSTY has built-in optical properties for the most common types of astronomical dust. The stellar spectrum can be specified in a numerical form as a separate user-supplied input file. In our case, the best-fitting COMARCS stellar atmosphere model, defined in Sect. 5.4.1, is used as central source. The code can compute the wind structure by solving the hydrodynamic equations, including dust drift and the star's gravitational attraction, as a set coupled to radiative transfer (Ivezić et al. 1999). The calculation is performed for a typical wind in which the final expansion velocity exceeds 5 km s^{-1}, in agreement with the expansion velocity found for R Scl from 10.5 to 16.5 km s^{-1} (Schöier & Olofsson 2001, Wong et al. 2004). This allows derivation of the mass-loss rate of the object, fixing the dust grain bulk density ρ_s and the gas-to-dust mass ratio r_{gd}.
The input parameters of DUSTY related to the dusty circumstellar environment are the optical constants and the fractional abundances of the relevant dust grains, the grain size distribution, the overall radial optical depth at a given wavelength, the geometrical thickness, and the dust temperature at the inner boundary. Different types of grains can have different temperatures at the same location. However, DUSTY currently treats mixtures as single-type grains whose properties average the actual mix, therefore only one temperature is specified.

The determination of the parameters is done by fitting the COMARCS+DUSTY model to the photometric measurements, the ISO/SWS spectrometric data from 0.4 to 25 μm, and the MIDI spectrometric measurements from 8 to 13 μm, averaged over all the phases. Furthermore, the best-fitting model should also agree with the K-band VINCI and N-band MIDI interferometric measurements. For that, a least-square fitting minimization was completed first by testing different sets of optical constants for AmC and SiC grains and by computing a large grid of models varying the fractional abundances of the relevant dust grains ranging from 100% AmC to 100% SiC grains in 10% increments, the 0.55 μm overall radial optical depth from 0.05 to 1 ($\Delta\tau_{0.55\mu m}$=0.05), and the dust temperature at the inner boundary from 800 to 1500 K (ΔT_{in}=100 K). As the geometrical thickness does not have any significant impact on the model spectrum because of the very optically thin circumstellar environment ($\tau_{11.2\mu m}$=7.6×10^{-3}, see Table 5.5), we fixed this parameter to 1000 dust shell inner boundary radii knowing that the result is similar for values between 100 to 10^4. The grain size distribution was also fixed to a standard MRN grain size distribution as described by Mathis et al. (1977)[4].
We obtained the best fit model to the ISO/SWS spectrometric data from 2.4 to 25 μm with

[4] $n(a) \propto a^{-3.5}$ with minimum and maximum grain sizes of 0.005 μm and 0.25 μm, respectively

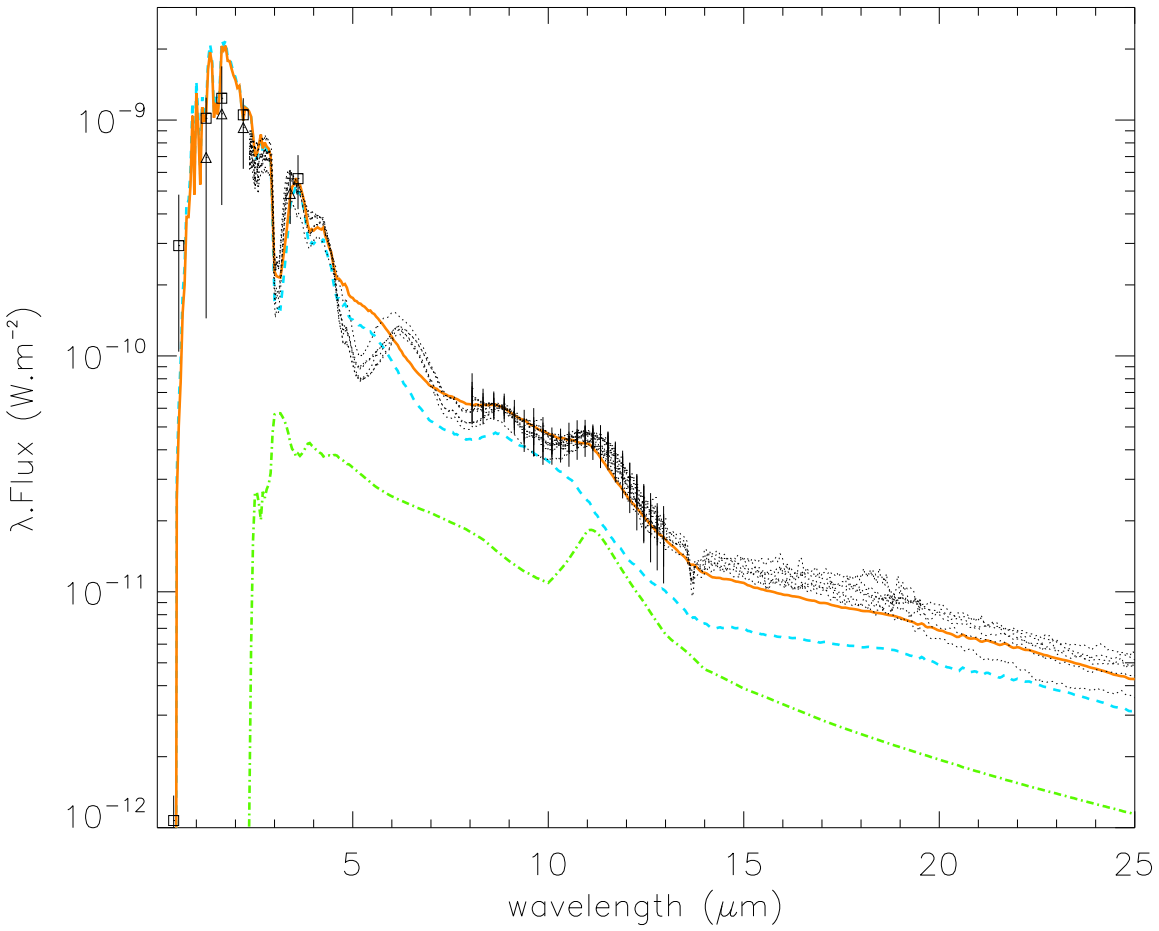

Figure 5.9: Best-fitting COMARCS+DUSTY model (red solid line) on the ISO/SWS (dotted lines), MIDI (error bars) spectrometric measurements, and photometric (squares and triangles; see Table 5.3) measurements of R Scl. The stellar contribution (blue dashed line) and the dust shell contribution (green dashed-dotted line) are also shown.

a reduced χ^2 of 3.5 (see Table 5.5).

Figure 5.9 shows the best-fitting COMARCS+DUSTY model on the spectrophotometric data of the star. Figures 5.10 and 5.11 present the best-fitting COMARCS+DUSTY model superimposed on the MIDI and VINCI visibility data, respectively. Table 5.5 summarizes the parameters of the dusty envelope found from the best-fitting COMARCS+DUSTY model on the spectrophotometric and the near- and mid-infrared interferometric measurements. These parameters are complementary to the stellar atmospheric parameters (see Table 5.4).

The resulting values agree well with the ones found in the literature. The inner radius of the dust shell is close to 5 $R_\star$ (see Table 5.4) as determined by Lorenz-Martins et al. (2001). The optical constants of AmC from Rouleau & Martin (1991) and SiC from Pégourié (1988), together with the fractional abundance of SiC/AmC of 0.08 found by Lorenz-Martins et

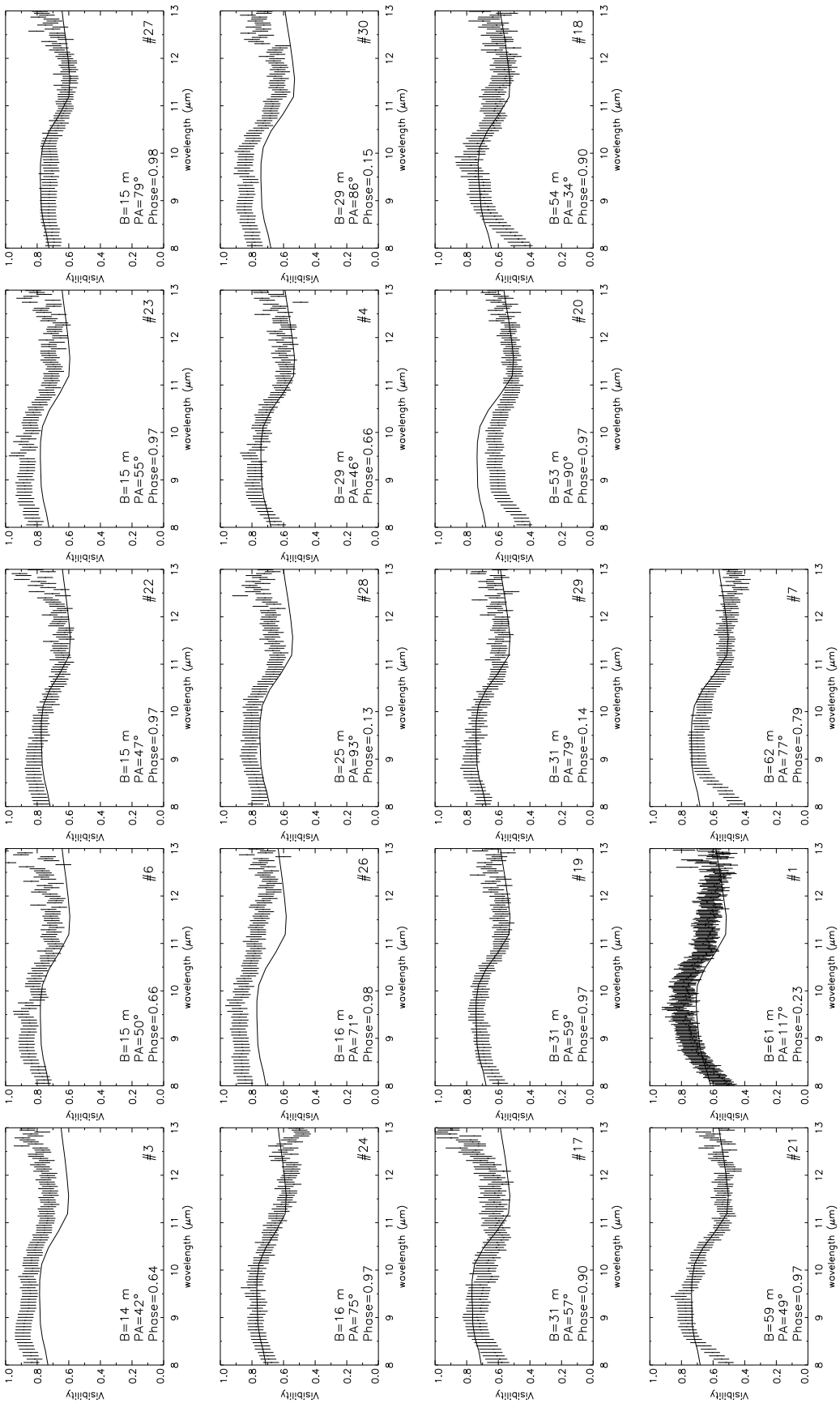

Figure 5.10: Best-fitting COMARCS+DUSTY model (solid line) on the spectrally-dispersed MIDI visibilities of R Scl (error bars) from the smallest to the largest projected baselines. The data set numbers are defined in Table 5.2.

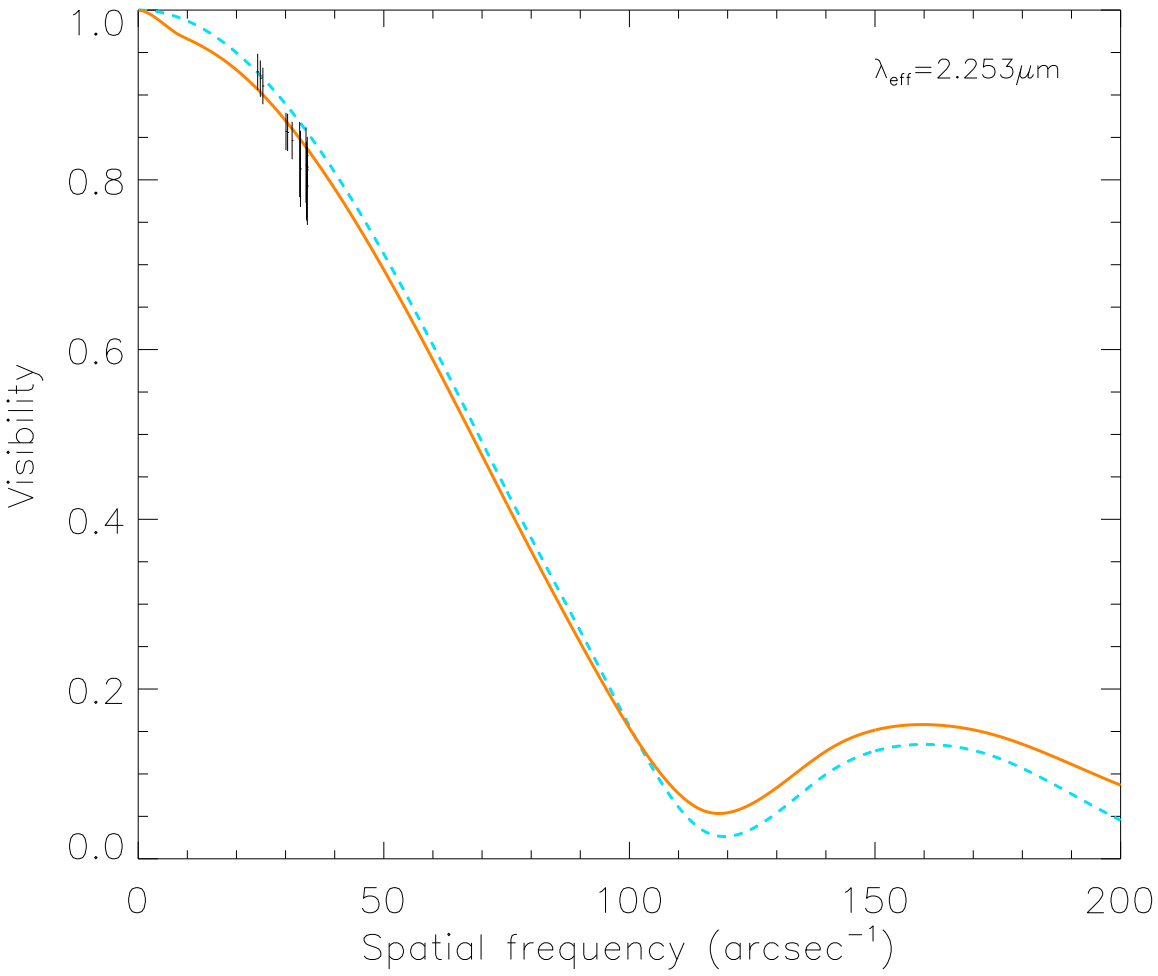

Figure 5.11: Best-fitting hydrostatic model (blue dashed line) and best-fitting CO-MARCS+DUSTY model (red solid line) on the VINCI visibilities of R Scl (error bars).

Table 5.5: Dusty circumstellar envelope parameters of R Scl deduced from the best-fitting COMARCS+DUSTY model on the spectrophotometric and the near- and mid-infrared interferometric measurements.(1) AmC^r stands for amorphous carbon of Rouleau & Martin (1991) and SiC^p for silicon carbide of Pégourié (1988).(2) grain size distribution as described by Mathis et al. (1977). (3) assuming a dust grain bulk density ρ_s=1.85 g cm^{-3} (Rouleau & Martin 1991) and a gas-to-dust mass ratio r_{gd}=590 (Schöier et al. 2005).

Parameter	Value
Shell inner radius: ϵ_{in} (mas)	22.4
Inner boundary temperature: T_{in} (K)	1200
Grain chemical composition(1)	90% AmC^r + 10% SiC^p
Grain size distribution(2)	MRN
Geometrical thickness: Y (inner radii)	1000
Visual optical depth: $\tau_{0.55\mu m}$	0.40
1.0 μm optical depth: $\tau_{1.0\mu m}$	0.18
11.2 μm optical depth: $\tau_{11.2\mu m}$	7.6×10^{-3}
Mass-loss rate(3): $\dot{M}$ ($M_\odot$ yr^{-1})	$(6.7\pm2)\times10^{-7}$

al. (2001), are also in good agreement with the values found in this work. These last two characteristics allow us to determine the opacities of SiC used to interpret the spectro-interferometric data of R Scl with the help of the dynamic model (see Sect. 5.4.3). The AmC dust grain optical constants from Rouleau & Martin (1991) are the same as adopted for the hydrodynamic calculation (Andersen et al. 2003, Höfner et al. 2003). Good agreement is also found with the works of Dehaes et al. (2007) and Lorenz-Martins et al. (2001), who determined a visual optical depth of $0.5^{+0.2}_{-0.3}$ and a 1.0 μm optical depth of 0.1, respectively. The dust shell inner boundary temperature of 1000^{+300}_{-200} K found by Dehaes et al. (2007) agrees well with the value determined in this work. Finally, the mass-loss rate of the star that we found also well agrees with the ones determined by Le Bertre (1997): $\dot{M}=10^{-7}$ $M_\odot$ yr^{-1}; Gustafsson et al. (1997): $\dot{M}=4\times10^{-7}$ $M_\odot$ yr^{-1}; and Wong et al. (2004): $\dot{M}$=2 to 5×10^{-7} $M_\odot$ yr^{-1}. Such low values of mass-loss rate are consistent with the very optically thin circumstellar environment that we found from the fit ($\tau_{11.2\mu m}=7.6\times10^{-3}$).

Comparison of the COMARCS+DUSTY model with observations

While the best-fitting COMARCS+DUSTY model is able to reproduce the largest part of the ISO/SWS spectra (see Fig. 5.9), we can see a discrepancy from 5 to 7 μm, which could be linked to wrong or incomplete C_3 line list opacities in that spectral range[5]. Another discrepancy between the model and the ISO/SWS spectrometric data appears around the 13.7 μm C_2H_2 absorption feature. Gautschy-Loidl et al. (2004) argue that this weak and sharp 13.7 μm absorption would come from cool layers above the 500 K dust and gas layer proposed by Jørgensen et al. (2000) to explain the lack of the 14 μm photospheric band.

The model matches the observed near- and mid-infrared visibilities data rather well (see Figs. 5.10 and 5.11), except for few measurements in the mid-infrared. The first disagree-

[5]Since there is only one C_3 line list available, a cross check of different line lists is not possible.

ment comes from the amplitudes of the model visibilities, which are either higher or lower than the amplitudes of the visibility measurements at certain baselines. The most probable reasons for that follow.

(i) **The geometry of the object:**
Potential deviations from spherical symmetry (corresponding to the geometry of the CO-MARCS+DUSTY model) of the object at certain position angles could explain the disagreement. As the object subsequently appears more or less extended from one position angle to another, the corresponding amplitude of the visibility measurements decreases or increases, respectively, in contrast to the constant visibility amplitude of the COMARCS+DUSTY model.

(ii) **The variability of the object:**
It has been shown that the motion of the dynamic model atmospheres without mass loss mainly follows the pulsation of the stellar interior, whereas in the case of mass-losing models, the dust formation may deform the corresponding sinusoidal pattern (see Fig. 2 of Höfner et al. 2003). As the object subsequently appears more or less extended from phase-to-phase, the corresponding amplitude of the visibility measurements decreases or increases (Paladini et al. 2009), respectively, in contrast to the constant visibility amplitude of the COMARCS+DUSTY model.

Another phenomenon that cannot be reproduced by the model is the slope in the N-band visibility data for the largest 60 m projected baselines in the 8-9 μm spectral range (see Fig. 5.10). As the model overestimates the visibility measurements, this reveals that the model is too optically thin. The regions probed at these baseline and spectral band are located between the photosphere of the star ($\sim$5 mas; see Table 5.4) and the dust shell inner radius ($\sim$22.4 mas; see Table 5.5). Because of the very low optical depth of the model in the 8-9 μm spectral range [$\bar{\tau}$(8-9 μm)=4.6×10^{-3}], leading to domination of the stellar flux over the flux of the dust shell, the model is therefore close to the central star's intensity distribution. A way to reproduce the MIDI measurements is to increase the optical thickness of the model at the corresponding spatial frequencies. This can be done by adding extended molecular layers of C_2H_2 and HCN emitting in that spectral range and located above the stellar photosphere.
Many works in interferometry revealed that diameters of Mira and non-Mira M- and S-type stars appear systematically larger than expected in the near-infrared (Mennesson et al. 2002, Ohnaka 2004, Perrin et al. 2004, Weiner 2004, Verhoelst et al. 2006) and in the mid-infrared (Weiner et al. 2000, 2003a,b, Weiner 2004, Ohnaka 2004, Ohnaka et al. 2005, Verhoelst et al. 2006, Sacuto et al. 2008). This increase cannot be attributed only to dust shell features, but also to the possible existence of extended gaseous shells above the stellar photosphere. Such a molecular shell, also called *MOLsphere* (Tsuji et al. 2000), is favored by the low surface gravity (log g=-0.7) and the high luminosity ($\sim$7000 $L_{\odot}$) of the star, allowing the levitation of the upper layers by shock waves or other dynamic phenomena in an easiest way. The temperatures in this levitated matter are low enough that large amounts

of polyatomic molecules can form (Hron et al. 1998, Woitke et al. 1999, Gautschy-Loidl et al. 2004, Verhoelst et al. 2006). Ohnaka et al. (2007) present their results on the modeling of the MIDI measurements of the carbon-rich Mira variable V Oph. The model consists of optically thick warm and cool C_2H_2 molecular layers and an optically thin AmC+SiC dust shell.

Although this *MOLsphere* is useful for increasing the optical thickness of the close circumstellar structure, it remains an inconsistent ad-hoc model. In the classical *MOLsphere* scenario, as is usually applied to interpreting interferometric or spectroscopic data, it is assumed that there are one or a few static layers with a certain concentration and temperature of a molecular species. The possible physical status and origin of such a layer is left unanswered, which is problematic for the following points.
(i) The radial temperature-density distribution of gas and dust around evolved objects is always a continuous and inconstant phenomenon.
(ii) The molecular (and dust) concentrations in a layer depend on each other, so it is impossible to freely choose the amount of certain species.
(iii) The radial structures are extremely time dependent.

As shown by Hron et al. (1998), Woitke et al. (1999), and Gautschy-Loidl et al. (2004), the hydrodynamic modeling leads to a self-consistent formation of extended molecular structures located between the photosphere and the dust formation zone. Finally, Höfner et al. (2003) argue that sequences of hydrostatic models with varying stellar parameters cannot reproduce the effects of shock waves, levitation, or winds. The only way to understand how the dynamic processes influence the atmospheric structure on different spatial scales is the use of time-dependent dynamic atmospheric modeling.

5.4.3 Dynamic model atmosphere for R Scl

The aim of this section is to show that a self-consistent hydrodynamic modeling forming a gaseous and dusty environment by itself is able to reproduce the time-dependent signature of the spectro-interferometric data of a carbon-rich, long-period variable star. Section 5.4.3 presents the dynamic model atmosphere used for the interpretation. Section 5.4.3 connects the bolometric phases given by the model with the visual phases of the observations which is needed to compare time-dependent models with real measurements of R Scl. Section 5.4.3 presents the specific dynamic atmospheric model that we chose for the comparison with the spectro-interferometric data of the star. Section 5.4.3 shows the ability of the dynamic model to form molecular layers located above the photosphere of the star in a self-consistent way. Finally, the last section (Sect. 5.4.3) compares the dynamic model with the time-dependent spectro-interferometric data.

Presentation of the hydrodynamic model atmospheres

The self-consistent hydrodynamic structures for dust-forming atmospheres and winds used here are taken from the models contained in Mattsson et al. (2008) and from additional models required for the present work (Mattsson, priv. comm.). The dynamic model atmosphere is based on the code described by Höfner et al. (2003) and Mattsson et al. (2010). The models were obtained by solving the coupled system of hydrodynamics and frequency-dependent radiative transfer in spherical symmetry, together with a set of equations describing the time-dependent formation and the growth and evaporation of dust grains. The formation of AmC dust is treated in a self-consistent way using the moment method described by Gail & Sedlmayr (1988) and Gauger et al. (1990). Optical properties of AmC grains were taken from Rouleau & Martin (1991). Each dynamic model starts from a hydrostatic initial structure, and the effects of stellar pulsation are simulated by a variable inner boundary just below the stellar photosphere (piston model). The dynamic code provides temporally varying temperature and density stratifications of the object. Based on such radial structures, at given instances of time, opacities are computed using the COMA code (see Sect. 5.4.1). The resulting opacities are used as input for a spherical radiative transfer code that computes the emergent intensity distribution for every frequency point of the calculation. This is used to calculate the synthetic spectra and visibility profiles, which are compared to the observational data of R Scl. Since only AmC dust is treated in the hydrodynamic calculation, opacities of SiC dust are added in the a posteriori radiative transfer computation. Those opacities are determined with COMA taking SiC optical constants into account and assuming that SiC dust is scaled with AmC dust. The scaling factor corresponds to the fractional abundance of SiC to AmC dust, which has condensed. Finally, SiC dust is assumed to follow the same temperature-density structure as AmC dust, derived from the full dynamic calculation.

Bolometric and visual phases

The phases of the dynamic model correspond to the bolometric phases derived from its bolometric lightcurve (Nowotny et al. 2005b). The phase-zero point was chosen at the maximum bolometric luminosity of the given dynamic model. As the radiation-hydrodynamic code stores atmospheric structures at more or less randomly distributed instances of time, the uncertainty in the choice of the phase-zero point amounts to a range of ± 0.03.
For O-rich Miras, a small shift between bolometric and visual lightcurves probably exists, such that bolometric phases lag behind visual ones by a value of ≈ 0.1 (Lockwood & Wing 1971, Nowotny et al. 2010). This phase shift is caused by the behavior of molecules occurring in atmospheres of red giants and their corresponding spectral features in the visual. Recently, Nowotny et al. (2010) have studied the photometric variation in the V-filter for similar dynamic model atmospheres as the ones used here. The authors find that, for models developing no wind such as their model W or the one used in this paper to represent R Scl (see Sect. 5.4.3), the visual lightcurves follow the bolometric light variation caused by the variable inner boundary (piston) closely. Therefore, in the following, bolometric phases of the model within a range of ± 0.03 around the observed visual phases of R Scl are used

for comparisons between model and observations.

Choice of a specific dynamic model

The choice of the best dynamic model for R Scl comes from the stellar parameters and the distance derived from the previous hydrostatic modeling (see Sect. 5.4.1).

Among the dynamic models that we have, one model shows parameter values of the hydrostatic initial structure close to the ones we derived from the hydrostatic COMARCS modeling (see Table 5.4). Table 5.6 compares the stellar parameters of the hydrostatic model initiating the hydrodynamic computation with the stellar parameters derived from the best-fitting hydrostatic model determined in Sect. 5.4.1.

Opacities of SiC dust are added in the a posteriori radiative transfer calculation using the SiC optical constants of Pégourié (1988) and a fractional abundance of SiC to AmC dust of 10%, as derived from the COMARCS+DUSTY modeling (see Sect. 5.4.2).

Table 5.6: Parameter values of the hydrostatic initial structure of the hydrodynamic model used in this work (first row) compared to the parameters derived from the best-fitting hydrostatic model determined in Sect. 5.4.1 (second row).

Model	$L_\star$ [$L_\odot$]	$M_\star$ [$M_\odot$]	$T_\star$ [K]	$Z_\star$ [$Z_\odot$]	ζ [km s^{-1}]	C/O
Hydrodynamic	7 080	1	2 800	1	2.5	1.35
Hydrostatic	7 000	1	2 700	1	2.5	1.40

Two other free parameters are required for the hydrodynamic computation (see Sect. 5.4.3):

P_{mod}: the pulsation period of the piston.
A pulsation period of P_{mod}=390 days, the closest to the pulsation period of R Scl (374 days), was used.

Δu_p: the amplitude of the piston velocity.
Different amplitudes of the piston velocity were tested from a range of Δu_p=2 to 6 km s^{-1}, with steps of 1 km s^{-1} (except for the Δu_p=3 km s^{-1} model not at our disposal).
Determination of the best-fitting piston velocity amplitude is done by comparing the synthetic spectra based on these models to the spectrophotometric data. Increasing the amplitude of the piston moves the material to larger distances from the star, which favors dust formation and reduces the effective gravitation (e.g. Winters et al. 2000).
For a piston velocity lower than 4 km s^{-1} (i.e. model with Δu_p=2 km s^{-1} in Fig. 5.12), it appears that the model shows too low a level of flux compared to the spectrometric data. Furthermore, as already discussed in Gautschy-Loidl et al. (2004), a broad and intense C_2H_2/HCN absorption band around 14 μm is present, in pronounced contrast to

the observed ISO/SWS spectra which show a continuum-like infrared excess with a weak and narrow C_2H_2 feature at 13.7 μm (see Fig. 5.12). Finally, the variability amplitude of the model is smaller than 0.3 in the V magnitude, as compared with the 1.4 variability amplitude of the cycle-to-cycle averaged visual magnitudes of the star. Therefore, in the case of too low a piston velocity, the dynamic model corresponds to a dust-free pulsating atmosphere without any wind (no mass-loss), leading to a pure photospheric spectrum such as the one shown by the blue dashed line of Fig. 5.9.

When the piston velocity amplitude exceeds 4 km s^{-1} (i.e. model with Δu_p=6 km s^{-1} in Fig. 5.12), the dynamic model shows too high a level of flux compared to the spectrometric data and a filling up of the whole molecular features at wavelengths longwards of 3.5 μm. Furthermore, the variability amplitude of the model is greater than 5.5 in the V magnitude, as compared with the 1.4 variability amplitude of the cycle-to-cycle averaged visual magnitudes of the star. In that case, the dynamic model develops a strong wind ($\dot{M}>10^{-6}$ $M_\odot\,yr^{-1}$) where the large amount of formed gas and dust, located in the outer layers, obscures the innermost structures of the stellar atmosphere, although not significantly enough to fill up the 3.05 μm feature.

A dynamic model with a piston velocity of 4 km s^{-1} gives the best overall match of the spectrophotometric data from 0.4 to 25 μm, even if the emission is still lower than the [13-25 μm] infrared excess of the ISO/SWS spectrum (see Fig. 5.12). The variability amplitude of the model of about 1 in the V magnitude is relatively close to the 1.4 variability amplitude of the cycle-to-cycle averaged visual magnitudes of the star. In that case, the model is, in some sense, a transition case between a simple, periodically pulsating dust-free atmosphere and an object featuring a dusty wind. The kinetic energy supplied by the pulsation (piston) causes strong, quasi-periodic atmospheric dynamics and some intermittent dust formation, but is not sufficient to start a dust-driven outflow.

The possible reasons for the discrepancy in the 5 to 7 μm wavelengths regions are similar to the ones expressed in Sect. 5.4.2 suggesting wrong or incomplete C_3 line list opacities in that spectral range. The model is also unable to reproduce the weak observed 3.05 μm C_2H_2/HCN feature.

Possible explanations of the discrepancy between the model and the measurements are discussed in more detail in Sect. 5.4.3. This last model is, however, considered as the best dynamic model for R Scl, among the ones available, and will be used in the comparison to the observed spectro-interferometric measurements of the star in the following.

Self-consistent formation of extended molecular structures

As discussed in Sect. 5.4.2, the N-band visibility data display a slope for the largest 60 m baseline in the 8-9 μm spectral range likely related to the emission of extended molecular structures of C_2H_2 and HCN. Figure 5.13 shows the comparison of the visibility of the best dynamic model for a given cycle with the best-fitting COMARCS+DUSTY model superimposed on the MIDI visibility data around 60 m for all the available phases: 0.23/079/0.97. From this figure, we can clearly see that the COMARCS+DUSTY model is too optically

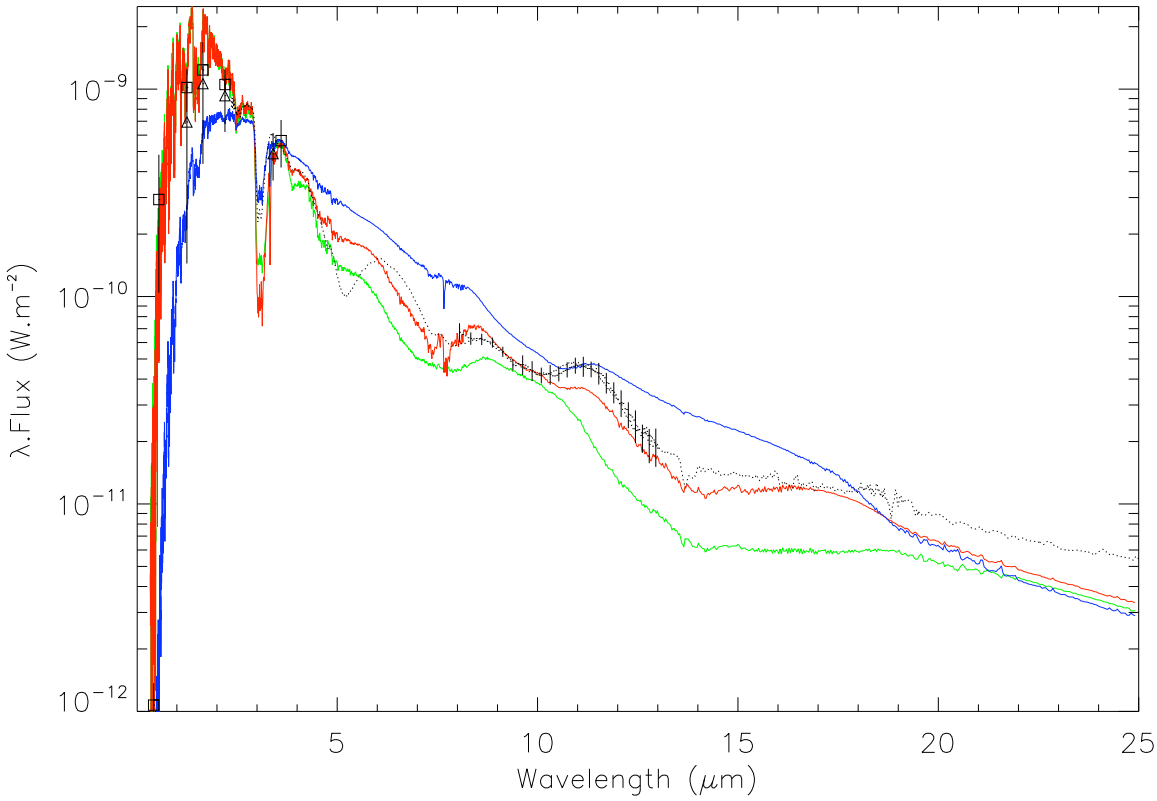

Figure 5.12: Synthetic spectra based on the dynamic models at phase 0.98 with piston velocities of 2 (green line), 4 (red line), and 6 km s^{-1} (blue line), keeping the same parameter values as the ones contained in Table 5.6. The dotted line is the ISO/SWS spectrum of the star at phase 0.97, whereas the error bars in the N-band correspond to the MIDI fluxes at phase 0.98. Squares and triangles correspond to the photometric measurements of the star (see Table 5.3).

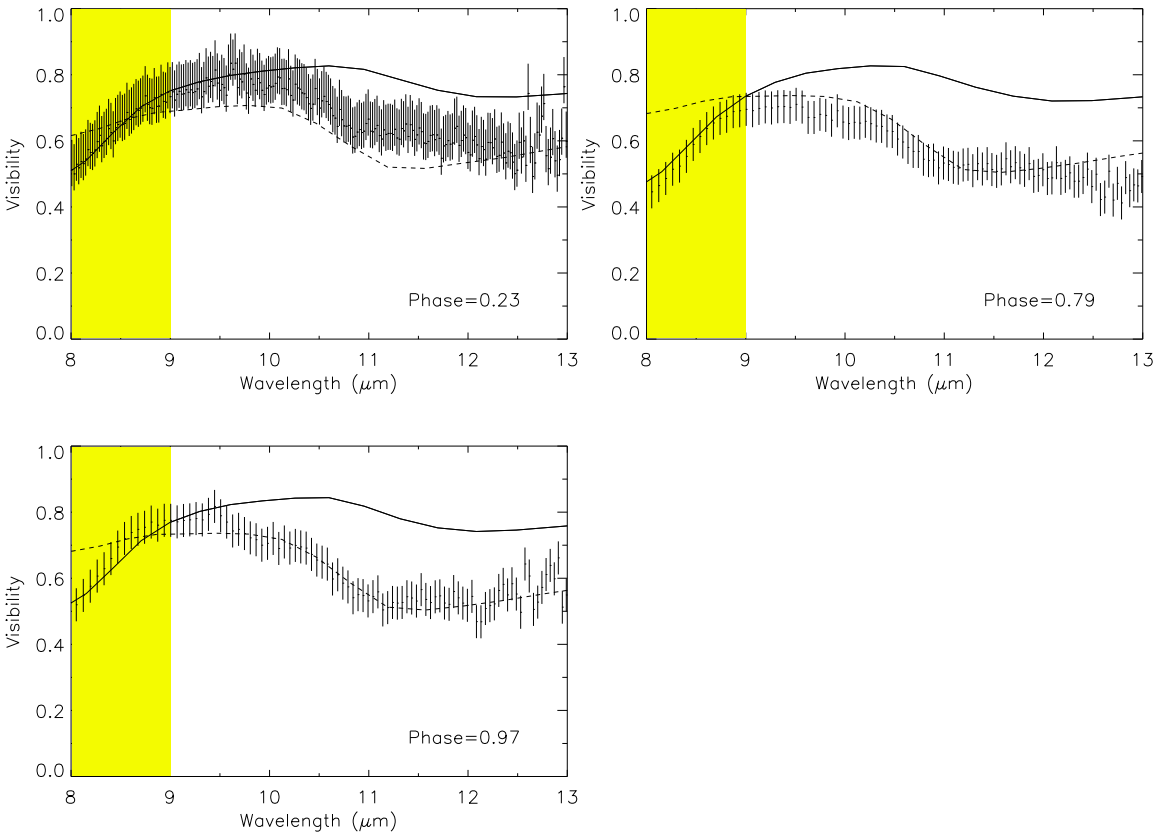

Figure 5.13: Comparison of the visibility of the best dynamic model (solid line) with the best-fitting COMARCS+DUSTY model (dashed line; see Sect. 5.4.2) superimposed on the 60 m MIDI visibility data (error bars) at phases 0.23/0.79/0.97 (data sets #1, #7, and #21, respectively). The yellow zone corresponds to the region dominated by warm molecular layers.

thin, showing a flat visibility profile in the 8-9 μm spectral range (see Sect. 5.4.2). On the contrary, the dynamic model is able to reproduce the slope of the MIDI visibilities well through this wavelength range. This means that the extension of the dynamic model is suitable for revealing the presence of the molecular structures of C_2H_2 and HCN, emitting in that spectral range and located above the stellar photosphere. However, the dynamic model is not optically thick enough to reproduce the measurements in the reddest part of the mid-infrared spectral band.

Comparison of the dynamic modeling results to the time-dependent spectro-interferometric data

In the following, we investigate 100 phases of the model randomly distributed over 56 cycles corresponding to a time sequence of 60 years. As there is no possibility to define the model cycle corresponding to the observations, we decide to follow a statistical approach and to represent all the available cycles for a phase range close to the observed one (see Sect. 5.4.3).

Figure 5.14 shows the time-dependent cycle-to-cycle averaged fluxes of the best dynamic

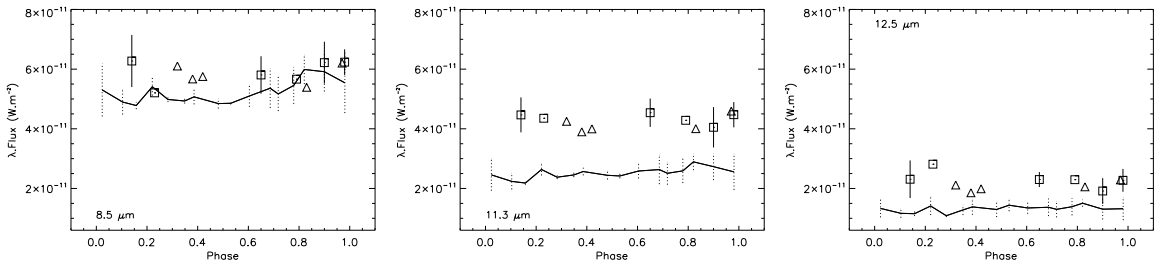

Figure 5.14: Time-dependent cycle-to-cycle averaged fluxes of the best dynamic model (solid line) superimposed on the MIDI (squares) and ISO/SWS (triangles) spectrometric data in the 8.5 (left), 11.3 (middle), and 12.5 μm (right) spectral bands. Dotted error bars give the dispersion created by the cycle-to-cycle variation.

model superimposed on the MIDI and ISO/SWS spectrometric data in the 8.5, 11.3, and 12.5 μm spectral bands. The figure shows that the model agrees relatively well with the time-dependent flux data at 8.5 μm, whereas the model is fainter than the measurements in the 11.3 and 12.5 μm spectral bands.

In compliance with the observations, the comparison of the cycle-to-cycle averaged visibilities of the best dynamic model from phase-to-phase, considering the same baselines and phases as the observations of R Scl (see Sect. 5.3.4), does not show any significant variability of the object in the K and N bands.

Figure 5.15 shows the cycle-to-cycle averaged visibility of the best dynamic model superimposed on the VINCI data at phases 0.17 and 0.23. The model shows good agreement with the data implying that the extension of the model is suitable in the K-band.

Figure 5.16 shows the time-dependent cycle-to-cycle averaged visibilities of the best dynamic model superimposed on the [14-16 m], [29-31 m], and [59-62 m] baselines MIDI data in the 8.5, 11.3, and 12.5 μm spectral bands. The figure only presents measurements showing a deviation from the best-fitting COMARCS+DUSTY model (see Fig. 5.10) smaller than the object variability scattering at 15 and 31 m baselines (see Fig. 5.7). This allows us to avoid comparing the spherically symmetric model with visibility measurements exhibiting a potential departure of the object from sphericity. As we do not have any information on the variability effect at the 60 m baseline, all the measurements are represented. From this figure, it is obvious that the model is not extended enough to reproduce the level of the mid-infrared interferometric data. Only the visibility measurements at the highest spatial frequencies (B=60m and λ=8.0-9.5 μm), probing regions corresponding to the warm extended molecular layers (from 1.5 to 2 $R_\star$), are in good agreement with the model.

Besides the possibility of an inaccurate estimation of the parameter values of the hydrostatic initial structure, the most probable reasons for the discrepancy between the dynamic model and the spectro-interferometric measurements are the following ones.

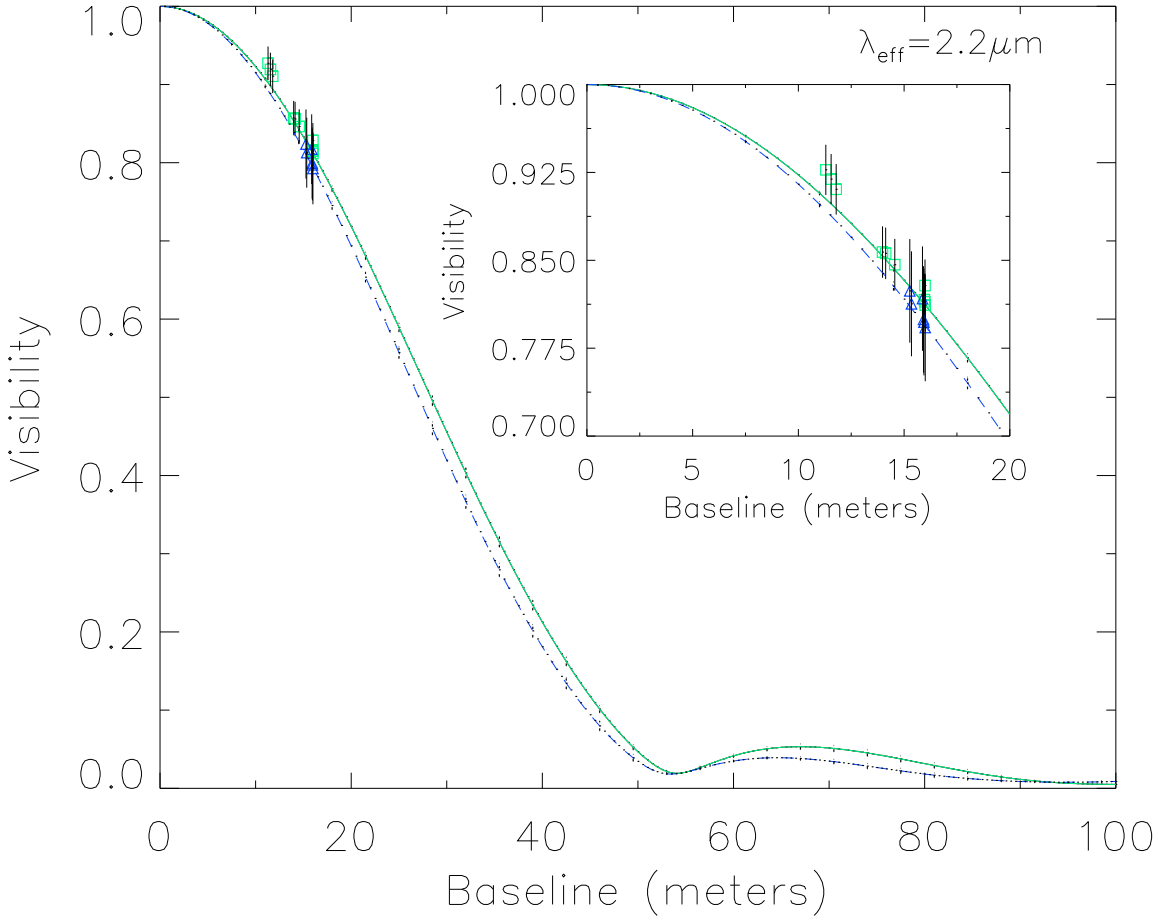

Figure 5.15: Cycle-to-cycle averaged visibility profiles of the best dynamic model (green solid line: phase 0.17; blue dashed line: phase 0.23) superimposed on the VINCI data at phase 0.17 (green squares) and phase 0.23 (blue triangles). Dotted error bars give the dispersion created by the cycle-to-cycle variation. In the inset, a zoom of the relevant frequency region is represented.

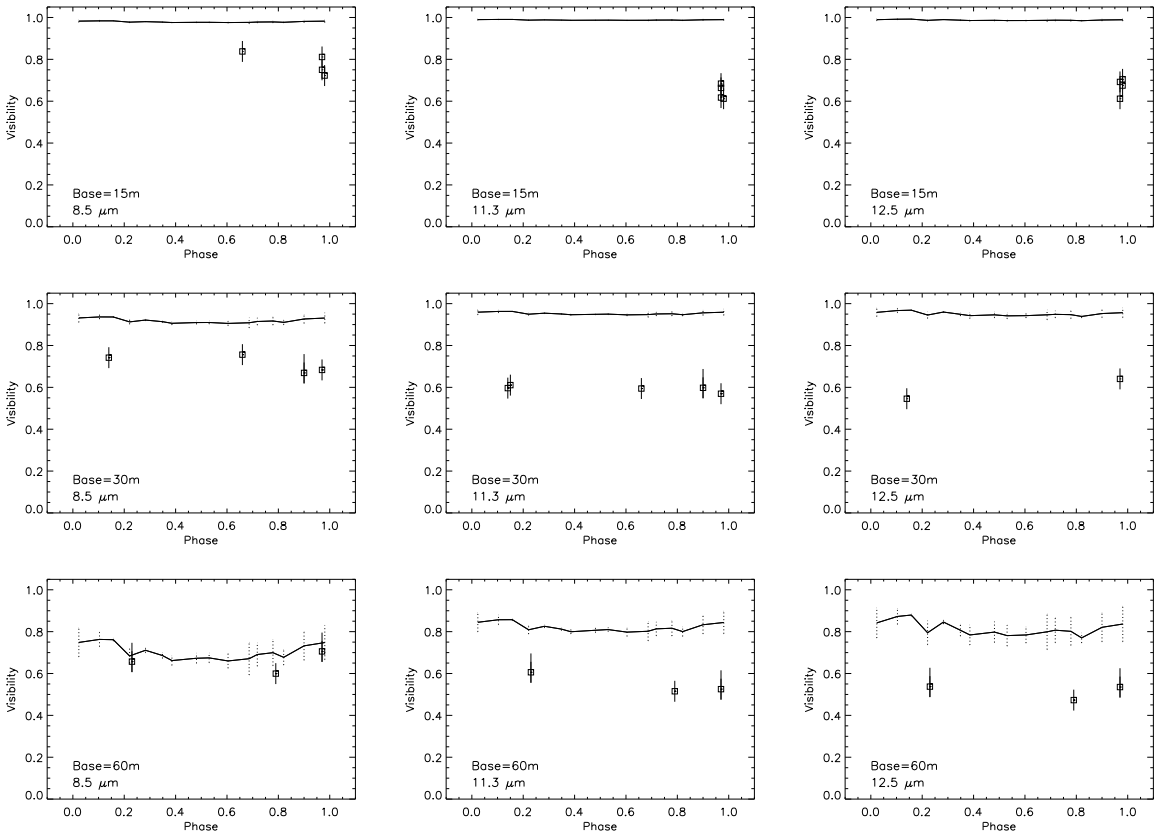

Figure 5.16: Time-dependent cycle-to-cycle averaged visibilities of the best dynamic model (solid line) superimposed on the [14-16 m], [29-31 m], and [59-62 m] baselines MIDI data (squares) in the 8.5 (left), 11.3 (middle), and 12.5 μm (right) spectral bands. Dotted error bars give the dispersion created by the cycle-to-cycle variation.

(i) **The sparse sampling of the transition region from windless models to models with considerable outflows in certain critical stellar parameters:**
The 100 K higher value of the dynamic model effective temperature compared to the hydrostatic model could be a reason for the discrepancy of the model to the MIDI interferometric measurements, given the closeness of the model to the mass-loss threshold defined by Mattsson et al. (2010). Another critical parameter for dynamic models, in particular for relatively weak winds, is the C/O ratio. After testing a model having a C/O ratio of 1.47, while all the other parameters are identical to the best dynamic model, we found that the model appears, in that case, too much extended compared to the 15 m baseline VINCI visibility data, whereas the levels of the 60, 30, and 15 m baselines MIDI visibility data are reproduced relatively well. The transition from windless models to models with considerable mass-loss rates occurs in a very narrow range of stellar parameters especially for the pulsation amplitude, the C/O ratio, and the effective temperature, as already pointed out by Gautschy-Loidl et al. (2004). In summary, a better sampling of parameter space beyond the models currently available Mattsson et al. (2008, 2010), especially in effective temperature and C/O, could help reduce the discrepancies between models and observations. Such a study is, however, beyond the scope of this paper.

(ii) **The approximation of the stellar pulsation with the sinusoidal piston:**
As the star is a semi-regular variable showing two main periods (374 and 1804 days) with harmonics in the smallest period (Whitelock et al. 1997), using the simple sinusoidal piston to describe the stellar pulsation could be a crude approximation for such a star. The overall wind properties are mostly affected by the pulsation amplitude and not so much by the actual form of the piston motion (see models based on different types of pulsation descriptions presented by Freytag & Höfner 2008). However, the particular phase coupling between dynamic and radiative properties of the models imposed by the sinusoidal piston might cause some of the discrepancies between models and observations encountered here.

(iii) **The approximation of a complete momentum and position coupling of gas and dust (i.e., absence of drift) and the approximation of the small-particle limit (or Rayleigh limit) in the determination of the dust grain opacity in the dynamic computations:**
Gas and dust decouple when the gas of the wind is diluted as is the case for low mass-loss rate stars like R Scl. Sandin & Höfner (2003, 2004) find that decoupling the dust and gas phase increases the dust formation, which could reconcile the dynamic model with the mid-infrared spectro-interferometric measurements. Similar arguments, regarding the difficulty of producing low mass-loss rate models, have also been pointed out by Mattsson et al. (2010).
It is found by Mattsson et al. (2010) that dust grains forming in slow wind atmospheres may grow beyond sizes where their opacities can be approximated by the small-particle limit. Moreover, it has been demonstrated by Höfner (2008) that radiation pressure on micron-sized silicate grains may play a key role in driving outflows in M-type AGB stars. Similar arguments could also apply to low mass-loss rate carbon-rich stars like R Scl.

5.5 Conclusions and perspectives

In this work, we have presented the first interpretation of combined photometric, spectrometric, and interferometric measurements of a carbon-rich star based on state-of-the-art, self-consistent dynamic atmospheric models.

Interferometric observations do not show any significant variability effect at the 16 m baseline between phases 0.17 and 0.23 in the K band. This is, however, not surprising given the short time interval and because the VINCI broadband measurements average out the short term effects of a shock front in CO or CN lines. No significant variability effect is found for both 15 m baseline between phases 0.66 and 0.97, and 31 m baselines between phases 0.90 and 0.97 in the N band. This means that the stellar radiative pressure is not strong enough to reveal a movement of the warm mass dust shells larger than 3 AU, in good agreement with the amplitude of the mass shell of theoretical carbon-rich dynamic models.

The spectro-interferometric predictions of the dynamic model atmosphere are in relatively good agreement with the dynamic picture that we deduced from observations. We find rather good agreement between the dynamic model and the spectrophotometric data from 0.4 to 25 μm. The model agrees relatively well with the time-dependent flux data at 8.5 μm, whereas the model is too faint compared to the measurements in the 11.3 and 12.5 μm spectral bands. The 15 m baseline VINCI visibilities are reproduced well for the two post-maximum brightness phases, meaning that the extension of the dynamic model is suitable in the K-band. In the mid-infrared, the slope of the 60 m baseline MIDI visibilities in the 8-9 μm spectral range is reproduced well for all the available phases. This means that the dynamic model has the proper extension to reveal the molecular structures of C_2H_2 and HCN located above the stellar photosphere, whereas the non consistent CO-MARCS+DUSTY model fails to do so.

The discrepancy between the dynamic model and the spectro-interferometric data could be related to inaccurate estimation of parameter values of the hydrostatic initial structure, a difference between the parameter values deduced from the hydrostatic modeling and the ones related to the hydrostatic initial structure of the dynamic model, the sinusoidal piston simulating the stellar pulsation, the inclusion of SiC opacities in the a posteriori radiative transfer, or a combination of all these effects. However, it seems that, owing to the strong nonequilibrium process of dust formation in AGB stars, the transition from models without wind to models with considerable mass-loss rates occurs in a very narrow parameter range. The most sensitive parameters allowing this sharp and strong transition between models with and without wind are the effective temperature, the amplitude of the piston velocity, and the C/O ratio. Therefore, it seems necessary to improve the sampling of critical regions in parameter space in the grid of hydrodynamic models for further investigations of the extended structures of low mass-loss carbon stars like R Scl.

Finally, the complete dynamic coupling of gas and dust, and the approximation of grain opacities with the small-particle limit in the dynamic calculation, both probably unsuitable for low mass-loss rate object like R Scl, could also contribute to the disagreement between the dynamic model and the spectro-interferometric data. First tests with C-star models based on opacities that take grain size into consideration (Mattsson & Höfner 2011) show

that wind characteristics may be affected considerably in models close to a mass-loss threshold (Mattsson et al. 2010), such as the one used here to represent the low mass-loss C-star R Scl, resembling recent wind models for M-type AGB stars (Höfner 2008).

Chapter 6

Spectro-interferometric study of the C-rich Mira R Fornacis

In this chapter the MIDI observations (Sect. 6.2), the data reduction (Sect. 6.3), the variability (Sect. 6.4), and a preliminary interpretation with geometric and atmospheric models (Sect. 6.6, Sect. 6.7) will be presented for the C-Mira R Fornacis. Section 6.9 summarises the status of the investigations and presents an outlook. A more detailed interpretation is still ongoing, and will be the subject of a paper to be submitted in the coming months.

6.1 Introduction

The C-star R For is classified in the General Catalogue of Variable Stars as a Mira variable. The objects which are part of this variability class show photometric variations with amplitudes larger than 2.5 mag in the V band, and with long periods (> 100 days). The lightcurves of Mira variables are usually described as regular with sinusoidal behaviour, nevertheless, there is a fraction of objects which shows asymmetries or even double peak maxima in their lightcurve. The most extensive study of the shape of a lightcurve was published by Vardya (1988). The study found that only a small fraction of the Miras deviate from the symmetric lightcurve, and there seems to be a correlation between this and the chemistry of the object (M, S, and C-stars). More recently, Lebzelter (2011) studied a sample of 454 Mira lightcurves from the All-Sky Automated Survey `ASAS`[1]. In this recent work it is found that 30% of the lightcurves differ from a sinusoidal pattern. Moreover, it is more frequent to have S or C-stars than M-stars with asymmetries or double maximum peak in the lightcurve. Long term observations of some Mira variables evidence erratic

[1] Pojmanski (2002), `http://www.astrouw.edu.pl/asas/`

drops in their brightness (Barthes et al. 1996, and references therein). The process behind these obscuration events is still unknown.

The lightcurve of R For was discussed for the first time by Feast et al. (1984), and later by Le Bertre (1988). Both works concluded that the lightcurves show a deep minimum in 1983 (see Fig. 6.1). The reason of this decrease was attributed to an increased dust obscuration.

Four scenarios can be envisaged in order to explain the obscuration event:

(i) The first scenario involves the interplay of two dynamic processes: pulsation and dust formation. The combined SAAO and ESO data from October 22, 1981 (JD 2444900) to March 14, 1989 (JD 2447600) were discussed by Winters et al. (1994) and compared with synthetic lightcurves for long period variables. The latter were based on dynamic models of circumstellar dust shells from Fleischer et al. (1992). The models included time-dependent hydrodynamics, a detailed treatment of the dust (formation, growth, and evaporation of the carbon grains), and frequency-dependent radiative transfer from Winters et al. (1994a). Winters et al. (1994) suggested that dust obscuration events may occur periodically as a result of the interplay of two dynamic processes with different time scales: the regular pulsation of the star, which provides the short dynamic time scale, and the process of dust formation and growth, which, according to the dynamic calculations has a time scale of four up to five times longer.

(ii) The second scenario was proposed by Feast (1997) and it explains the minimum in the lightcurve as an effect of further dust-condensation in an existing shell. This kind of event is common in the atmospheres of R Coronae Borealis stars. The dust forms at a temperature of ~ 1500 K. At this temperature a spherically symmetric shell with graphite particles of $0.02\,\mu$m of diameter is thick enough to produce a drop in the lightcurve similar to the one observed for R For.

(iii) The third scenario involves an asymmetric dust ejection. Whitelock et al. (1997) hypothesized that the obscuration event is due to an eclipse caused by a dust cloud ejected along the line of sight. The dust might be expelled randomly or in preferential directions.

(iv) The fourth scenario, involving a disc-like structure, was suggested already by Cohen & Smith (1982) in order to explain the polarization observations of the C-star RW LMi that shows similarities with R For.

High angular observations in the mid-infrared allow to probe the dust-forming region of nearby Asymptotic Giant Branch stars. In the case of C-enriched objects, a detailed study was performed on V Oph by Ohnaka et al. (2007), and on R Scl by Sacuto et al. (2011). The last object was compared for the first time with the dynamic model atmospheres from Höfner et al. (2003). The comparison of the multi-epoch VLTI/MIDI observations of R Scl with the model atmosphere allowed the authors to constrain the movements of the mass-shells as a function of time. This kind of study, applied to R For could disentangle or reject the first and second scenario proposed for the obscuration event of 1983. VLTI/MIDI was

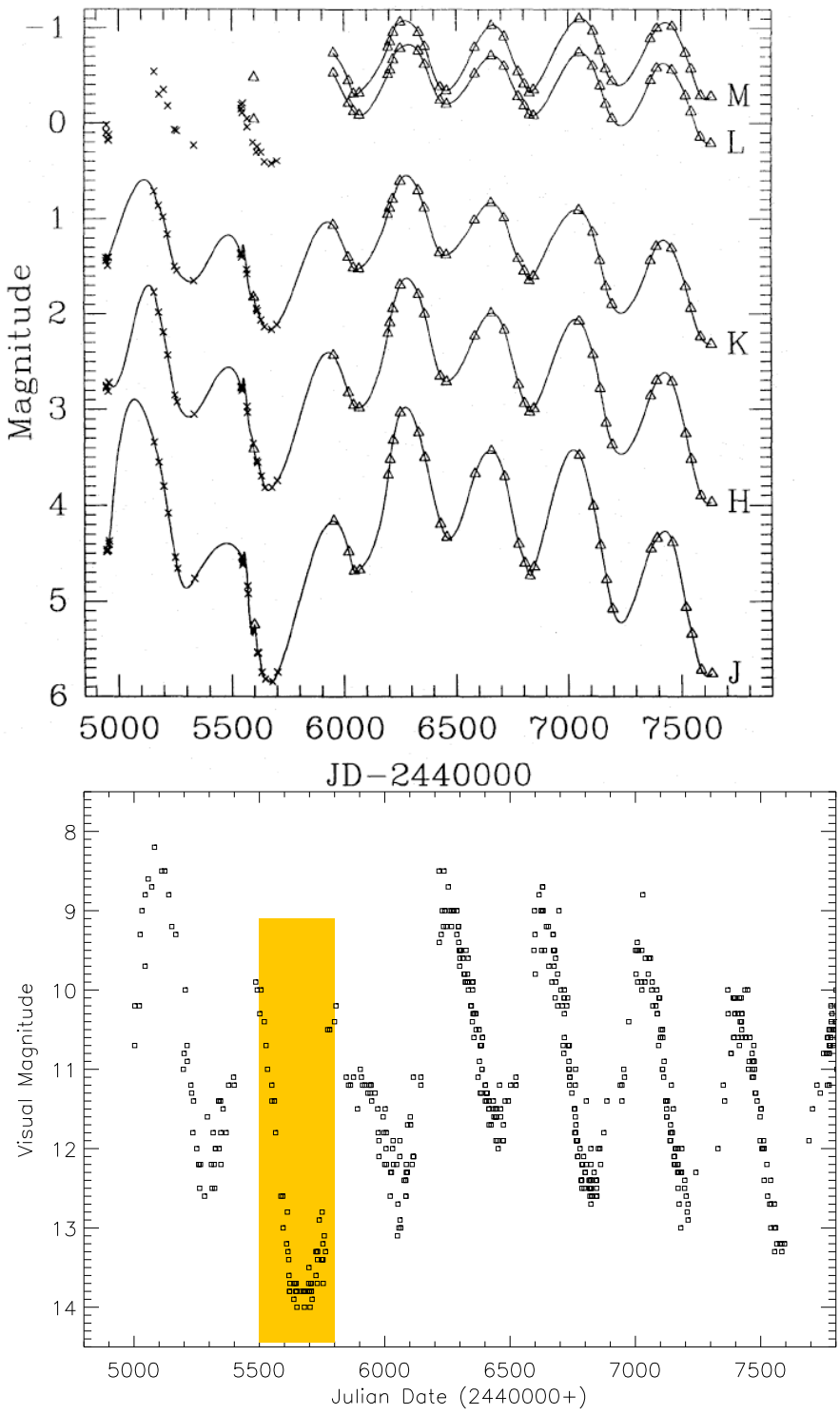

Figure 6.1: Lightcurves of R For in different bands. **Upper panel**: observed infrared J, H, K, L', and M lightcurves. The triangles are data from Feast et al. (1984), while the crosses are from Le Bertre (1992). The unusual minimum detected in 1983 is shown (JD$\sim$ 2445500). The full lines are a cubic spline interpolation between the points. *(Fig. 9 from Winters et al., 1994).* **Lower panel**: visual lightcurve for the same period downloaded from the American Association of Variable Stars Observers (AAVSO) webpage. The shadowed region marks the minimum of 1983.

already used by Leao et al. (2007) in order to study the circumstellar environment of the R CrB star RY Sgr. This star showed a drop in the J and H lightcurve similar to the one observed for R For. The observations of RY Sgr evidenced that the star is surrounded by a single dusty cloud located at ~ 100 stellar radii. A wise choice of the $u-v$ covarage could help to disentangle eventual deviations from spherical structure for R For, that would point to confirm or reject the third and fourth scenario.

6.2 VLTI/MIDI interferometric observations

In order to study the close circumstellar environment morphology of R For, high angular resolution measurements were acquired in the mid-infrared with the ESO-VLTI/MIDI facility. The choice of the instrument is rather straightforward since this is the only infrared astronomical facility with adequate angular resolution and spectral coverage to probe the close dusty circumstellar environment. A detailed description of this instrument is given in Sect. 2.2.3.

The observations of R For were planned to have a good $u-v$ coverage to study potential asymmetries of the object, and also to study the variability and cycle-to-cycle effects. The data were acquired within the frame of two different ESO service mode observing programs, one in 2007, and one in 2009 with the following IDs: 080.D-0231 (P.I.: K. Ohnaka), and 084.D-0361 (P.I.: S. Sacuto). In Table 6.1 the 29 visibility points acquired for the science target are presented. Seven different baseline configurations have been used for the observations, with lengths ranging between 15 m and 128 m. The $u-v$ coverage dispersed in wavelength (color-coded) of the MIDI observations is plotted in Fig. 6.2. Twenty-five points out of the original sample of 29 turn out to be of good enough quality to be used for the interpretation. The upper panel show the data acquired in P80, while the lower panel shows the data acquired in P84. More details on the reason of rejecting few points are given in the next section on the data reduction (Sect. 6.3).

Every observation of R For is paired with the observation of a calibrator star. This star is ideally unresolved, very bright, and with known diameter. The list of calibrators used for the data reduction is given in Table 6.2. By using only one calibrator for the visibility point of the target, there is the risk to underestimate the error on the science data. Fortunately, it is ESO policy to make all the calibrator data in the archive public (immediately). Hence, the list of calibrators given in Table 6.2 includes also objects which were not specifically in the program of R For, but they were observed during the corresponding nights. The calibrators from other programs were selected according to the observing mode of the science target (HIGH_SENS, PRISM), and in a range of time ± 2 hours around the R For observations. In a few cases, where no calibrators in HIGH_SENS mode were available, calibrators observed in SCI_PHOT were used. In this case the SCI_PHOT data were reduced in HIGH_SENS mode according to the data reduction manual. A detailed description of the MIDI data reduction process is given in the following section.

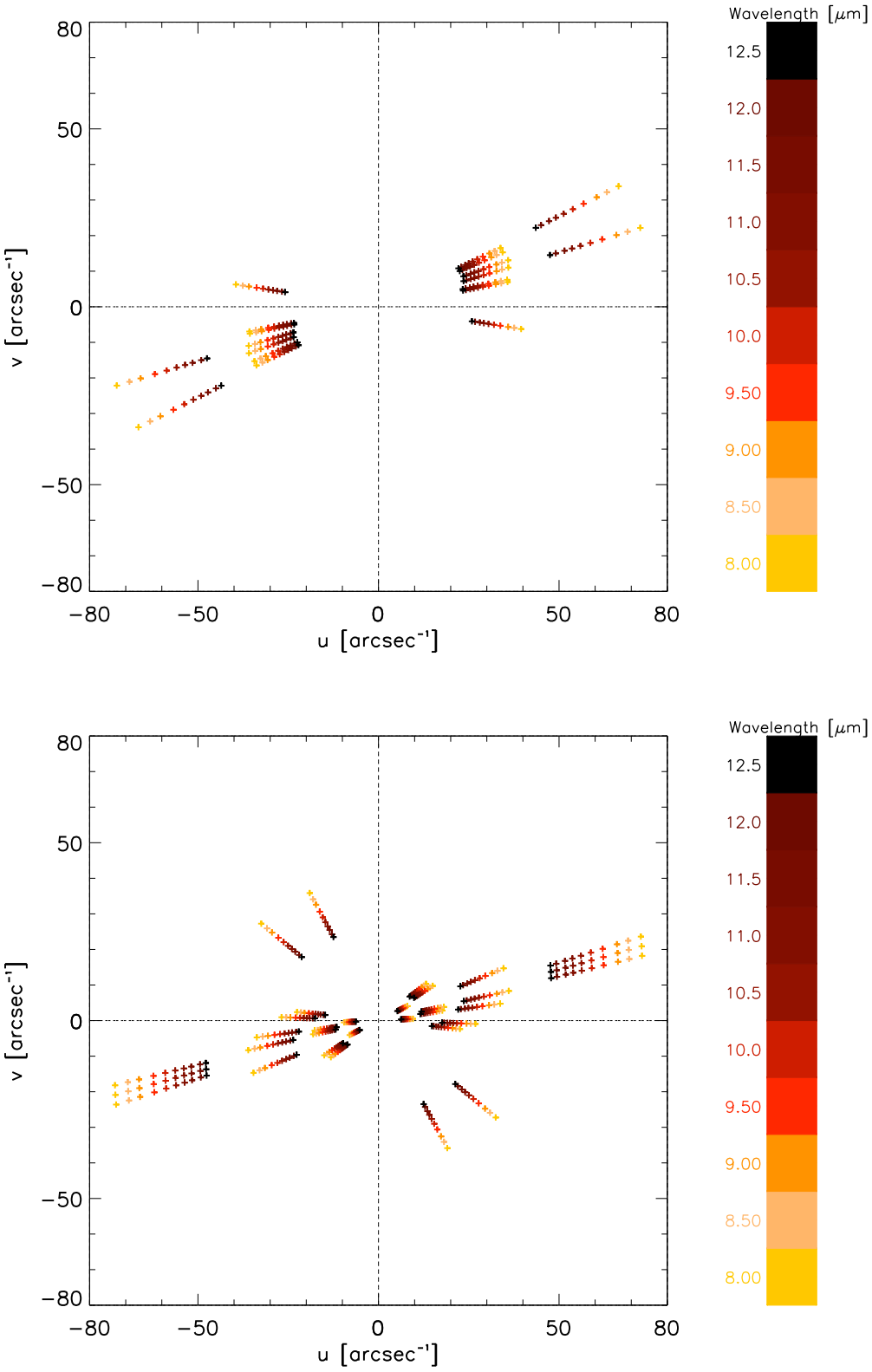

Figure 6.2: $u-v$ coverage dispersed in wavelength of the R For observations acquired during the programs 080.D-0231 (upper panel), and 084.D-0361 (lower panel).

Table 6.1: Journal of the MIDI observations for the C-star R For. In the col. 1 an identification number is assigned to each observation; col. 2 listes the date and time when the observation was acquired; in col. 3 the visual phase is reported together with a letter in order to group the phase for the model comparison (details in Sect. 6.4); the VLTI baseline configuration is indicated in col. 4; the projected baseline $B_{\rm p}$ is given in col. 5; the position angle (PA) in col. 6, and finally the value of the seeing in the last col. 7.

#	Date & Time [UT]	Phase	VLTI Configuration	$B_{\rm p}$ [m]	PA [deg]	Seeing [arcsec]
01	2007-10-04 03:17:13	1.07 (a)	G0-H0	26	43	0.82
02	2007-10-05 04:58:33	1.08 (a)	G0-H0	31	61	0.88
03	2007-10-29 03:17:27	1.14 (a)	A0-K0	122	60	1.13
04	2007-12-02 01:47:31	1.23 (b)	D0-H0	63	66	2.05
05	2007-12-02 02:51:00	1.23 (b)	D0-H0	63	73	-
06	2007-12-02 03:00:50	1.23 (b)	D0-H0	63	74	-
07	2007-12-06 01:10:17	1.24 (b)	A0-K0	125	63	1.35
08	2007-12-06 02:36:01	1.24 (b)	A0-K0	127	73	0.88
09	2007-12-10 00:58:46	1.25 (b)	D0-H0	63	64	1.17
10	2007-12-10 01:50:54	1.25 (b)	D0-H0	64	70	1.28
11	2007-12-12 03:11:41	1.25 (b)	D0-H0	61	79	1.44
12	2007-12-29 01:54:08	1.30 (b)	D0-H0	61	78	1.32
13	2008-02-27 01:07:55	1.45 (c)	D0-H0	67	99	0.99
14	2009-09-06 07:32:39	2.89 (d)	D0-H0	63	67	1.08
15	2009-09-06 09:06:52	2.89 (d)	D0-H0	62	77	0.95
16	2009-09-07 05:43:04	2.89 (d)	G0-H0	28	52	0.76
17	2009-09-07 06:18:38	2.89 (d)	G0-H0	30	57	0.48
18	2009-09-07 09:10:11	2.89 (d)	H0-K0	31	78	1.30
19	2009-09-07 09:44:55	2.89 (d)	H0-K0	30	81	1.45
20	2009-09-21 07:53:15	2.93 (d)	A0-G1	126	76	1.08
21	2009-09-26 09:00:58	2.94 (d)	D0-G1	68	152	0.75
22	2009-09-27 06:01:02	2.94 (d)	D0-G1	71	130	0.68
23	2009-09-27 08:43:21	2.94 (d)	D0-H0	57	82	0.65
24	2009-10-01 05:21:32	2.95 (d)	E0-G0	15	63	1.15
25	2009-10-01 05:59:46	2.95 (d)	E0-G0	16	67	1.09
26	2009-11-18 03:31:27	3.08 (a′)	A0-G1	128	72	0.90
27	2009-11-18 03:50:10	3.08 (a′)	A0-G1	127	74	0.65
28	2010-01-11 03:13:02	3.22 (b′)	D0-H0	38	96	0.65
29	2010-01-11 03:48:17	3.22 (b′)	D0-H0	45	92	0.76

Table 6.2: List of the stars used as calibrators for R For. The name of the calibrator is listed in col. 1, the date and time of the observations in col. 2, the seeing values in col. 3, the IRAS fluxes at 12 μm, and the diameters in col. 4 and 5, respectively. Col. 6 records the ID of the target calibrated with that particular observation, moreover comments concerning the quality of the data point are given. TF is the acronym used for Transfer Function. $\star$ This object was not used as calibrator, see detailed discussion Sect. 6.3.5.$^{(a)}$ ESO/MIDI database;$^{(b)}$ JMMC database.

Calibrator	UT time [UT]	Seeing [arcsec]	F_{12} [Jy]	$\theta_{\rm UD}$ [mas]	#SCI
HD 224935	2007-10-04 02:50:11	0.94	86.90	7.24 ± 0.03 $^{(a)}$	#1 TF> 1 (not used)
	2007-10-04 04:41:10	0.65			#1 TF> 1 (not used)
	2007-12-02 01:21:20	-			#4;#5
HD 25025	2007-12-02 02:12:33	1.81	109.6	8.76 ± 0.624 $^{(b)}$	#4; #5; #6
	2007-12-02 03:45:02	-			bad TF (not used)
	2007-12-02 03:56:58	1.11			bad TF (not used)
	2007-12-06 02:14:11	-			#7; #8
	2007-12-10 01:25:44	1.58			#9; #10
	2007-12-10 02:14:20	1.54			#9; #10
	2007-12-29 01:15:52	1.67			#12
	2008-02-27 00:46:47	0.95			#13
HD 20720	2009-09-06 07:13:16	0.85	112.8	10.03 ± 0.1 $^{(a)}$	#14; #15
	2009-09-06 08:48:01	1.0			#14; #15
	2009-09-07 05:58:59	0.51			#16; #17
	2009-09-07 06:42:26	0.55			#16; #17
	2009-09-07 08:54:21	-			#18; #19
	2009-09-07 09:27:37	1.28			#18; #19
	2009-09-21 07:29:16	1.5			#20 TF> 1
	2009-09-26 08:44:52	0.8			#21
	2009-09-27 05:44:46	0.86			#22
	2009-09-27 08:28:24	0.61			#23
	2009-10-01 04:58:54	0.88			#24; #25
	2009-10-01 05:40:04	1.12			#24; #25
	2009-11-18 03:12:21	0.67			#26; #27
	2009-11-18 04:09:00	0.80			#26; #27
	2010-01-11 03:30:42	1.42			#28; #29
	2010-01-11 04:04:21	0.78			#28; #29
HD 4128*	2007-10-04 03:39:22	0.76	59.93	5.25 ± 0.25 $^{(a)}$	
	2007-10-05 03:37:41	0.58			
	2007-10-05 04:35:53	0.63			
	2007-10-29 03:52:56	0.80			
	2007-12-06 00:46:21	1.53			
	2007-12-10 00:34:27	1.06			
	2007-12-12 03:39:42	1.85			
	2009-09-06 07:53:01	1.06			
	2009-09-06 09:26:13	1.16			
	2009-09-07 08:12:34	1.22			
	2009-09-26 08:25:36	0.83			

Table 6.2: continued.

Calibrator	Date & Time [UT]	Seeing [arcsec]	F_{12} [Jy]	$\theta_{\rm UD}$ [mas]	#SCI
	2009-09-27T05:10:22	0.76			
HD 12929	2007-12-06 02:55:18	1.20	77.80	7.43 ± 0.52 (c)	#7; #8
	2009-09-06 06:34:13	0.99			#14
	2009-09-07 07:01:04	0.66			#16; #17
	2009-09-21 08:20:14	1.10			#20
	2009-09-21 08:29:02	1.12			#20
HD 48915	2007-12-10 03:21:20	1.49	143.10	5.85 ± 0.15 (a)	#9; #10
	2007-12-12 04:43:32	1.96			#11
	2007-12-12 05:38:46	0.91			#11
	2007-12-29 02:21:47	1.29			#12
	2009-09-27T06:39:12	0.64			#23

6.3 MIDI HIGH_SENS data reduction

The data were reduced with the MIDI Interactive Analysis (MIA), and Expert Workstation (EWS) package version 1.7.1 (Köhler 2005, Jaffe 2004). The MIA+EWS[2] data reduction software is written in the C-programming language. The package provides an IDL interface which calls the various routines for the data reduction. In the specific case of this work, it was run on IDL Version 7.0 (`linux x86_64 m64`).

In this paragraph the list of steps needed to go from raw to calibrated MIDI data are presented. The description of the data reduction software MIA+EWS is based on Köhler (2005), Jaffe (2004), Ratzka (2005), and Zhao-Geisler (2010). MIA and EWS use the same method to determine the photometry, this will be described in Sect. 6.3.1. The different methods used by MIA and EWS to derive the visibilities are described in Sects. 6.3.1 6.3.2. Following the procedure generally used by the interferometric community, the data were first reduced with the MIA package, then with the EWS package, and finally compared. The calibration, check of the data quality, and error estimation are described in Sects. 6.3.3, 6.3.4, and 6.3.5 respectively.

6.3.1 MIA interferometric data reduction

MIA data reduction is based on the power spectrum analysis, and the fringe amplitude is determined incoherently. The Fast Fourier transform is used in order to calculate the Fourier amplitude of the fringe packets. This method is quite robust when reducing data for bright objects, but the phase information cannot be retrieved. The details of the data reduction are given in Leinert et al. (2004), Ratzka (2005), and in Chesneau (2007).

Photometric Flux and Masks

The first step of the data reduction involves the photometric set of data. The flux coming from the two beams of the two apertures is treated individually. Every set of photometric

[2] `http://www.strw.leidenuniv.nl/~nevec/MIDI/index.html`

data is averaged and sky-subtracted. The sky-subtracted frame contains the spectrum of the object (versus wavelength) horizontally oriented on the chip. The code reads the file and searches for the position of the spectrum. Even if the chopping technique is used to subtract the sky, often the data are contaminated by background. In order to remove this background MIA (and also EWS) makes use of a mask. In MIA the mask is created iteratively by fitting the position and the width of the spectrum. This can be done by starting from the interferometric or from the photometric channels, the later one being preferred because of less background contamination. The mask (M) is used to extract the data of the object from the fringe tracking datasets (photometric and interferometric channels). The photometric measurements after the sky-subtraction consist of four spectra: $P_{i,j}$ where $i = A, B$ corresponds to a given beam, and $j = 1, 2$ corresponds to the detector window. Keeping in mind that $M_{i,j}$ is the mask, and t is the integration time of the detector, it is possible to derive the flux of the spectrum ($I_{i,j}$) as a function of the wavelength from the following equation:

$$I_{i,j}(\lambda) = \frac{1}{t} \sum_{y} P_{i,j}(\lambda, y) M_{i,j}(\lambda, y). \tag{6.1}$$

The total photometric flux for a given beam in the subarray j is obtained integrating by $I_{i,j}$ over the wavelength. The result of this operation is I_A, and I_B that will be used in Equ. (6.3) to derive the visibility.

Interferometric Flux

The next steps to determine the power spectrum, or Fourier amplitude are: compression, subtraction, sorting, binning, and finally selection of the frames. The steps are illustrated in Fig. 6.3.

The data extracted with the mask from the interferometric channel are collapsed (or *compressed*) from a 2D flux distribution to a 1D spectrum. This is done by multiplying every frame of the fringe data by the mask. A weighted integral is performed on the result along the direction perpendicular to the spectral dispertion. The two interferometric channels determined in this way are then *subtracted*, and an optimal subtraction of the background should be achieved. For R For and the calibrator 4000 frames were recorded during 200 OPD scans. The frames are *sorted* in arrays according to the scans, this means $4000/200 = 20$ arrays with optical wavelength and OPD as axes. The next step of the data reduction is the *binning*. Every pixel is ≈ 0.05 μm wide in wavelength. Usually every scan is *binned* into stripes with steps of n pixels. The minimum value of the step is 1, but in this case the noise channel by channel is often too large to see the trend of the curve. The default value for the step of the binning should be 3 or 4 in order to improve the S/N. This binning corresponds to the resolution of the prism, but it is also similar to the PSF of the beam, i.e., the smallest resolution (independent) element.

A Fourier transform is performed on every scan, and the value of the amplitude of the white-light fringe (amplitude of the fringes seen after integrating signal over the wavelengths) is used in order to decide whether the scan should be used for the determination of the correlated flux or not. This last step is the so called *selection*. MIA gives the possibility to plot the histogram of all the white-light fringe amplitudes. If the data have good quality

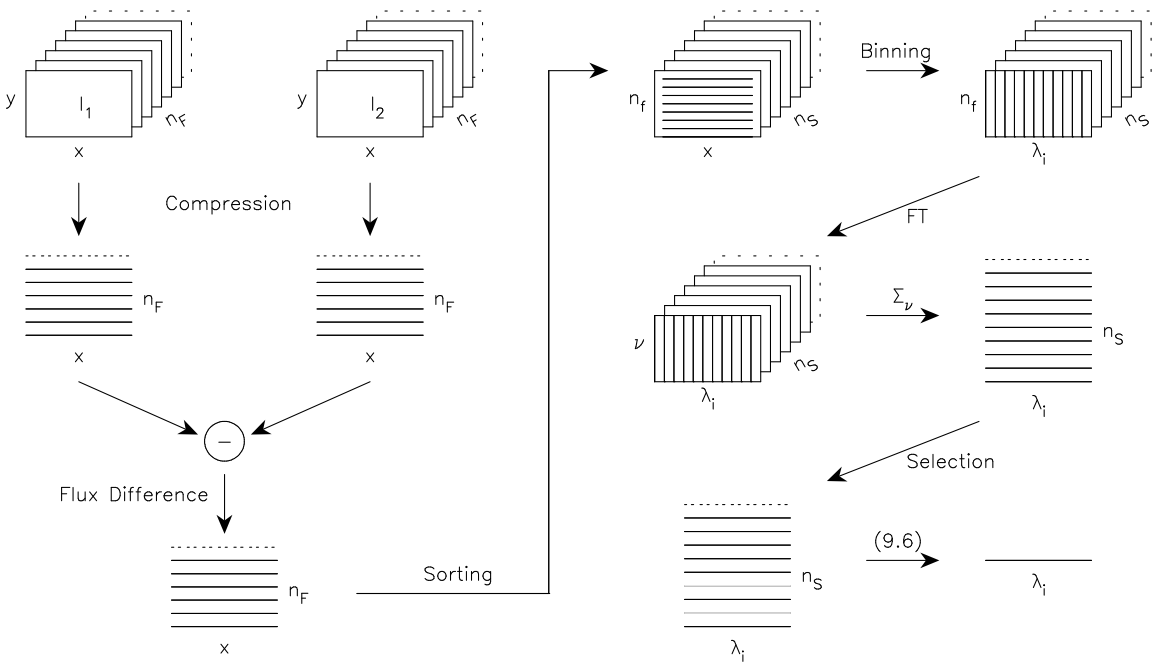

Figure 6.3: Flowchart of the steps that MIA follows to derive the interferometric flux.(Adopted from Ratzka (2005)).

this should be nicely peaked at high amplitudes. The threshold for the selection can be chosen interactively, and it should be put right below the high peaked histogram. In order to determine the Fourier amplitude the cube of wavelength-frame-scan are summed over the wavelength range of every bin. The result is Fourier transformed, and the power spectrum is finally summed over the appropriate spatial frequency range. The interferometric flux in every wavelength bin (λ_1, λ_2) is the square root of the fringe power spectra $(\mathcal{I}_\nu)$ and it can be written as:

$$I(\lambda_1, \lambda_2) = \frac{2}{t}\sqrt{\frac{1}{N_{scans}}\sum_{scans}\sum_{\nu_1}^{\nu_2}|\mathcal{I}_\nu^{\rm bin}(\nu, s)|^2} \tag{6.2}$$

where the number of scans (N_{scans}) is the number of "good" scans within a bin, t is the integration time, and $\nu = c/\lambda$. In this formula the term which includes the bad scans is neglected. More details are given in the thesis of Ratzka (2005).

Raw Visibility

The raw (sometimes called instrumental) visibility of the object as function of wavelength is obtained by dividing the correlated flux $I(\lambda_1, \lambda_2)$ for a correction factor which includes the photometric flux from the two beams (A, B) previously determined:

$$V(\lambda_c) = \frac{I(\lambda_1, \lambda_2)}{2\sum_{\lambda=\lambda_1}^{\lambda_2}\sqrt{I_A(\lambda)I_B(\lambda)}} \tag{6.3}$$

where λ_c is the central wavelength of the interval $[\lambda_1, \lambda_2]$.

6.3.2 EWS interferometric data reduction

EWS data reduction applies a coherent algorithm in order to derive the interferometric observables: correlated flux, visibility, and in addition also the differential phase. This data reduction package was developed by Jaffe (2004) and it is optimized for faint targets. In addition, compared to MIA, it has the advantage that it provides the differential phase. In this paragraph the EWS algorythm will be briefly described, the discussion of the differential phase is based on Tubbs et al. (2004) and Deroo (2007).

In EWS the fringes, dispersed in wavelength through the PRISM (or GRISM, according to the chosen mode) are analysed in the frequency space, rather than in the OPD space. The first step of the EWS data reduction is *data compression*. The signal recorded by the two interferometric channels is compressed in the spatial space after multiplying by a defined mask. This is similar to what happens in MIA, but the mask applied by EWS is a fixed mask (see Sect. 6.3.4). The signals coming from the two beams are subtracted for each j spectral channel in order to obtain a 1D spectrum. The result of this operation can be written as:

$$I(j) = I_{\rm resid}(j) + \frac{I_{\rm corr}(j)}{2}\left[\exp(i\,\Phi(j)) + \exp(-i\,\Phi(j))\right] \tag{6.4}$$

where $I_{\rm resid}$ is the residual of the background, $I_{\rm corr}$ is the correlated flux, and Φ is the phase (optical path difference offset from the white-light center) which has the opposite sign for the two beams. A high-pass filter is applied to the compressed data to *remove the background*. Some noise is still superimposed on the fringes because of the modulation of the OPD (instrumental + atmosphere). In order to get rid of the instrumental noise the signal is demodulated. The estimation of the OPD atmospheric component is made following the approach of Group Delay estimation from Meisner (2001).

After reducing all the frames to the same OPD, they are added coherently, and the visibility can be finally derived.

The phase obtained after this summing is subtracted from the phase of the individual spectral channels. This operation corresponds to a correction for the change of the index refraction of the air with wavelength. The resulting differential phase should be zero, unless the object has an intrinsic deviation from a central symmetry, or there is a visibility null, in which case the differential phase shows a jump of 180°.

6.3.3 Calibration

The calibrated visibility (V) of the object is linked to its raw visibility ($V^{\rm sci}_{\rm raw}$) measured by the interferometer via the relation:

$$V = \frac{V^{\rm sci}_{\rm raw}}{TF}. \tag{6.5}$$

TF is the transfer function or response of the instrument. In order to evaluate TF the target observation is paired with the observation of a calibrator (CAL-SCI sequence[3]). The

[3]The sequence CAL-SCI is well suited for differential measurements. If the science case requires absolute measurements, than the sequence CAL-SCI-CAL needs to be used.

calibrators are objects which are very bright and ideally point sources (unresolved, $V \simeq 1$). The uniform disc diameter ($\theta_{\rm UD}$) of the calibrator is listed in dedicated catalogues therefore it is possible to derive an "expected" or "theoretical" visibility:

$$V_{\rm theo} = \frac{2J_1(\frac{\pi B\theta_{\rm UD}}{\lambda})}{(\frac{\pi B\theta_{\rm UD}}{\lambda})} \tag{6.6}$$

where B and λ are in meters, and $\theta_{\rm UD}$ in radians. The TF is finally obtained dividing the raw visibility measurement of the calibrator ($V^{\rm cal}_{\rm raw}$) by its theoretical visibility ($V_{\rm theo}$).

6.3.4 Identifying problems

After reducing the data with the two software packages, the resulting visibilities were compared, since the two different methods can deliver sometimes different results. One of the most commonly encountered problems is that the mask used by the program is not appropriate for the data. This may happen when dealing with faint objects (target or calibrator) with strong background, since it is difficult to obtain reliable measurements of the photometric flux and fringe amplitude. Differences within the order of $10\% - 15\%$ are usually considered normal.

When the difference is larger than 10%, the data reduction is repeated first by using EWS with the MIA mask, and then with MIA plus the EWS mask. The MIA mask is interactively fitted to the data while EWS uses a fixed broad mask. After "exchanging" the masks, the results are compared, and hopefully the discrepancy between the results disappears. If this is not the case, further tests are needed.

In the specific case of the data set of R For, the mask of EWS turned out to be not adequate for the data reduction. The data reduction performed with the EWS+MIA mask was solving the problem of the discrepancy between MIA and EWS results in all the cases (for a detail discussion on the use of the masks in MIDI see Chesneau 2007, Sect. 2.6).

6.3.5 Interferometric data products and errors

Once the data quality was verified, only the 'MIA' calibrated visibilities were taken into account for the scientific interpretation, since this method works very well for bright targets such as R For. The calibrated visibilities obtained with different calibrators (observed during the same night) were averaged, and the errors were derived from the standard deviation of all the calibrated visibilities. This is a conservative error estimation but it is also rather robust. When only one calibrator is available the error is set to 10%. This number is justified by the fact that HIGH_SENS mode measures the photometry and the correlated flux separately within an interval of a few minutes. This introduces an error of $7 - 15\%$ to the measurements, and this value is variable according to the atmospheric conditions during the night (Chesneau 2007).

The differential phase is partially influenced by atmospheric fluctuations. The pipeline EWS performs a linear fit to the index of refraction of water vapour, in order to get rid of the atmospheric effects. The residual error of this operation can be estimated easily by

extracting a differential phase of a calibrator with another calibrator. This operation was repeated with many calibrators (when possible). Usually it is considered that a differential phase reveals deviations from central symmetry when it is larger than 5 up to 20°, depending on the night.

The visibility

All the visibilities were derived as described above. During the data reduction it was noted that the calibrator HD 4128 in almost all the cases produced a transfer function larger than 1 beyond 11 μm. This might be due to the presence of an infrared excess for example caused by a dust shell that contributes at longer wavelengths, or maybe due to a problem with the photometry (although the 12μm flux is not close to the instrumental limit). This object was discarded from the calibration process, as all the observations (including the one of other programs, D. Klotz and S. Sacuto priv. comm.) appear suspicious. This turns out to be a problem for dataset #3, when HD 4128 was the only calibrator observed. Beside HD 4128, HD 224935 was observed as calibrator in SCI_PHOT mode during the night when datasets #1 and #2 were acquired. Unfortunately, in both cases the resulting transfer function is larger than 1, therefore, these data sets will be not considered for the final interpretation. Other observations not considered for the interpretation, are #6 and #14. The first one shows bad photometry, while the fringe power of the second observation is underestimated.

All the data are shown in Figs. 6.4, 6.5, and 6.6 where they are grouped according to the visual phase (see discussion in Sect. 6.4) and the projected baseline (cf. Table 6.1). The visibility curves exhibit the typical $S-$shape of the N-band interferometric observations of C-stars with SiC feature at 11.3 μm (Ohnaka et al. 2007, Sacuto et al. 2011). The visibility is usually lower in the $8-9\,\mu$m region where the major contributors to the opacity are C_2H_2 and HCN. In the $9-10\,\mu$m there is a typical plateau, and it drops down between $10-11\,\mu$m where the SiC dust feature is located. The visibility stays more or less constant between 11 μm and the edge of the N-band. The decrease of visibility in the $8-9\,\mu$m region appears to be less pronounced for the shorter baselines, as can be seen in the upper panel of Fig. 6.5. The platoo of $9-10\mu$m region is not present for the observation #13 shown in Fig. 6.4. But this visibility should be treated carefully since it was calibrated using only one calibrator. The long baseline observations shown in Fig. 6.6 exhibit a shape quite different from the other observations. The difference is even more pronounced for the different period (upper panel versus middle and bottom panels), and it will be discussed in the following sections.

The differential phase

All the differential phases show zero signal, except for the ones observed with the longest baselines. The jump in the differential phase is not equal to 180°, which would typically correspond to a zero visibility. Therefore, the phase information points to a non central symmetric structure. *This is the first time that MIDI detects a signature of departure from central symmetry for a carbon Mira variable through the differential phase.* The differential phases of the long baseline observations (#07, #08, #20, #26, #28) of R For are shown in Fig. 6.7 (full lines). The upper left panel shows the differential phase of the observation #14,

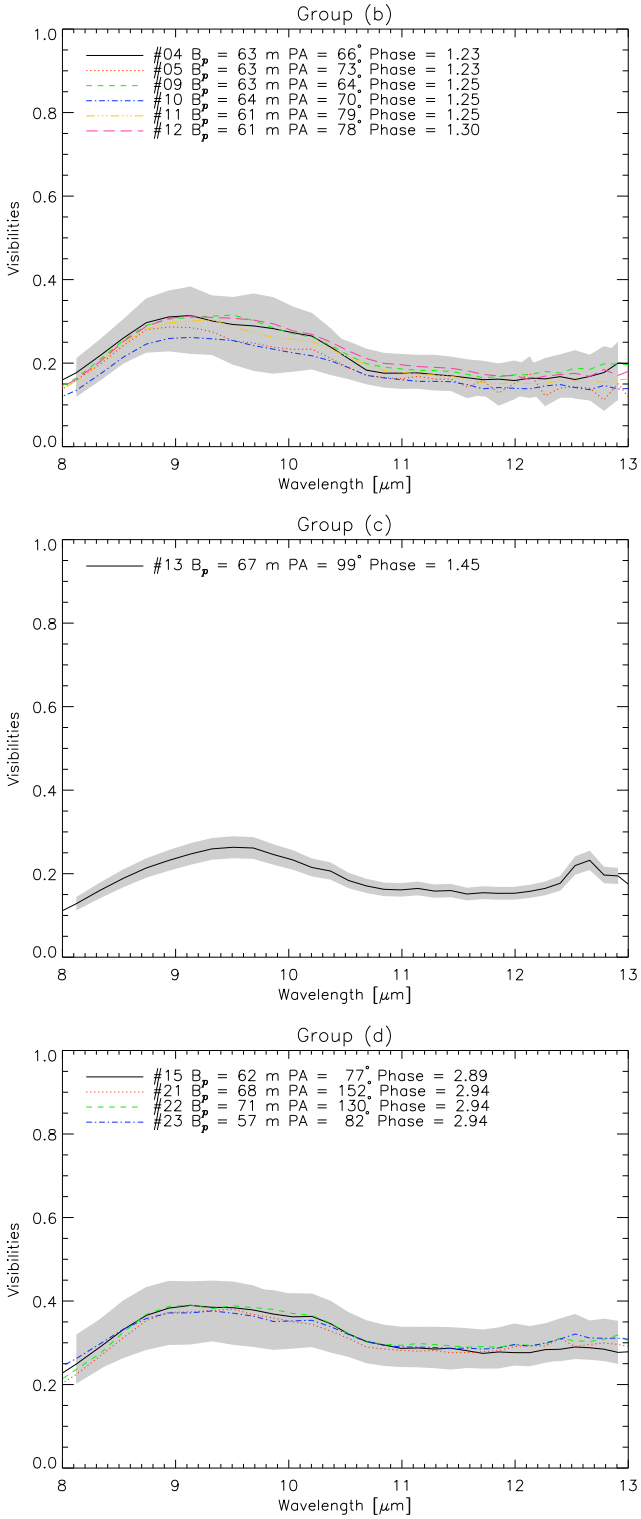

Figure 6.4: Visibilities grouped according to the baseline and the phase. The errorbars are shown as a shaded region.

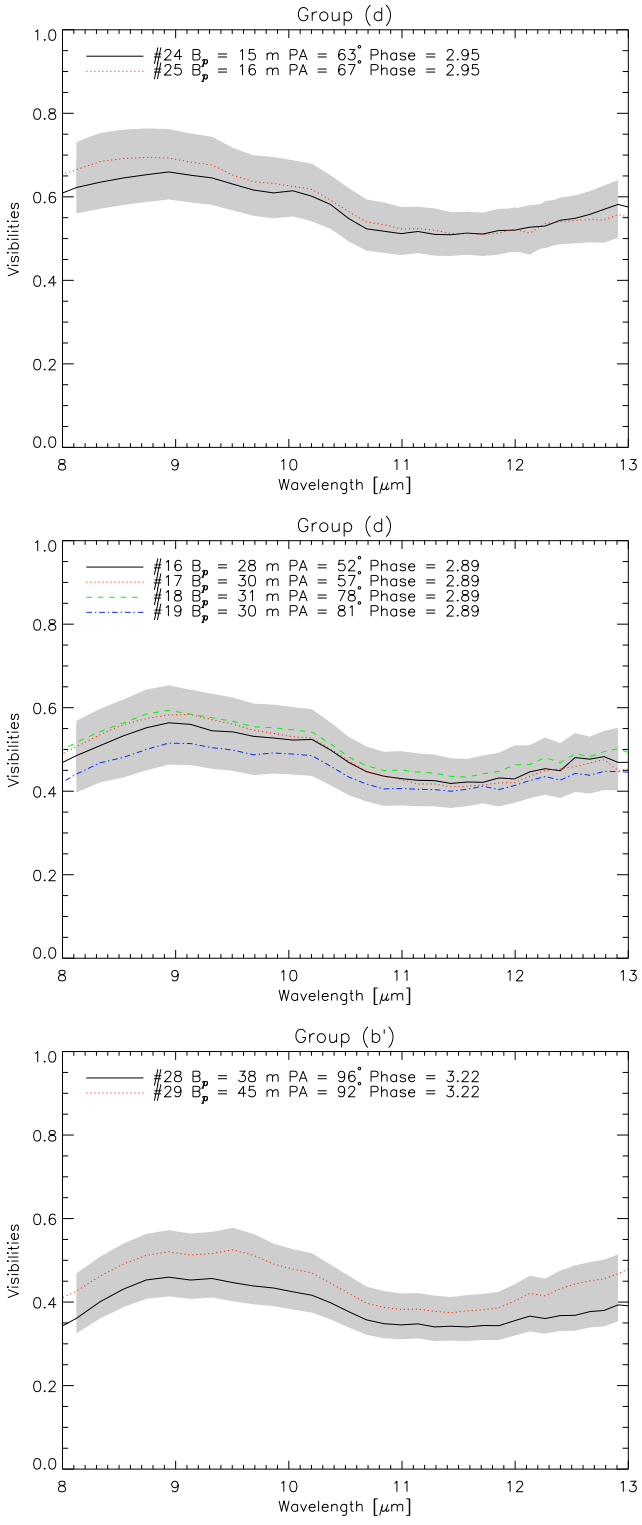

Figure 6.5: Same as Fig. 6.4.

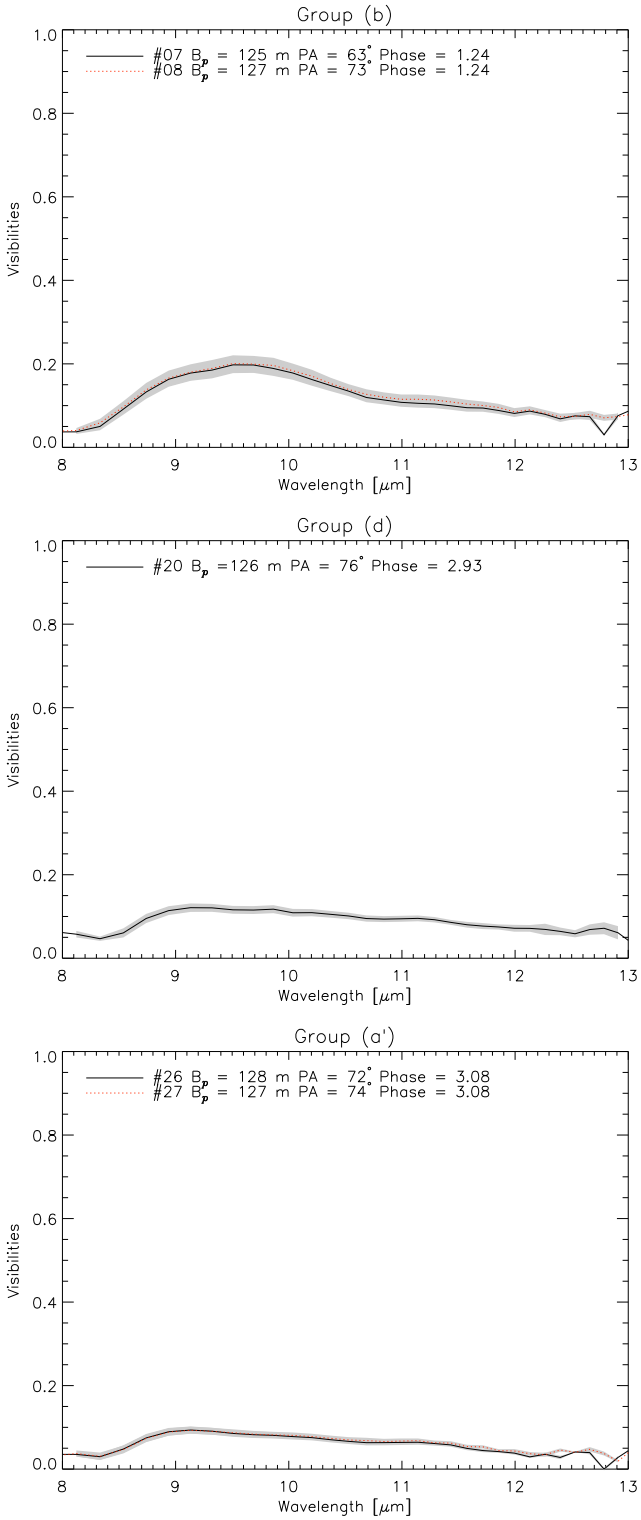

Figure 6.6: Same as Figs. 6.4 and 6.5.

one of the 60 m baseline data, for comparison. All the panels show also the instrumental visibility of the calibrators (dashed and dotted lines). The observations of 2007 (#07, #08) have a slightly worse quality, but the signature of asymmetric structure is clear and comfirmed in the data of 2009 (#20, #26, #28). The jump from zero phase is more steep for the observations of 2009, pointing at a possible evolution of the asymmetry during this period of 2 years between the observations. Further discussion are given in Sect. 6.6.1.

6.3.6 Spectroscopic reduction

Beside the interferometric observables, MIDI allows also to obtain a low resolution $N-$band spectrum of the source. The calibration of the flux is made using the ISO or IRAS spectrum of the calibrator.

6.4 The interferometric variability

One of the goals of this investigation is to constrain the variability (intra-cycle, and cycle-to-cycle) of the object. Only observations with the same baseline and a very similar position angle but different visual phase can be compared for detecting the variability. In order to assign a visual phase to the MIDI observations, the visual magnitudes of R For were downloaded from the AAVSO webpage[4]. The pulsation phase was assigned to the MIDI observations of R For using the formula:

$$\Phi = \frac{(t - T_0)}{P}. \tag{6.7}$$

P stands for the period, a value of 387 days was used according to Whitelock et al. (1997); t is the Julian date; T_0 is the Julian date assumed with a reference for the zero-phase (maximum of visual brightness). T_0 is marked as a red star in Fig. 6.8. The visual phases derived for the MIDI observations are listed in col. 3 of Table 6.1. The observations cover two cycles (2007, 2009) separated by one cycle. Within the two cycles the observations cover the portion of the lightcurve around the maximum of visual phase. The two sets of MIDI data are marked in Fig. 6.8 with shaded regions: blue for P80 (MIDI 2007), and yellow for P84 (MIDI 2009). The observations are grouped in sets according to the determined visual phase. The sets are identified with a letter in Table 6.1 beside the visual phases.

Group(a) includes the observations #1, #2, and #3 ($1.07 < \Phi < 1.14$) that unfortunately have a bad data quality.

Group(b) includes the observations of 2007 between #4 and #12 with ($1.23 < \Phi < 1.30$). This group includes two different baseline configurations: the 60 m and the 125 m projected baselines.

Group(c) includes the observation #13 with $\Phi = 1.45$ and 67 m baseline.

Group(d) includes the observations #14 until #25 ($2.89 < \Phi < 2.95$). The covarage in baseline is wide, including observations with 15, 30, 60, 70 and 125 m baselines.

Group(a′) includes long projected baseline observations with visual phase $\Phi = 3.08$ and

[4] `http://www.aavso.org/`

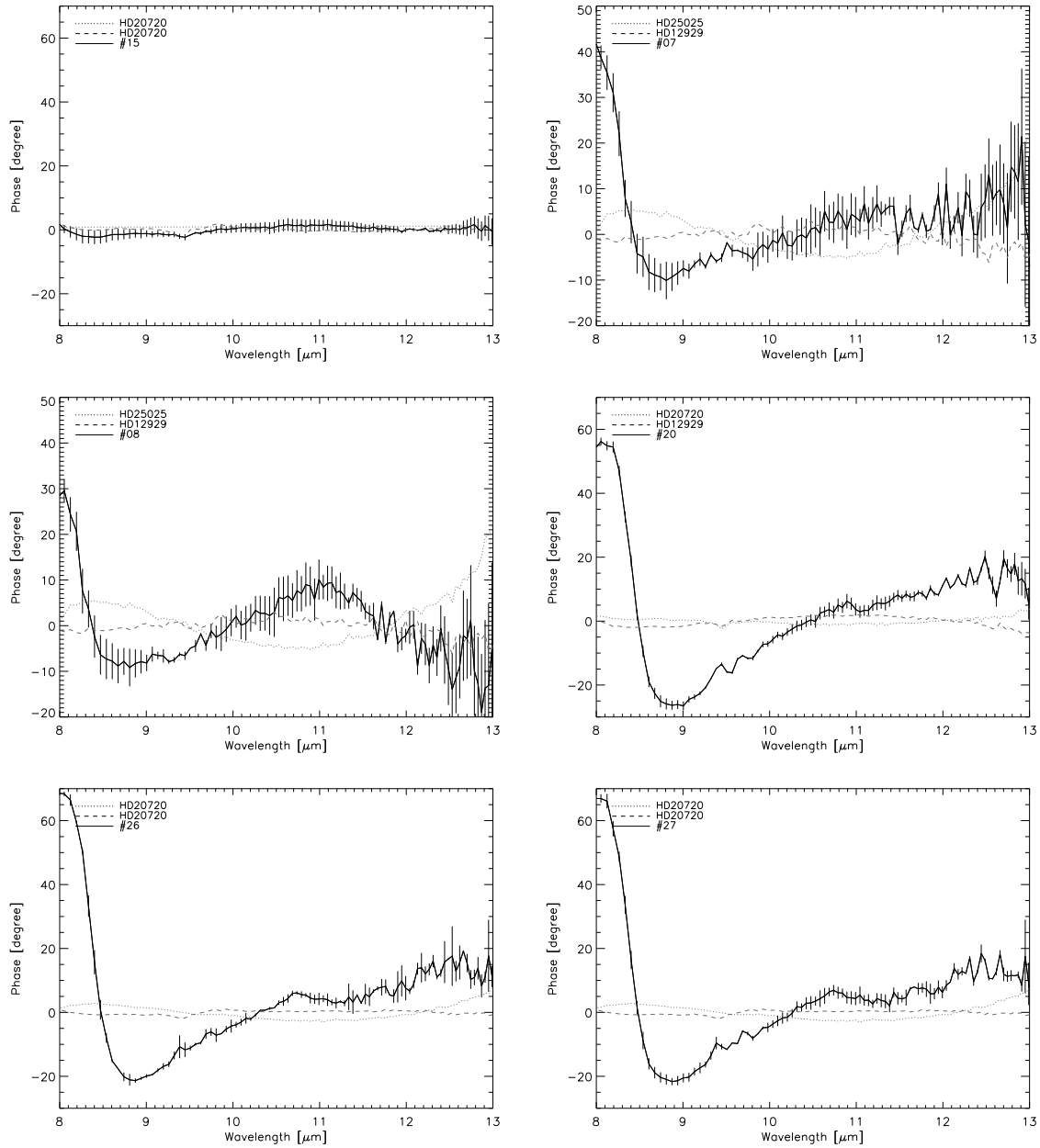

Figure 6.7: Calibrated differential phases versus wavelength of R For (full line) for different baselines and epochs. The dashed and the dotted line show the instrumental phases of the calibrators. The upper left panel shows the differential phases of the observation #14 which was obtained with the 60 m projected baseline. This phase is around zero. All the other panels show the differential phase of the long baselines observations (#07, #08, #20, #26, #28). The signature of deviation from central symmetric structure is clearly visible for all these observations around 8.3 μm. Moreover the observations from 2009 show a more steep jump from the zero differential phase if compared to the ones from 2007 observations. This might be a sign of evolution in time in the asymmetry.

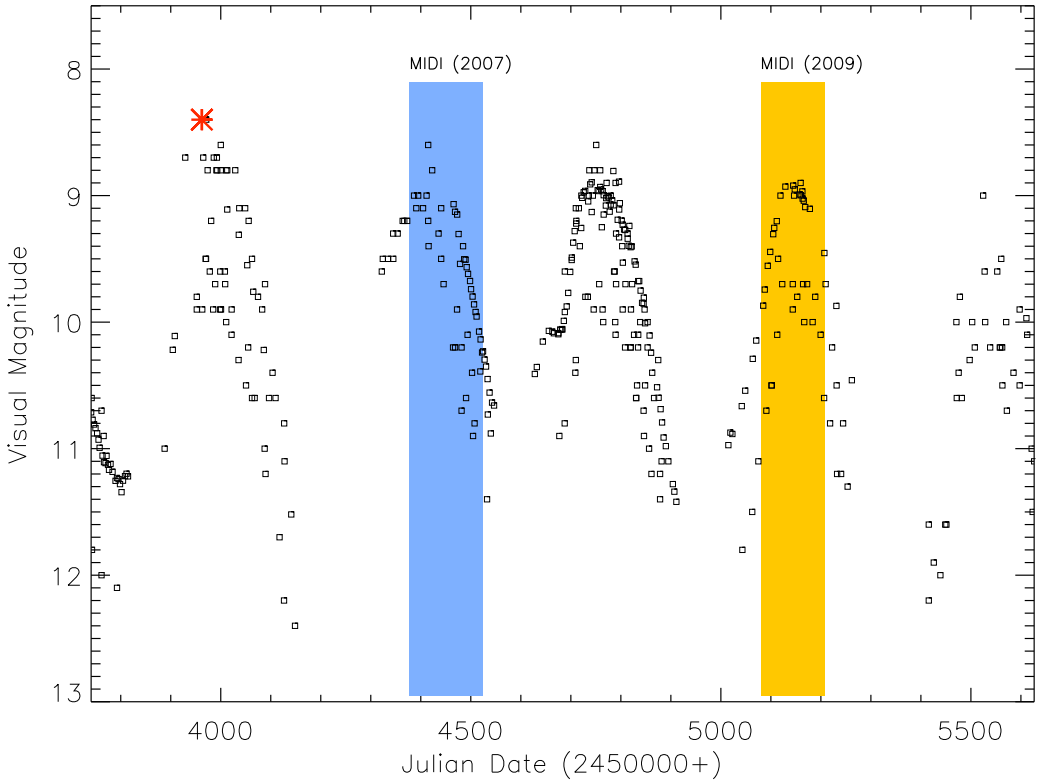

Figure 6.8: Visual lightcurve of R For from AAVSO. The blue and yellow shaded regions mark the period (P80 and P84, respectively) when the MIDI observations have been obtained. The red star indicates the maximum of visual lightcurve assumed as a reference to derive the visual phase for the MIDI observations (see Table 6.1).

the long baselines.
Group(b′) includes observations #28, #29 from 2009 with similar visual phase ($\Phi = 3.22$). These are the only observations with 38 and 45 m baselines.

In Figs. 6.4, 6.5, and 6.6 the visibilities versus wavelength are shown for the various groups and baselines. Eventual intracycle and cycle-to-cycle variability can be studied for selected observations (see Fig. 6.9). The left panel of Fig. 6.9 shows the comparison between the observations #11, #12, and #15. The first two were observed in P80, while the third in P84. The difference in visual phase is very small (0.05) and the first two observations agree quite nicely. The third observation shows a difference over all the wavelength range, such that the visibilities are systematically higher than the previous two. This difference may point to a cycle-to-cycle variability effect. The range of PAs of the complete set of observations coincides with the PA of the observations where the asymmetry is recognised. Therefore, an effect of the asymmetry could be invoked in order to explain the difference.

The right panel of Fig. 6.9 evidences a difference in the observations taken at long baselines. The difference is observed for observations taken within the same pulsation cycle (#20 vs #26 and #27), and within two different cycles (#20, #26 and #27 vs #08). Even though it is clear that there is an evolution from period 2007 to period 2009, and within the period 2009. This variation cannot be interpreted simply as due to pulsation because of the evidence of asymmetric structure detected at long baselines.

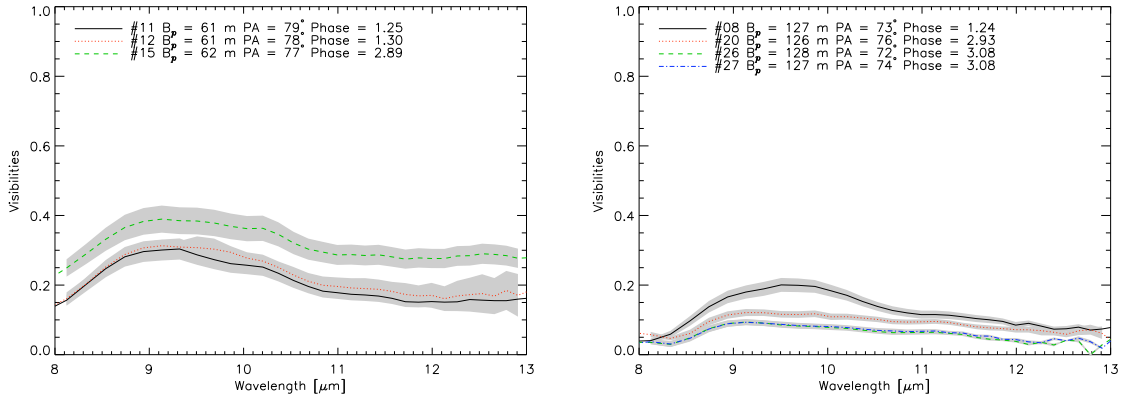

Figure 6.9: Visibilities versus wavelength for a set of observations with the same baselines, position angles, and different visual phase. The shaded region represents the error range.

6.5 Uniform disc diameter vs. wavelength

In order to have more insights into the size change on each baseline, a uniform disc diameter was derived for every baseline (set) and wavelength point. The long baselines were excluded in this analysis because of the asymmetry detected. In Fig. 6.10 the result of this single point fit is shown for the group of 15 and 30 m baselines (upper panels, left and right, respectively), 40-50 and 60 m (middle panels, left and right, respectively). From this

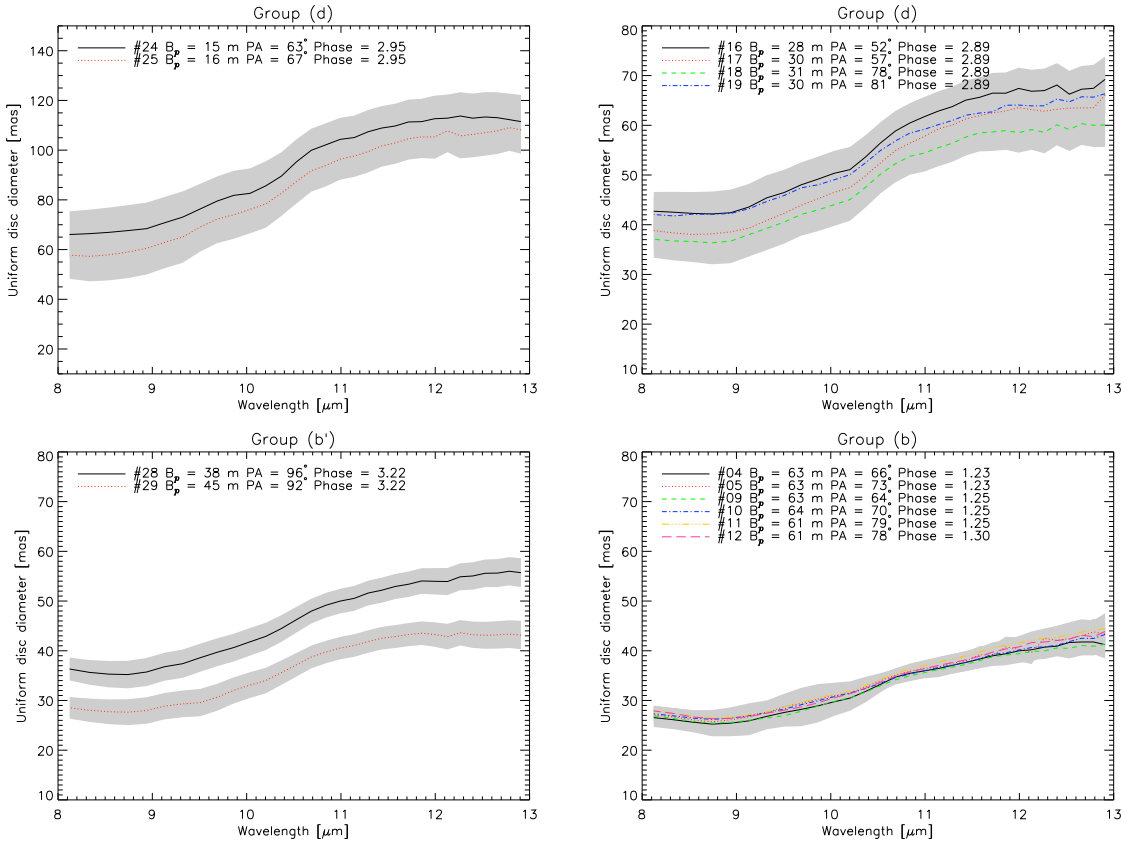

Figure 6.10: Uniform disc diameter versus wavelength for different sets of baselines.

analysis the target appears to be always slightly smaller in the $8-9\,\mu$m region, and larger at longer wavelength. The 15 m baselines (upper left panel) sample the outer part of the dusty envelope, and the UD-diameter ranges between 60 and 120 mas. The UD-diameter derived by the 30 m baseline (upper right panel) observations ranges between $40-70$ mas, while for the 38 and 45 m the UD-diameter is 40-50 and 30-40 mas, respectively. The 60 m baseline observations give a UD-diameter between 30-40 mas, similar to the one derived for the 45 m baseline. The UD-diameter of R For in the near-IR is around 9 mas (K. Ohnaka, private comm.). Assuming this diameter as a reference for the size of the star, then it is possible to infer that the MIDI observations are covering the atmosphere of the star between 2 (including the long baseline observations) and 13 stellar radii.

6.6 Morphological study

One of the aims of this work is to constrain the morphology of the dusty envelope of R For. Departures from spherical symmetry may confirm the scenario envisaged by Whitelock et al. (1997): obscuration by a dust puff ejected in the direction of our line of sight, or more generally a non symmetric mass-loss.

MIDI observations offer two ways to check for potential deviations from central symmetry. The first way, and also the most straightforward one, is described in Sect. 6.6.1 and it involves the differential phase which results from EWS data reduction. If the differential phase shows values which largely differ from zero degrees, this is a clear sign that the target is not centrally symmetric. The second way to check the morphology is to look at the visibility for different position angles, same baselines and, since this object pulsates same pulsation phase. If the visibilities are the same within the errorbar a spherically symmetric morphology can be assumed. This seems to be the case looking at the Figs. 6.4, 6.5, and 6.6. Before proceeding with the interpretation of the data with model atmospheres (Sect. 6.7), three geometrical models have been compared to the visibility curves: uniform disc, gaussian, and uniform disc plus gaussian. This is described in Sect. 6.6.2.

6.6.1 Asymmetry detection through the MIDI differential phases

All the differential phases of the MIDI observations for mid- and short-baselines are very close to zero as can be seen for example in the upper left panel of Fig. 6.7. The differential phase for the long-baseline (~ 125 m) shows a clear signature of departure from spherical symmetry. This signature is the same for all the long baselines observations: #7, #8, #20, #26, #27. The signature is located at $8.3\,\mu$m, as can be seen in Fig. 6.7, in the region where the main contributors of the opacity are C_2H_2+HCN molecules. The long baseline observations are all in a very small range of position angles ($63-76^\circ$), they cover two different cycles, and three different visual phases (0.08, 0.24, 0.93). If the first observation appeared suspicious, the repeated appearence of this signature at separated points in time and always in the same position angle are a comfirmation that we are facing face *the first detection of an asymmetry in a C-Mira star via MIDI differential phases.* Signatures in the

differential phase have been reported for two silicate J-type C-stars[5]: IRAS 18006-3213 by Deroo et al. (2007), Deroo (2007), and BM Gem by Ohnaka et al. (2008). The first silicate J-type C-star, presented by Deroo et al. (2007) shows a signature in the differential phase which is very similar to the one observed for R For. As already described by Deroo (2007), with the applied long baseline one probes the atmosphere where dust emission is strongly (spatially) resolved. The authors speculate that the differential phase signature is due to an offset of the photocenter between the strongly resolved dust region, and the unresolved stellar photosphere. The authors conclude that the offset might be explained assuming a circumbinary disk. The second object, BM Gem presented by Ohnaka et al. (2008) shows a signature between $9 - 11\,\mu$m, a different wavelength region than the other J-type stars (and R For). Ohnaka et al. (2008) interpreted the differential phase signature as due to a circum-companion disk. The fact that the deviations are observed at differing wavelengths for the two objects (BM Gem and IRAS 18006-3213) is interpreted by Deroo and CoIs as an effect of different circumstellar mineralogy, optical thickness and geometry of a possible circumbinary or circum-companion disc.

For R For a possible interpretation involves surface inhomogeneities, but this is unlikely or difficult since the signature in the asymmetry is stable over long time (observed in both observing periods, and always at the same position angle). An argument in favour of this scenario comes from theoretical simulations. It is known from 3D-simulations of supergiants (Chiavassa et al. 2011) that there are two life-scales for convective cells. A short one, (week up to few months) which is observable in the visual, and a longer one (few years) which is observable in the infrared. Therefore, it is possible to speculate that the appearance of a convective cell on the surface of the star may drive an asymmetry in the atmosphere. This is also confirmed by the 3D + 1D simulations of AGB stars from Freytag & Höfner (2008). Another possibility is the interpretation of Deroo et al. (2007), Deroo (2007) or Ohnaka et al. (2008), which involves a circumbinary or circum-companion disc. It has to be noted that a binary component is not automatically another star, it could be also a dusty blob.

Further tests with geometric models of a binary, and a binary plus gaussian distribution will be performed in the near future. Evalueting the MIDI observations in terms of complex geometric structures is rather tricky because of the poor $u - v$ covarage. The final interpretation will only come from interferometric imaging (i.e. second generation VLTI instrument MATISSE, Lopez et al. 2006).

6.6.2 Modeling of the visibility

Due to the signature shown in the differential phases, the long baseline visibilities are discarded from further interpretation with central symmetric geometry and/or with model atmosphere. The geometrical models of the uniform disc, gaussian, and UD+gaussian are tested against the observations. The goal of this test is not to find the best fitting values of the function, but to have a qualitative check of the spherical symmetry hyphothesis for

[5]The silicate J-type C-stars are believed to be binaries. They show silicate emission (not always) that probably originates from a circumbinary or a circumcompanion disc. These objects show enhanced ^{13}C and depletion of s-process elements. They are still far from being understood.

the short baselines (15-60 m). The routines to fit the data with the geometric models are based on the Levenberg-Marquardt algorythm, and they are described in Klotz et al. (2011, subm.).

Uniform Disc

The UD-profile at a given wavelength for different baselines is shown in the panels of Fig. 6.11. The data set from 2009, marked with letter (d), are compared with the UD profile. The points can be identified through the position angle, and every panel corresponds to a wavelength. It is immediately clear that this kind of profile is too steep for reproducing the data, as already predicted by theoretical studies (this thesis Chap. 3; Paladini et al. 2009). The UD function cannot represent the observations, a more elaborate model is needed. The observations of 2007 show a similar behaviour.

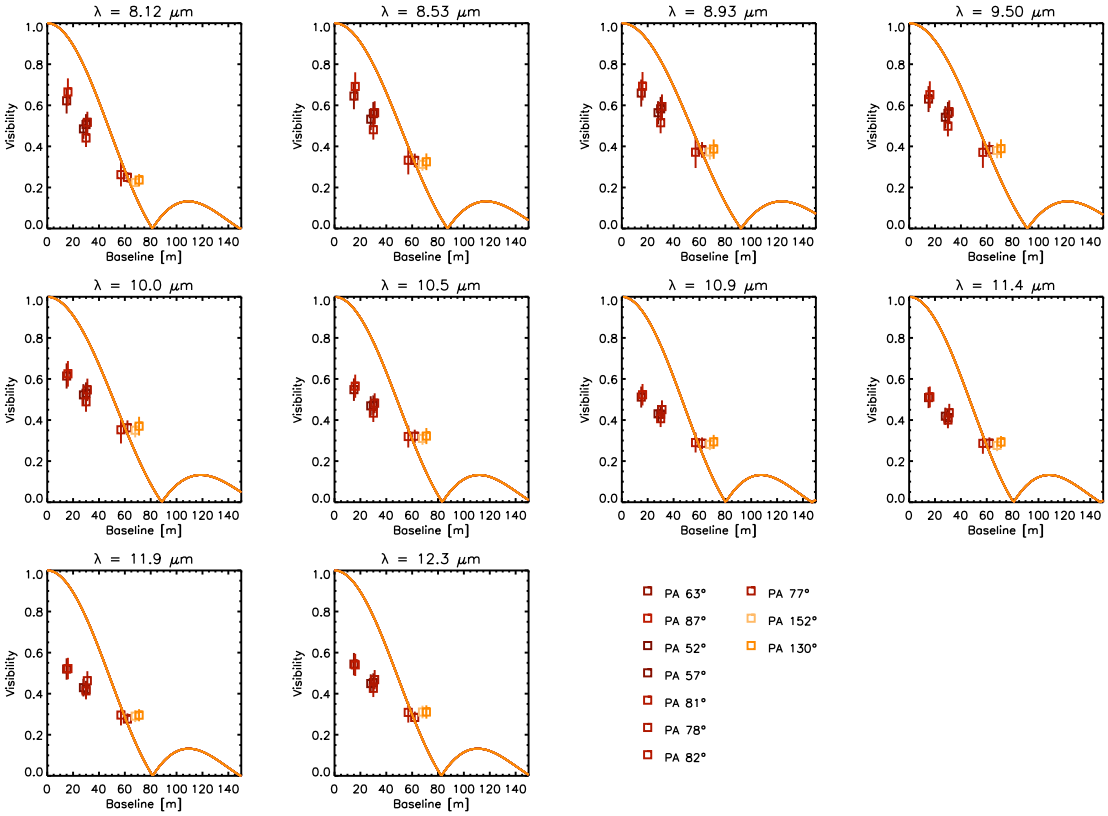

Figure 6.11: Uniform disc model versus MIDI observations of set (d) at different wavelengths. From this plot it is clear that the UD profile cannot represent this set of data.

Gaussian

The Gaussian profile at a given wavelength for different baselines is shown in Fig. 6.12. The plots are arranged as in the previous figure. The data set from 2010-marked with letter (d)-are shown together with the Gaussian profile. The points can be identified through the position angle, and every panel corresponds to one wavelength section in the $N-$band. The

gaussian profile is also not appropriate to reproduce the data.

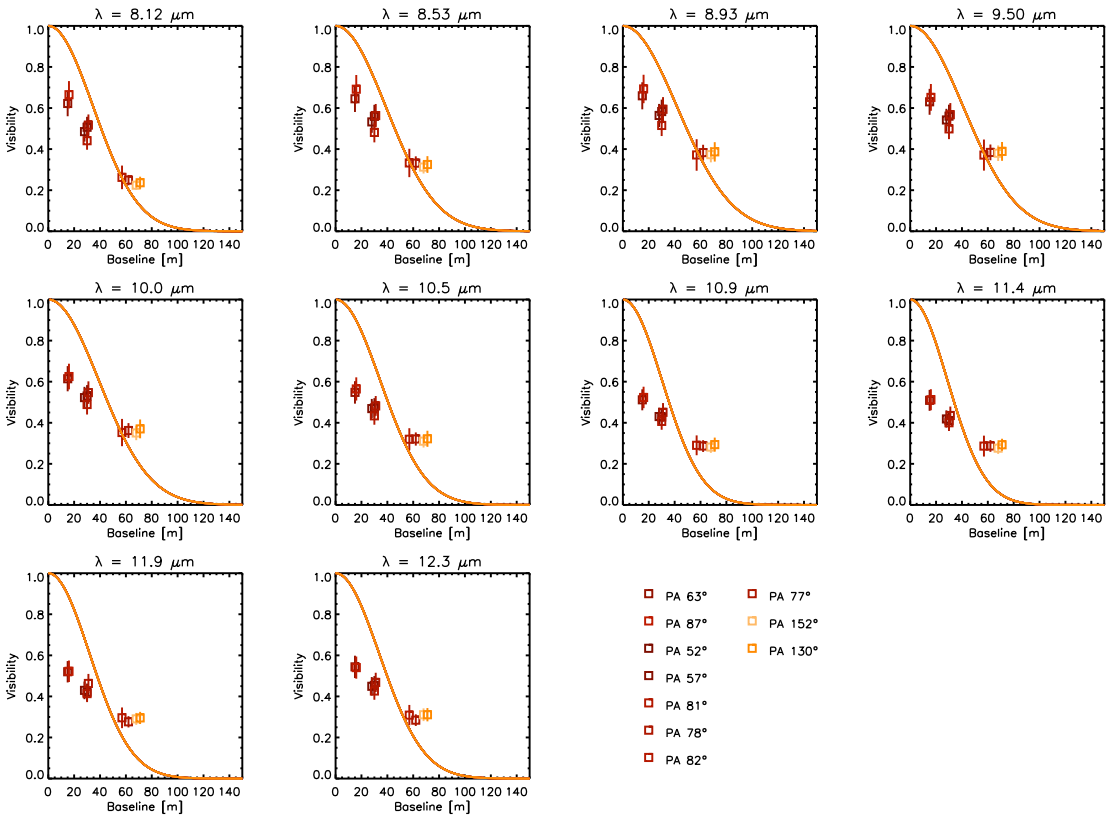

Figure 6.12: Gaussian profile (full line) versus MIDI observations (squared). Every panel corresponds to a wavelength in the N-band. The observations shown correspond to the data sets of 2009 labeled in Table 6.1 with (d). The gaussian is not a good approximation for these data.

Uniform Disc + Gaussian

Since at 10 μm we are deeply in the circumstellar envelope of the star, it is not a bad approximation to think of the central object as a uniform disc plus an envelope made of unresolved clumps of dust (Chap. 3 of this thesis, and Paladini et al. 2009). This envelope might be approximated with a gaussian. The MIDI observations are compared here here with such a composite model of UD + Circular Gaussian. For each wavelength point the FWHM of the envelope and brightness ratio central_star/envelope is derived applying a Levenberg Marquardt fit to the given baseline and position angle. The diameter of the central star is a fixed parameter. The comparison between this geometric model and the MIDI observations is shown in Fig. 6.13. The agreement between the observations and the model is qualitatively good for all the PAs. Therefore, it is possible to conclude that for this set of observations the spherical-symmetric approximation may be best suited.

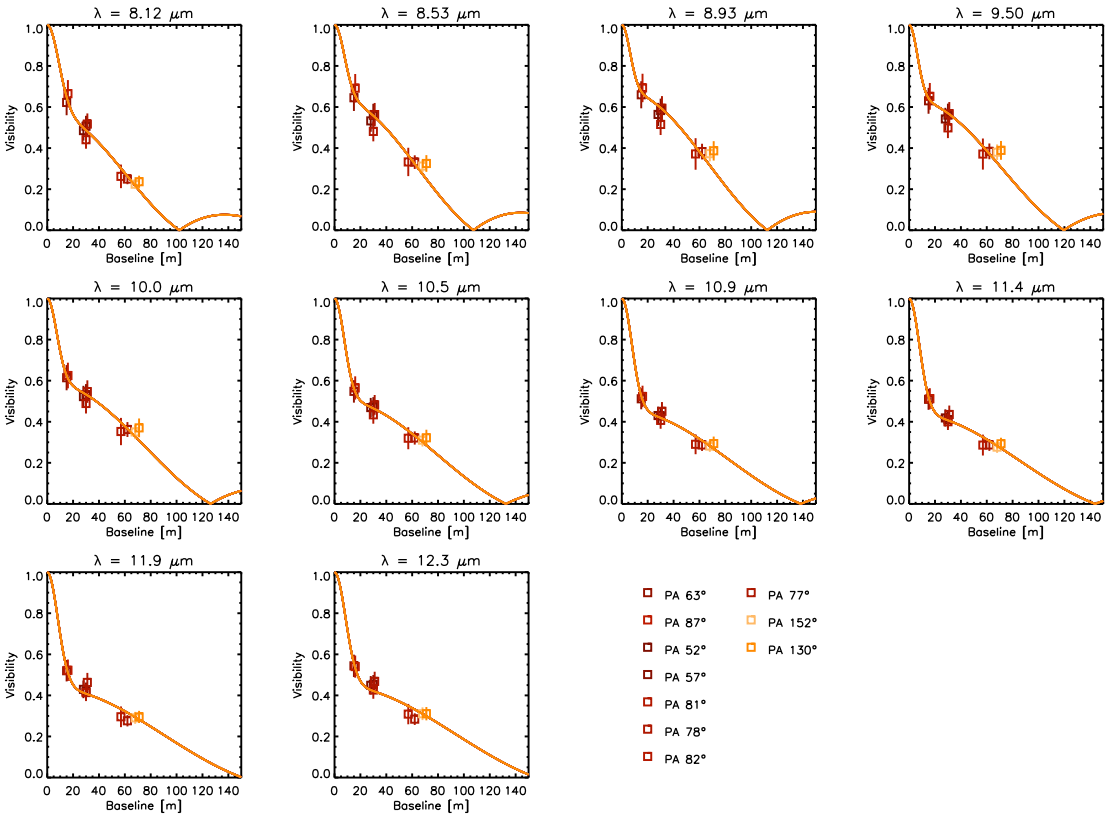

Figure 6.13: Uniform disc plus Gaussian profile (full line) versus MIDI observations (squared) at different wavelengths. This plot shows that the observations of the short baselines (15-60 m) can be represented with a spherical-symmetric model.

6.7 MIDI visibilities vs. dynamic model atmosphere

From the differential phase (Fig. 6.7), the comparison between visibilities observed with the same baselines and visual phase but different position angles (Fig. 6.9), and the comparison with geometrical models (Sect. 6.6.2), it is clear that at least for short baselines (15-60 m) the object does not show evidence of deviation from sphericity. An important step forward in the interpretation of the data is made once the observations are compared not only with geometrical models, but with a model atmosphere.

R For is a C-star with a mass-loss of $\sim 10^{-6}\,M_{\odot}\mathrm{yr}^{-1}$ (Bergeat & Chevallier 2005); it is a Mira variable with $(J-K) \sim 3$ (Whitelock et al. 2006), a visual amplitude of ~ 3 mag and a period of photometric variability of 378 days (Whitelock et al. 1997). The ISO/SWS spectrum of R For (Sloan et al. 2003) plotted in Fig. 6.14 shows, among other features, the SiC dust feature at 11.3 μm. All these informations point to the fact that R For is a dynamic object surrounded by dust, therefore, the dynamic model atmospheres (description in Sect. 6.7 of this thesis; models from Höfner et al. 2003, Mattsson et al. 2010) are the best tool to interpret the MIDI data.

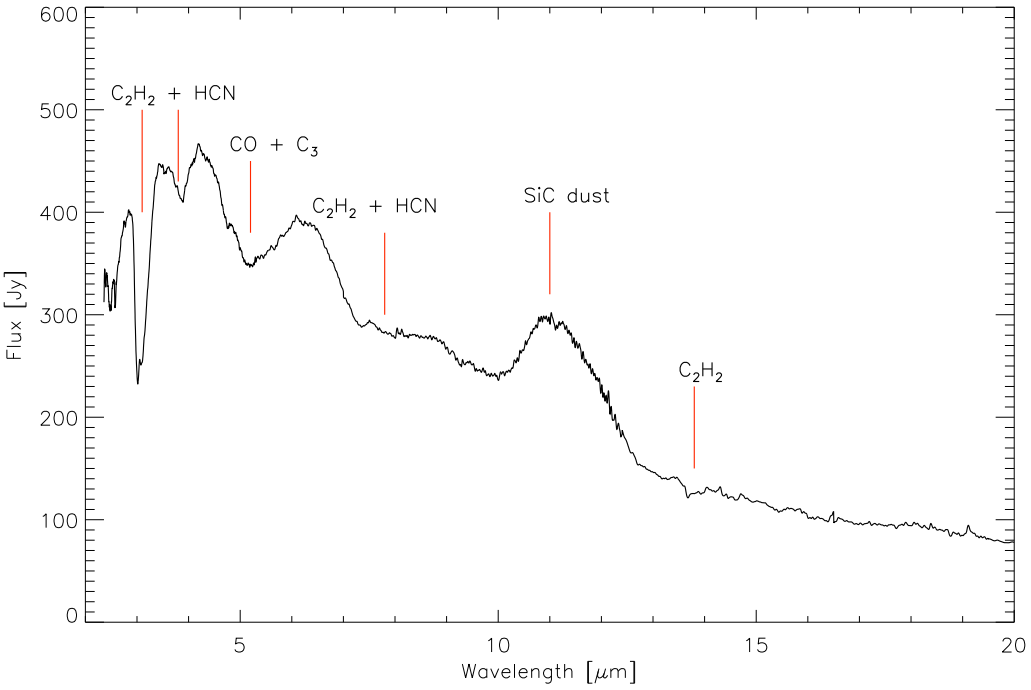

Figure 6.14: The ISO spectrum of R For taken from Sloan et al. (2003).

A set of dynamic models were selected from the grid of models of Mattsson et al. (2010), adopting the parameters from the literature listed in Table 6.3.

Two effective temperature estimates can be found in the literature for this object, but they were not used for the preselection of the parameters for the following reasons. According to Bergeat & Chevallier (2005) R For has an T_{eff} of 2 000 K, while according

Table 6.3: Comparison between the parameters of R For derived from the literature and the parameters of the dynamic model selected for the preliminary comparison.[(a)] Claussen et al. (1987), [(b)] Ohnaka priv. comm., [(c)] Whitelock et al. (1997) ,[(d)] Bergeat & Chevallier (2005).

	L	$T_{\rm eff}$	C/O	P	$<\dot{M}>$
	$[L_\odot]$	[K]		[d]	$[M_\odot\, yr^{-1}]$
l70t26c135u4	7 000	2600	1.35	393	1.0e-06
R For	10 000[(a)]	2470[(b)]	–	387[(c)]	1.0e-06[(d)]

to Lobel et al. (1999) the temperature is 3 200 K. The first temperature is too low, and out of the range covered by the grid of model atmospheres. The second temperature is too high and in the grid there are no models with such a temperature developing stellar winds. Lobel et al. (1999) justified this surprisingly high temperature with the fact that lower temperatures could not reproduce the observations of visual, near-IR photometry plus the corresponding mid-IR IRAS spectrum. The authors compared hydrostatic PHOENIX model atmospheres (models by Allard et al. 1995) with a visual spectrum, in particular with the region where the Na D lines are located, showing that only the model atmosphere with such a high temperature have the gas pressure reduced enough in order not to saturate the lines. In the future it would be very interesting to compare such kind of observations with the new generation of dynamic model atmosphere. A third temperature estimation comes from AMBER data (Ohnaka, priv. comm.). A diameter of 8 mas was measured at 2.2 μm. By combining this measurement with the photometry by Groenewegen et al. (1998) a temperature of 2470 K can be obtained. Based on this last estimation, models with $T_{\rm eff} = 2\,600$ and 2 800 K have been chosen.

The model atmospheres selected from the grid of Mattsson et al. (2010) are presented in Table 6.4. In this paragraph the observations will be compared with one model out of the list of seventeen models, leaving a detailed comparison for the near future. For the preliminary comparison the model with the parameters closest to the one of the star was chosen. This model (l70t26c135u4) is marked in boldface in Table 6.4.

Since the SiC dust is not included in the dynamic calculations, this was added *a posteriori* in the radiative transfer, as already done for R Scl in Sacuto et al. (2011). Many C-stars show a more or less prominent SiC feature in their spectrum centered at 11.3 μm. This feature shows up also in the visibilities (giving a typical S-shape) as can be seen for R Scl in Sacuto et al. (2011), and for V Oph in Ohnaka et al. (2007). In Fig. 6.15 a blue line shows the typical profile of a synthetic visibility based on a hydrostatic model atmosphere (model without dust outflow from the grid of Aringer et al. 2009), a black line shows the synthetic visibility of the DMA l10t26c170u4 without SiC, and a red line the same model but this time with SiC included. Following Sacuto et al. (2011) 10% of the amorphous carbon dust produced in the dynamic calculations is artificially assigned to SiC. The temperature-density structure of the SiC is assumed to be the same as the one of the amorphous carbon.

Intensity and visibility profiles have been calculated using the procedure already described in Paladini et al. (2009). The distances of 680 pc and 770 pc, given by Bergeat

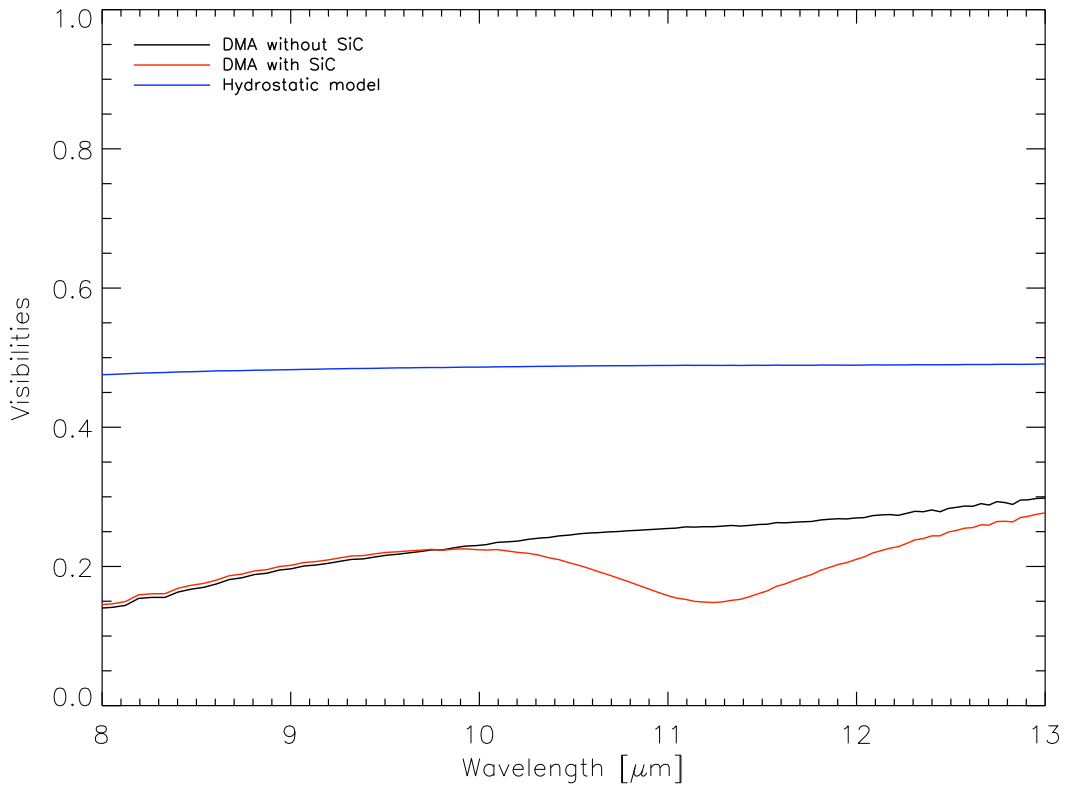

Figure 6.15: Comparison between the visibilities from the model l10t26c170u4 computed with SiC (red line), without SiC (black line), and a dust-free hydrostatic model (blue line).

Table 6.4: Input parameters (luminosity L, mass M, effective temperature $T_{\rm eff}$, C/O, period P, piston velocity $\Delta u_{\rm P}$) and properties of the resulting wind (mass-loss rate $<\dot{M}>$, mean velocity at the outer boundary $< u >$, mean degree of condensation at the outer boundary $< f_{\rm c} >$) for a subset of the grid of dynamic models from Mattsson et al. (2010). The model used for the preliminary comparison is marked in bold-face.

Model	L [$L_\odot$]	M [$M_\odot$]	$T_{\rm eff}$ [K]	C/O	P [d]	$\Delta u_{\rm P}$ [km s^{-1}]	$<\dot{M}>$ [M$_\odot$ yr^{-1}]	$< u >$ [km s^{-1}]	$< f_{\rm c} >$
l70t26c135u4	7 000	0.75	2 600	1.35	393	4.00	$1.0{\cdot}10^{-6}$	0.62	0.22
l70t26c170u4	7 000	0.75	2 600	1.70	393	4.00	$4.1{\cdot}10^{-6}$	1.10	0.20
l70t26c170u6	7 000	0.75	2 600	1.70	393	6.00	$6.0{\cdot}10^{-6}$	1.20	0.21
l70t28c170u4	7 000	0.75	2 800	1.70	393	4.00	$2.5{\cdot}10^{-6}$	1.00	0.14
l70t28c170u6	7 000	0.75	2 800	1.70	393	6.00	$3.8{\cdot}10^{-6}$	1.10	0.17
l70t26c170u2	7 000	1.00	2 600	1.70	393	2.00	$1.4{\cdot}10^{-6}$	1.20	0.20
l70t26c170u4	7 000	1.00	2 600	1.70	393	4.00	$1.7{\cdot}10^{-6}$	6.20	0.17
l70t26c170u6	7 000	1.00	2 600	1.70	393	6.00	$3.4{\cdot}10^{-6}$	10.00	0.22
l70t28c170u6	7 000	1.00	2 800	1.70	393	6.00	$2.1{\cdot}10^{-6}$	14.00	0.24
l70t26c170u6	7 000	1.50	2 600	1.70	393	6.00	$2.7{\cdot}10^{-6}$	11.00	0.31
l10t26c170u4	10 000	1.00	2 600	1.70	524	4.00	$4.9{\cdot}10^{-6}$	10.00	0.16
l10t28c170u4	10 000	1.00	2 800	1.70	524	4.00	$3.7{\cdot}10^{-6}$	13.00	0.17
l10t26c170u6	10 000	1.00	2 600	1.70	524	6.00	$7.2{\cdot}10^{-6}$	11.00	0.18
l10t28c170u6	10 000	1.00	2 800	1.70	524	6.00	$5.4{\cdot}10^{-6}$	15.00	0.21
l10t26c170u4	10 000	1.50	2 600	1.70	524	4.00	$2.2{\cdot}10^{-6}$	15.00	0.25
l10t26c170u6	10 000	1.50	2 600	1.70	524	6.00	$6.8{\cdot}10^{-6}$	21.00	0.47
l10t28c170u6	10 000	1.50	2 800	1.70	524	6.00	$2.2{\cdot}10^{-6}$	14.00	0.22

& Chevallier (2005) and Claussen et al. (1987), were initially assumed. A rescaling to a distance of 350 pc was needed afterwards to fit the level of the observed visibility. In order to derive this value of the distance, the agreement between model and observations at 8 μm was taken as reference. The comparison of the synthetic profiles based on the model l10t26c170u4, with the MIDI observations of R For is shown in Fig. 6.16. The three panels show different sets of observations plotted as errorbars in grey shaded: the upper left panel shows the $\sim$ 15 m projected baseline observations #24 and #25; the upper right panel shows the observations with $\sim$ 30 m projected baseline #17 and #18 and, finally, the lower panel shows the observations with $\sim$ 60 m projected baseline #4, #5, #09, #10, #11, and #12. The red lines are the predicted visibilities for a selected cycle. Every single line corresponds to a different visual phase. The 30 and 60 m baselines observations fits the level of observed visibilities with the new distance, while for the 15 m baselines the model is too small compared to the observations. The region of the $8-9$ μm, where the C_2H_2+HCN molecules dominate, is fitted reasonably well. This was already the case for R Scl in Sacuto et al. (2011). They also recognised the discrepancy observed at longer wavelength for R Scl.

It seems that the synthetic profile is tilted, and the drop of the SiC is too sharp and shifted compared to the observations. This might be ascribed to different reasons, where not only one but a combination of all of them might explain this discrepancy.

- One of the most obvious reasons behind this discrepancy might be that this is not

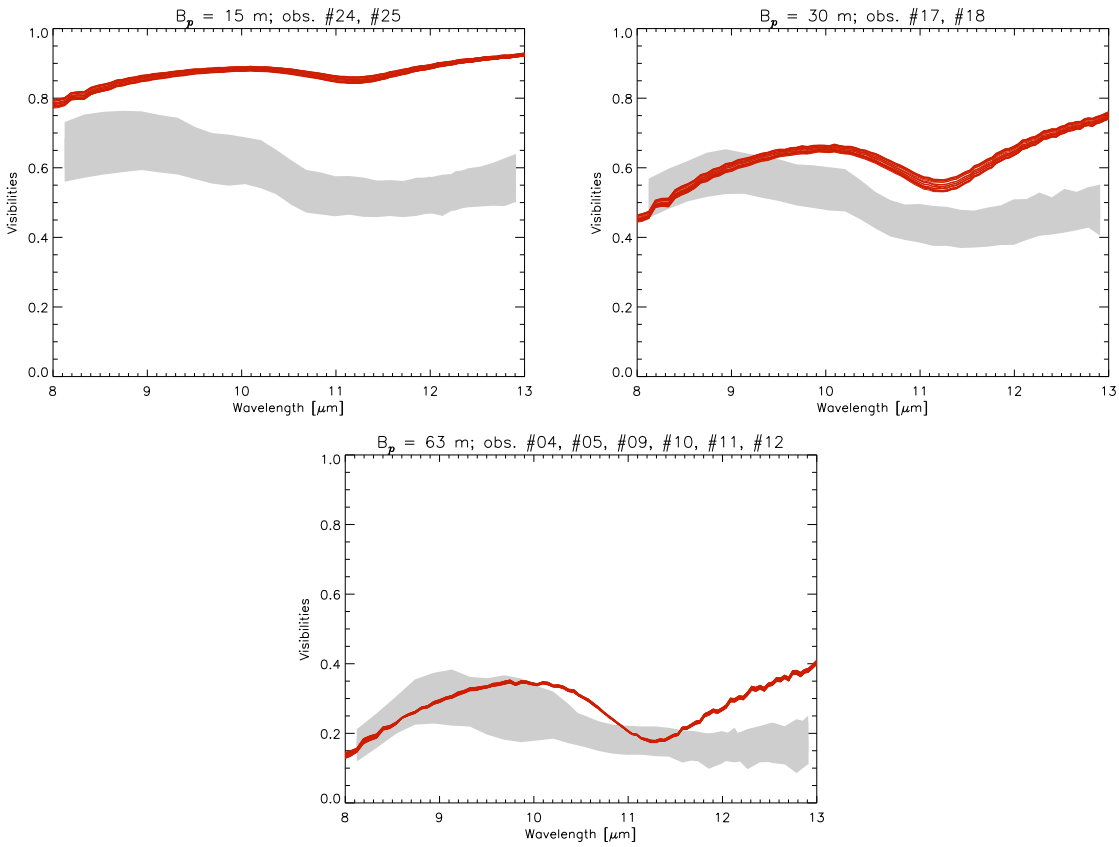

Figure 6.16: Comparison of the synthetic visibilities based on the model l10t26c135u4 (red lines, profiles computed for one period of variability), with the MIDI observations of the 15 m baseline (upper left panel), 30 m baseline (upper right panel), and 60 m baseline (lower panel).

the correct dynamic model. An important complication when dealing with dynamic atmospheres is that they cannot be described by just an effective temperature, gravity and luminosity. There is no obvious link between the characteristics of an observed object and the model parameters, like it is for example in the case of hydrostatic models. An extensive discussion about this topic is presented in Sect. 3 of Nowotny et al. (2005a). The authors point out how dynamic model computations start from an initial hydrostatic model with given parameters (luminosity, mass, effective temperature, C/O), but then pulsation can modify strongly the appearence of the atmosphere, and the parameters do not necessarily correspond anymore to the one of the initial model. Nevertheless, the fact that a similar discrepancy is observed for R Scl points to some other additional reasons to be explored and taken into account.

- The *a posteriori* inclusion of the SiC is made in a non self-consistent way. Although the abundance of SiC is very small, this should contribute partly to the observed discrepancy.

- In the work of Gautschy-Loidl et al. (2004) the authors confine their fit of the ISO spectra with DMAs to wavelength $< 10\,\mu$m. This is because around 13.7 μm there is an absorption feature from C_2H_2+HCN which is filled up by emission in the models. The authors conclude that one of the reasons for the discrepancy might be that in the long-wavelength region of the ISO spectrum one does not see the pure photospheric spectrum. The opacities of these molecules which strongly contribute in this wavelength range (see Fig. 6.17) might be responsible for the discrepancy between models and observations observed for R For. The comparison of the observed spectrum with the synthetic one, foreseen for the near future, will clarify the eventual role of the C_2H_2+HCN molecular opacity in the discrepancy between observations and models.

A comparison of the MIDI observations plus other observables (like the ISO spectrum available for this star), with the grid of DMAs is definitely needed before drawing any further conclusion.

6.8 Discussion

New MIDI observations for the carbon-Mira R For are presented in this work. R For is a well studied object that showed a deep drop in the lightcurve in 1983 (Feast et al. 1984, Le Bertre 1988). Various mechanisms were invoked in order to explain this deep minimum: the interplay of two dynamic processes (pulsation and dust formation) with different time-scales (Winters et al. 1994); dust condensation in an existing shell with a mechanism similar to what happens in the RCrB stars (Feast 1997); an asymmetric dust ejection with the obscuration event due to an eclipse from a dust cloud in the line of sight direction (Whitelock et al. 1997); a disk-like structure already invoked to explain the polarization observations of an object with similarities with R For (Cohen & Smith 1982).

The first scenario is not enough to explain the drop of the lightcurve. The two time-scales discussed by the authors are the pulsation, which is 387 days, and dust formation

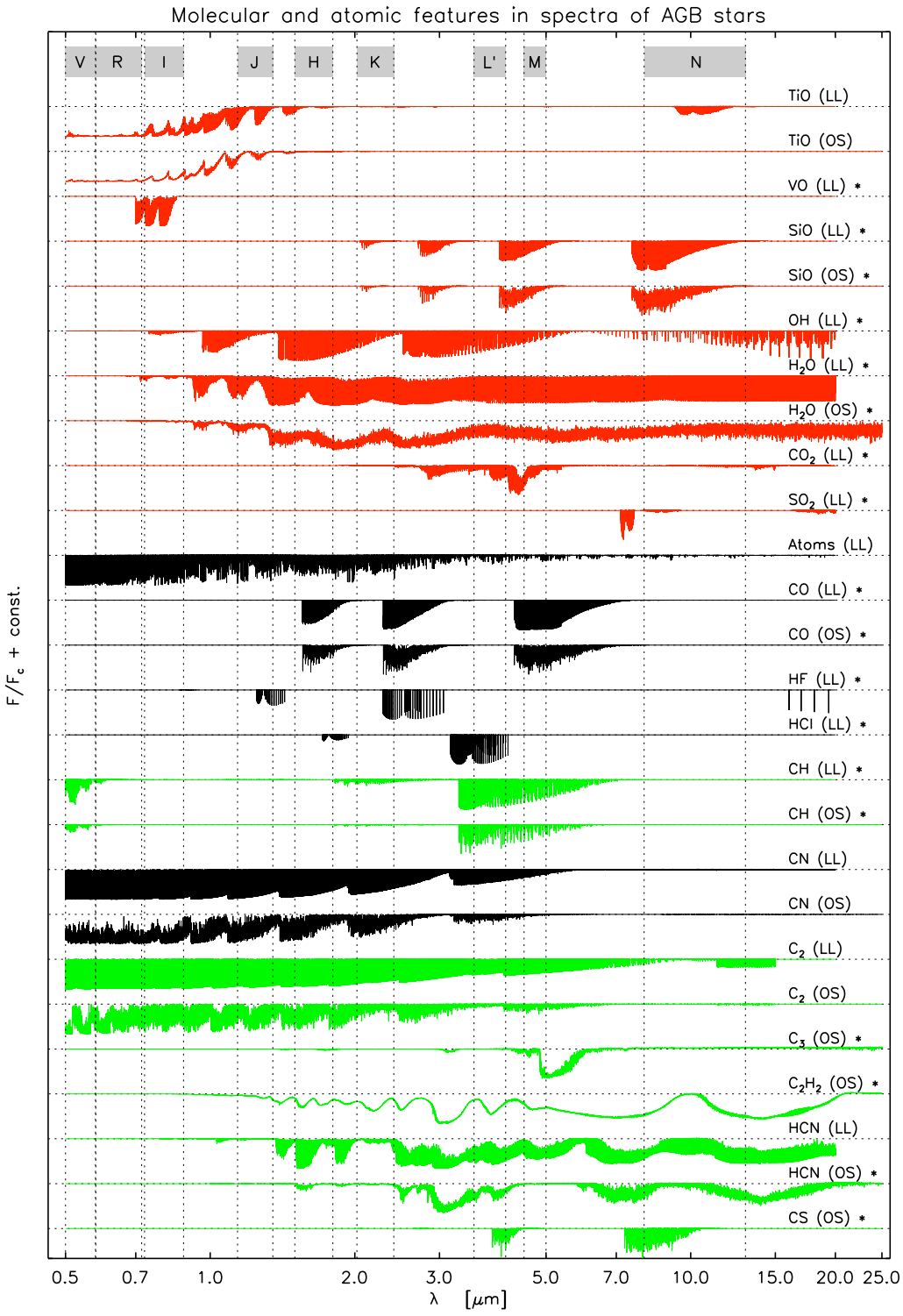

Figure 6.17: Contribution of the different molecular species in the spectrum of an AGB star. In red are shown the molecules that contribute in the chemistry of an O-rich star, in green for the C-rich star, and in black the molecules and atoms tha contribute to both the classes of objects. Adopted from Nowotny (2005).

which is expected to be 4-5 times the pulsation period. If this would the case, then one should observe this kind of event every 4-5 years but this did not happen, as can be seen from the AAVSO lighcurve of the object over the last 100 years (Fig. 6.18)

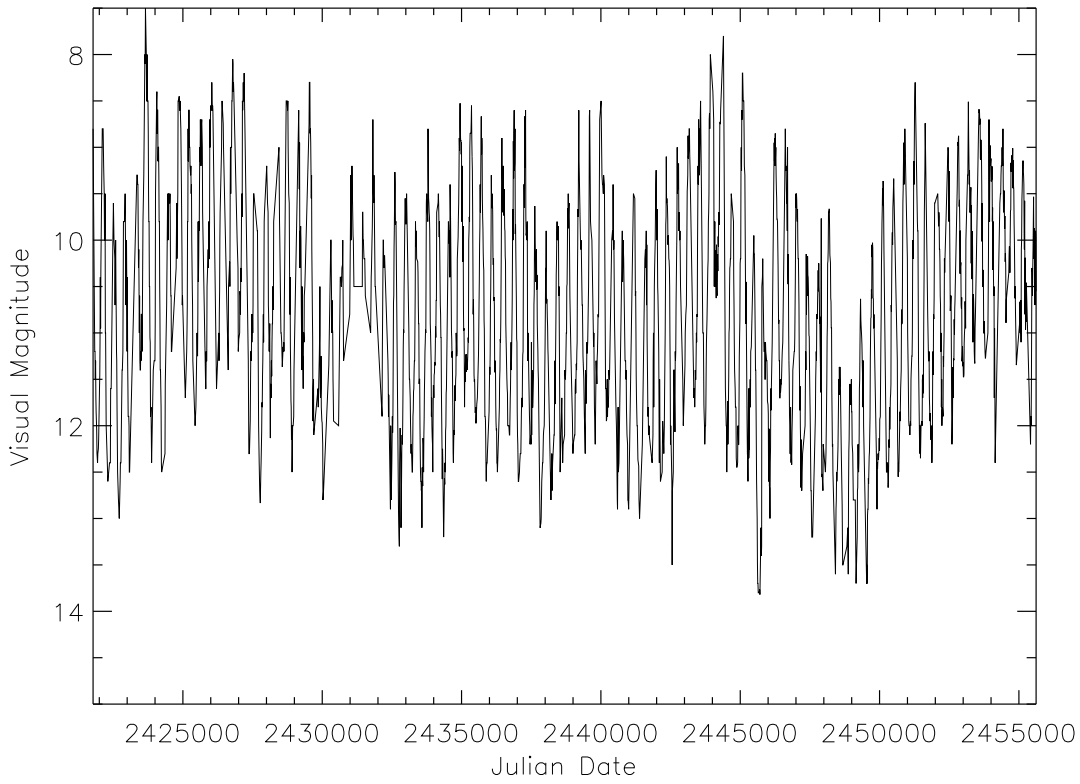

Figure 6.18: AAVSO visual lightcurve of R For over the last 100 years.

The MIDI observations are taken around 20 years after the 1983 event, when the star "already recovered" from the deep minimum, therefore, a connection between these data and the event is rather difficult. What it is very interesting in these new data is the detection of an asymmetry at the very long baselines and at PA$\sim$ 70 degrees. The asymmetry is deep inside the atmospehre of the star, at around 2 stellar radii if the AMBER $K-$band radius is used as a reference. The asymmetry is observed in the same position angle after 2 years, and there is an evidence of evolution, maybe an expansion (see changes in the visibilities in the right panel of Fig. 6.9). Such kind of signature in the differential phase was already detected for two silicate-carbon stars by Deroo (2007) and Ohnaka et al. (2008). In the case of the star of Deroo (2007) the signature shows up in the same wavelength range as the one detected for R For. The authors interpreted this signature as evidence of a circumbinary or circum-companion disc. This might be also the case for R For, confirming the scenario of Cohen & Smith (1982). Another option to explain the asymmetry is that this is a blob of dust moving outwards. Assuming that the star is at the distance of 680 pc, the size of the object is $\sim$ 8 mas, the blob is at 2 stellar radii and is moving with a constant speed of 10 km s^{-1}. After two years the blob would be still within 2-3 stellar radii, therefore,

observable with the same VLTI configuration.

The MIDI observations at short baselines do not show evidence of asymmetry. The morphology of the visibility profile can be interpreted with the one of a central object (UD) surrounded by a Gaussian envelope. There is evidence of cycle-to-cyle variability in the 60 m baseline observations. The variability is also detected in the long baseline observations, but this cannot be attributed completely to pulsation because of the asymmetry detected.

The short baseline observations are compared with a DMA out from the grid of models from Mattsson et al. (2010). A more detailed comparison needs to be done, involving also the use of other observables such as the MIDI spectrum, and the ISO spectrum.

6.9 Outlook

- One of the observables of MIDI which was not used up to now is the spectrum. The MIDI spectrum will be investigated in the coming months in terms of variability. Le Bertre (1992) presented lightcurves of a set of 23 C-stars in the wavelength range $1 - 20\,\mu$m. R For is included in this investigation, and it shows a lightcurve in the $N-$band with an amplitude of variability of less than 0.5 mag. According to this result a significant variability in the MIDI spectrum is not expected. The MIDI spectrum will be also compared with existing ISO observations, as well as with synthetic spectra based on dynamic models.

- Repeated observations with a triangular configuration with very long baselines at VLTI would help to clarify the picture of the asymmetry detected for R For. Unfortunately, at the moment this is not offered. This object is definitely a perfect target for imaging with the second generation VLTI instrument MATISSE (Lopez et al. 2006). This instrument will allow imaging in the $LMN-$bands. In this way, it will be possible to study also the stratification of the C_2H_2+HCN molecules for C-stars, in order to clarify if the corresponding features observed at long wavelengths are photospheric or not.

- Lobel et al. (1999) justifies the surprisingly high temperature determined for R For with the fact that lower temperature models would not fit the Na lines in the visual spectrum. A comparison of the new generation of COMARCS hydrostatic spectra, and of the DMA synthetic spectra with UVES observations would be very interesting in this respect.

- At the time of writing, there are no polarimetric investigations available R For. Considering the detected asymmetry, this kind of study would be very interesting. Spectro-polarimetric time series will allow to detect an eventual change of position angle of the continuum polarization. Such a detection would point to a similarity with the prototype of RCB star, R CrB, where the bipolar geometry includes a thick disk and diffuse dust above the poles (Clayton et al. 1997). This kind of study could help to clarify the geometry of the process of dust formation.

Chapter 7

Conclusion and Prospects

7.1 Results

In this thesis, the optical interferometric technique was applied to investigate different aspects of carbon-rich AGB stars. The link between model atmospheres and interferometric observables was explored, different strategies to determine stellar parameters were investigated, and a detailed analysis of the atmosphere of two variables was presented. The main conclusions of the work can be summarised as follows:

- **Link between models and observables**
  Studying the morphology of the synthetic visibility profiles produced using dynamic model atmospheres, one recognises immediately that the appearance of the corresponding objects are very far from a UD-like shape. This is true especially in the case of models with wind. These kind of models show a strong dependence of the derived radius with wavelength and there are no wavelength regions where one can measure the pure photospheric radius (or an equivalent to the Rosseland radius). All the wavelength ranges explored are contaminated by molecular opacities. In the L- and the N-band the models predict a radius larger than in the JHK-bands. Separating the models observationally on the basis of broad-band interferometric measurements is rather difficult because of the distance uncertainty. This is a consequence of the fact that in the interferometric broad-band observables predicted by the models appear the same, they just scale with the distance. A way to find the correct dynamic model fitting the observations best, would be to combine spectroscopic with interferometric observations, or to use the L-band. The latter, is the wavelength region which is most sensitive to stellar parameter changes, because of the $3\,\mu$m C_2H_2+HCN.

- **Stellar parameters**
  The stellar parameter determination is rather tricky for the class of objects investigated here. Different techniques need to be combined and the main problem is still the lack of accurate distance measurements. The best strategy to constrain the parameters of the investigated object is by using a spectrum in combination with interferometric observations. The perfect situation would be to have a spectrum which covers both the L- and M-band. Jørgensen et al. (2000) demonstrated that these regions strongly constrain the effective temperature and the C/O. In this thesis it is shown that it is still possible to accurately determine temperatures of the weekly-pulsating objects using only the L-band. The power of this combined approach (spectroscopy + interferometry) was shown also for mildly-pulsating objects such as R Scl (Chap. 6 and Sacuto et al. 2011). By combining these two techniques with appropriate model atmospheres the full set of stellar parameters was determined. In the case of the quasi-hydrostatic objects the parameters determined agree rather well with the region of the HR-diagram where the evolutionary models would predict the studied C-stars to be found.

- **Models vs. Observations**
  The combined set of interferometric and spectroscopic observables is a perfect testbed for model atmospheres. From the comparison between hydrostatic models and observations it is shown that dust opacities influence the shape of the spectrum even in the near-infrared. Nevertheless, if the star is only weakly pulsating one the effect on the stellar parameter determination (mainly temperature) is possible, provided that the $L-$band region is available. The MIDI interferometric observations in the 8-9 μm region can be fitted reasonably well with the dynamic model atmospheres. Beyond 10 μm the slope of the synthetic visibility seems to be tilted in comparison to the observations. Various explanations are suggested for this discrepancy. In the case of R Scl the assumption of a complete dynamic coupling of gas and dust, and the small particle approximation for the grain opacities are among the likely reasons of the discrepancy. In the recent theoretic work of Mattsson & Höfner (2011) the authors showed that in some critical cases close to the thresholds of dust-driven outflows, the small particle approximation tends to underestimate the mass-loss rates and wind velocities. It is interesting to note that the discrepancy at long wavelength in the MIDI ranges appears not only for objects with low mass-loss (i.e. R Scl). Among the preliminary results of Chap. 6 there is the indication that even for a high mass-loss star like R For the discrepancy between models and observations goes in the same direction. If this indication will be confirmed in the detailed analysis of the data, one may need to search for another explanation than the small-particle approximation, e.g., the opacities of C_2H_2.

- **Morphology of the atmosphere**
  The MIDI observations of R For showed clear evidence of a deviation from central-symmetry in the inner part of the atmosphere of the star ($\sim 1.5 - 2$ stellar radii). It is not possible with the available data to discriminate among different scenarios, (but

only giving educated guesses). The two scenarios that may explain the asymmetry are the presence of a circum-binary or circum-companion disc, or the presence of a very large dust cloud. The latter scenario might be supported by theoretical calculations of Freytag & Höfner (2008). Only further observations with wider $u - v$ coverage, and similar data for a statistically significant sample of stars will allow to answer this question. Ultimately, optical interferometric imaging might provide the solution. Outside of this region, between 4 and 8 stellar radii, the atmosphere does not seem to show any evidence of asymmetry. This is the case for both R Scl and R For, and it justifies the use of the spherical-symmetric model atmospheres.

7.2 Future Plans

In this thesis the model atmospheres were compared with broad-band near-IR and mid-IR spectrally-dispersed interferometric observations. A very important testbed for the available theoretical models (i.e. for our knowledge of the physics behind several phenomena) will be to compare the observations with spectrally-dispersed near-IR observations. In this wavelength region it is possible to study the molecular layers and how they are influenced by the pulsation. During the last year our team successfully applied for VLTI/AMBER and MIDI observations of a sample of C-rich AGB stars with different mass-loss rates. The aim of the work is to improve our understanding of how the mass-loss depends on basic stellar properties. Another more ambitious aim is to provide a more profound basis to check/calibrate the evolutionary tracks for the thermally-pulsing AGB phase. Such kind of work extended to other spectral types (M- and S-type AGB stars, but earlier spectral type as well) will provide strong constraints for the evolutionary models.

Optical interferometry showed already to offer the capability to dig inside the atmosphere of the star, unveiling the characteristics of its layers. One of the unanswered questions concerning the mass-loss process is the geometry. Thanks to the accuracy of the new generation of ground and space facilities, the time is mature for a combined effort in order to answer questions as the following: Is the dusty mass-loss an episodic process? At which height in the atmosphere can asymmetries develop? How does this change with the evolutionary phase of the star? We started a project that foresees the synergy of MIDI, VISIR and Herschel/PACS. A sub sample (Fig. 7.1) of the objects studied by Herschel satellite in the frame of the guaranteed time key program MESS (Groenewegen et al. 2011) was selected for observations. The targets are AGB stars with different chemistry and variability type. This combined effort will map the atmospheres between 2 and 10 stellar radii with MIDI, and between 25 and 2 500 stellar radii with VISIR.

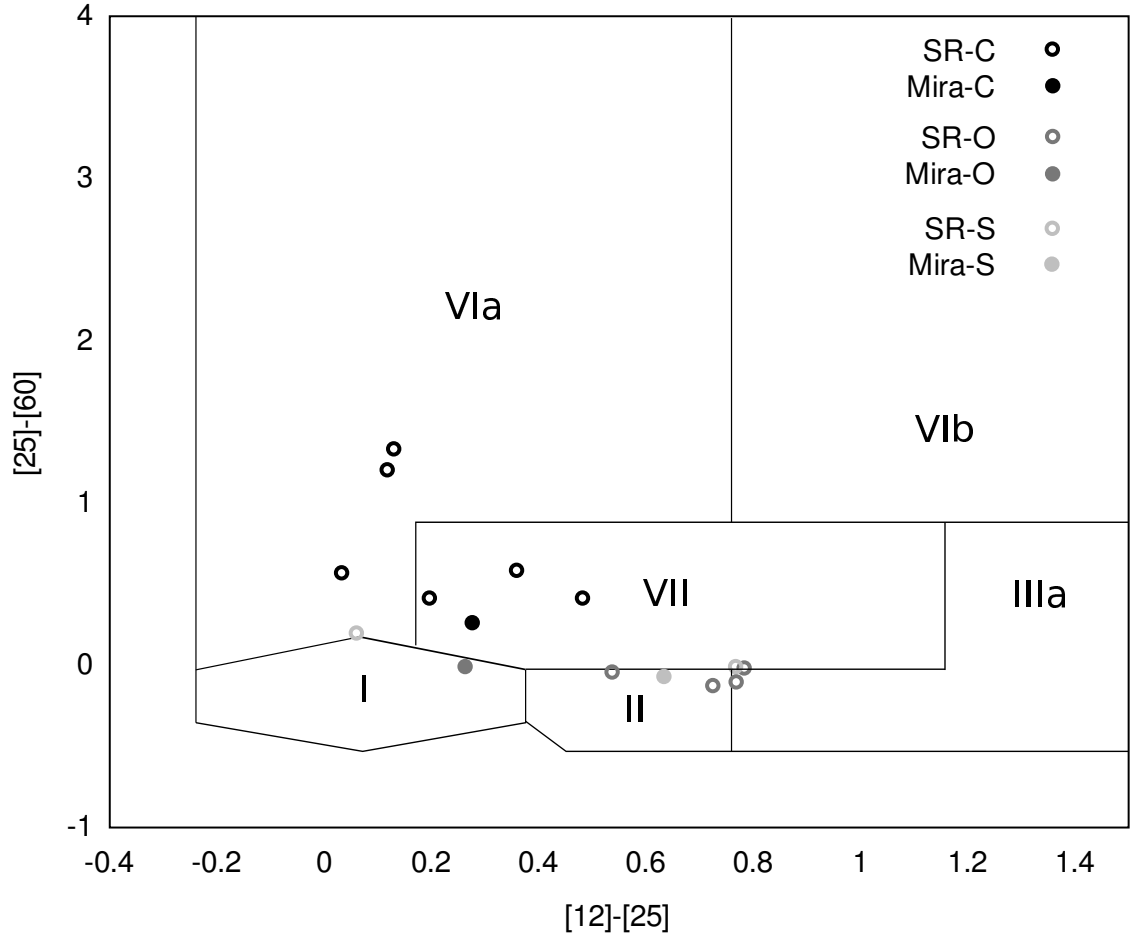

Figure 7.1: Subset of the targets observed by the Herschel MESS program in the IRAS two-colour diagram (van der Veen & Habing 1988). According to the evolutionary tracks the objects evolve from the bottom left to the upper right box. **I**: oxygen-rich non-variable stars with no extended circumstellar shells are expected. **II:** the objects are surrounded by young oxygen-rich shells. **IIIa:** the shells are more evolved. **IVa:** most of the carbon-rich objects with relatively cold dust are here located. **VIb:** the objects with hot dust close to the star, and cold dust at larger diameters are here located. **VII** typical variables with more evolved C-rich shells.

Appendix

Statistical approach at temperature determination

In order to assign an observed spectrum to one out of a sample of available models, a statistical approach is employed: each model represents a Gaussian-shaped sandheap the width of which (in terms of standard deviation) is determined by the point-to-point scatter p of the spectrum. The height of the sandheaps can be adjusted by statistical weights. Thus, the shape of the nth sandheap is given by the Gaussian probability density function

$$G\left(d_n\right) = \exp\left(\frac{d_n^2}{2p^2}\right) . \tag{7.1}$$

The "distance" d_n between the observed spectrum and the model is the rms deviation between the observed and the synthetic spectrum. The statistical analogy of the model assignment is to pick out a single grain of sand at the given distances from the synthetic spectra. Now the question is, how high is the probability of the picked grain to belong to the nth sandheap?

The total number of available grains at the selected position is determined by the sum of densities for all N models,

$$\nu = \sum_{n=1}^{N} G\left(d_n\right) , \tag{7.2}$$

which represents our normalisation condition. Thus, the relative amount of grains belonging to model n – and hence the probability of th e observed spectrum to represent this model – evaluates to

$$\mathrm{Pr}_n = \frac{G\left(d_n\right)}{\nu} . \tag{7.3}$$

In the context of our application, the only parameter of interest is the effective temperature, whence the temperature interval covered by the models is divided into a set of intervals I_t, $t = 1, ..., \tau$. Because the number of models belonging to such a temperature bin is not unique, the marginal probability density of temperature has to be corrected for this bias. In the sandheap metaphor, we would have to provide each temperature interval to be represented by a unique number of grains, and the probability of our spectrum to be assigned to the temperature interval I_t evaluates to the weighted sum of individual model assignment probabilities

$$\mathrm{Pr}\left(I_t\right) = \frac{m_t^{-1} \sum_{n=1}^{m_t} \mathrm{Pr}_n\left(I_t\right)}{\sum_{i=1}^{\tau} m_i^{-1} \sum_{k=1}^{m_i} \mathrm{Pr}_k\left(I_i\right)} , \tag{7.4}$$

m_t and denoting the number of models belonging to the interval I_t.

This normalisation is demonstrably valid, because the integral probability for all temperatures evaluates to

$$\sum_{t=1}^{\tau} \Pr\left(I_t\right) = \frac{\sum_{t=1}^{\tau} m_t^{-1} \sum_{n=1}^{m_t} \Pr_n\left(I_t\right)}{\sum_{i=1}^{\tau} m_i^{-1} \sum_{k=1}^{m_i} \Pr_k\left(I_i\right)} = 1\,. \tag{7.5}$$

Bibliography

Abia, C., & Isern, J. 1997, MNRAS, 289, 11

Abia, C., Domínguez, I., Gallino, R., et al. 2002, ApJ, 579, 817

Abia, C., Cunha, K., Cristallo, S., et al. 2010, ApJ, 715, 94

Alksnis, A., Balklavs, A., Dzervitis, U., et al. 2001, "General Catalogue Of Galactic Carbon Stars", Baltic Astronomy, 10, 1

Allard, F., Lawlor, T., Alexander, D. R., & Hauschildt, P. H. 1995, AAS, 18710311

Amôres, E. B., & Lépine, J. R. D. 2005, AJ, 130, 659

Andersen, A. C., Höfner, S., & Gautschy-Loidl, R. 2003, A&A, 400, 981

Aringer, B., Jørgensen, U. G., & Langhoff, S. R. 1997, A&A, 323, 202

Aringer, B. 2000, Ph.D. Thesis, University of Vienna

Aringer, B., Nowotny, W., & Höfner, S. 2008, "Perspective in Radiative Transfer and Interferometry", S. Wolf, F. Allard and Ph. Stee (eds), EAS Pubblications Series 28, 67-74

Aringer, B., Girardi, L., Nowotny, W., Marigo, P., & Lederer, M. T. 2009, A&A, 503, 913

Aufdenberg, J., Ridgway, S., & White, R. 2009, in astro2010: The Astronomy and Astrophysics Decadal Survey, Science White Papers, astro2010S, 8

Bagnulo, S. 1996, Ph.D. Thesis, Belfast University

Bagnulo, S., Doyle, J. G., & Andretta, V. 1998, MNRAS 296, 545

Baschek, B., Scholz, M., & Wehrse, R. 1991, A&A, 246,374

Barthes, D., Chenevez, J., & Mattei, J. A. 1996, AJ, 111, 2391

Beichman, C. A., Neugebauer, G., Habing, H. J., Clegg, P. E., & Chester, T. J. 1988, NASAR, 1190, 1

Bergeat, J., Knapik, A., & Rutily, B. 2002, A&A, 390, 967

Bergeat, J., & Chevallier, L. 2005, A&A, 429, 235

Bessel, M. S., Wood, P. R., LLoyd Evans, T. 1983, MNRAS, 202, 59

Bessel, M. S., & Brett, J. M 1988, PASP100, 1134

Bessel, M. S., Brett, J. M., Scholz, M., & Wood, P. R. 1989, A&A, 213, 209

Bessel, M. S., Scholz, M., & Wood, P. R. 1996, A&A, 307, 481

Boden, A. F., Colavita, M. M., van Belle, G. T., & Shao, M. 1998, SPIE, 3350, 872

Boden, A. F., et al. 1999, ApJ, 515, 356

Boffin, H.M.J., Abia, C., & Rebolo, R. 1993, A&AS, 102, 361

Bordé, P., Coudé du Foresto, V., Chagnon, G., Perrin, G., 2002, A&A 393, 183

Bracewell, R. N. 1965, "The Fourier Transform and its Applications", McGraw-Hill, New York

Bright, S. N., Chesneau, O., Clayton, G. C., et al. 2011, MNRAS, 414, 1195

Chagnon, G., Mennesson, B., Perrin, G., et al. 2002, AJ, 124, 2821

Cardelli, J.A., Clayton, G.C., & Mathis, J.S. 1989, ApJ, 345, 245

Cavanagh, B., Hirst, P., Jenness, T., et al. 2003, ASPC, 295, 237

Chesneau, O., Meilland, A., Rivinius, T., et al. 2005, A&A 435, 275

Chesneau, O. 2007, New Astron. Rev., 51, 666

Chiavassa, A., Pasquato, E., Jorissen, A., et al. 2011, A&A, 528, 120

Claussen, M. J., Kleinmann, S. G., Joyce, R. R., & Jura, M. 1987, ApJS, 65, 385

Clayton, G. C., Bjorkman, K. S., Nordsieck K. H., Zellner, N. E. B., & Schulte-Labeck, R. E. 1997, ApJ, 476, 870

Cohen, M., & Schmidt, G. D. 1982 ApJ, 259, 693

Cohen, M., Walker, R. G., Carter, B., et al., 1999, AJ, 117, 1864

Colavita, M. M., et al. 1999, ApJ, 510, 505

Coudé du Foresto,V., Perrin, G., Ruilier, C., et al. 1998, SPIE, 3350, 856

Cruzalèbes, P., Jorissen, A., Sacuto, S., & Bonneau, D. 2010, A&A 515, A6

Cutri, R. M., Skrutskie, M. F., van Dyk, S., et al. 2003, in The IRSA 2MASS All-Sky Point Source Catalog, NASA/IPAC Infrared Science Archive

Davis, J., Tango, W. J., Booth, A. J. 2000, MNRAS, 318, 387

Dehaes, S., Groenewegen, M. A. T., Decin, L., Hony, S., et al., 2007, MNRAS 377, 931

Delplancke, F., 2008, New Astron. Rev., 52, 199

Delplancke, F., Mosoni, L. 2009, New Astron. Rev., 53, 277

Deroo P. 2007, PhD thesis, University of Leuven

Deroo, P., Van Winckel, H., Verhoelst, T., et al. 2007, A&A, 467, 1093

Dyck, H. M., van Belle, G. T., & Benson, J. A. 1996, AJ, 112, 294

Epchtein, N., Le Bertre, T., Lepine, J. R. D. 1990, A&A, 227, 82

Eglitis, I., & Eglite, M. 1995, Ap&SS, 229, 63

Eisenhauer, F., Perrin, G., Brandner, W. 2008, SPIE, 7013, 69

Erspamer, D., & North, P. 2003, A&A, 398,1121

Feast, M. W., Whitelock, P. A., Catchpole, R. M., Roberts, G., & Overbeek, M. D. 1984, MNRAS, 211, 331

Feast, M. W. 1997, MNRAS, 285, 339

Feast, M. W. 1999, IAUS, 191, 109

Fitzpatrick, E. L. 1999, PASP 111, 63

Fleischer, A. J., Gauger, A., & Sedlmayr, E. 1992, A&A, 266, 321

Freytag, B., Steffen, M., & Dorch, B. 2002, Astron Nachr., 323, 213

Freytag, B., Steffen, M., Wedemeyer-Böhm, S., & Ludwig, H.-G. 2004, CO5BOLD User Manual, `http://www.astro.uu.se/~bf/co5bold_main.html`

Freytag, B., & Höfner, S. 2008, A&A, 483, 571

Gail, H. P., & Sedlmayr, E. 1988, A&A, 206, 153

García-Hernández, D. A., García-Lario, P., Plez, B., et al., 2007, A&A, 462, 711

Gauger, A., Gail., H. P., & Sedlmayr, E. 1990, A&A, 235,245

Gautschy-Loidl, R., Höfner, S., Jørgensen, U. G., & Hron, J. 2004, A&A, 422, 289 (GL04)

Glindemann, A. 2011, in "Principles of Stellar Interferometry", Astronomy and Astrophysics Library, Springer-Verlag Berlin Heidelberg

Goebel, J. H., Bregman, J. D., Wittenborn, F. C., & Taylor, B. J. 1981, ApJ, 246, 455

Goorvitch, D. & Chackerian, Jr. C. 1994, ApJS, 91, 483

Groenewegen, M. A. T., & Whitelock, P. A. 1996, MNRAS, 281, 1347

Groenewegen, M. A. T., Whitelock, P. A., Smith, C. H., & Kerschbaum, F. 1998, MNRAS, 293, 18

Groenewegen, M. A. T., Waelkens, C., & Barlow, M. J, et al. 2011, A&A, 526, 162

Gustafsson, B., Bell, R. A., Eriksson, K., & Nordlund, Å. 1975, A&A, 42, 407

Gustafsson, B., Eriksson, K., Kiselman, D., Olander, N., & Olofsson, H. 1997, A&A 318, 535

Gustafsson, B., Edvardsson, B., Eriksson, K., et al. 2008, A&A, 486, 951

Habing, H. J., & Olofsson, H. editors 2004, Asymptotic Giant Branch Stars

Harris, G. J., Tennyson, J., Kaminsky, B. M., Pavlenko, Y. V., & Jones, H. R. A. 2006, MNRAS, 367, 400

Hauschildt, P. H., Allard, F., Ferguson, J., Baron, E. ,& Alexander, D. R. 1999, ApJ, 525, 871

Henden, A. A., 2009, Observations from the AAVSO International Database, priv. comm.

Herbst, T. M., Ragazzoni, R., Andersen, D., et al. 2002, SPIE, 4838,110

Hofmann, K.-H., Scholz, M., & Wood, P. R. 1998, A&A, 339, 846

Höfner, S., & Dorfi, E. 1997, A&A, 319, 648

Höfner, S., Gautschy-Loidl, R., Aringer, B., & Jørgensen, U. G. 2003, A&A, 399, 589

Höfner, S. 2005, "13th Cambridge Workshop on Cool Stars. Stellar Systems and the Sun", ESASP, 560 ed. F. Favata, G. A. J. Hussian and B. Battrick, p.335

Höfner, S. 2007, Why Galaxies Care About AGB Stars, ed. F. Kerschbaum, C. Charbonnel and R. F. Wing, ASP. Conf. Ser., 378, 145

Höfner, S. 2008, A&A, 491, 1

Höfner, S. 2009, "Cosmic Dust - Near and Far", Th. Henning, E. Grün, J. Steinacker (eds.) ASP Conf. Ser., 414, 3

Houk, N. 1963, AJ, 68, 253

Hron, J., Loidl, R., & Höfner, S., et al. 1998, A&A, 335, L69

Hron, J., Aringer, B., Nowotny, W., & Paladini, C. 2008, "Evolution and Nucleosynthesis in AGB stars", ed. Guandalini, R., Palmerini, S., & Busso, M., AIP Conference Proceedings, Volume 1001, pp.185-192

Huang, R. Q., & Yu, K. N. 1998, Stellar Astrophysics

Hughes, S. M. G., & Wood, P. R. 1990,A&A, 99, 784

Iben, I., & Renzini, A. 1983, ARA&A, 21, 271

Ireland, M. J., Scholz, M., & Wood, P. R. 2004, MNRAS, 352, 318

Ireland, M. J., Scholz, M., Tuthill, P. G., & Wood, P. R. 2004, MNRAS, 355, 444

Ireland, M. J., Mérand, A., ten Brummelaar, T. A., et al. 2008, in Optical and Infrared Interferometry, Proc. SPIE, 7013, 701324

Isaak, K., Priddey, R. S., McMahon, R. G., et al. 2002, MNRAS, 329, 149

Ivezić, Z., & Elitzur, M. 1997, MNRAS, 287, 799

Ivezić, Z., Nenkova, M., & Elitzur, M. 1999, "User Manual for DUSTY"

Jacob, A. P., & Scholz, M. 2002, MNRAS, 336, 1377

Jaffe, W. 2004, Proc. SPIE, 5491, 715

Jørgensen, U. G., Almlof, J., Siegbahn, P. E. M. 1989, ApJ, 343, 554

Jørgensen, U. G., Johnson, H. R., & Nordlund, Å. 1992, A&A, 261, 263

Jørgensen, U. G. 1997, in "Molecules in Astrophysics: Probes and Processes", ed. E. F. van Dishoeck, IAU Symp. 178 (Kluwer), 441-456

Jørgensen, U. G., Hron, J., & Loidl, R. 2000, A&A, 356, 253

Jorissen, A., Frayer, D. T., Johnson, H. R., Mayor, M., & Smith, V. V. 1993, 271, 463

Joyce, R. R. 1998, AJ, 115, 2059

Kerschbaum, F., Lazaro, C., & Habison, P. 1996a, A&AS, 118, 397

Kerschbaum, F., Olofsson, H., & Hron, J. 1996b, A&A, 311, 273

Kervella, P., Coudé du Foresto, V., Glindemann, A., & Hofmann, R. 2000, SPIE, 4006, 31

Kervella, P., Thévenin, F., Ségrasan, D., et al. 2003, A&A, 404, 1087

Kervella, P., Ségransan, D., & Couddu Foresto, V. 2004, A&A, 425, 1161

Kervella, P. 2007, A&A, 464, 1045

Kippenhahn, R., & Weigert, A. editors 1991, Book Review: Stellar structure and evolution

Köhler, R. 2005, Astronomische Nachrichten, 326, 563

Kraemer, K. E., Sloan, G. C., Price, S. D., & Walker, H. J. 2002, ApJS, 140, 389

Kurucz, R. L. 1993, ASPC, 44, 87

Labeyrie, A., Lipson, S. G., Nisenson, P., & Haniff, C. 2007, "An Introduction to Optical Stellar Interferometry", Obs, 127, 140

Lacour, S., Thiébaut, E., Perrin, G., et al. 2009, ApJ, 707, 632

Ladjal, D. 2011, PhD thesis, University of Leuven

Lambert, D. L., Gustafsson, B., Eriksson, K., & Hinkle, K. H. 1986, ApJS, 62, 373

Lançon, A., & Wood, P. R. 2000, A&AS, 146, 217

Lattanzio, J. C., & Wood, P. R. 2003, in "Book Review: Asymptotic Giant Branch Stars", Habing & Olofsson editors, Springer, The Observatory, vol. 124, no. 1182, pag. 23

Lawson, P. R. ed. 2000, "Principles of Long Baseline Stellar Interferometry", 12

Leao, I. C., de Laverny, P., Chesneau, O., Mékarnia, D., de Medeiros, J. R., 2007, A&A, 466, 1

Le Bertre, T. 1988, A&A, 190, 79

Le Bertre, T. 1992, A&AS, 94, 377

Le Bertre, T. 1997, A&A, 324, 1059

Le Bouquin, J. B., Berger, J. P., Lazare, B., et al., 2011, A&A accept., (arXiv:1109.1918)

Lebzelter, T. 2011, AN, 332, 140

Lederer, M. T., & Aringer, B. 2009, A&A, 494, 403

Leech, K., Kester, D., Shipman, R., et al. 2003, in "The ISO Handbook, Volume V - SWS - The Short Wavelength Spectrometer Version 2.0.1", series edited by T.G. Mueller, J.A.D.L. Blommaert, & P. Garcia-Lario.

Leinert, C., Graser, U., Przygodda, F., et al. 2003, Ap&SS 286, 73

Leinert, C., van Boekel, R., Waters, L. B. F. M.,et al. 2004, A&A, 423, 537

Lester, J., & Neilson, H. 2008, A&A, 491, 633

Lindegren, L., Babusiaux, C., Bailer-Jones, C., et al. 2008, in A Giant Step: from Milli- to Micro-arcsecond Astrometry, ed. W. J. Jin, I. Platais, & M. A. C. Perryman (Cambridge: Cambridge University Press), IAU Symp. 248, 217

Lloyd, E. T. 1978, MNRAS, 183, 305

Lloyd, E. T. 1980a, MNRAS, 193, 87

Lloyd, E. T. 1980b, MNRAS, 193, 97

Lloyd, E. T. 1983, MNRAS, 204, 985

Lloyd, E. T. 2010, JAA, 31, 177

Lobel, A., Doyle, J. G., & Bagnulo, S. 1999, A&A, 343, 466

Lockwood, G. W., & Wing, R. F. 1971, ApJ, 169, 63

Loidl, R., Lançon, A., Jørgensen, U. G. 2001, A&A, 371, 1065

Lopez, B., Wolf, S., Lagarde, S., et al. 2006, SPIE, 6268, 31

Lorenz-Martins, S., de Araújo, F. X., Codina Landaberry, S. J., de Almeida, W. G., & de Nader, R. V. 2001, A&A, 367, 189

Malbet, F., & Perrin, G. 2007, NewAR, 51, 563

Marigo, P., Girardi, L., Bressan, A., Groenewegen, M.A.T., Silva, A., & et al. 2008, A&A, 482, 883, 905

Masana, E., Jordi, C., & Ribas, I 2006, A&A, 450, 735

Mathis, J. S., Rumpl, W., & Nordsieck, K. H. 1977, ApJ, 217, 425

Mattsson, L., Wahlin, R., Höfner, S., & Eriksson, K. 2008, A&A, 484, 5

Mattsson, L. 2009, PhD thesis, Uppsala University

Mattsson, L., Wahlin, R., & Höfner, S. 2010 A&A, 509, 14

Mattsson, L., & Höfner, S. 2011, A&A, 533, 42

Meisner, J. 2001, LIACo, 36, 225

Mennesson, B., Perrin, G., Chagnon, G., et al. 2002, ApJ, 579, 446

Milne, D. K., & Aller, L. H. 1980, AJ, 85, 17

Monnier, J.D., et al., 2006, Proc. SPIE, 6268, 62681P

Mourard, D., Clausse, J. M., Marcotto, A., & et al. 2009, A&A, 508

Mozurkewich, D., et al. 1991, AJ, 101, 2207

Neilson, H. R. & Lester, J. B. 2008, A&A, 490, 807

Nowotny, W., Aringer, B., Höfner, S., et al. 2005a, A&A, 437, 273

Nowotny, W., Lebzelter, T., Hron, J., & Höfner, S. 2005b, A&A, 437, 285

Nowotny, W. 2005c, PhD thesis, University of Vienna

Nowotny, W., Höfner, S., Aringer, B. 2010, A&A, 514, 35

Nowotny, W., Aringer, B., Höfner, S.; Lederer, M. T. 2011, A&A, 529, 129

O'Donnell, J.E. 1994, ApJ, 422, 1580

Ohnaka, K., & Tsuji, T. 1996, A&A, 310, 933

Ohnaka, K., 2004 A&A, 424, 1011

Ohnaka, K., Bergeat, J., Driebe, T., et al., 2005 A&A 429, 1057

Ohnaka, K., Driebe, T., Weigelt, G., & Wittkowski, M. 2007, A&A, 466, 1099

Ohnaka, K., Izumiura, H., Leinert, Ch., et al., 2008, A&A, 490, 173

Olnon, F. M., Raimond, E., Neugebauer, G. et al., 1986, A&AS. 65, 607

Omont, A., Cox, P., Bertoldi, F., McMahon, R. G., et al. 2001, A&A, 374, 371

Paladini, C., Aringer, B., Hron, J., Nowotny, W., Sacuto, S., et al. 2009, A&A, 501, 1073

Paladini, C., van Belle, G. T., Aringer, B., et al. 2011, A&A, 533, 27

Pégourié, B. 1988, A&A, 194, 335

Perrin, G., Ridgway, S. T., Mennesson, B., et al. 2004, A&A, 426, 279

Perryman, M. A. C., Lindegren, L., Kovalevsky, J., Hoeg, E., Bastian, U., et al. 1997, A&A, 323, 49

Perryman, M. A. C., de Boer, K. S., Gilmore, G., et al. 2001, A&A, 369, 339

Pettini, M., Smith, L. J., Hunstead, R. W., & King, D. L. 1994, ApJ 426,79

Petrov, R. G., Malbet, F., Weigelt, G., et al. 2007, A&A 464, 1

Pojmanski, G. 2002, Acta Astronomica, 52,397

Querci, F., Querci, M., & Tsuji, T. 1974, A&A, 31, 265

Quirrenbach, A., Mozurkewich, D., Hummel, C. A., et al., 1994, A&A. 285, 541

Ragland, S., Traub, W. A., Berger, J.-P., et al., 2006, ApJ, 652, 650

Ragazzoni, R., Herbst, T., Andersen, D., et al. 2002, SPIE, 4839-65

Ramsay Howat, S., Todd, S., Legget, S., et al. 2004, Proc. SPIE, 5492, 1160

Ratzka, T. 2005, PhD Thesis, Heidelberg University

Ratzka, T., Leinert, C., Henning, T., et al. 2007, A&A 471, 173

Renard, S., Thiébaut, E., & Malbet, F. 2011, A&A, 533 64

Renzini, A., Voli, M. 1981, A&A, 94, 175

Richichi, A., Percheron, I., & Khristoforova, M. 2005, A&A, 431, 773

Rouleau, F., & Martin, P.G. 1991, ApJ, 377, 526

Sacuto, S., Jorissen, A., Cruzalèbes, P., et al., 2008, A&A 482, 561

Sacuto, S., & Chesneau, O. 2009, A&A, 493, 1043

Sacuto, S., Aringer, B., Hron, J. et al., 2011, A&A, 525, 42

S. Sacuto,S., Jorissen, A., Cruzalèbes, P., et al. 2011, in "Why Galaxies care about AGB stars II", ASP Conf. Series, Vol. 445 Kerschbaum, Lebzelter, and Wing

Salaris, M., & Cassisi, S. editors 2006, Evolution of Stars and Stellar Populations

Samus, N.N., et al. 2009, "General Catalogue of Variable Stars", yCat, 102025S

Sandin, C., & Höfner, S. 2003, A&A, 404, 789

Sandin, C., & Höfner, S. 2004, A&A, 413, 789

Scholz, M., & Takeda, Y. 1987, A&A, 186, 200

Scholz, M. 2003, Proc. SPIE, 4838, p.163 (S03)

Schöier, F. L., & Olofsson, H. 2001, A&A, 368, 969

Schöier, F.L., Lindqvist, M., & Olofsson, H. 2005, A&A, 436, 633, 646

Schwarzschild, M., & Härm, R. 1965, ApJ, 142, 855

Schwarzschild, M. 1975, ApJ, 195, 137

Sedlmayr, E. 1994, in "Molecules un the stellar environment", IAU Coll. 146, ed. U. G.Jørgensen, Lecture Notes in Physics 428, Springer, p.163

Ségransan, D. 2007, NewAR, 51, 597

Shane, C. D. 1928, Lick Obs.Bull., 13, 123

Schöier, F. L., & Olofsson, H. 2001, A&A 368, 969

Shulyak "Terminator", D. V., Tsymbal, V., Ryabchikova, T., Stütz Ch., & Weiss, W. W. 2004, A&A, 428, 993

Sloan, G. C., Little-Marenin, I. R., & Price, S. D. 1998, AJ, 115, 809-820

Sloan, G. C., Kraemer, K. E., Price, S. D., & Shipman, R. F. 2003, ApJS, 147, 379

Smail, I., Ivison, R. J., & Blain, A. W. 1997, ApJ, 490, L5

Solano, E., & Fernley, J. 1997, A&AS, 122, 131

Tanaka, M., Letip, A., Nishimaki, Y., Yamamuro, T., Motohara, K., & et al. 2007, PASJ, 59, 939

Tatebe, K., & Townes, C. H. 2006, ApJ, 644, 1145

Tej, A., Lançon, A., & Scholz, M. 2003a, A&A, 401, 347

Tej, A., Lançon, A., Scholz, M., & Wood, P. R. 2003b, A&A, 412, 481

Thompson, R.R., Creech-Eakman, M.J., & van Belle, G. T. 2002, ApJ, 577, 447

Tsuji, T. 1973, A&A, 23, 411

Tsuji, T. 1986, ARA&A, 24, 89

Tsuji, T. 2000, ApJ, 540, L99

Tubbs, R. N., Meisner, J. A., Bakker, E. J., Albrecht, S. 2004, in "New Frontiers in Stellar Interferometry", Proceedings of SPIE Vol. 5491. Edited by Wesley A. Traub. Bellingham, WA: The International Society for Optical Engineering, 2004., p.588

Uttenthaler, S., & Lebzelter, T. 2010, A&A, 510, 62

van Belle, G. T., Dyck, H. M., Thompson, R. R., et al. 1997, AJ,114, 2150

van Belle, G. T., & van Belle, G. 2005, PASP, 117, 1263

van Belle, G. T., et al. (The Espri Consortium) 2008, Messenger, 134, 6

van Belle, G. T., et al. 2008, ApJS, 176, 276

van der Bliek, N. S., Morris, P. W., Vandenbussche, B., et al. 1998, in "Fundamental Stellar Properties: The Interaction between Observation and Theory", IAU Symp. 189, p. 89

van der Veen, & Habing 1988, A&A, 194, 125

Van Eck, S., Neyskens, P., Plez, B., et al. 2010, arXiv:1011.2092

Vanture, A. D., Smith, V. V., Lutz, J., et al. 2007, PASP, 119, 147

Vardya, M. S. A&AS 73, 181

Verhoelst 2005, PhD thesis, University of Leuven

Verhoelst, T., Decin, L., van Malderen, R., et al., 2006 A&A, 447, 311

Wallerstein, G., & Knapp, G. R. 1998, ARAA, 36, 369

Weigert, A. 1966, ZA, 64, 395

Weiner, J., Danchi, W. C., Hale, D. D. S., et al. 2000, ApJ, 544, 1097

Weiner, J., Hale, D. D. S., & Townes, C. H. 2003a, ApJ, 588, 1064

Weiner, J., Hale, D. D. S., & Townes, C. H. 2003b, ApJ, 589, 976

Weiner, J. 2004, ApJ, 611, L37

Whitelock, P. A., Feast, M. W., Marang, F., & Overbeek, M. D. 1997, MNRAS, 288, 512

Whitelock, P. A.,Feast, M. W., Marang, F., & Groenewegen, M. A. T. 2006, MNRAS, 369, 751

Whitelock, P. A., Feast, M.W.,& van Leeuwen, F. 2008, MNRAS, 386, 313

Willson, L. A. 2000, ARA&A, 38, 573

Winters, J. M., Dominik, C.,& Sedlmayr, E. 1994, A&A, 288, 255 (Winters et al., 1994a)

Winters, J. M., Fleischer, A. J., Gauger, A., & Sedlmayr, E. 1994, A&A, 290, 623

Winters, J. M., Le Bertre, T., Jeong, K. S., Helling, Ch., & Sedlmayr, E. 2000, A&A, 361, 641

Wittkowski, M., Hummel, C. A., Johnston, K. J., et al., 2001, A&A, 377, 981

Wittkowski, M. 2004, Proc. of the 37th Liege International Astrophysical Colloquium "Science Case for Next Generation Optical/Infrared Interferometric Facilities (the post VLTI era)"

Wittkowski, M, Aufdenberg, J. P., & Kervella. P. 2004, A&A, 413,711

Wittkowski, M., Aufdenberg, J. P., Driebe, T., et al. 2006a, A&A, 460, 855

Wittkowski, M., Hummel, C. A., Aufderberg, J. P., & Roccatagliata, V. 2006b, A&A, 460, 843

Wittkowski, M. 2007, NewAR, 51, 639

Woitke, P., Helling, C., Winters, J. M., Jeong, K. S. 1999, A&A, 348, 17

Woitke, P. 2003, in "Modelling of Stellar Atmospheres", ed. N. Piskunov, W. W. Weiss, & D. F. Gray, IAU Symp.,210,387

Woitke, P. 2006, A&A, 452, 549

Wong, T., Schöier, F. L., Lindqvist, M., Olofsson, H., 2004, A&A 413, 241

Wood, P. R. 1990, in "From Miras to Planetary Nebulae: Which Path for Stellar Evolution", ed. M. O. Mennessier & A. Omont (Gif-sur-Yvette: Editions Frontieres), 67

Yamamura, I., & de Jong, T. 2000, ESASP, 456, 155Y

Yamashita, Y., 1972, Ann. Tokyo Astron. Obs., 13, 169

Yamashita, Y., 197, Ann. Tokyo Astron. Obs., 15, 47

Yudin, R. V., & Evans, A. 2002, A&A, 391, 625

Zhao-Geisler, R. 2010, PhD thesis, Heidelberg University

Zijlstra, A. A., Matsuura, M., Wood, P. R., et al. 2006, MNRAS, 370, 1961

Acknowledgements

The work presented in this thesis was supported by the Austrian Science Fund FWF under project number AP19503 and AP23006. The research leading to the results presented in Chap. 4 has received funding from the European Community's Seventh Framework Program under Grant Agreement 226604.

Thanks to Josef for the support as Supervisor and keeping the door of his office always open. Special thanks to all the people of the AGB group of Vienna for their support during these years and for switching almost always to English every time I was around. I list them in alphabetic order: Bernhard Aringer, Angela Baier, Franz Kerschbaum, Daniela Klotz, Thomas Lebzelter, Michael Lederer, Denise Lorenz, Armin Luntzer, Andi Mayer, Marko Mecina, Walter Nowotny, Roland Ottensamer (SuperRoland), Thomas Posch, Hannes Richter, Stephane Sacuto, Stefan Uttenthaler, Bernhard Wenzel.

During these years I met a lot of nice scientists and by discussing or just by listening to them I could really learn a lot: thanks to Susanne Höfner, Tijl Verhoelst, Markus Wittkowski, Olivier Chesneau, Eric Lagadec, Gerard van Belle, Andrea Chiavassa, Ronny Zhao-Geisler, Andrea Richichi, Keiichi Ohnaka, Thorsten Ratzka.

Thanks to my family and friends for being always around.

Claudia Paladini

Curriculum Vitae

Personal Informations

First Name:	Claudia
Surname:	Paladini
Birth place:	Leverano (Lecce), Italy
Birth date :	October 6^{th}, 1977
Citizenship:	Italian
Current address:	Institut für Astronomie der Universität Wien
	Türkenschanzstrasse 17
	A-1180 Wien, Österreich
Telephone:	+43/1/4277-53853
e-mail:	claudia.paladini@univie.ac.at

Spoken Languages

Italian (mother language); English (fluent)

Educational Background

2007 - 2011:	Ph.D student in Astronomy, University of Vienna
	Thesis title: *"Interferometry of carbon-rich Asymptotic Giant Branch Stars."*
	Supervisors: Prof. F. Kerschbaum, Prof. J. Hron
2006:	Laurea (Master Thesis) in Astronomy, University of Padova
	Thesis title: *"Rotation Velocities of Hot Horizontal Branch Stars in the Globular Cluster NGC2808."*
	Supervisors: Prof. G. Piotto, Dr. A. Recio Blanco

Primary Research Interest

- Spectroscopy and Interferometry of late type stars;
- Modeling of AGB stars atmosphere;
- Globular Clusters and stellar population.

Known Softwares

- Operating Systems: UNIX/LINUX, Windows, MAC/OSX;
- Programming languages: Fortran, Supermongo, IDL, Unix Shell Script;
- Word processing: Latex, Microsoft Word/Excel/PowerPoint, Open Office;

- Astronomical Software: IRAF, MIDAS, DAOPHOTII/ALLFRAME, ESO pipelines (UVES, UVES-FIBRE, GIRAFFE, SOFI), MIDI data reduction pipeline (MIA+EWS), AMBER data reduction pipeline (amdlib).

Reduction and analysis of astronomical data

- Good experience in reducing interferometric data: MIDI observations of AGB stars.
- Good experience in modeling interferometric data: VLTI/VINCI, MIDI, AMBER interferometry of AGB stars with dynamic and hydrostatic model atmospheres.
- Good experience in reducing and analysing infrared spectra: SOFI and UKIRT/UIST spectroscopy of AGB stars.
- Good experience in reducing and analysing optical spectra: FLAMES/UVES and FLAMES/GIRAFFE spectroscopy of HB stars.
- Good experience in reducing and analysing photometric data: ESO/DUTCH photometry of galactic globular cluster.

Observational Experiences

- ESO (Paranal, Chile): VLTI/AMBER (June 2011).
- Telescopio Nazionale Copernico 1.82m (Asiago, Italy): AFOSC. Long slit spectroscopy.
- Telescopio Galileo 1.22m (Asiago, Italy): Boller & Chivens. Long slit spectroscopy.

Membership in Professional Societies

- European Astronomical Society
- Austrian Society for Astronomy and Astrophysics

Publications in international refereed journals

- Bailey J. D., Landstreet J. D., Bagnulo S., Fossati L., Kochukhov O., **Paladini C.**, et al. 2011, A&A, subm.
- Cusano F., **Paladini C.**, Richichi A. et al., 2011, A&A, subm.
- Fossati L., Folsom C. P., Bagnulo S., Grunhut J. H., Kochukhov O., Landstreet J. D., **Paladini C.** et al. 2011, MNRAS, 413, 1132
- Klotz D., Sacuto S., Kerschbaum F., **Paladini C.**, et al., 2011, A&A, subm.
- **Paladini C.**, van Belle G. T., Aringer B. et al., 2011, A&A, 533, 27

- **Paladini C.**, Aringer B., Hron J., Nowotny W., Sacuto S. et al. 2009, A&A, 501, 1073
- Sacuto S., Aringer B., Hron J., Nowotny W., **Paladini C.** et al. 2011, A&A, 525, 42

Conference Proceedings and Posters

- Hron, J.; Aringer, B.; Nowotny, W.; **Paladini, C.**:
  "Optical Interferometry and C-rich AGB-Stars"
  published in "Evolution and nucleosynthesis in AGB stars", ed. Guandalini, R., Palmerini, S., & Busso, M., AIP Conference Proceedings; Vol. 1001, pp.185-192.

- **Paladini, C.**; Aringer B.; Höfner S., Hron J., Nowotny W., Sacuto S.:
  Testing dynamic models of AGB C-stars with uniform disc fits.
  poster presented at the VLTI school "Astrometry and Imaging with the Very Large Telescope Interferometer", 2008.
- **Paladini, C.**; van Belle G. T., Aringer B. et al.:
  "Determination of stellar parameters of C-rich hydrostatic stars from spectro-interferometric observations", ASP Conference Series, Vol. 445, Kerschbaum, Lebzelter, & Wings eds., 2011.

Selected talks, seminars and colloquia

- August 2011 - Contributed talk at the NCAC Symposium (Warsaw, Poland)
- June 2011 - Talk at ESO Vitacura
- March 2011 - Talk at the "AMBER Science and Data Reduction JMMC Workshop, Grenoble
- November 2010 - Seminar at the University of Padova
- August 2010 - Talk at the AGB conference (Vienna)"Why Galaxies care about AGB stars II
- March 2010 - Talk at the ESO Garching Workshop "Origin and Fate of the Sun"
- December 2009 - SAGA seminar, MPA (Garching)
- June 2008 - Talk at the VLTI school "Astrometry and Imaging with the VLTI"

Successful Observing Proposals as PI

- ESO VLTI Period 88, AMBER 9h, 088.D-0340:
  Infrared interferometry of dynamic C-rich stars: a tool to study the stellar atmosphere and to constrain evolutionary models.

- ESO VLTI Period 87, MIDI 113.5h, VISIR 2.6nts, 187.D-0924:
  A joint venture in the red: the Herschel+MIDI+VISIR view on mass loss from evolved stars

- ESO VLTI Period 86, AMBER 12h, MIDI 6h, 086.D-0899:
  Infrared interferometry of dynamic C-rich stars: a tool to study the stellar atmosphere and to constrain evolutionary models.

- ESO VLTI Period 85, MIDI 6h, 085.D-0756:
  Mid-IR interferometric constraints on the dynamic process of dust formation in C-rich stars.

Successful Observing Proposals as CoI

- ALMA, (PI Maerker):
  Piecing the shell together: ALMA and the detached shell around R Scl

- ESO VLTI Period 88, AMBER, 088.D-0620 (PI Cusano):
  Testing the CORS method: the case of U Car

- ESO La Silla Period 88, PolCor, 088.D-0867 (PI Maerker):
  Digging into the dusty envelopes of evolved stars with PolCor

- ESO VLTI Period 87, AMBER, 087.D-0415 (PI Cusano):
  Unveiling the morphology of C-rich stars

- ESO VLTI Period 86, AMBER, 086.D-0303 (PI Cusano):
  Resolving the photosphere and the inner shell of the cool carbon star TX Psc with AMBER

- ESO VLTI Period 86, AMBER, 086.D-0221 (PI Cusano):
  Calibrating Evolutionary Tracks Measuring Angular Diameters of Giant Stars: Understanding the Formation of Exoplanets

- ESO VLTI Period 86, MIDI, 086.D-0069 (PI Sacuto):
  Origin of inhomogeneity in the mass-loss of the oxygen-rich stars: EP Aqr and SV Psc

- ESO VLTI Period 84, MIDI, 084.D-0361 (PI Sacuto):
  Highlighting the obscuration event in the close environment of the carbon Mira R Fornacis

- ESO VLTI Period 84, MIDI, 084.D-0776 (PI Sacuto):
  Morphology and dynamics of the carbon-rich star R Sculptoris

- ESO VLTI Period 82, MIDI, 082.D-0389 (PI Sacuto):
  Origin of inhomogeneity in the mass-loss of the oxygen-rich stars: EP Aqr and SV Psc

Astronomy and Astrophysics
Editor in Chief: C. Bertout

C. Bertout
Observatoire de Paris
61, avenue de l'Observatoire
75014 Paris, France

Tel.: 33 0(1) 43 29 05 41
Fax: 33 0(1) 43 29 05 57
e-mail: aanda.paris@obspm.fr
Web: http://www.aanda.org

merging
Annales d'Astrophysique
Arkiv for Astronomi
Bulletin of the Astronomical Institutes of the Netherlands
Bulletin Astronomique
Journal des Observateurs
Zeitschrift fur Astrophysik
Bulletin of the Astronomical Institutes of Czechoslovakia

Paris, October 7, 2011

Reprint Permission

Material:
Paladini, C. et al., 2011A&A, 533, A27
Paladini, C. et al., 2009A&A, 501, 1073
Sacuto, S. et al., 2011A&A, 525, A42

To be used in:
PhD thesis, University of Vienna

Permission granted to:
Claudia Paladini
Institut f. Astronomie
Tuerkenschanzstr. 17
A-1180 Vienna / Austria
mail to: claudia.paladini@univie.ac.at

I hold copyright on the material referred to above, and hereby grant permission for its use as requested herewith. The credit should be given as follows:
Credit: Author, A&A, vol, page, year, reproduced with permission © ESO.

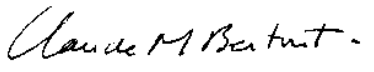

Claude Bertout
A&A Editor-in-Chief

Sponsored by Argentina, Austria, Belgium, Brazil, Chile, Czech Republic, Denmark, Estonia, Finland, France, Germany, Greece, Hungary, Italy, Netherlands, Poland, Portugal, Slovak Republic, Spain, Sweden, and Switzerland.
Produced and distributed by EDP Sciences for ESO.

A&A 501, 1073–1085 (2009)
DOI: 10.1051/0004-6361/200911938

Astronomy & Astrophysics

Interferometric properties of pulsating C-rich AGB stars

Intensity profiles and uniform disc diameters of dynamic model atmospheres

C. Paladini[1], B. Aringer[1,2], J. Hron[1], W. Nowotny[1], S. Sacuto[1], and S. Höfner[3]

[1] Department of Astronomy, University of Vienna, Türkenschanzstrasse 17, 1180 Wien, Austria
e-mail: claudia.paladini@univie.ac.at
[2] INAF-OAPD, Vicolo dell'Osservatorio 5, 35122 Padova, Italy
[3] Department of Physics and Astronomy, Uppsala University, Box 515, 75120 Uppsala, Sweden

Received 24 February 2009 / Accepted 10 April 2009

ABSTRACT

Aims. On the basis of a set of dynamic model atmospheres of C-rich AGB stars, we present the first theoretical study of centre-to-limb variation (CLV) properties and relative radius interpretation on narrow and broad-band filters. We computed visibility profiles and the equivalent uniform disc (UD) radii to investigate the dependence of these quantities on the wavelength and pulsation phase.
Methods. After an accurate morphological analysis of the visibility and intensity profiles determined in narrow and broad-band filters, we fitted our visibility profiles with a UD function simulating the observational approach. The UD-radii were computed using three different fitting-methods to investigate the influence of the visibility sampling profile: single point, two points and a least squares method.
Results. The intensity and visibility profiles of models characterises by mass loss show a behaviour very different from a UD. We found that UD-radii are wavelength dependent and that this dependence is stronger if mass loss is present. Strong opacity contributions from C_2H_2 affect all radius measurements at 3 μm and in the N-band, resulting in higher values for the UD-radii. In the case of models with mass loss the predicted behaviour of UD-radii versus phase is complicated, while the radial changes are almost sinusoidal for models without mass loss. Compared to the M-type stars, for the C-stars no windows are available for measuring the pure continuum.

Key words. techniques: interferometric – stars: AGB and post-AGB – stars: carbon – stars: atmospheres – stars: late-type

1. Introduction

The Asymptotic Giant Branch (AGB) is a late evolutionary stage of stars with masses lower than about 8 $M_\odot$. The objects on the AGB are characterised by a degenerate C-O core and He/H-burning shells, a convective envelope, and a very extended atmosphere containing molecules and in many cases even dust grains. The atmospheres are affected by the pulsation of the interior creating shocks in the outer layers. Because of the third dredge-up, the AGB stars may have C/O > 1 (Iben & Renzini 1983) and therefore their spectra maybe dominated by features of carbon species such as C_2, C_2H_2, C_3, CN, and HCN (Goebel et al. 1981; Joyce 1998; Lançon et al. 2000; Loidl et al. 2001; Yamamura & de Jong 2000). These are the classical carbon stars. In these objects, dust is mainly present in the form of amorphous carbon grains.

Studying stellar atmospheres is essential to a clearer comprehension of this late stage of stellar evolution, the complicated interaction of pulsation and atmospheric structure, and the processes of dust formation and mass loss. The atmospheres of C-rich AGB stars with no pronounced pulsation can be described by hydrostatic models (Jørgensen et al. 2000; Loidl et al. 2001). As the stars evolve, the effective temperatures decrease and the atmospheres become more extended. At the same time, the effects of time-dependent phenomena (dynamic processes) become important and static models are no longer a good approximation. More sophisticated tools are needed to describe these objects i.e., dynamic model atmospheres. The status of modelling atmospheres of cool AGB stars is summarised in different reviews by Willson (2000), Woitke (2003), and Höfner (2005, 2007, 2009). Comparison of dynamic models with spectroscopy for C-rich stars can be found in Hron et al. (1998), Loidl et al. (2001), Gautschy-Loidl et al. (2004, henceforth GL04), Nowotny et al. (2005a,b), Nowotny (2005), and Nowotny et al. (2009).

Because of their large atmospheric extension and their high brightness in the red and infrared, AGB stars are perfect candidates for interferometric investigations. Moreover, since most observed AGB stars are very far away (at distances larger than 100 pc), only the resolution reached by optical interferometry allows a study of the close circumstellar environment of these objects.

The complex nature of their atmospheres raises the question of how a unique radius can be defined for these stars. Several radius definitions have been used, as summarised in the reviews of Baschek et al. (1991) and Scholz (2003, henceforth S03). This is not an important problem when dealing with objects that have a less extended and almost hydrostatic atmosphere, because in most cases the different definitions of radius converge to a similar final result. However, one can find large differences when the envelope of the star is affected by the phenomena of pulsation and mass loss. Baschek et al. (1991) proposed the use of the intensity radius, which is "a monochromatic (or filter-integrated) quantity depending on wavelength or on the position and width of a specific filter". This radius is determined from the

centre-to-limb variation (CLV) as the point of inflection of the CLV curve, in other words as the point where the second derivative of the intensity profile equals zero. To determine this value, a very accurate knowledge of the CLV must, however, be available. For AGB stars, this can be difficult because the intensity profile of an evolved object can exhibit a quite complicated behaviour and only a few data points are generally measured. In the case of a poorly measured CLV, the standard procedure is to use analytical functions such as the uniform disc (UD), a fully darkened disc (FDD), or a Gaussian fit to the profile. The result of this fit is the so-called fitting radius (S03).

Various theoretical and observational studies have been completed of the different properties of the CLV and radius interpretations for M-type stars, which are summarised in the review of S03. According to this review paper, the CLV shapes can be classified into four types:

- *small to moderate limb-darkening*, when the behaviour of the profile is well fitted by a UD;
- the *Gaussian-type CLV* is typical of extended atmospheres, where there is a large difference in temperature between the cool upper atmosphere layers and the deep layers where the continuum is formed;
- the *CLV with tail or protrusion-type extension* consists of two components, a central part described by the CLV of a near-continuum layer, and a tail shape given by the CLV of an outer shell;
- the *uncommon CLVs*, which are profiles exhibiting strange behaviour that is characteristic of complex extended and cool atmospheres.

The fitting radius is usually converted into a monochromatic optical depth radius R_λ, defined as the distance between the centre of the object and a layer with $\tau_\lambda = 1$ at a given wavelength. However this conversion must be confirmed very carefully: even in the case of near-continuum bandpasses, spectral features can contaminate the measurement of the fitting radius, as demonstrated by Jacob & Scholz (2002) or Aringer et al. (2008), which will then no longer represent a good approximation to the radius of the continuum layer.

Following the definition given by Scholz & Takeda (1987), a filter radius

$$R_{\rm filt} = \frac{\int R_\lambda I_\lambda^{\rm c} f_\lambda {\rm d}\lambda}{\int I_\lambda^{\rm c} f_\lambda {\rm d}\lambda} \quad (1)$$

requires a good knowledge of the filter transmission curve, and the filter itself must be chosen carefully to avoid impure-filter-like effects (see Sect. 5 of S03 for more details). A very common definition of radius is the Rosseland radius, which corresponds to the distance between the stellar centre and the layer with Rosseland optical depth $\tau_{\rm Ross} = 1$. As in the case of the monochromatic optical depth radius, this quantity is not an observable, but is model dependent, and molecular contaminations are the main effect that has to be taken in account.

A suitable window at 1.04 μm for determining the continuum radius of M-type stars was discussed by Scholz & Takeda (1987), Hofmann et al. (1998), Jacob & Scholz (2002), and Tej et al. (2003a,b). These authors defined a narrow-bandpass located in this part of the spectrum, mostly free from contamination by molecules and lines. They indicated that this radius is the most appropriate for studying the geometric pulsation. Unfortunately, such a window does not exist for C-rich AGB stars (cf. Sect. 5), and model assumptions must be made in defining a continuum radius. On the other hand, available dynamic atmospheric models for carbon-stars (Höfner et al. 2003) are more advanced than for M-type stars, the main reason being a clearer understanding of the dust formation.

Following the same approach adopted for M-stars by Scholz and collaborators, we started investigating the CLV characteristics of a set of dynamic models of pulsating C-stars (Hron et al. 2008). We summarise the main properties of the intensity and visibility profiles in narrow and broad-band filters for dynamic model atmospheres with and without mass loss (Sect. 2.2). We then use the UD function to determine the UD-radius of the models, and investigate the dependence of the latter upon wavelength and pulsation phase. We also discuss a new definition of a continuum radius for the carbon stars (Sect. 5).

2. Dynamic models and interferometry

The dynamic models used in this work are described in detail in Höfner et al. (2003), GL04, and Nowotny et al. (2005a).

2.1. Overview of the dynamic models

The models are spherically symmetric and characterised by time-dependent dynamics and frequency-dependent radiative transfer. Assuming LTE for both gas and dust, the radiative energy transport in the atmosphere and wind is computed using opacity sampling in typically 50–60 wavelength points. For the gas component, an energy equation is solved together with the dynamics, defining the gas temperature stratification (and allowing, in principle, for deviations from radiative equilibrium, e.g., in strong shocks). For the dust, on the other hand, the corresponding grain temperature is derived by assuming radiative equilibrium. Dust formation (in this sample only amorphous carbon dust is considered) is treated by the "moment method" (Gail & Sedlmayr 1988; Gauger et al. 1990), while the stellar pulsation is simulated by a piston at the inner boundary. Assuming a constant flux there, this leads to a sinusoidal bolometric light curve, which can be used to assign bolometric phases to each "snapshot" of the model with $\phi = 0$ corresponding to phases of maximum light.

In Table 1, the main parameters of the models used are summarised (see also GL04). Luminosity $L_\star$, effective temperature $T_\star$, and C/O ratio refer to the initial hydrostatic model used to start the dynamic computation. This model can be compared with classical model atmospheres such as MARCS (Gustafsson et al. 2008). The stellar radius $R_\star$ of the initial hydrostatic model is derived from $L_\star$ and $T_\star$ and corresponds to the Rosseland radius. The piston-velocity amplitude $\Delta u_{\rm p}$ and the period P are also input parameters that control the pulsation, while the mass-loss rate $\dot{M}$ and the mean degree of condensation $\langle f_{\rm c} \rangle$ are the result of the dynamic computations. The free parameter $f_{\rm L}$ is introduced to adjust the amplitude of the luminosity variation at the inner boundary such that $L_{\rm in}(t) \propto f_{\rm L} \cdot R_{\rm in}^2(t)$ (GL04). All the initial models have a mass $M_\star = 1\ M_\odot$ and solar metallicity.

The models used in this work were chosen to investigate the effects of the different parameters on radius measurements, mass-loss, primarily, but also effective temperature, C/O and piston amplitude. Keeping this purpose in mind, the sample can be divided into two main groups: models with and without mass-loss (in Table 1, series D and N, respectively).

It was already mentioned that the pulsation of the inner layers can influence the outer atmosphere of the star. The propagation of the shock waves causes a levitation of the outer layers and

Table 1. Parameters of the dynamic model atmospheres used in this work.

Model	$L_\star$ [$L_\odot$]	$T_\star$ [K]	$R_\star$ [$R_\odot$]	C/O	Δu_p [km s^{-1}]	P [d]	f_L	ΔM_{bol} [mag]	$\langle f_c \rangle$	$\dot{M}$ [$M_\odot$ yr^{-1}]
D1	**10 000**	**2600**	492	**1.4**	**4.0**	**490**	**2.0**	**0.86**	**0.28**	**4.3×10^{-6}**
D2	10 000	2600	492	1.4	4.0	525	1.0	0.42	0.37	5.9×10^{-6}
D3	7000	2600	412	1.4	6.0	490	1.5	1.07	0.40	2.5×10^{-6}
D4	7000	2800	355	1.4	4.0	390	1.0	0.42	0.28	2.4×10^{-6}
D5	7000	2800	355	1.4	5.0	390	1.0	0.53	0.33	3.5×10^{-6}
N1	**5200**	**3200**	**234**	**1.1**	**2.0**	**295**	**1.0**	**0.13**	**–**	**–**
N2	7000	3000	309	1.1	2.0	390	1.0	0.23	–	–
N3	7000	3000	309	1.4	2.0	390	1.0	0.24	–	–
N4	7000	3000	309	1.4	4.0	390	1.0	0.48	–	–
N5	7000	2800	355	1.1	4.0	390	1.0	0.42	–	–

in certain cases formation of dust grains can take place. The radiation pressure on the dust grains may drive a stellar wind characterised by terminal velocities V_∞ and mass-loss rates $\dot{M}$. In Fig. 1, an example of the radial structure of the dynamic model atmosphere D1 (scaled to $R_\star$) is plotted for different phases. For comparison, the area covered by the model N1 is also shown grey-shaded. In particular, we show the effect of the dust-driven wind that appears on the model structure D1. The different atmospheric extensions of the two models are clearly evident.

In the series D of Table 1, two models, D1 and D2, differ from the others in having a higher luminosity ($L_\star$). The only distinction between these two models are different values of the period P and the parameter f_L. The effect on the structure of the atmosphere is that dust shells observed at a few $R/R_\star$ are more pronounced in the case of D2. The models D4 and D5 have the same luminosity, temperature, and period but different piston velocities and different resulting degrees of dust condensation. In the structure of D4, compared with D5, there is a smoother transition between the region dominated by pulsation and the one dominated by the dust-driven wind (see Fig. 2 of Nowotny et al. 2005a).

In the N set of models, we can identify N1 on the basis of its higher temperature and lower luminosity. All the other models have the same luminosity but differ in terms of other parameters. Both N3 and N4 are examples of studying the effect of different piston velocities on models without mass-loss. The atmospheric structure of N4 is more extended but the outer layers are not yet cool and dense enough for dust formation. N2 and N3 have different C/O ratios causing differences in their spectral features and in the estimation of the diameter at certain wavelengths (Sect. 5).

We use model D1 as a reference for models with mass-loss. GL04 compared this model with observed spectra of the star S Cep and demonstrated that different phases of D1 can reproduce the S Cep spectra shortward of $\approx 4\,\mu$m. The same model is in qualitative agreement with the observed CO and CN line-profile variations of S Cep and other Miras (Nowotny et al. 2005a,b). Concerning models without mass-loss, we use model N1 as a reference, which provides the best-fit solution of spectra and colour measurements for TX Psc in GL04. Each of these reference models also represents the most extreme case of its sub-group.

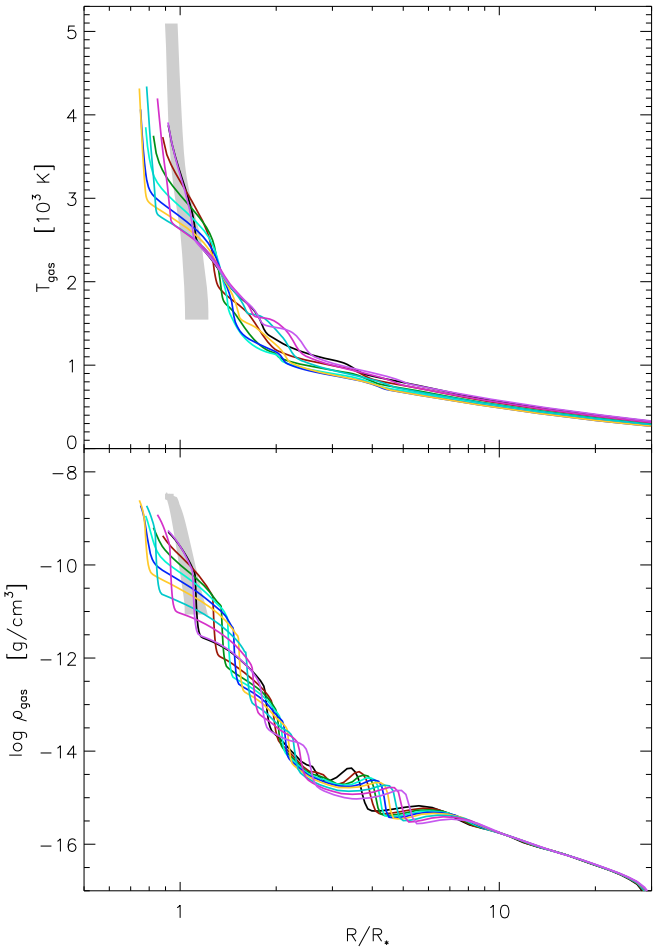

Fig. 1. Radial structure of the dynamic model D1. Gas temperature (*upper panel*) and density (*lower panel*) are plotted for different phases during the pulsation period. For comparison, the grey-shaded area marks the range where the structure of the model N1 at different phases can be found. More details about the structure of the models can be found in the text and in Nowotny et al. (2005a,b).

2.2. Synthetic intensity and visibility profiles

To compute the intensity and visibility profiles for each model we proceeded in the following way. For a given atmospheric structure (where temperature and density stratifications were both taken directly from the dynamical simulation), opacities were computed using the COMA code, originally developed by Aringer (2000): all important species, i.e., CO, CH, C_2, C_3, C_2H_2, HCN, and CN were included. The data sources used for the continuous opacity were presented in Lederer & Aringer (2009). Voigt profiles were used for atomic lines, while Doppler

profiles were computed for the molecules. Conditions of LTE and a microturbulence value of $\xi = 2.5\,\mathrm{km\,s^{-1}}$ were assumed. All references to the molecular data are listed in Table 2 of Lederer & Aringer (2009). The source for the amorphous carbon opacity is Rouleau & Martin (1991). These input data agree with the previous works (Nowotny 2005; Lederer & Aringer 2009; Aringer et al. 2009), and with the opacities used in computing the dynamic models. Information about recent updates to the COMA code and opacity data can be found in Nowotny (2005), Lederer & Aringer (2009), Aringer et al. (2009), and Nowotny et al. (2009). The resolution of the opacity sampling adopted in our computations is 18 000. The resulting opacities were used as input to a spherical radiative transfer code that computes the spectrum at a selected resolution for a chosen wavelength range. In addition, the code computes the spatial intensity profiles for every frequency point of the calculation. Velocity effects were not taken into account in the radiative transfer.

The monochromatic spatial intensity profiles were subsequently convolved with different filter curves (narrow and broad-band) in the near- to mid-IR range to obtain averaged intensity profiles. The narrow-band filters were rectangular (transmission 1), while the broad-band filters are the standard filters from Bessel & Brett (1988). The visibility profiles were the two-dimensional Fourier transform of the intensity distribution of the object, but under the condition of spherical symmetry (as for our 1D models), this reduces to the more simple Hankel transform of the intensity profiles (e.g., Bracewell 1965).

The intensity and visibility profiles in the case of the broad-band filters were computed with the following procedure. Each broad-band filter was divided into a set of 10 narrow-band subfilters[1] and the squared broad-band visibility was computed as

$$V^2_{\mathrm{broad}} = \frac{\sum_i (S_i^2 F_i^2 V_i^2)}{\sum_i (S_i^2 F_i^2)}, \qquad (2)$$

where the sum was calculated over all the narrow subfilters, S_i is the transfer function of the broad-band filter within the corresponding narrow-band subfilter, F_i is the flux integrated over the corresponding narrow-band subfilter, and V_i is the visibility of the narrow-band subfilter computed from the average intensity profile of the corresponding filters.

In the following two sections, we discuss the characteristics of the intensity and visibility profiles for different models and the effects of using different filters. In the case of broad-band filter we also discuss the so-called *band-width smearing effect* (Verhoelst 2005; Kervella et al. 2003).

3. Synthetic profiles for narrow-band filters

Twenty-one narrow-band filters were defined in the near-to mid-IR range with a "resolution" ranging from 50 to 200 to study effects of different molecular features characteristic for C-star spectra, following the approach described in Bessel et al. (1989, 1996). Figure 2 shows the location of the filters on top of a typical synthetic (continuum-normalised) spectrum of a C-type star for illustration. Table 2 gives an overview of our complete set of filters with name of the bands, characteristic features (for narrow-bands), central wavelengths, band widths, and morphological class. A few of these filters are labelled "cont" meaning that the contamination by molecular features is comparably low in this spectral region, but this does not necessarily represent the true continuum. At extremely high spectral resolutions, it may be possible to identify very narrow windows in the spectrum of a C-star, where no molecular lines are located (e.g., Fig. 6 in Nowotny et al. 2005b). However, in general and at the resolutions available nowadays, the observed spectra of evolved C-type stars in the visual and IR are crowded with absorption features. Because of this blending, the continuum level $F/F_c = 1$ is never reached as in Fig. 2. This effect is more and more pronounced with lower effective temperatures and decreasing spectral resolutions (cf. Nowotny et al. 2009).

Table 2. Definitions of the narrow- and broad-band filters.

Filter	Features	λ_c [μm]	$\Delta\lambda$ [μm]	Class
1.01	C_2, CN	1.01	0.02	I
1.09	CN	1.09	0.02	I
1.11	"cont"	1.11	0.02	I
1.51	CN+	1.51	0.02	I
1.53	C_2H_2, HCN, CN	1.53	0.02	**I**
1.575	CN	1.575	0.05	I
1.625	CN, CO	1.625	0.05	I
1.675	"cont"	1.675	0.05	I
1.775	C_2	1.775	0.05	I
2.175	CN	2.175	0.05	I
2.375	CO	2.375	0.05	I
3.175	C_2H_2, HCN, CN	3.175	0.05	**III**
3.525	"cont"	3.525	0.05	II
3.775	C_2H_2	3.775	0.05	II
3.825	C_2H_2	3.825	0.05	II
3.975	"cont"	3.975	0.05	II
9.975	"cont"	9.975	0.05	**II**
11.025	"cont"	11.025	0.05	II
12.025	C_2H_2	12.025	0.05	III
12.475	C_2H_2	12.475	0.05	III
12.775	C_2H_2	12.775	0.05	III
J		1.26	0.44	
H		1.65	0.38	
K		2.21	0.54	
L'		3.81	0.74	

As a first step, we study the morphology of different intensity and visibility profiles. We then proceed to investigate the main opacity contributors to the features that appear in the profiles. For this purpose, we compute three different sets of intensity and visibility profiles for the two reference models: (i) profiles including all necessary opacity sources, i.e., continuous, atomic, molecular, and dust opacities; (ii) profiles where the opacities of dust were neglected, to analyse only molecular and atomic contributions; and (iii) profiles for which only the continuous gas opacity is considered, to derive theoretical continuum profiles.

For the narrow-band filters, the intensity profiles of models with mass-loss can be divided into three morphological classes listed in the last column of Table 2. It turns out that this classification is related mainly to the wavelength region with the exception of the filter 3.175 μm, which belongs to the third class (that contains filters centred around 12 μm) instead of the second (that contains all the other filters in the 3 μm region, plus the 9 and 11 μm filters). In Fig. 3, the intensity and visibility profiles

[1] In principle, this should be done monochromatically but for computational reasons the usual number of narrow-band subfilters was limited to 10. However, we compared the resulting broad-band filters computed with a set of 10 narrow-band subfilters with the one computed with a set of 100 and 200 subfilters without finding any significant difference in the resulting broad-band visibility profile. We also emphasise that the maximum resolution for the computation of the broad-band filter is given by the opacity-sampling resolution.

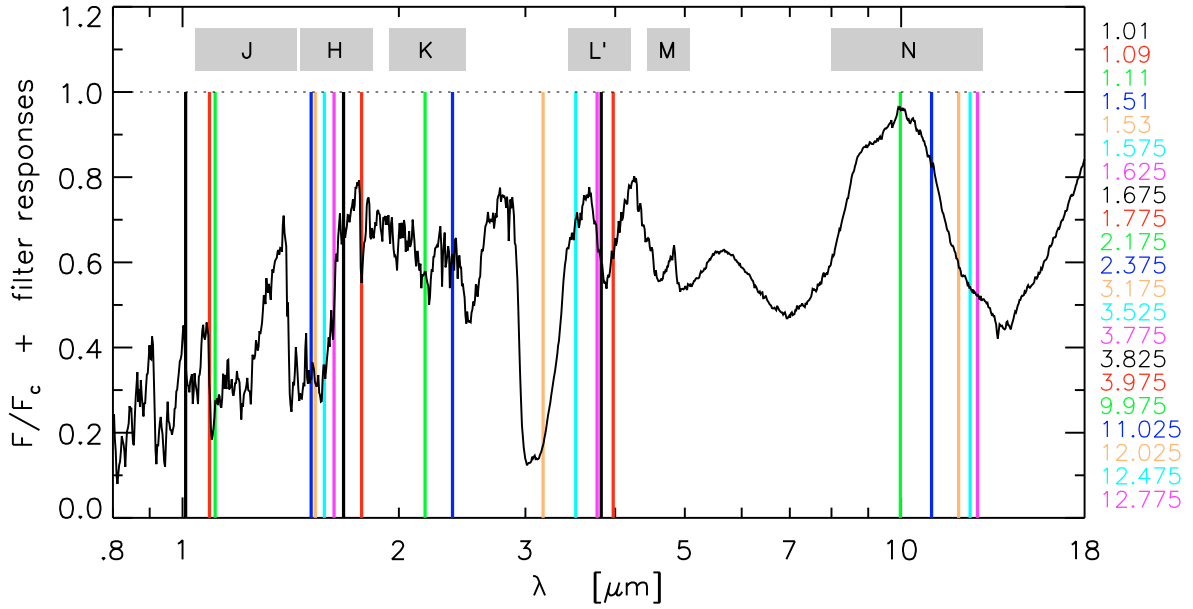

Fig. 2. Synthetic spectrum ($R = 360$) calculated on the basis of the hydrostatic initial atmospheric structure of model D1. All necessary opacity sources (continuous, atoms, molecules, dust) are included for the spectral synthesis, (see Fig. 4 of Aringer et al. (2009) for the individual contributions of the different molecular species). The flux is normalised to a calculation for which only the continuous opacities were taken into account. Overplotted are the narrow-band filters as defined in Table 2, for which the central wavelengths in [μm] are given in the legend. In addition, the ranges of the broad-band filters are marked grey-shaded.

for the representative filters of each class are illustrated. Models with mass-loss (left panels) are more extended than models without mass-loss (right), and their intensity profiles fit into the category of "uncommon profiles" of S03.

The first class of profiles contains the filters in the near IR from 1.01 μm to 2.375 μm. It can be well represented by filter 1.53 (C_2H_2, HCN, CN). Its morphology is characterised first by a limb-darkened disc, followed by a bump caused by molecular contributions, and a peak indicating the inner radius of the dust shell. At 1.53 μm, a feature due to the molecular species of C_2H_2 and HCN is predicted by some of the cool dynamic models with a wind (GL04). This feature was observed in the spectra of cool C-rich Miras, such as R Lep (Lançon et al. 2000), V Cyg, cya 41 (faint Cygnus field star), and some other faint high-Galactic-latitude carbon stars (Joyce 1998).

The third class of profiles is represented by filter 3.175 (C_2H_2, HCN), which is placed right in the centre of an extremely strong absorption feature characteristic of C-star spectra (Fig. 2). Observations in this spectral region are a very powerful tool in understanding the upper photosphere. Here, the inner central part of the intensity profile can be described by an extended plateau due to the strong molecular opacity. All the filters defined around 12 μm – where C_2H_2 has an enhanced absorption – also belong to this class.

The second class of profiles has a behaviour in-between that of the two illustrated before with an indication of an outer dust shell around 8 AU. It is represented by filter 9.975 ("cont") and covers the behaviour of the filter at 11.025 μm plus those defined in the 3 μm region (except 3.175 μm).

In Fourier space, the three representative visibility profiles also differ markedly (lower left panel of Fig. 3). The UD function, computed by fitting the point at visibility[2] $V = 0.3$ of the 3.175 μm profile (for details, see Sect. 5), is shown for comparison in Fig. 3. The visibility profiles from the model and the UD differ at visibility <0.2, and in this region the model profile is less steep and has a less pronounced second lobe compared with the UD.

In the right panel of Fig. 3 we present the intensity and visibility profiles for the phase of maximum luminosity of the reference model without mass-loss. As expected from the model structures, the intensity profiles are more compact than those for models with mass-loss. In the intensity profile corresponding to the filter 9.975 around 1.3 AU, a peak related to the molecular opacity of C_3 is visible. Jørgensen et al. (2000) showed that C_3 is particularly sensitive to the temperature-pressure structure and, hence, tends to be found in narrower regions than other molecules. The peak visible at 3 AU of the profile of the model D1 is produced mainly by C_3 but also produce other molecular and dust opacity contributions. These 9.975 μm peaks in the intensity profiles mean a marginally "ring"-type appearance of the disc. The shape of the intensity profiles for the models without mass-loss can be classified as having small to moderate limb-darkening (S03). In the Fourier space, the visibility profiles of the three filters for the series N look very similar, apart from tiny differences especially in the second lobe. In all cases, they can be approximated well by a UD in the first lobe.

Plots of theoretical continuum profiles for both reference models are very similar to UDs. The classification of filters is also valid for all other models in our sample listed in Table 1.

4. Synthetic profiles for broad-band filters

We also investigated intensity and visibility profiles for the broad-band filters J, H, K, and L', because several observations of C-stars exist in these filters.

In Fig. 4, the resulting broad-band visibility profiles computed for the maximum phase of the reference models are shown together with the corresponding UD visibility, which was

[2] All the visibility values V have to be interpreted as normalised visibilities V/V_0.

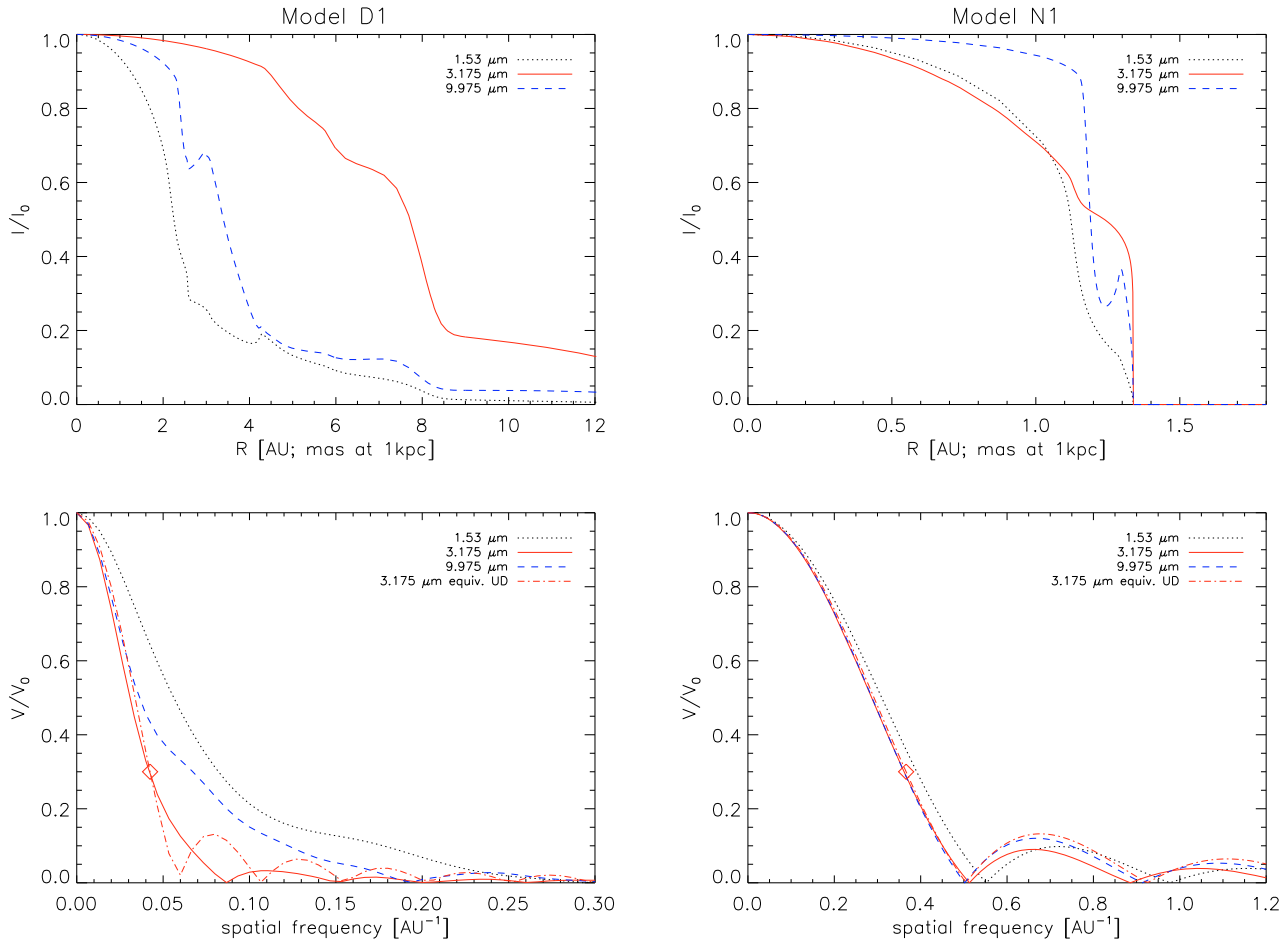

Fig. 3. Intensity and visibility profiles for the narrow-band filters at the maximum phase of the mass-loss model D1 on the left side, and the model without mass-loss N1 on the right side. All the opacities are included in the computations. Profiles for three representative filters are shown together with the equivalent UD function for the 3.175 μm filter. The UD is fitted to the visibility point $V = 0.3$ marked with the diamond (details in Sect. 5).

calculated with the one-point-fit method at $V = 0.3$. In the case of model D1 (with mass-loss), the broad-band profiles exhibit a completely different behaviour from that of the UD. The slopes of the model profiles are always less steep than the corresponding UD at $V \lesssim 0.2$. The synthetic visibility profile shows a characteristic tail-shape instead of the clearly pronounced second lobe in the UD. The broad-band visibilities for the model N1 are represented well by a UD and, as in the case of the narrow-bands, the major (but small) differences occur in the second lobe of the profiles.

When comparing observations with in a broad-band filter, particular attention must be paid to the smearing effect (also known as bandwidth smearing) affecting the measurements (Davis et al. 2000; Kervella et al. 2003; Verhoelst 2005). This is the chromatic aberration caused by observations never being monochromatic but integrated over a certain wavelength range defined by the broad-band filter curve. Furthermore, each physical baseline, B, corresponds to a different spatial frequency u with $u = \frac{B}{\lambda}$. Calculated at a given projected baseline, a broad-band visibility will result in a superposition of all the monochromatic profiles over the width of the band.

According to Kervella et al. (2003) and Wittkowski et al. (2004), the bandwidth smearing is stronger at low visibilities close to the first zero of the visibility profile. We demonstrated that the shape of the profile also plays an important role in the smearing effect.

We investigated this effect with the help of our reference models in the J, H, K, and L' filters. As explained in Sect. 2.2, the broad-band profile was computed by dividing the broad-band interval into ten narrow-band subfilters and then averaging the resulting profiles. To take into account the bandwidth smearing, we again divided the broad-band interval into the same set of 10 narrow-band subfilters. The spatial frequencies were then converted from AU^{-1} to baselines in meters, fixing the distance for an hypothetical object (500 pc) and using as corresponding "monochromatic wavelength" the respective central wavelength of the narrow-band filter. The resulting broad-band profile was then obtained using the above Eq. (2).

Figure 5 illustrates the bandwidth-smearing effect in the K band for the two reference model atmospheres (D1 on the left and N1 on the right). In the upper panels, it is clearly visible in the upper panels that the profiles of the narrow-band subfilters reach the first zero at different baselines. The bandwidth-smearing causes the broad-band profile to never reach zero, as noted in Kervella et al. (2003). We compared the resulting visibility curve with a corresponding one obtained without taking into account the bandwidth effect. The result of this experiment can be seen in the lower panels of Fig. 5, where we plot the difference (in percentage) between the visibility with

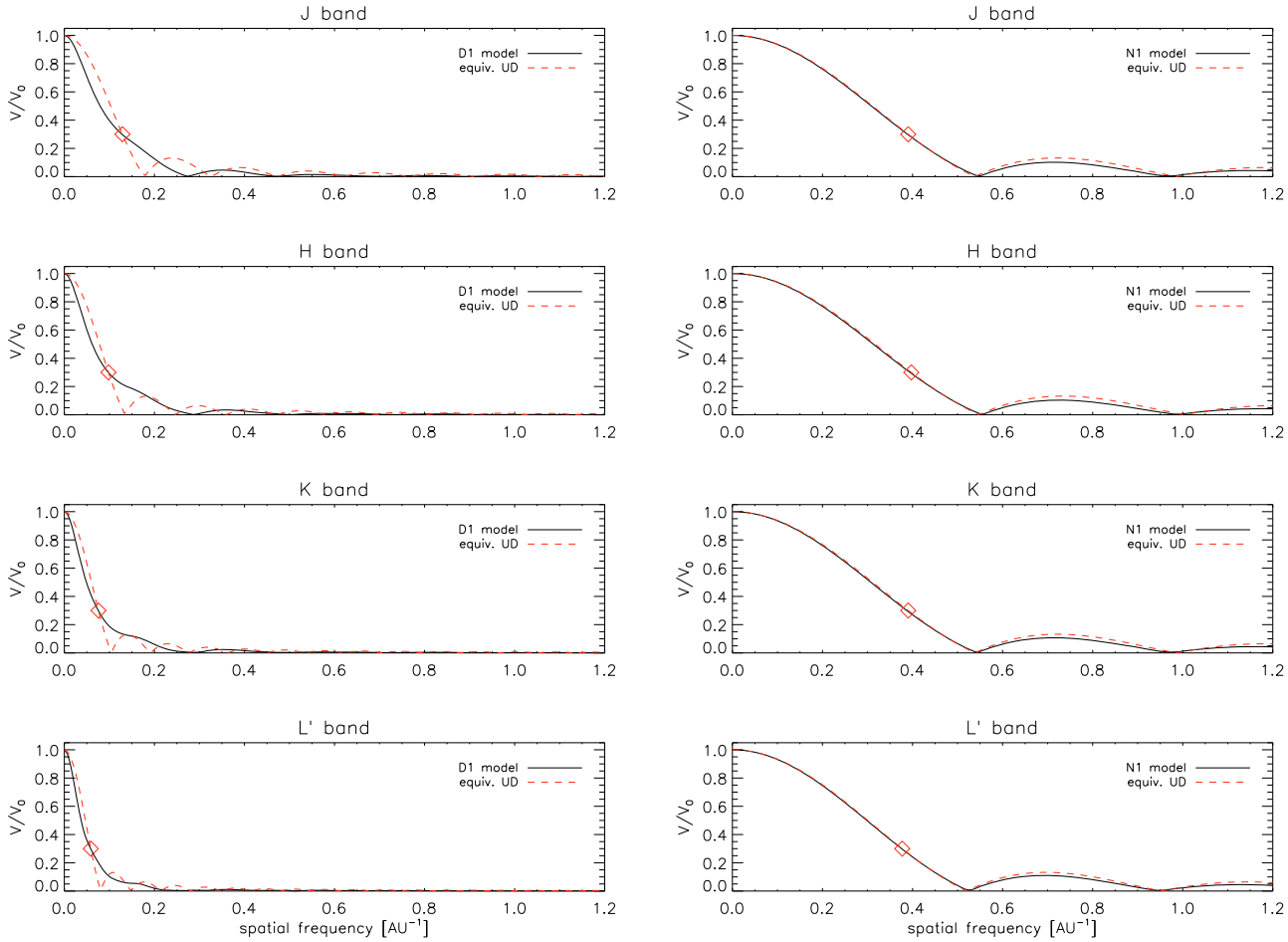

Fig. 4. Visibility profiles computed in broad-band filters for the maximum phase of the model D1 with mass-loss on the left side, and the model N1 without mass-loss on the right side. The solid line corresponds to the model, while the dashed line is the equivalent UD computed by fitting one point at visibility $V = 0.3$.

and without taking into account the bandwidth smearing (BW and NBW respectively). For both types of models – with and without mass-loss – the smearing accounts for the differences in the profiles, which at certain baselines reaches more than 70%. For model N1, the major difference occurs close to the first and the second zero and is negligible elsewhere (as already shown in Kervella et al. 2003; Wittkowski et al. 2004), while in the case of the model D1 the behaviour of the relative difference is less obvious. This result is also confirmed for the other broad-band profiles. However, it obviously depends on the shape of the visibility profile and hence on the model.

In all the cases, we conclude it is important to compute accurate profiles by taking into account the bandwidth smearing.

5. Uniform disc (UD) diameters

For all models in the sample and all considered filters, we computed the equivalent UD-radii using three different methods: (i) a single-point fit at visibility $V = 0.3$; (ii) a two-point fit at visibilities $V = 0.1$ and 0.4; and (iii) finally a non-linear least squares fit using a Levenberg-Marquardt algorithm method, and taking into account all the points with visibility $V > 0.1$. As emphasised in Sect. 5 of Ireland et al. (2004a), none of these procedures are fully consistent because the UD does not represent the true shape of the profile (especially in the case of models with mass-loss). However, the UD is often chosen to interpret interferometric data with a small sampling of the visibility curve. Thus, the three different methods were used in this work to investigate the influence of the visibility profile sampling, in particular when only a few visibility measurements are available. We used the visibility $V = 0.3$ for the one-point-fit following Ireland et al. (2004a,b), who identified this point as a good estimator of the object size. While this is true for the M-type models presented in Ireland et al. (2004a,b), it is not obvious for our C-rich models with mass-loss, which are very far from exhibiting a UD behaviour (Sect. 3). However, keeping in mind that a UD is a first approximation, we also used this value for our computations of the one-point fit.

The aim of this section is to study the behaviour of the UD-radius versus both wavelength and phase, as well as the dependence on the different parameters of the models.

As we pointed out previously, while for the M-type stars the continuum radius can be measured around 1.04 μm (e.g. Jacob & Scholz 2002), our calculations show that the C-star spectra do not contain any suitable window for this determination. However, the continuum radius is a relevant quantity to modelling the stellar interior and pulsation. Therefore, we computed for our sample of dynamic model atmospheres a set of profiles by taking into account only the continuous gas opacity. The resulting profiles correspond to the pure theoretical continuum absorption of the models. An equivalent UD-continuum radius was computed for this theoretical "pure-continuum" profile. This

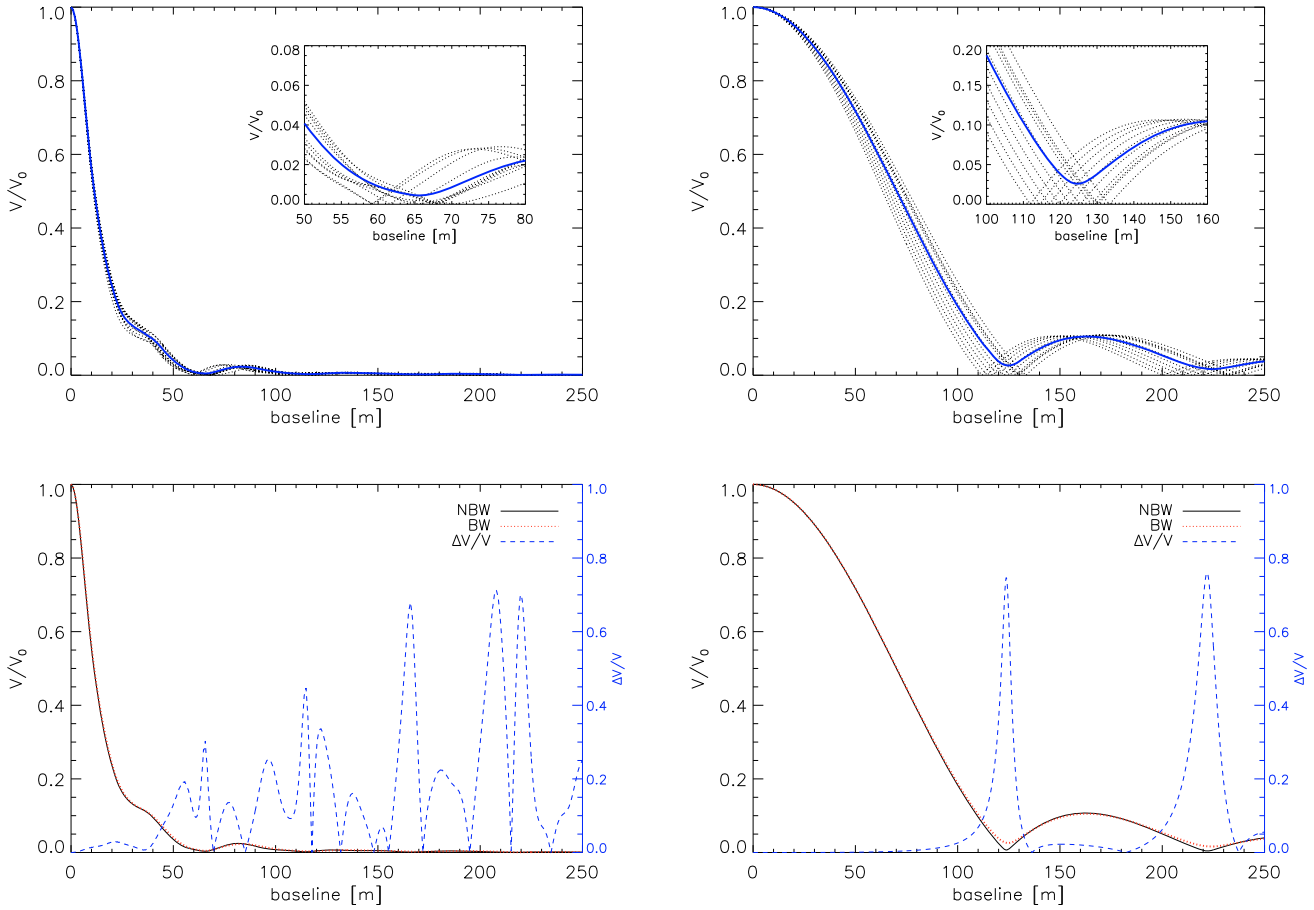

Fig. 5. Representation of the bandwidth smearing effect for the phase maximum of the model D1 (*left panels*) and N1 (*right panels*) in the *K*-band. In the upper panels, visibility profiles are shown as a function of baseline for the individual narrow-band subfilters (dotted lines) and for the resulting broad-band filter (solid line), computed by taking into account the bandwidth smearing. In the inset, a zoom of the region around the first zero is represented. The lower panels show the visibility profiles computed with bandwidth smearing (BW, solid line), and profiles computed neglecting the effect (NBW, dotted line). The dashed lines present the difference between the two profiles (scale on the right *y*-axis).

allows us to study how the UD-continuum radius depends upon wavelength and phase and may provide a possibility of converting observed radii into the continuum radius.

5.1. Uniform disc radii as a function of wavelength

The UD-radii resulting from least square fits at the maximum phase of all models are plotted versus wavelength in Fig. 6. They are scaled to $R_\star$ to minimise the effects of the initial stellar parameters and enhance the effects of the dynamics and dust formation. The UD-continuum radii are represented with the cross symbols for D1 (upper panel) and N1 (lower panel). The major difference is found between models with and without mass-loss. In both cases, the UD-radius generally increases with wavelength, but this behaviour is more pronounced for mass-loss models. At 3.175 μm, there is a notable "discontinuity" (value significantly higher than its surroundings) in the UD-radius due to the high C_2H_2 opacity. The UD-continuum radius is almost completely independent of wavelength and can thus be adopted as a good reference radius (although it is not observable for C-stars!). In fact, a small increase in its size can hardly be noted at longer wavelengths (see Fig. 6), and at 1.6 μm the minimum opacity of H^- is visible. The ratio of the apparent size of the continuum radius at 11 μm to that at 2.2 μm is 1.14 in the case of the model with mass-loss D1 and 1.06 for the model without mass-loss N1. This change in apparent size can be explained by the electron-hydrogen continuum, according to Tatebe & Townes (2006). All the models show a value of UD-continuum radius that is lower than the stellar radius $R_\star$. This is a consequence of the definition of $R_\star$.

Comparing the effect of the different model parameters, we can say that model extensions increase with decreasing effective temperature and higher mass-loss values. The models D1 and D2 for example are identifiable as having a higher mass-loss rate for D2 because of the different period and f_L value. The resulting UD-radii for D2 are systematically higher than that for D1. D5 has a higher piston velocity, and consequently a higher mass-loss, compared to D4, and the UD-radii obtained are larger. A comparison between D1-D2 and D4-D5 in Fig. 6 shows that the effect of the mass-loss rate on the UD-radius is larger beyond 3 μm. The model D3 has a systematically larger UD-radii than the one in the model D4 for the region between 1 and 2 μm and at 9 μm. At 3.175 μm, the trend is inverted, while for the other filters at 3 μm and at the longer wavelengths, the resulting UD-radii is the same for the two models. D3 and D4 differ in terms of temperature (2600 K for D3 and 2800 K for D4), piston velocity, period, and f_L, while the resulting mass-loss rate is quite similar.

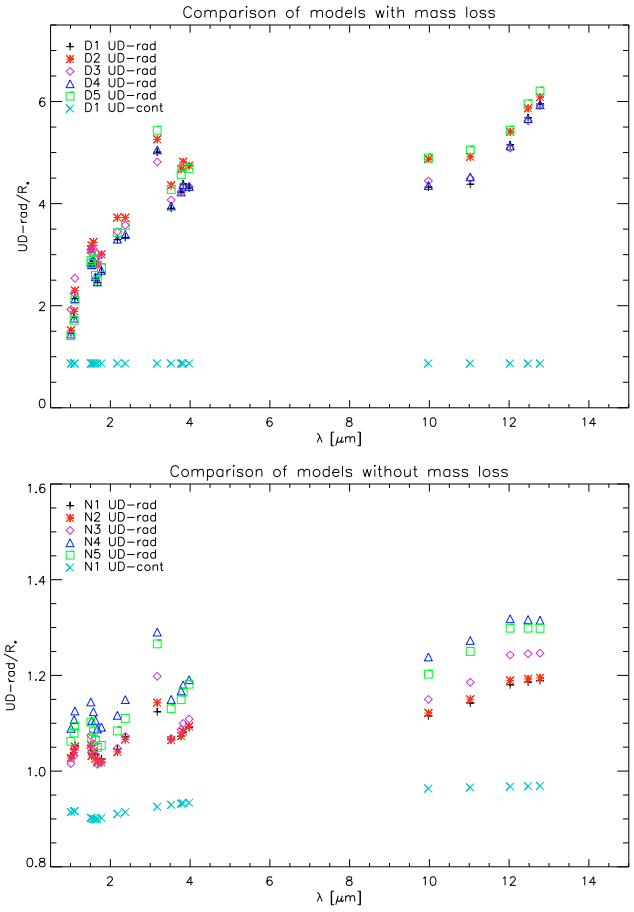

Fig. 6. UD-radii versus wavelength for the maximum phase of different models with (*upper panel*) and without (*lower panel*) mass-loss. The cross symbol represents the UD-continuum radius computed for the two reference models (D1, N1). The method used for the UD determination is a least squares fit using all the points of the synthetic profile with visibility >0.1.

On the other hand, in the absence of dusty winds the models with the same parameters except for C/O (N2 versus N3) have very similar radii. The difference is barely detectable at 3 μm and at longer wavelengths. If, besides different C/O ratios, the temperature of the model also changes (e.g., as between N4 and N5), the resulting UD-radii show more pronounced differences. The UD-radii of N1 always overlap with that of N2, even if the models have different temperatures (higher for N1), luminosity (higher for N2), and period (longer for N2). N3 and N4 have all the same parameters except for the piston velocity, and the resulting UD-radii is larger for the second model, which has a higher value of $\Delta u_{\rm p}$. Model N4 is also the most extended among its subgroup.

5.2. Separating models observationally

Compared with classical hydrostatic models, the dynamic model atmospheres provide, a self-consistent treatment of time-dependent phenomena (shock propagation, stellar wind, dust formation). It is thus of course highly interesting if observed UD-radii at different wavelengths can be used to distinguish between the different models and then assign a given model to a given star.

If the model UD-radii are *not* scaled to their respective $R_\star$, the D models differ between 30% and 50%. These differences should be detectable given the typical distance uncertainties of 20%. However, as discussed above, this would mostly separate the effects of the fundamental stellar parameters (initial radius, luminosity) and allows to differentiate between N and D models, but dynamic effects within each series are only of the order of between 10% and 25%. This can be seen in Fig. 6 or if one scales each model to e.g., its UD-radius in the K-band. The latter approach would be the most sensitive since it eliminates errors in the distance (provided the measurements were completed at the same pulsating phase, better within the same pulsation cycle). Assuming that individual UD-radii can be determined with an accuracy between 5% and 10%, the dynamic effects are (barely) identifiable in the D models. The most sensitive wavelengths in this respect would be filters in the *K*- and *L*-band. The *N*-band shows a similar sensitivity to dynamic effects, although at a reduced observational accuracy. For the N models, these effects are less then 10%, the largest difference again occurring redward of the *K*-band. Nevertheless, the optimal strategy for choosing the correct dynamic model is to combine spectroscopic and interferometric observations.

Finally, we note, that for a larger grid of models (e.g., Mattsson et al. 2009), a wider separation of models might become evident. This will however be the subject of a future paper.

5.3. UD-radii as a function of time

The behaviour of the UD-radius as a function of phase predicted by the models is rather complex, especially in the case of mass-losing models. In Fig. 7, the UD-radius at a given wavelength/filter versus phase is plotted for the two reference models. The presence of molecular and dust opacities increases the UD-radius significantly compared to the UD-continuum radius. In both types of models, we can observe the periodic movement in the stellar interior, which is pronounced to a different degree for different models of Table 1. The periodic variation in the UD-radius in all the models without mass-loss reflects how the movement of the complete atmosphere closely follows the pulsation. The time scales introduced by dust formation in the atmosphere of the models with mass-loss may deform the sinusoidal pattern, a behaviour that can be reproduced by outer layers that do not move parallel to the inner ones. This is represented well in Fig. 2 of Höfner et al. (2003), but one should keep in mind that the movement of theoretical mass shells should not be directly compared to the changes in the atmospheric radius-density structure that we observe by interferometric measurements.

From the lower three panels of Fig. 7 (no mass-loss), it is obvious that there is no significant difference between the UD-radius and UD-continuum radius for the model N1, especially for the 1.53 μm and 9.975 μm filter close to minimum luminosity. We find the largest difference for the maximum luminosity (ϕ = 0), where the ratio of the UD-radius to the UD-continuum radius is 1.09 for the filter 3.175 μm and 1.04 for the other two filters. For the model D1 (upper panels), the value of the same ratio is 3.03 for the filter 1.53 μm, 4.29 for 3.175 μm, and 4.12 for 9.975 μm, much higher than the values found for the models without mass-loss.

The three different fitting methods provide mostly the same result in the case of the model without mass-loss, while in the case of models with mass-loss, the UD-radius is smaller for the first 2 methods (one- and two-points fit) than for the least squares result. This last result can be explained by going back to our initial classification of profiles (Sect. 3). The first and third class of profiles belong to the "uncommon" profiles of S03, which cannot be approximated by UD functions. The third class of profiles

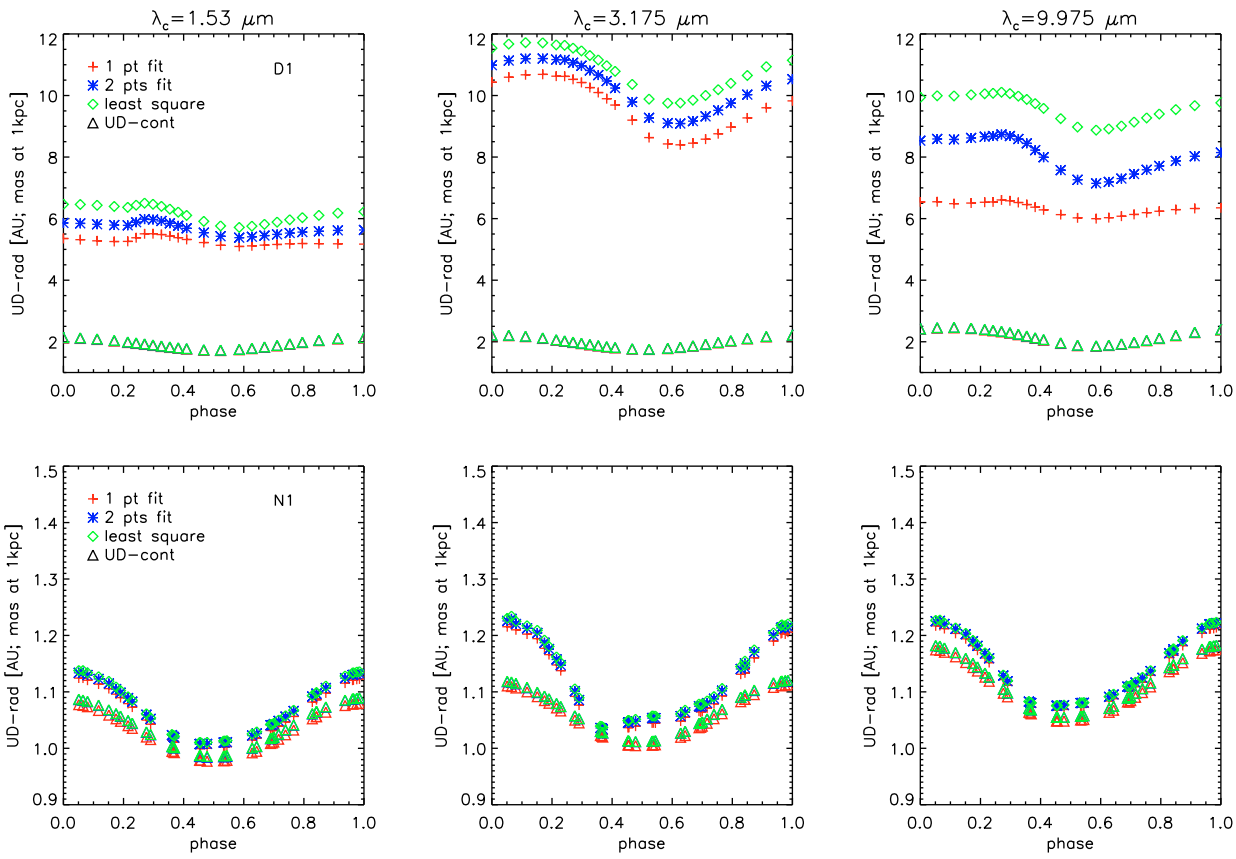

Fig. 7. UD-radii versus phase are shown for three different narrow-band filters. The three upper panels represent results for the dynamic model D1 with mass-loss, the three panels at the bottom being for the model N1 without mass-loss. Triangles are for UD-radius computed by taking into account only continuum opacity. For the continuum, the same symbol is used for the different methods because there is no appreciable difference between the results. Crosses, stars, and diamonds represent the different methods (one point, two points, least squares, respectively) used for fitting the visibility profiles of models with UDs.

(9.975 μm) in particular deviates the most from a UD (see Fig. 3).

Even after increasing the number of fitting points, the resulting UD-radius cannot be considered reliable because of the particular shape of the profiles. From Fig. 7, for the narrow-filter it is also clear that it is impossible to define a single, phase-independent scaling factor that enables the UD-radii to be converted to the UD-continuum radii.

We also computed the equivalent UD-radii and UD-continuum radii for the broad-band filters. The results are shown in Fig. 8. The broad-band has the effect of smoothing the visibility profile as can be inferred in the UD-radii behaviour versus phase from the smaller amplitude of the radius variation. As for the narrow-band, in the case of broad-band filters the UD-radius versus phase for the set of models D also shows a behaviour that is not synchronised with the pulsation. The ratio of the UD-radius to UD-continuum radius is not constant with phase and/or with wavelength. For the phase zero, it corresponds to 2.08 in J, 2.83 in H, 2.14 in K, and 2.54 in L' band. In the lower panels of Fig. 8, where the model N1 is represented, the resulting UD-radius is always closer to the UD-continuum radius. The ratio of the UD-radius to the UD-continuum radius for the phase zero is almost constant: 1.03 for J and H, 1.04 for K and L'. Again, the amplitudes of variation in the radius for the N models are smaller than for the narrow-band filters, and the variation follows the near-sinusoidal behaviour of the inner layers.

For the broad-band filters, the difference in the fitting methods confirms the trend found for the narrow-band case. For the models with mass-loss, the one-point and two-points fit methods produce smaller UD-radii than those produced by the least squares method. The UD-radii, resulting from different methods, agree closely in the case of models without mass-loss and the same result is also obtained for all the UD-continuum measurements.

The dependence of UD-radius on the pulsation cycle is not covered by this contribution, and it will be topic of a future contribution.

5.4. Comparison with M-type stars

Compared to the M-type stars, for the C-stars we emphasise the lack of a spectral window for measuring a pure continuum radius. A model-dependent definition of the continuum radius is thus needed for the cool carbon stars. In Ireland et al. (2004a), the phase variation in filter radii in units of the parent star radius R_p[3] is represented for different near-continuum narrow and broad-band filters. They demonstrate how measurements of radii in near-continuum band passes are affected by molecular contaminations that mask the geometrical pulsation. This

[3] R_p is defined as the Rosseland radius that "the Mira variable would assume if the pulsation stopped and the stratification of the star becomes static" (Jacob & Scholz 2002).

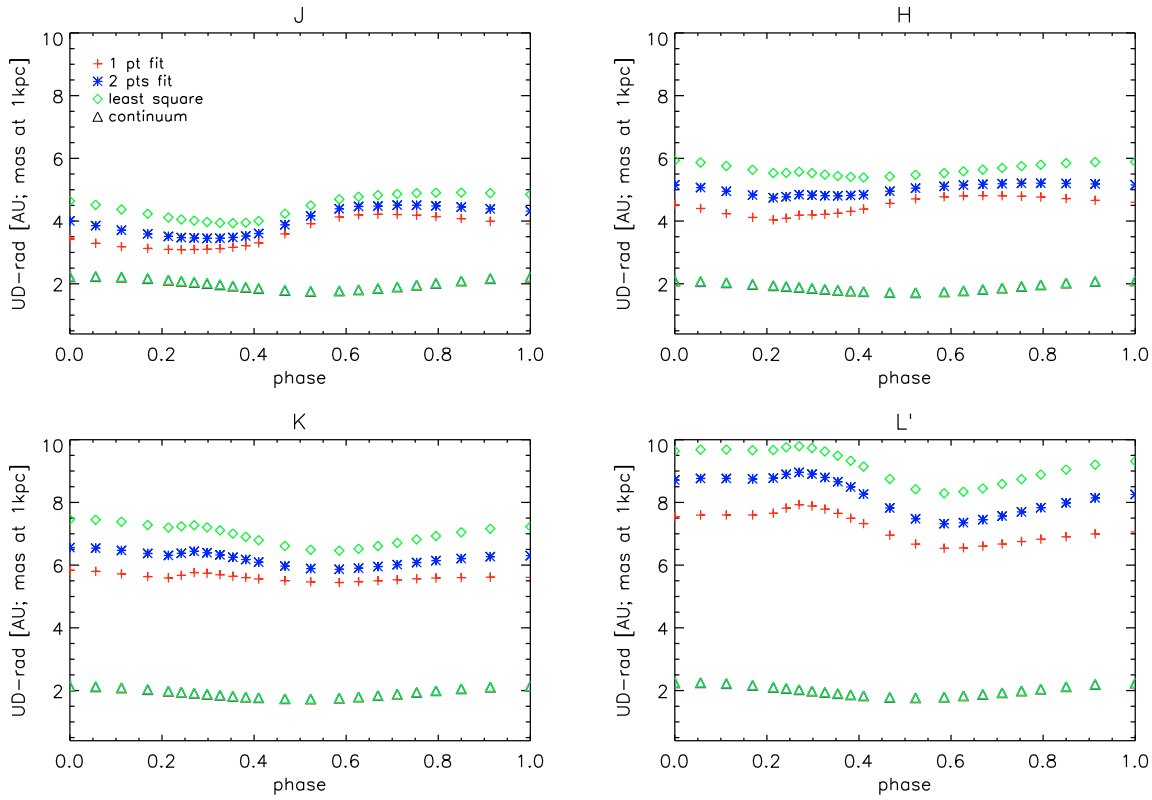

Fig. 8. UD-radius versus phase for *JHKL′* broad-band filters. The four panels show the results for the model D1 with mass-loss.Plot symbols are the same as in Fig. 7.

contamination is negligible only close to the visual maximum. Other suitable band passes for measuring the pulsation of the continuum layers for M-type stars are the broad-band filters *J* and *H*, or the sub-bandpasses of *H* and *K*.

It is difficult to complete a consistent comparison between the UD-radii computed in this work for C-stars and the resulting UD-radii of Jacob & Scholz (2002) for M-type stars because of the intrinsic differences between the modelling approaches, and because of the different stellar parameters. However as a general statement we can say that the ratios of UD-radii to UD-continuum that we obtain are systematically larger for our models with mass-loss than those presented for M-type stars in Figs. 4 and 5 of Ireland et al. (2004a). More comparable are the resulting ratios for models without mass-loss. The largest difference is caused by the strong molecular (first of all C_2H_2) and dust opacities that characterise the C-star spectra. The UD-radius increases with wavelength and in the case of carbon-rich model atmospheres with mass-loss, this increase is larger than that found by Jacob & Scholz (2002) for M-type stars. In particular, the ratio of the UD-radius in *J* to the UD-radius in *L′* for our model D1 at phase zero is 2.07, while for the M-type models presented in Fig. 4 and Fig. 5 of Jacob & Scholz (2002), it is 1.4 in the case of largest discrepancy (phase 1.5). The same ratio for our N1 model is 1.03, meaning that this model without mass-loss shows an increase in the UD-radius with wavelength lower than that of the M-type stars.

6. Conclusions

We have presented, for the first time, a theoretical study of the intensity and visibility profiles computed for a set of dynamic model atmospheres of C-rich AGB stars. The main results of our investigation can be summarised as follows:

- The profiles computed in the narrow-band filters for our set of models can be divided into 3 morphological classes mainly according to wavelength region, with the exception of the filter located at 3.175 μm in the middle of a strong absorption feature characteristic of C-star spectra. This filter shows a behaviour more closely related to one of the narrow-band filters in the region around 12 μm than to the surrounding wavelength range. We have chosen three filters to represent the morphology of intensity and visibility profiles: 1.53, 9.975, and 3.175 μm, for the first, second, and third class, respectively. The intensity profile of the first class is characterised by a limb-darkened disc followed by a tail-shape with a bump and a peak. The 3.175-like profiles show an extended plateau due to strong molecular opacity. The second class is intermediate between the other two.
- The morphology of the profiles (narrow and broad-band) of models with mass-loss is very far from the UD shape. Models without mass-loss, and all theoretical continuum profiles can be approximated quite well by a UD.
- Bandwidth smearing affects the resulting broad-band profiles with an error of about 70% for certain baselines. For models with mass-loss, the difference is notable not only close to the first zero but also on the flank of the first lobe of the visibility profile. When comparing models with observations in broad-band, it is important to take this effect properly into account.
- C-star UD-radii are wavelength-dependent. The dependency is stronger in the case of models with mass-loss, in this case the UD-radii also exhibit significant large phase dependence. Around 3 μm and in the *N*-band, the star appears more

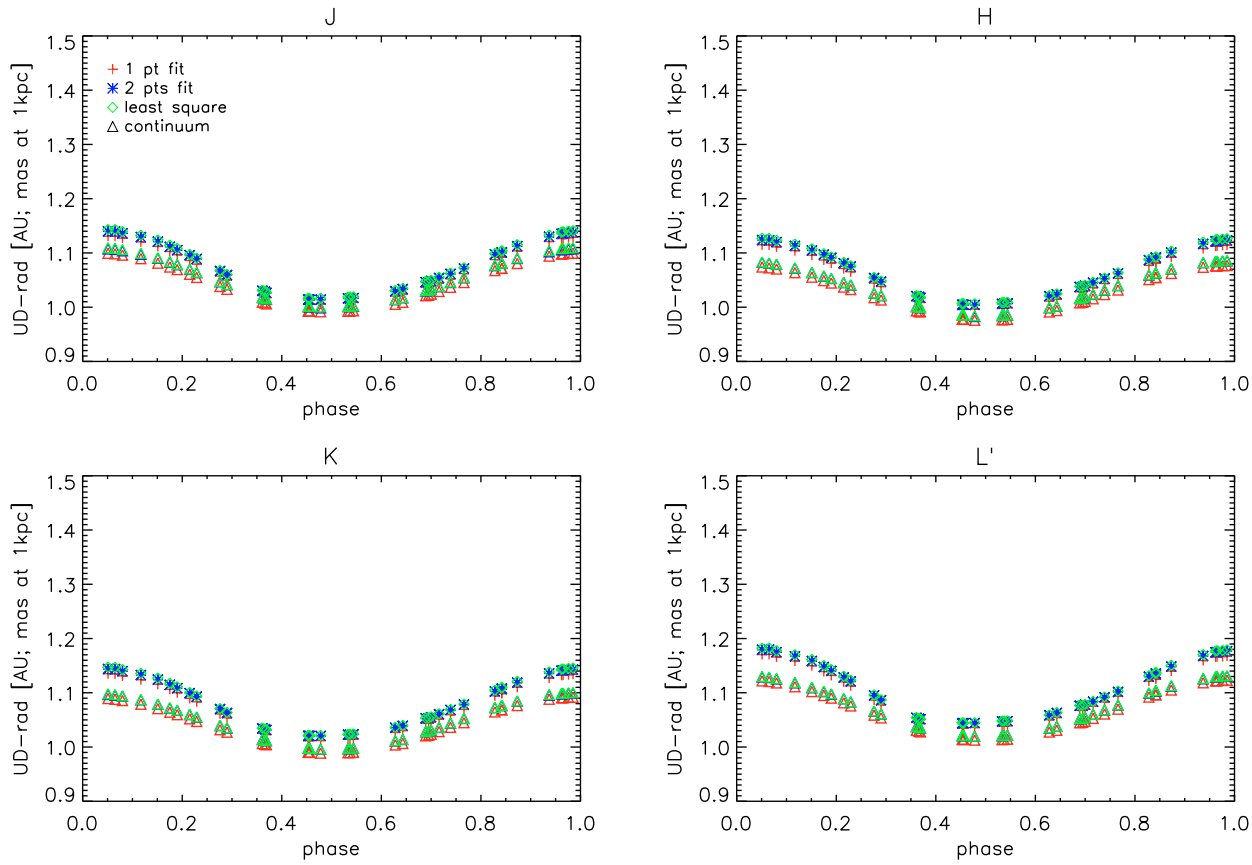

Fig. 9. UD-Radius versus phase for *JHKL'* broad-band filters. The four panels show the results for the model N1 without mass-loss. Plot symbols the same as in Fig. 7.

extended because of C_2H_2 opacity. The UD-continuum radius is mostly independent of the wavelength and phase.

- The extensions of the models increase for higher mass-loss rates and lower temperatures.
- Models with mass-loss show a complicated behaviour of the UD-radius versus phase compared to models without mass-loss. This behaviour is not dependent on the pulsation of the interior.
- Using only one or two points of visibility to determine the UD-radii of objects characterised by strong pulsation and mass-loss,it is shown that the radius of the star is smaller than the one measured using more points (least squares method). In the case of models without mass-loss, the different methods of fitting yield the same UD-radii.
- The UD-radius is very close to the UD-continuum radius in the case of models without mass-loss.
- The trend of the UD-radii versus phase in broad-band is smoother than in the case of the narrow-band filters.
- In contrast to O-rich stars, for C-rich stars no spectral windows for observing the continuum radius are available in the case of C-stars, and some assumptions based on models are necessary. A useful replacement for a measured continuum radius is the UD-continuum radius defined in Sect. 5, which is basically independent of wavelength and pulsation phase.
- The difference in the UD-radii between the models should be detectable observationally, in particular in the *L*-band where MATISSE (Lopez et al. 2006) will provide new observational opportunities.
- The radius computed with the UD function must be considered only as a first guess of the true size of the star. The intensity and visibility profiles of a C-star, especially in the case of models producing mass-loss, are very far from being UD-like.

A comparison of the dynamic models with available sets of observations is under way, and the intensity and visibility profiles of specific models can be provided upon request.

Acknowledgements. This work has been supported by Projects P19503-N16 and P18939-N16 of the Austrian Science Fund (FWF). It is a pleasure to thank T. Verhoelst and T. Driebe for many helpful comments and suggestions. BA acknowledges funding by the contract ASI-INAF I/016/07/0.

References

Aringer, B. 2000, Ph.D. Thesis, University of Vienna
Aringer, B., Nowotny, W., & Höfner, S. 2008, Perspective in Radiative Transfer and Interferometry, ed. S. Wolf, F. Allard, & Ph. Stee, EAS Publ. Ser., 28, 67
Aringer, B., Girardi, L., Nowotny, W., et al. 2009, A&A, accepted
Baschek, B., Scholz, M., & Wehrse, R. 1991, A&A, 246,374
Bessel, M. S., & Brett, J. M. 1988, PASP100, 1134
Bessel, M. S., Brett, J. M., Scholz, M., & Wood, P. R. 1989, A&A, 213, 209
Bessel, M. S., Scholz, M., & Wood, P. R. 1996, A&A, 307, 481
Bracewell, R. N. 1965, The Fourier Transform and its Applications (New York: McGraw-Hill)
Davis, J., Tango, W. J., & Booth, A. J. 2000, MNRAS, 318, 387
Gail, H. P., & Sedlmayr, E. 1988, A&A, 206, 153
Gauger, A., Gail., H. P., & Sedlmayr, E. 1990, A&A, 235, 245
Gautschy-Loidl, R., Höfner, S., Jørgensen, U. G., & Hron, J. 2004, A&A, 422, 289 (GL04)
Goebel, J. H., Bregman, J. D., Wittenborn, F. C., & Taylor, B. J. 1981, ApJ, 246, 455

Gustafsson, B., Edvardsson, B., Eriksson, K., et al. 2008, A&A, 486, 951
Hofmann, K.-H., Scholz, M., & Wood, P. R. 1998, A&A, 339, 846
Höfner, S., Gautschy-Loidl, R., Aringer, B., & Jørgensen, U. G. 2003, A&A, 399, 589
Höfner, S. 2005, 13th Cambridge Workshop on Cool Stars, Stellar Systems and the Sun, ed. F. Favata, G. A. J. Hussian, & B. Battrick, ESA SP-560, 335
Höfner, S. 2007, Why Galaxies Care About AGB Stars, ed. F. Kerschbaum, C. Charbonnel, & R. F. Wing, ASP Conf. Ser., 378, 145
Höfner, S. 2009, Cosmic Dust - Near and Far, ed. Th. Henning, E. Grün, & J. Steinacker, ASP Conf. Ser., in press [arXiv:0903.5280]
Hron, J., Loidl, R., & Höfner, S., et al. 1998, A&A, 335, L69
Hron, J., Aringer, B., Nowotny, W., & Paladini, C. 2008, Evolution and Nucleosynthesis in AGB stars, ed. Guandalini, R., Palmerini, S., & Busso, M., AIP Conf. Proc., 1001, 185
Hughes, S. M. G., & Wood, P. R. 1990,A&A, 99, 784
Jacob, A. P., & Scholz, M. 2002, MNRAS, 336, 1377
Jørgensen, U. G. 1997, in Molecules in Astrophysics: Probes and Processes, ed. E. F. van Dishoeck, IAU Symp., 178 (Kluwer), 441
Jørgensen, U. G., Hron, J., & Loidl, R. 2000,A&A, 356, 253
Joyce, R. R. 1998, AJ, 115, 2059
Kervella, P., Thévenin, F., Ségrasan, D., et al. 2003, A&A, 404, 1087
Iben, I., & Renzini, A. 1983, ARA&A, 21, 271
Ireland, M. J., Scholz, M., & Wood, P. R. 2004a, MNRAS, 352, 318
Ireland, M. J., Scholz, M., Tuthill, P. G., & Wood, P. R. 2004b, MNRAS, 355, 444
Lançon, A., & Wood, P. R. 2000, A&AS, 146, 217
Lederer, M. T., & Aringer, B. 2009, A&A, 494, 403
Loidl, R., Lançon, A., & Jørgensen, U. G. 2001, A&A, 371, 1065
Lopez, B., Wolf, S., Lagarde, S., et al. 2006, SPIE, 6268, 31
Mattsson, L., Wahlin, R., & Höfner, S. 2009, A&A, subm.
Nowotny, W. 2005, Ph.D. Thesis, University of Vienna
Nowotny, W., Aringer, B., Höfner, S., et al. 2005a, A&A, 437, 273
Nowotny, W., Lebzelter, T., Hron, J., & Höfner, S. 2005b, A&A, 437, 285
Nowotny, W., Aringer, B., & Höfner, S. 2009 A&A, submitted
Rouleau, F., & Martin, P. G. 1991, ApJ, 377, 526
Scholz, M. 2003, Proc. SPIE, 4838, 163 (S03)
Scholz, M., & Takeda, Y. 1987, A&A, 186, 200
Tatebe, K., & Townes, C. H. 2006, ApJ, 644, 1145
Tej, A., Lançon, A., & Scholz, M. 2003a, A&A, 401, 347
Tej, A., Lançon, A., Scholz, M., & Wood, P. R. 2003b, A&A, 412, 481
Verhoelst 2005, Ph.D. Thesis, University of Leuven
Willson, L. A. 2000, ARA&A, 38, 573
Wittkowski, M., Aufdenberg, J. P., & Kervella. P. 2004, A&A, 413, 711
Woitke, P. 2003, in Modelling of Stellar Atmospheres, ed. N. Piskunov, W. W. Weiss, & D. F. Gray, IAU Symp., 210, 387
Yamamura, I., & de Jong, T. 2000, ESA SP, 456, 155

A&A 533, A27 (2011)
DOI: 10.1051/0004-6361/201116538

Astronomy & Astrophysics

Determination of the stellar parameters of C-rich hydrostatic stars from spectro-interferometric observations⋆

C. Paladini[1], G. T. van Belle[2], B. Aringer[3], J. Hron[1], P. Reegen[1,⋆⋆], C. J. Davis[4], and T. Lebzelter[1]

[1] Department of Astronomy, University of Vienna, Türkenschanzstrasse 17, 1180 Vienna, Austria
e-mail: claudia.paladini@univie.ac.at
[2] European Southern Observatory, Karl-Schwarzschild-Str. 2, 85748 Garching bei München, Germany
[3] INAF-OAPD, Vicolo dell'Osservatorio 5, 35122 Padova, Italy
[4] Joint Astronomy Centre, 660 North A'ohōkū Place, University Park, Hilo, Hawaii 96720, USA

Received 18 January 2011 / Accepted 20 May 2011

ABSTRACT

Context. Giant stars, and especially C-rich giants, contribute significantly to the chemical enrichment of galaxies. The determination of precise parameters for these stars is a necessary prerequisite for a proper implementation of this evolutionary phase in the models of galaxies. Infrared interferometry opened new horizons in the study of the stellar parameters of giant stars, and provided new important constraints for the atmospheric and evolutionary models.
Aims. We aim to determine which stellar parameters can be constrained by using infrared interferometry and spectroscopy; for C-stars in particular we aim to determine the precision that can be achieved as well as its limitations.
Methods. For this purpose we obtained new infrared spectra and combined them with unpublished interferometric measurements for five mildly variable carbon-rich asymptotic giant branch stars. The observations were compared with a large grid of hydrostatic model atmospheres and with new isochrones that include the predictions of the thermally pulsing phase.
Results. For the very first time we are able to reproduce spectra in the range between 0.9 and 4 μm, and K broad band interferometry with hydrostatic model atmospheres. Temperature, mass, log(g), C/O and a reasonable range for the distance were derived for all objects of our study. All our targets have at least one combination of best-fitting parameters that lies in the region of the HR-diagram where C-stars are predicted.
Conclusions. We confirm that low-resolution spectroscopy is not sensitive to the mass and log(g) determination. For hydrostatic objects the 3 μm feature is very sensitive to temperature variations, therefore it is a very powerful tool for accurate temperature determinations. Interferometry can constrain mass, radius, and log(g), but a distance has to be assumed. The large uncertainty in the distance measurements available for C-rich stars remains a major problem.

Key words. stars: AGB and post-AGB – stars: atmospheres – stars: carbon – stars: fundamental parameters – techniques: spectroscopic – techniques: high angular resolution

1. Introduction

The basic properties and evolutionary status of a star can be determined knowing its mass, luminosity, radius, and chemical composition. Nowadays we are reaching a point where mass estimates are available not only for binary, but also for single objects (see the recent review by Aufdenberg et al. 2009). This major advance has been mainly achieved by establishing interferometry as a standard tool for investigating stars (Wittkowski 2004). The combination of high angular and spectral resolution gives the possibility to study the spatial structure of single stellar objects, which were treated before as point sources only. Red giant stars are very good targets for interferometric investigations because of their extended atmosphere and their brightness in the infrared. These stars are the main contributors to the infrared light and to the chemical enrichment of galaxies. Therefore, an accurate determination of their fundamental parameters is mandatory for a proper implementation in the models of galaxies.

Wittkowski et al. (2001) made a first attempt at deriving the parameters of a sample of asymptotic giant branch (AGB) stars by comparing the spectro-interferometric observations with Kurucz model atmospheres. The uncertainty in parallax and bolometric flux dominate the errors. Recently, Neilson & Lester (2008) determined the fundamental parameters of three M-type stars. They combined infrared interferometry with spectro-photometric observations. The interferometric data were obtained with the VLTI/VINCI instrument and were previously interpreted by using Phoenix and Atlas atmospheric models (Hauschildt et al. 1999; Kurucz 1993, respectively) in the work of Wittkowski et al. (2004, 2006a,b). Neilson & Lester (2008) used the new generation of SAtlas models (Lester & Neilson 2008) for the interpretation of the data: in this way the authors were able not only to determine the fundamental parameters, but also to constrain the atmospheric models they used. The typical approach followed in these works to determine the stellar parameters is: (i) determination of the limb darkened radius by fitting the interferometric observations, the resulting radius is converted into a Rosseland radius; (ii) a linear radius is derived by assuming a distance; (iii) an effective temperature is derived by fitting the SED; (iv) the luminosity is obtained through the radius and

⋆ Appendix A is available in electronic form at http://www.aanda.org
⋆⋆ Deceased 5 February 2011.

Table 1. Target list, available photometry, and variability information.

ID	RA	Dec	J [mag]	H [mag]	K [mag]	L [mag]	$f_{[12\,\mu m]}$ [Jy]	Var. type	Amplitude [mag]	Period [days]
CR Gem	06:34:23.92	+16:04:30.30	3.36	2.07	1.46	0.88[a]	39.31	Lb	1.20 B	250
HK Lyr	18:42:50.00	+36:57:30.89	3.23	2.15	1.62	0.99[b]	22.74	Lb	0.40 V[e]	186[e]
RV Mon	06:58:21.49	+06:10:01.50	3.06	1.96	1.43	0.85[c]	31.13	SRb	2.19 B	131
Z Psc	01:16:05.03	+06:10:01.50	2.11	1.10	0.70	0.41[d]	33.42	SRb	1.30 p	144
DR Ser	18 47 21.02	+05 27 18.60	4.12	2.79	2.08	1.38[a]	15.9	Lb	0.50 V[f]	196[f]

Notes. The amplitude and the period (unless otherwise stated) are derived from the General Catalogue of Variable Stars (GCVS; Samus+ 2007–2009). The band used for amplitude of variability measurement is also reported; "p" denotes photographic plates. [(a)] Kerschbaum et al. (1996a); [(b)] Kerschbaum et al. (1996b); [(c)] Epchtein et al. (1990); [(d)] Bagnulo (1996); [(e)] Beichman et al. (1988); [(f)] Pojmanski (2002).

$T_{\rm eff}$; (v) the gravity and the mass of the star are constrained by comparison with the theoretical models.

The targets of our study are an important subclass of the AGB objects: the carbon-rich AGB stars. According to theory, only stars with a range of mass between 1 and 4 $M_{\odot}$ undergo the third dredge-up during their AGB phase, with the result of increasing their C/O ratio (Iben & Renzini 1983). The spectra of these giants are consequently dominated by the absorption features of carbonaceous molecular species such as CO, CN, HCN, C_2, C_3, and C_2H_2 (Tsuji 1986; Jørgensen et al. 2000; Loidl et al. 2001). As a result, these objects are the main contributors to the C-enrichment of the ISM.

The state-of-the-art model atmospheres for C-stars are very promising, because they are able to produce large grids of models (Aringer et al. 2009; Mattsson et al. 2010) that describe the observed properties of these objects reasonably well. The hydrostatic model atmospheres for C-stars were compared with optical and infrared spectroscopy in Jørgensen et al. (2000), Loidl et al. (2001), and Abia et al. (2010) and references therein. The major difference between an earlier generation of models as used by Jørgensen et al. (2000), and Loidl et al. (2001), and the hydrostatic atmospheres applied in our work (Aringer et al. 2009) is the inclusion of atomic opacities and an update to new and more accurate molecular opacities.

The stellar evolutionary calculations reached a highly sophisticated level as well, being able to include a detailed thermally pulsing phase with third dredge-up, hot-bottom burning and variable molecular opacity (Marigo et al. 2008).

The purpose of this work is to find out which stellar parameters can be determined for weakly variable C-stars (visual amplitude $\leq$2 mag) by using spectroscopy, infrared interferometry, and hydrostatic model atmospheres; and to assess the accuracy. We aim to test the stellar atmospheric models with different techniques and a multiwavelength approach. This is a very important step because errors in the model structure limit quantitative checks of stellar evolution. Our approach in the parameter determination is slightly different from the one adopted by Neilson & Lester (2008) for a few simple reasons: (1) the Rosseland radius is not a direct observable, and in the C-stars (in contrast to M-type AGB stars) there are no windows in the near-infrared where to measure a "continuum" radius (Paladini et al. 2009); (2) it is very rare to obtain simultaneous multiwavelength photometric observations, which is mandatory when dealing with variable stars. Nevertheless, the parameters determined in this work will be compared in a follow-up paper (van Belle et al., in prep.) with that obtained by combining photometric and interferometric observations.

A short description of the acquired observations and of the data reduction for both spectroscopy and interferometry will be given in Sect. 2. The hydrostatic model atmospheres and the methods for determining the observables will be presented in Sect. 3. The approach used to determine the stellar parameters (temperature, C/O, mass, $\log(g)$) is presented in Sect. 4, while in Sect. 5 we summarise the comparison with the evolutionary tracks. We present a detailed discussion of the single objects studied in this work in Sect. 6, followed by a more general discussion of the obtained results (Sect. 7) and the conclusions (Sect. 8).

2. Observations and data reduction

Five mildly variable stars were selected for this investigation: CR Gem, HK Lyr, RV Mon, Z Psc, DR Ser. In Table 1 the coordinates of the objects, near-infrared photometry, and the 12 μm IRAS flux are presented together with period (P) and amplitude (A) of variability. Unless otherwise stated, A and P are derived from the General Catalogue of Variable Stars (GCVS; Samus+ 2007–2009). The amplitude values list the maximum amplitude recorded, and might be based only on few data points, sometimes recorded on photographic plates. More recent observations from the public surveys such as ASAS (Pojmanski 2002) and the Hipparcos Variability Annex (Beichman et al. 1988) show the smaller V amplitude variations, often quite stable over a long period. These more recent values are listed in the discussion of the individual targets (Sect. 6). The objects selected are semiregular or irregular variables. The variability amplitude and the period indicate that the atmospheres of our targets can be represented with hydrostatic models. The literature values of A and P are low compared to dynamic objects such as Mira stars (P longer than one year, and A of several V magnitudes). In the recent grid of dynamic models for C-stars from Mattsson et al. (2010) almost all models with a period lower than 250 days do not develop a stellar wind. The few exceptions are models with extremely low temperature or a very high C/O value. The same applies to the predictions of the previous generations of dynamic models (i.e. Table 1 Gautschy-Loidl et al. 2004). The temperature-density structure of these windless models varies only slightly around the hydrostatic configuration. These small variations of the atmospheric structure are also reflected in the resulting spectra, but as can be seen in Fig. A.1 of Nowotny et al. (2010), the spectra of objects with very mild pulsations and no mass loss do not differ significantly from the corresponding one based on a hydrostatic model. The hydrostatic spherical symmetric approximation will also be checked with interferometric observations (where possible) in Sect. 2.2. We collected for all the targets $IJHKL$ infrared spectroscopy and K broad band interferometric observations.

Table 2. Spectral type, photometry, and effective temperature of the standard stars used for the spectroscopic calibration.

ID	Sp. type	V [mag]	J [mag]	H [mag]	K [mag]	$T_{\rm eff}$ [K]
HIP 92946	A5V	4.62	4.160	4.163	4.085	7880[a]
HIP 33024	F0V	5.753	5.308	5.232	5.088	7400[b]
HIP 5544	F0V	5.160	4.764	4.545	4.393	7500[c]

Notes. The photometry is from the 2MASS All Sky catalogue (Cutri et al. 2003); [(a)] Erspamer & North (2003); [(b)] Masana et al. (2006); [(c)] Solano & Fernley (1997).

2.1. Spectroscopy

The spectra for our targets were obtained with the UIST instrument (Ramsay et al. 2004) on the United Kingdom InfraRed Telescope (UKIRT) as part of the UKIRT Service Programme: `u/serv/1790` and `u/serv/1810`. The first run of observations was on 29 June 2008; the second one on 20, 23, 25, and 26 January 2009. Four grism spectra were collected for every target, covering the following spectral ranges: IJ with wavelengths in the interval[1] [0.862, 1.418] μm; HK with wavelengths in the interval [1.395, 2.506] μm; short L, and long L bands covering [2.905, 3.638] and [3.620, 4.232] μm, respectively. We also obtained spectra for three standard stars to be used for the calibration procedure. The spectral type, photometry, and effective temperature of the standard stars are listed in Table 2. Because our objects were bright, we observed with a 2-pixel (0.24 arcsec) wide slit. Targets and standard stars were nodded along the slit, with spectra being taken in an A-B-B-A sequence to facilitate first-order sky subtraction. Exposure times of 2-coadds × 2 s or 1-coadd × 4 s were used with each grism, depending on the brightness of the source. The nodding sequence was executed twice, resulting in a total integration time of 32 s per source in each grism. The resolution of the spectra ranges between 400 (IJ) and 1800 (long L). HIP 92946 was used to remove telluric features for targets observed in 2008 (HK Lyr, DR Ser), while HIP 33024 and HIP 5544 were used for the 2009 observations (CR Gem, RV Mon and Z Psc, respectively).

Data reduction was performed using the ORAC-DR UIST pipeline (Cavanagh et al. 2003). The subtraction of the sky removes the OH lines and the thermal background emission. At this stage the spectrum is made of a positive and a negative part, which can be extracted. An Argon lamp is used for the calibration of the object in wavelength. Before every target observation a telluric standard was observed. The observations of target and reference star are always carried out in a range of airmass between 1.0 and 1.3. Only in one case we had airmass 1.5. The airmass difference between target and standard is usually of the order of 0.1, which produces a negligible error in the flux calibration. Once object and standard were calibrated in wavelength, the telluric correction was performed. For this purpose we used the routine `IRFLUX` from the Starlink[2] software package. `IRFLUX` divides the standard spectrum by a black body with assigned temperature (the one of the standard). The outcome of this operation is a spectrum that only includes the telluric features and atmospheric and instrumental effects. Finally, the target is divided by this last determined spectrum and the telluric calibration is performed. The standard stars are hot enough to be approximated with a black body in the covered wavelength range.

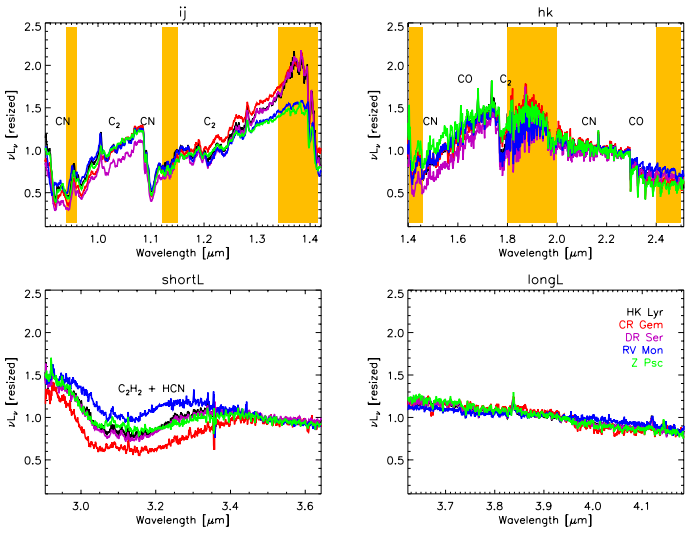

Fig. 1. Comparison between all the spectra of our targets. The main molecular features are indicated. The shaded (yellow) regions are affected by absorption of the Earth's atmosphere.

Once the telluric correction was performed, a few emission lines appeared in the spectrum of the targets. Those are the residual of the atmosphere of the standards, which in this part of the spectrum does not contribute to the continuum (this is flat), but it shows few hydrogen lines. We identified those lines by comparing the spectrum of the standards with the corresponding hydrostatic models from Shulyak et al. (2004). The region where the lines are located was not taken into account in the fitting procedure, neither were the data at the edge of the atmospheric windows (shaded region in Fig. 1).

The reddening correction is always a very delicate task in spectroscopy. Every spectrum was dereddened using the `EXTIN.PRO` IDL procedure (Amôres & Lepíne 2005). The code computes the visible extinction ($A_{\rm V}$) along a path from the Sun to any point in the Galaxy, specified by galactic coordinates and distance. Unfortunately, the distance measurements associated with our objects are very uncertain. We selected three reference distances for each target from the literature: the distance measured by the Hipparcos satellite (Perryman et al. 1997), a distance estimated assuming a constant K magnitude (Claussen et al. 1987), and a distance estimated by Bergeat & Chevallier (2005), which is based on Hipparcos measurements but takes into account three distinct biases (see Sect. 2.3 of Bergeat et al. 2002). Hereafter, the different distances will be indicated with the abbreviation $d_{\rm Ber}$, $d_{\rm Cla}$, $d_{\rm Hipp}$.

The distances for each object are listed in Table 4. The values are in most of the cases very different, but no trend or systematic behaviour can be identified. For the Hipparcos measurements the errors associated to the distances are also given. No error estimation was found in the literature for $d_{\rm Berg}$ and $d_{\rm Clau}$, therefore we assume at least 20% of uncertainty. This corresponds to 40% error on the luminosity.

Although the distances have very different values, the resulting reddening correction is very similar (as expected because these are nearby objects). We tested the effect of the different reddening correction on the estimation of the parameters (in

[1] Although the wavelengths range of the IJ grism starts at 0.86 μm, only the part beyond 0.9 μm is usable because the spectral blocking filter blocks emission (essentially has zero transmission) below this wavelength and, in any case, the instrumental throughput drops considerably towards the I band.

[2] Starlink software is available for downloading on the webpage `http://starlink.jach.hawaii.edu/`.

particular the temperature). The typical shift for the temperature determinations is of the order of 10 K, which is low compared to the error bar.

Except for DR Ser, where no correction was applied (see detailed discussion in Sect. 6.5), we used for our computation the reddening correction estimated for the Hipparcos distance.

2.2. Interferometry

Observations for this investigation were primarily taken with the Palomar Testbed Interferometer (PTI). The PTI was an 85 to 110 m baselines H and K band (1.6 μm and 2.2 μm) interferometer located at the Palomar Observatory in San Diego County, California, and is described in detail in Colavita et al. (1999). It had three 40-cm apertures used in pairwise combination for measurements of stellar fringe visibility on sources that range in angular size from 0.05 to 5.0 milliarcsec, being able to resolve individual sources $\theta > 1.0$ mas in size. The PTI had been in nightly operation since 1997 and was decommissioned in 2009, with minimum downtime during the intervening years. In addition to the carbon stars observed as part of this investigation, appropriate calibration sources were observed as well and can be found in van Belle et al. (2008).

The calibration of the squared visibility (V^2) data is performed by estimating the interferometer system visibility ($V^2_{\rm SYS}$) using the calibration sources with model angular diameters and then normalising the raw carbon star visibility by $V^2_{\rm SYS}$ to estimate the V^2 measured by an ideal interferometer at that epoch (Mozurkewich et al. 1991; Boden et al. 1998), (van Belle & van Belle 2005). Uncertainties in the system visibility and the calibrated target visibility are inferred from internal scatter among the data in an observation using standard error-propagation calculations (Boden et al. 1999). Calibrating our point-like calibration objects against each other produced no evidence of systematics, with all objects delivering reduced $V^2 = 1$.

The PTI's limiting night-to-night measurement error is $\sigma_{V^2_{\rm SYS}} \approx 1.5$–$1.8\%$, the source of which is most likely a combination of effects: uncharacterised atmospheric seeing (in particular, scintillation), detector noise, and other instrumental effects. This measurement error limit is empirically established from the previous study of Boden et al. (1999).

In our sample there is one star, Z Psc, without PTI observations. One visibility measurement taken with IOTA (Infrared Optical Telescope Array) is available in the literature for this object. The visibility point value was obtained in the K-filter ($\lambda = 2.2$ μm, $\Delta\lambda = 0.4$ μm) and is published in Table 1 of Dyck et al. (1996). We will use this value for our investigation.

Table A.1 gives an overview of the observational parameters of the interferometric observations used, namely UT date, baseline, position angle, and the calibrated visibility with associated error.

From the relationship between visibility and uniform disk (UD) angular size, $V^2 = [2J_1(x)/x]^2$, where $x = \pi B \theta_{\rm UD} \lambda^{-1}$, we may establish uniform disk angular sizes for the carbon stars observed by the PTI because the accompanying parameters (projected telescope-to-telescope separation, or baseline, B and wavelength of observation λ) are well-characterised during the observation. This uniform disk angular size will be connected to a more physical limb-darkened angular size in Sect. 4. By plotting the UD diameter versus time, we were able to check the reliability of our approximation with hydrostatic models. From the UD diameter versus position angle the assumption of spherical symmetry is checked. In Fig. 2 we present the interferometric observations for three of our five targets. The missing objects (CR Gem, Z Psc) have only one available measurement. The panels in the first row, identified with the letter "a", represent the measurements for DR Ser. In the row "b" the points for HK Lyr are plotted, and in the row "c" there are the points for RV Mon. In Col. "1" we present the uv coverage. In Col."2" the visibility points are presented versus the baseline. HK Lyr and RV Mon are observed always with the same baseline setup. The variation in the projected baseline is caused by the Earth's rotation. The UD diameter is plotted versus position angle in Col. "3". In Col. "4" the UD diameter are presented versus the visual phase to investigate eventual variations in the angular size that might be caused among other reason by the pulsation of the stars. The phase estimation for RV Mon and DR Ser is based on the visual light curve from the ASAS database (Pojmanski 2002); while for HK Lyr it is based on the light curve from the Hipparcos Variability Annex (Beichman et al. 1988). Small trends can be identified in the case of RV Mon and HK Lyr, they may be caused by cycle-to-cycle variation, but we can neither completely exclude an instrumental problem (see detailed discussion in Sect. 6.3).

3. Hydrostatic models and synthetic observables

For the determination of the parameters we used the new grid of hydrostatic and spherically symmetric model atmospheres of Aringer et al. (2009). They are computed with COMARCS, a programme based on the MARCS code (Gustafsson et al. 1975, 2008) in the version used by Jørgensen et al. (1992) and Aringer et al. (1997). The models are generated assuming hydrostatic local thermal and chemical equilibrium. The molecular and atomic opacity is treated in the opacity sampling (OS) approximation. The parameters that characterise a model are effective temperature, metallicity, $\log(g)$, mass, and C/O.

3.1. Synthetic spectra

Our observed spectra have higher resolution than those of the grid published in Aringer et al. (2009), therefore new synthetic spectra were computed for a subset of the initial grid of hydrostatic models.

We assumed solar metallicity for our targets. The subset of new spectra covers the following parameters[3]: $2400 \le T_{\rm eff} \le 4000$ K with steps of 100 K; $Z/Z_\odot = 1$; $-1.0 \le \log(g[{\rm cm\,s^{-2}}]) \le +0.0$; $M = 1$ or $2\ M_\odot$; C/O = 1.05, 1.10, 1.40.

The COMA code (Aringer 2000) was used to compute the opacities for the different layers of a given temperature-density atmospheric structure. The opacity sources included in the calculations for the continuum are listed in Table 1 of Lederer & Aringer (2009). Voigt profiles were used for atomic lines and Doppler profiles for the molecules. All main molecular opacities typical for C-stars were included: CO (Goorvitch & Chackerian 1994), C_2 (Querci et al. 1974), HCN (Harris et al. 2006), CN (Jørgensen 1997) in the form of line lists, while C_2H_2 and C_3 (Jørgensen et al. 1989) as OS data. This agrees with previous works (Loidl et al. 2001; Aringer et al. 2009; Lederer & Aringer 2009) with the exception of the C_2 linelist, which was not scaled in the infrared range.

The scaling of the gf values for C_2 was suggested for the first time by Jørgensen (1997) and afterwards introduced by Loidl et al. (2001) for fitting spectra of C-rich stars in the range of

[3] In the model grid the lower limit of $\log(g)$ varies according to the temperature. For more details see Table 1 in Aringer et al. (2009).

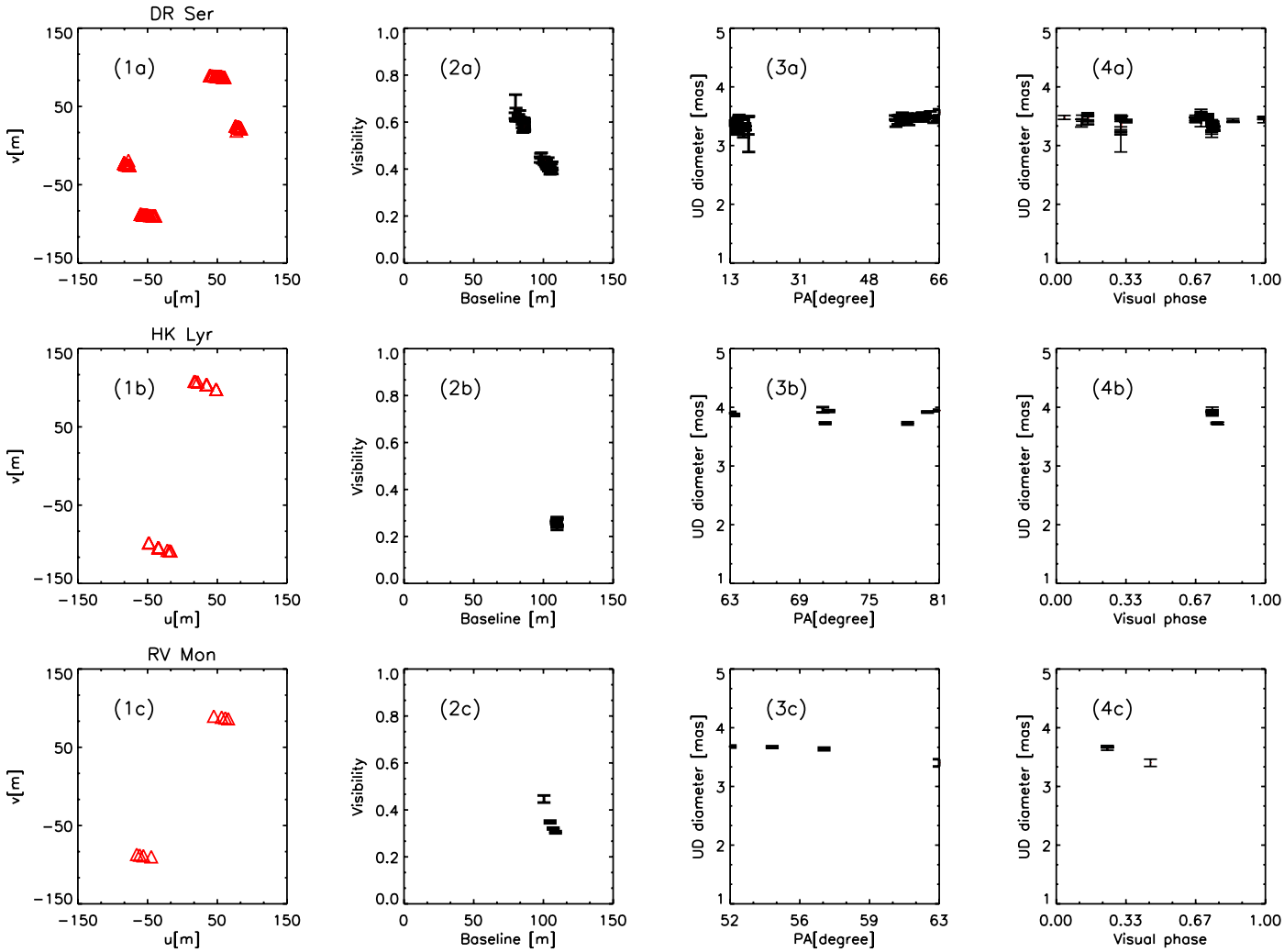

Fig. 2. Checking of the hydrostatic and spherical symmetric approximation for the interferometric data. The series of panels "a" refers to DR Ser data, panels "b" to HK Lyr, and panels "c" to RV Mon. The plots in Col. "1" represents the *uv*-coverage of the observations, in Col. "2" the visibility points acquired are plotted versus the baselines. In Col. "3" the correspondent UD diameter is plotted versus position angle. In Col. "4" the UD diameter is plotted versus the visual phase.

0.5−2.5 μm. The authors keep the original linelist up to 1.15 μm, they scale it by a factor of 0.1 beyond 1.5 μm, and use a linear extrapolation in the transition region. Different authors already pointed out the need of new C_2 line data. Aringer et al. (2009) showed that the C_2 scaling does not affect the model structure so much, but it introduces a variation in the spectral range between 1.3 and 2.1 μm. In the same work a discrepancy was observed when comparing synthetic and observed $(H-K)$ colours. This discrepancy was investigated in terms of C_2 opacity. The authors show in their Fig. 15 how the photometry obtained for unscaled models better agrees with observations. Aringer et al. (2009) conclude that this could be an indication that the use of the linelist in its original version is more appropriate, as long as there are no other more precise sources available.

In order to check this conclusion further, we performed the χ^2 test as explained in García-Hernandez et al. (2007) and Uttenthaler & Lebzelter (2010). In most of the cases we obtained a lower result of the χ^2 test for the C_2-unscaled linelist of Querci et al. (1974). This result was also judged by eye in order to test the method. In Fig. 3 the effect of the C_2-scaling in the HK-band is shown. The full line is the spectrum of the star Z Psc (upper panel) and HK Lyr (lower panel) convolved to a resolution of 200. The dotted line is the synthetic spectrum corresponding to a model with scaled C_2 opacity, while the dashed line is the same model with the original C_2 list. The result of the χ^2 test, the check by eye and the arguments of previous work of Aringer et al. (2009) led us to opt for the original C_2-unscaled linelist.

The resulting opacities are used as input for a spherically symmetric radiative transfer code that gives the synthetic spectra with a resolution of 18 000 in the wavelength range 0.8−25 μm. We convolved these spectra to obtain same resolution as the observed data.

3.2. Synthetic visibility profiles

The spherical radiative transfer code produces an additional output besides the total spectrum: a monochromatic spatial intensity profile. Synthetic visibility profiles for the K-broad band PTI setup were computed for a subset of the grid of hydrostatic models. The metallicity, the temperature range and the C/O ratio were fixed (more details in Sect. 4.1). To compute the visibility profiles, i.e. the interferometric observables, we proceeded as follows.

We defined a set of narrow-band filters centred on the sampled wavelength of the transfer function for the PTI K-broad

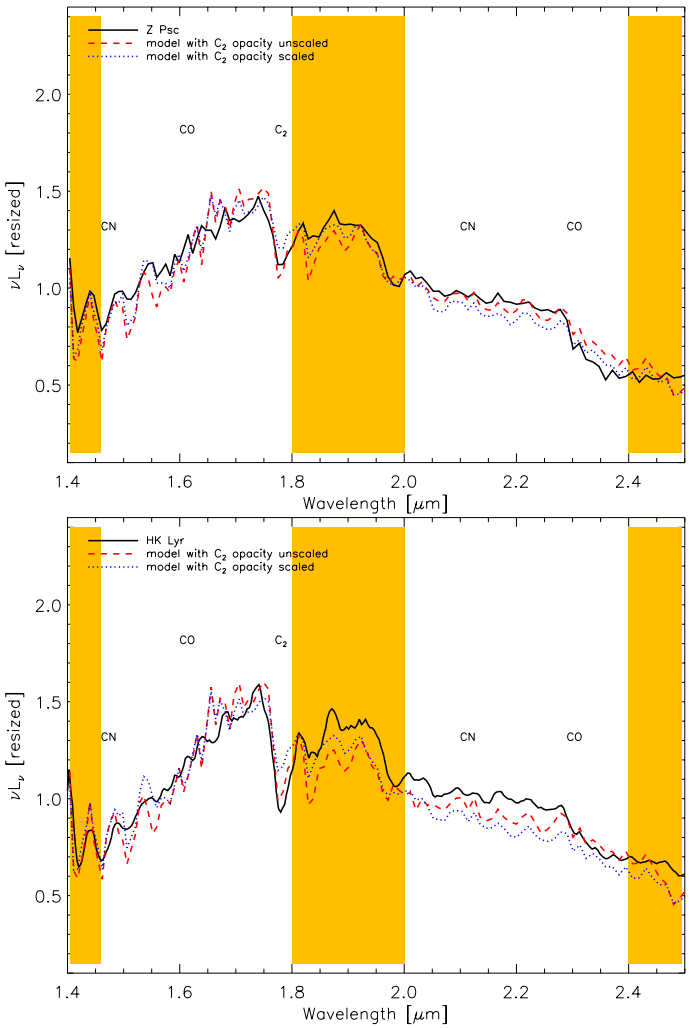

Fig. 3. Comparison between the observed spectrum of two targets (black full line, Z Psc in the upper panel and HK Lyr in the lower), a spectrum computed assuming scaled C_2 opacity (dotted line) and the spectrum with unscaled C_2 (dashed line). Shaded bands mark regions of poor atmospheric transmission.

band setup. Then the monochromatic intensity profiles were convolved with the filters so defined. The visibility profiles were computed as Hankel transform of the narrow-band intensity profiles. The spatial frequencies were converted from AU^{-1} to baselines in meters for a given distance. The squared visibility broad band profile finally is obtained as

$$V^2_{\rm broad} = \frac{\sum_i (S_i^2 F_i^2 V_i^2)}{\sum_i (S_i^2 F_i^2)}, \quad (1)$$

were the sum was calculated over the "i" narrow band filters; S_i is the transfer function of PTI in the K broad band setup; F_i is the flux integrated over the narrow band filter, and finally V_i is the visibility corresponding to the narrow band filters. Following this approach for the computation of the broad band visibility profile, the bandwidth smearing effect is properly taken into account (Kervella et al. 2003; Verhoelst 2005; Paladini et al. 2009).

4. Parameter determination

All spectra of the targets appear to be very similar (Fig. 1). They are dominated by the CN, C_2 and CO bands between 0.9 and

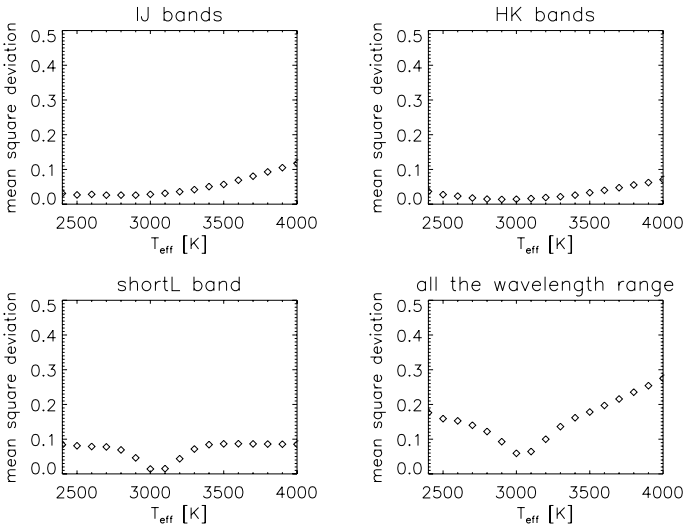

Fig. 4. Four plots show the mean squared deviation obtained by fitting single portions of the spectra (IJ, HK, short L), and by fitting all the portions of spectra at once (all the wavelength range) for HK Lyr. These plots demonstrate the accuracy of the short L measurement.

2.5 μm, while the main absorption feature at 3 μm in the L-band is due to HCN and C_2H_2. In Fig. 1 the regions affected by telluric absorption are shaded. These regions were of course not considered in our fitting procedure. Loidl et al. (2001) computed the flux ratio of various hydrostatic models (e.g. Fig. 3 of their paper) to investigate the effect of changes in the stellar parameters. They demonstrated that spectral features are mainly sensible to $T_{\rm eff}$ and C/O. Moreover, Aringer et al. (2009) showed that the synthetic spectrum below 2.5 μm of stars with $T_{\rm eff} \geq 3000$ K mildly changes for different values of $\log(g)$ and mass.

Therefore, we determined $T_{\rm eff}$ and C/O from spectroscopy and turn to the PTI interferometric observations to determine the remaining characteristic parameters of the models: mass and $\log(g)$.

4.1. Temperature and C/O ratio

The ratio between the 3 μm (C_2H_2) and the 5.1 μm (C_3) features is the most powerful tool for determining temperature and C/O ratio for hydrostatic C-stars (Jørgensen et al. 2000). Unfortunately, our spectral coverage does not reach the C_3 feature at 5.1 μm.

Following the approach of Loidl et al. (2001), we used the energy distribution of the available spectra as main temperature indicator. The observed spectrum was convolved to a lower resolution of $R = 200$. Every target of our list was compared with a grid of synthetic spectra with the same resolution. The grid of models is dense enough in temperature to allow an accurate statistic approach, which is described in detail in Appendix A. The $T_{\rm eff}$ value was separately estimated for every wavelength range, except for the long L band. This range of the spectrum is mostly flat and free from features, therefore not very sensitive for the temperature estimation. We also computed a temperature taking into account all four parts of the spectrum. The resulting temperatures are presented in Table 3. Figure 4 shows the mean-squares deviation[4] derived by first fitting single pieces of the spectrum ("IJ", "HK", "short L") and then by fitting all

[4] One root mean square value (rms) was derived by fitting each model. The models were divided into bins of temperature; the single rms values were squared (mean square deviation) to be summed to obtain one value

Table 3. Summary of temperature, C/O determination, and rms values corresponding to the different C/O.

ID	$T_{\rm eff}(IJ)$ [K]	$T_{\rm eff}(HK)$ [K]	$T_{\rm eff}$(short$L$) [K]	$T_{\rm eff}$ (all spec) [K]	$\rm rms_{1.05}$	$\rm rms_{1.10}$	$\rm rms_{1.40}$
CR Gem	2700 ± 200	2860 ± 200	**3070 ± 50**	2920 ± 190	**0.021**	0.027	0.038
HK Lyr	2740 ± 220	2920 ± 210	**3090 ± 50**	3080 ± 120	0.015	0.016	**0.013**
RV Mon	2950 ± 300	2930 ± 230	**3170 ± 50**	3210 ± 140	**0.006**	0.008	0.009
Z Psc	3000 ± 330	3080 ± 210	**3130 ± 60**	3170 ± 130	**0.014**	0.017	0.016
DR $\rm Ser_{no\,redd\,correct}$	2790 ± 250	2820 ± 200	**3080 ± 40**	3030 ± 170	**0.011**	0.013	0.014

Notes. The boldface corresponds to the best values of temperature and C/O. More details in Sect. 4.1.

pieces of the spectrum at once ("the entire wavelength range") for HK Lyr. Our intention is to look for possible minima in the temperature distribution.

The temperature values obtained from the different ranges of wavelength show a trend: by using the IJH bands as indicators, cooler temperatures are obtained. This trend can hardly be explained with problems during the calibration. The data reduction procedure (see Sect. 2.1) was accurate enough that we do not expect systematic errors in the overall flux distribution, which are large enough to explain the systematic variations in the temperature. The temperature difference might be explained as the effect of an optically thin dust shell surrounding the star. The effect of a dusty shell on the energy distribution of a star is shown in Figs. 3 and 4 of Nowotny et al. (2011). The model used for this simulation corresponds to a very dynamic star. Our objects are fairly static, but we speculate that a thin dust shell would affect the spectrum in the same way with scaled-down intensity. This shell would absorb the light in the IJH band and emit it at longer wavelength. As a direct consequence, a temperature determination based on IJH band is systematically lower, as can be seen in the upper panels of Fig. 4. If the shell is thin enough, the effect on the short edge of the L band is negligible. This makes the short L band temperature determination quite robust, as can be seen in the lower left panel of Fig. 4.

We note that this is not the case if the star is a strongly pulsating variable (such as a Mira). In this case the profile of the 3 μm feature, which is the result of the superposition of molecular opacity and dust continuous emission (Gautschy-Loidl et al. 2004), will be sensitive to the dynamic processes of the atmosphere. The respective temperature derived for every star by fitting the short L band will be assumed below.

The second quantity that mainly modifies the appearance of a C-rich spectrum is the C/O ratio. Unfortunately, the relatively low resolution of the spectra available limits the precision of this measurement. The CO band at 2.29 μm, the C_2 bands at 1.02 and 1.20 μm, and the C_2H_2+HCN at 3 μm were considered as indicators for the C/O ratio. Following to Loidl et al. (2001), the C_2 features longward of 1.20 μm were not used because of the uncertainty in the C_2 opacity. Two reference wavelengths were chosen to indicate start and end of every selected band. In low-resolution spectroscopy no continuum window is available for C-stars (Paladini et al. 2009), therefore a *pseudo-continuum* was obtained by linear interpolation of the points at the edge of the chosen band. The selected portion of spectrum was normalised to this pseudocontinuum. Following this approach, we derived the equivalent width for the observed spectrum and for all models with the temperature determined from the previous step. Grouping the models in sets according to the C/O (i.e. every "C/O group" includes models with same temperature, but different log(g) and mass), a root mean-squares value was obtained for every C/O by comparing the observed equivalent width and the synthetic one.

In Cols. 6–8 of Table 3 the resulting rms for the three C/O values (1.05, 1.10, and 1.40) is given. The minimum rms is shown in bold. All stars of the sample have a low value of C/O ratio, which corresponds to 1.05, except for HK Lyr, where the C/O = 1.4.

4.2. Mass, log(g), and distance

As already pointed out by other authors, it is hard to detect the effect of mass and log(g) from low-resolution spectroscopy of C-rich stars. This is confirmed in our series of plots in Figs. 6–10, where models with the same parameters except mass and log(g) are compared with the spectra of the targets. The temperature and C/O ratio of the models were determined following the procedure described above.

Owing to these considerations, we decided to treat the observables of interferometry as completely independent quantities. Because interferometry aims to measure the radius of the target, the distance becomes an important parameter. Unfortunately, the distance measurements available for these objects are quite imprecise (typical error of the order of 20%) and often contradict each other with differences between measurement relative to the same objects that are larger than errors. The problem we face is degenerate because we have to deal with radius, distance, mass, and all these quantities are related to each other.

We handled the problem in the following way. Three distances obtained with different methods were chosen from the literature for every object (see Sect. 2.1 and Table 4), and a set of synthetic visibility profiles was scaled to every distance. The set has a fixed temperature and C/O ratio. We obtained for every distance the combination of stellar parameters (M, log(g)) from the best-fitting profile.

5. Comparison with evolutionary tracks

At this point of our investigation, we have one combination of stellar parameters for every object and every distance. To constrain the choice of the parameters even more, we compare them with the recent isochrones for thermally pulsing AGB stars from Marigo et al. (2008). The selection of the isochrones follows the same criteria as Marigo et al. (2008): ages log(t/yr) between 7.8 and 10.2, and the spacing in log(t) is 0.1 dex.

Figure 5 shows a zoom into the region of the H-R diagram where AGB stars are located. The shaded area identify the region where C-stars are expected. Owing to the discrete sampling of the points in the isochrones (small square), the transition region from M- to C-stars is not very well defined. According to

for every bin. The number of models in every bin is not constant, therefore, the final mean-squares deviation was normalised by the number of models in every bin.

Table 4. Distance measurements and stellar parameters of the model that best fits spectroscopic and interferometric measurements.

Distance	CR Gem	HK Lyr	RV Mon	Z Psc	DR Ser
$d_{\rm Berg}$	920 pc	**730 pc**	**670 pc**	465 pc	1295 pc
	$L = 11\,000\ L_\odot$	$L = 7\,186\ L_\odot$	$L = 6\,400\ L_\odot$	$L = 4\,534\ L_\odot$	$L = 18\,050\ L_\odot$
	$T_{\rm eff} = 3\,100$ K	$T_{\rm eff} = 3\,100$ K	$T_{\rm eff} = 3\,200$ K	$T_{\rm eff} = 3\,100$ K	$T_{\rm eff} = 3\,100$ K
	C/O = 1.05	C/O = 1.4	C/O = 1.05	C/O = 1.05	C/O = 1.05
	$M = 2\ M_\odot$	$M = 2\ M_\odot$	$M = 1\ M_\odot$	$M = 2\ M_\odot$	$M = 2\ M_\odot$
	$\log(g) = -0.40$	$\log(g) = -0.20$	$\log(g) = -0.40$	$\log(g) = +0.0$	$\log(g) = -0.60$
$d_{\rm Clau}$	**780 pc**	**900 pc**	**1000 pc**	**600 pc**	**990 pc**
	$L = 9\,025\ L_\odot$	$L = 11\,389\ L_\odot$	$L = 12\,932\ L_\odot$	$L = 7\,170\ L_\odot$	$L = 11\,390\ L_\odot$
	$T_{\rm eff} = 3\,100$ K	$T_{\rm eff} = 3\,100$ K	$T_{\rm eff} = 3\,200$K	$T_{\rm eff} = 3\,100$ K	$T_{\rm eff} = 3\,100$ K
	C/O = 1.05	C/O = 1.40	C/O = 1.05	C/O = 1.05	C/O = 1.05
	$M = 1\ M_\odot$	$M = 2\ M_\odot$	$M = 2\ M_\odot$	$M = 1\ M_\odot$	$M = 2\ M_\odot$
	$\log(g) = -0.60$	$\log(g) = -0.40$	$\log(g) = -0.40$	$\log(g) = -0.50$	$\log(g) = -0.40$
$d_{\rm Hipp}$	323^{+357}_{-111} pc	$1\,369^{+671}_{-NN}$ pc	450^{+369}_{-140} pc	323^{+119}_{-68} pc	$1\,690^{+2810}_{-1120}$
	-	-	$L = 2\,574\ L_\odot$	$L = 2\,267\ L_\odot$	-
	-	-	$T_{\rm eff} = 3\,200$ K	$T_{\rm eff} = 3\,100$ K	-
			C/O = 1.05	C/O = 1.05	
			$M = 1\ M_\odot$	$M = 1\ M_\odot$	
			$\log(g) = +0.0$	$\log(g) = +0.0$	

Notes. The boldface distances correspond to the most likely values found by our stellar parameter analysis.

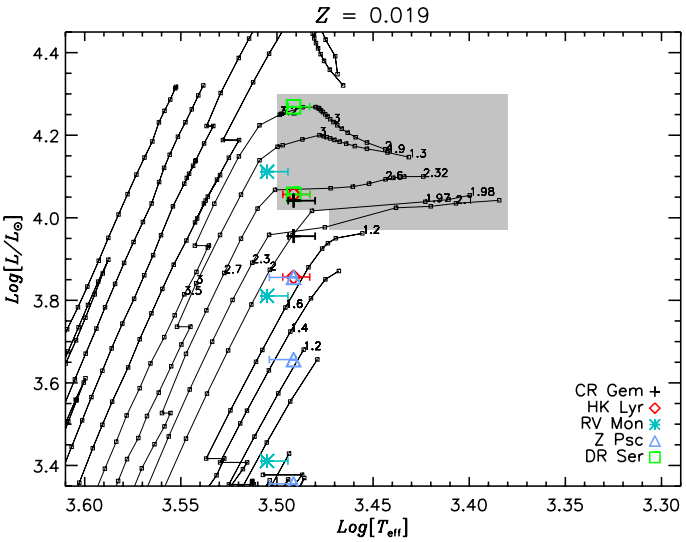

Fig. 5. Zoom into the H-R diagram where C-stars are located. The solar metallicity isochrones (Marigo et al. 2008) are plotted in grey and the small numbers indicate the predicted present mass. The sampling of points in the isochrones is shown with tiny squares. The position of the C-stars is indicated by a shaded area, the uncertainty about this area is discussed in Sect. 5. The different symbols plotted correspond to the parameters determined for every star and distance assumed: plus for CR Gem, asterisk for HK Lyr, diamond for RV Mon, triangle for Z Psc, and square for DR Ser.

the stellar evolution calculations (P. Marigo, priv. comm.), all stars on the cool side of the "hook" of the isochrones are C-stars. Some values of the present mass are marked on the isochrones: they will be compared with the mass of the best-fitting hydrostatic models (see Sect. 7).

We overplot on the isochrones the points corresponding to the parameters we determined. Every star is indicated with a different symbol centred on the temperature and luminosity associated to the model: a plus for CR Gem, an asterisk for HK Lyr, diamond for RV Mon, triangle for Z Psc, and square for DR Ser. The error bars of the temperature are the ones associated to the short L band $T_{\rm eff}$ determination, therefore, they are centred on the $T_{\rm eff}$ (short L) values given in Col. 3 of Table 3. The errors on the luminosity are not plotted here to avoid confusion but they are of the order of 40% (corresponding to the uncertainty on the distance measurements $d_{\rm Berg}$, $d_{\rm Clau}$).

6. Discussion of individual targets

6.1. CR Gem

CR Gem is classified as an irregular Lb variable with a variability amplitude in the B-band of 1.20 mag in the General Catalogue of Variable stars (GCVS; Samus+ 2007–2009). Nevertheless, Whitelock et al. (2008) classify this star as SRb with a period of 250$^{\rm d}$ and the ASAS V band light curve shows an amplitude of 0.5 mag (Pojmanski 2002). The spectral classification given in the GCVS is C8,3e(N).

The 3 μm short L temperature we determine is around 100 K higher than the 2960 K measured by Bergeat & Chevallier (2005). The C/O we get is 1.05, we could not find other estimates for this value in the literature. The observed spectrum is presented in Fig. 6. It is in general well reproduced with a few exceptions: the range 1.2−1.4 μm and the K-band between 2.1 and 2.3 μm, where the real data show an excess compared to the models (see general discussion in Sect. 7).

For this star we collected only one point of PTI visibility (Fig. 6 lower right panel), therefore it is not possible to check for asymmetries. All visibility profiles corresponding to the Hipparcos distance are not extended enough to fit the visibility point, therefore this distance can be excluded. For the Claussen distance the best-fitting model has mass 1 $M_\odot$ and $\log(g) = -0.60$, the luminosity is 9000 $L_\odot$ and the radius of the star 330 $R_\odot$. For the Bergeat distance, the highest value of distance estimated for this star, the best-fitting model has 2 $M_\odot$ and $\log(g) = -0.4$, the luminosity is 11 000 $L_\odot$, and the radius 370 $R_\odot$.

6.2. HK Lyr

According to the GCVS, the visual amplitude of HK Lyr is 1.80 mag, the spectral classification C6,4(N4), and the star is classified as irregular Lb. The Hipparcos Variability Annex

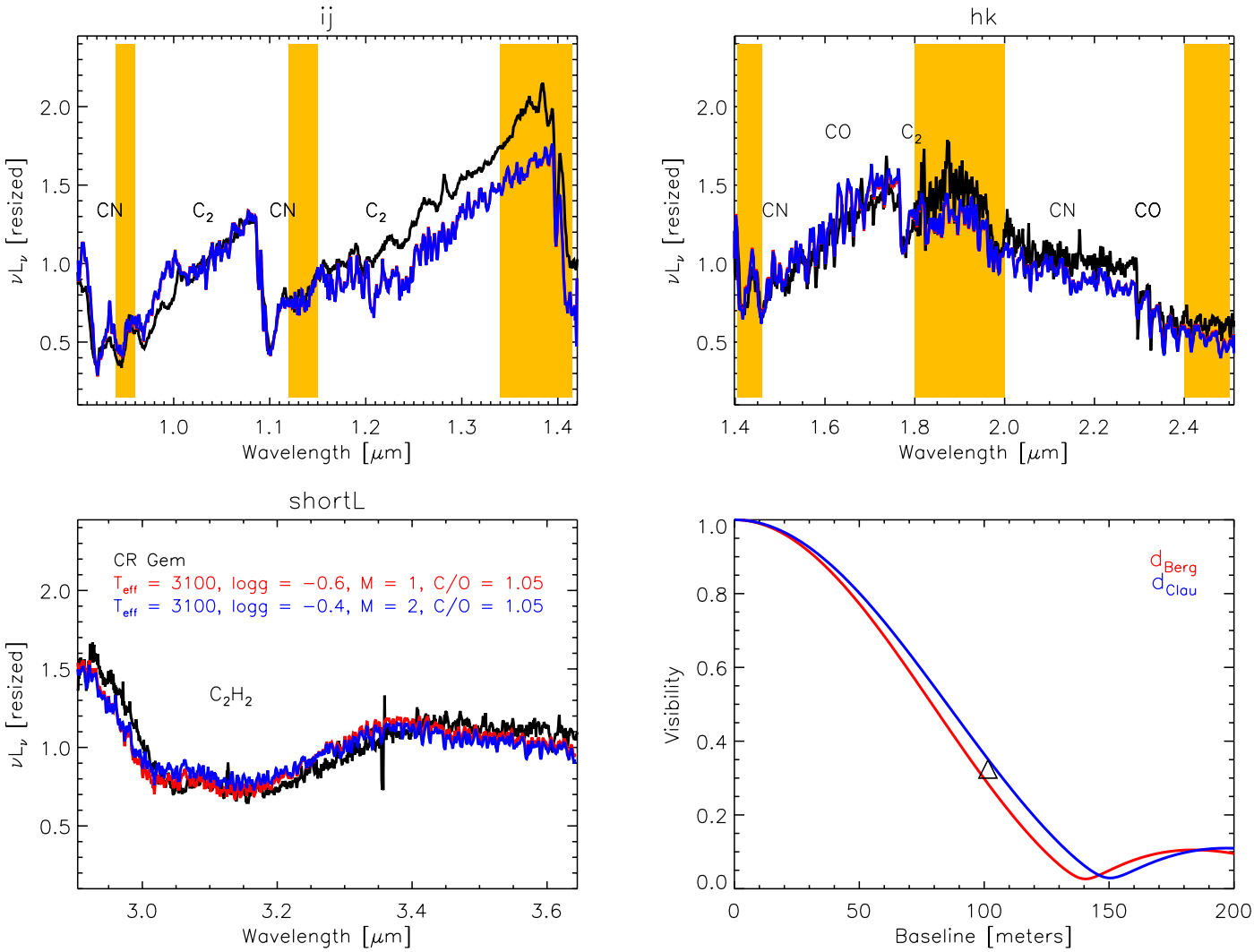

Fig. 6. Comparison of the UKIRT/UIST spectra (black line) and PTI interferometric measurements (black triangle) of CR Gem with hydrostatic model predictions. The *upper left panel* illustrates the *IJ* range of the spectrum, the *upper right panel* shows the *HK* wavelength range. The *lower left panel* shows the short *L* range. The shaded bands mark the region with poor atmospheric transmission. The molecules that contribute to the spectrum are also indicated. The synthetic spectra are overplotted in grey (blue, and red in the electronic version). The *lower right panel* shows the interferometric data point with the models which best fit the data for different distances overplotted.

(Beichman et al. 1988) reports for this star a period of 196^{d} and an amplitude of variability of 0.4 in the Hipparcos magnitude. From optical spectroscopic analysis, this star is enriched in lithium and technetium (Abia et al. 2002; Boffin et al. 1993).

From our spectroscopic investigation the temperature and C/O ratio, obtained are higher than the ones estimated in literature (Table 3). While our temperature is 3080 K, Ohnaka & Tsuji (1996) give 2866 K and Bergeat & Chevallier (2005) estimate 2945 K. Concerning the C/O ratio we obtain 1.4, while Abia et al. (2002) estimate 1.02. The fit of the spectroscopic data is quite successful except for the region between 1.2 and 1.45 μm (Fig. 7 upper left panel).

Eight visibility points are available from PTI observations. The UD diameters computed by fitting the single points do not differ. Over the time interval and position angle of the observations, the star does show no notable variation nor evidence of asymmetries (Fig. 2, row "b"). We fitted all visibility points with synthetic profiles scaled for different distances (Fig. 7 lower right panel).

None of the models corresponding to the Hipparcos distance can fit the points, therefore we excluded this distance. The best-fitting parameters corresponding to $d_{\rm Berg}$ are 2 $M_{\odot}$ and $\log(g) = -0.2$. This model has a luminosity of $L = 7200\ L_{\odot}$ and a radius $R = 300\ R_{\odot}$. The best-fitting model corresponding to $d_{\rm Clau}$ has again mass 2 $M_{\odot}$ but $\log(g) = -0.4$. This model has a luminosity of $L = 11\,400\ L_{\odot}$ and a radius $R = 370\ R_{\odot}$. In Fig. 5 the resulting parameters for HK Lyr are plotted with asterisks.

6.3. RV Mon

RV Mon is a C4,4-C6,2(NB/R9) star, its variability class is SRb with a primary pulsation period of 131^{d} and a long secondary period detected by Houk (1963) of 1047^{d}. The amplitude of variability given in the GCVS is 2.19 mag in the *B*-band, while the ASAS light curve suggests a *V* amplitude of 0.3 mag.

The temperature obtained with our fitting procedure is between the values given in the literature. Ohnaka & Tsuji (1996) get $T_{\rm eff} = 3330$ K, we obtained 3170 K while Bergeat & Chevallier (2005) give 2910 K. No estimation of C/O was found in the literature to be compared with our 1.05. The model we adopted for RV Mon matches the spectroscopic observations in all ranges quite well except for the region of the CO bands

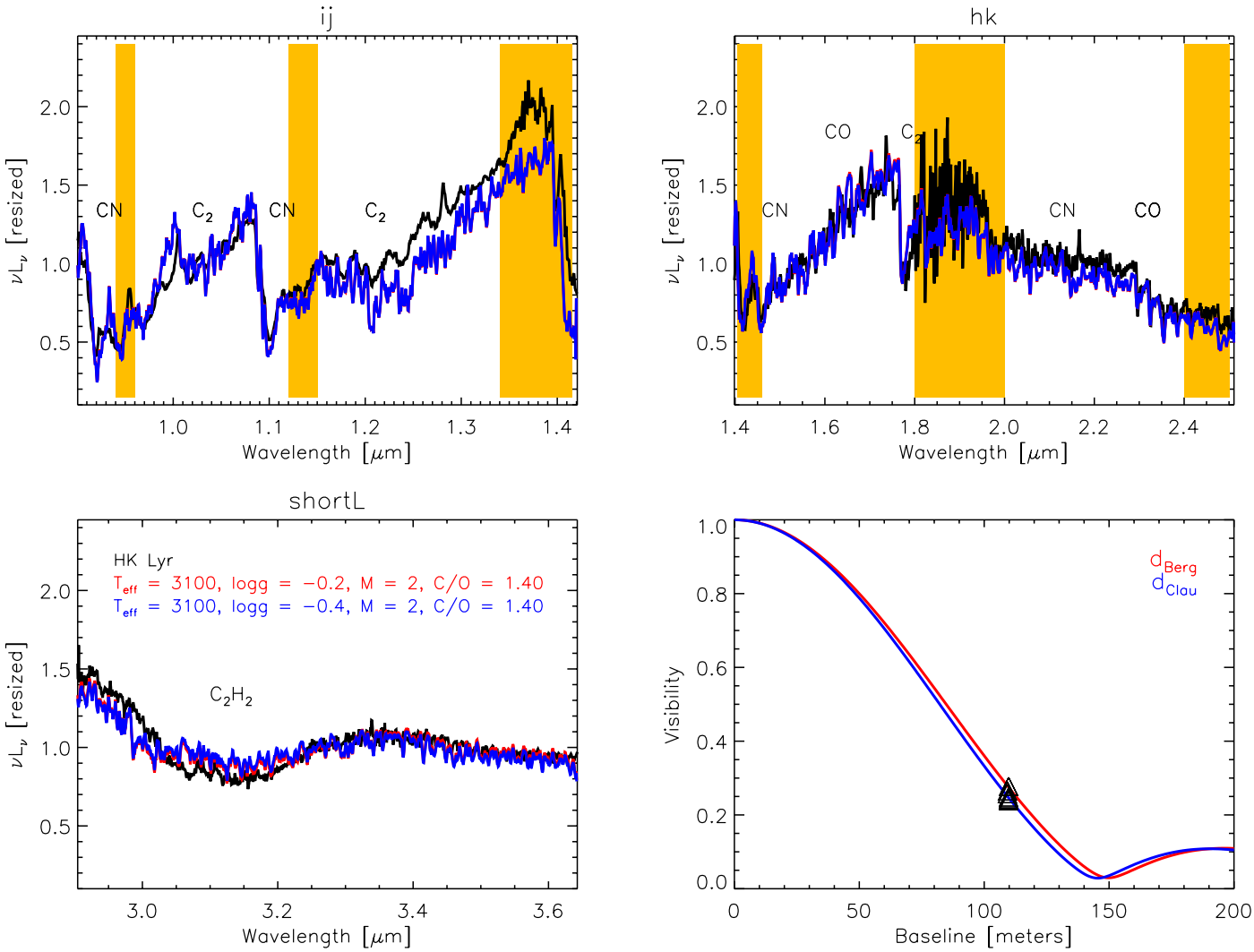

Fig. 7. Same as in Fig. 6 for HK Lyr.

(longward 2.29 μm), where the observations show an IR excess compared to the synthetic spectra. The intensity of the C_2 feature at 1.77 μm is not well reproduced but this is at the border of an atmospheric window.

For this star we collected four visibility points. The first one is in 1999, the other three in 2008. Although the observations were carried out at very similar baseline, the visibility jumps by 0.1 between the two epochs of observation. This jump is visible also in the UD-diameter where it amounts to ~0.16 mas, which is larger than the estimated error on the UD diameters (~0.06 in the worst case). This difference is also noted in the plot of the UD-versus-position angle. A careful check was performed to exclude any problem coming from the calibration procedure, but still we cannot completely exclude that the fluctuation in the visibility is caused by an instrument problem. From the astrophysical point of view, the observed trend could be explained in different ways: (i) it could be an asymmetry plus a temporal variation (for example a large convective shell), (ii) or an effect of the pulsation (panel "4c"). The temporal variation caused by the primary short period of variability is not enough to explain the jump in the visibility. We derived from the light curve a difference in phase for the primary period of 0.16 between the two sets of observations. According to the predictions of the dynamic model atmospheres (Paladini et al. 2009, see Figs. 7 and 9), a hot C-star should show a difference in UD-diam of 0.06 mas, definitely smaller than 0.16. The two sets of observations have been obtained with a time difference of 3.5 times the length of the long secondary period. This longterm variation may, therefore, be responsible for the observed variation in size. Additional observations are necessary to reach a conclusive interpretation. Keeping this in mind, we performed a fit of the interferometric points with a hydrostatic model atmosphere as a first step. This might be followed by more investigations. From the lower right panel of Fig. 8 it is immediately obvious that no synthetic visibility profile can fit all observations at the same time. The best-fitting model obtained for the Hipparcos or Claussen distances can only fit the single point observed in 1999. The other models are either too extended or not extended enough to fit the other observations. The best-fitting model for $d_{\rm Hipp}$ has $M = 1\ M_\odot$, $\log(g) = +0.0$, $L = 2600\ L_\odot$ and $R = 170\ R_\odot$. For the distance determined by Claussen et al. (1987) the single data point is fitted by the model with $2\ M_\odot$, $\log(g) = +0.4$, $L = 13\,000\ L_\odot$ and a radius $R = 370\ R_\odot$. On the other hand, for the distance determined by Bergeat & Chevallier (2005) the three points observed in 2008 are fitted by the model with $M = 1\ M_\odot$, $\log(g) = -0.4$, $L = 6400\ L_\odot$, and $R = 260\ R_\odot$. Nevertheless, the effect of

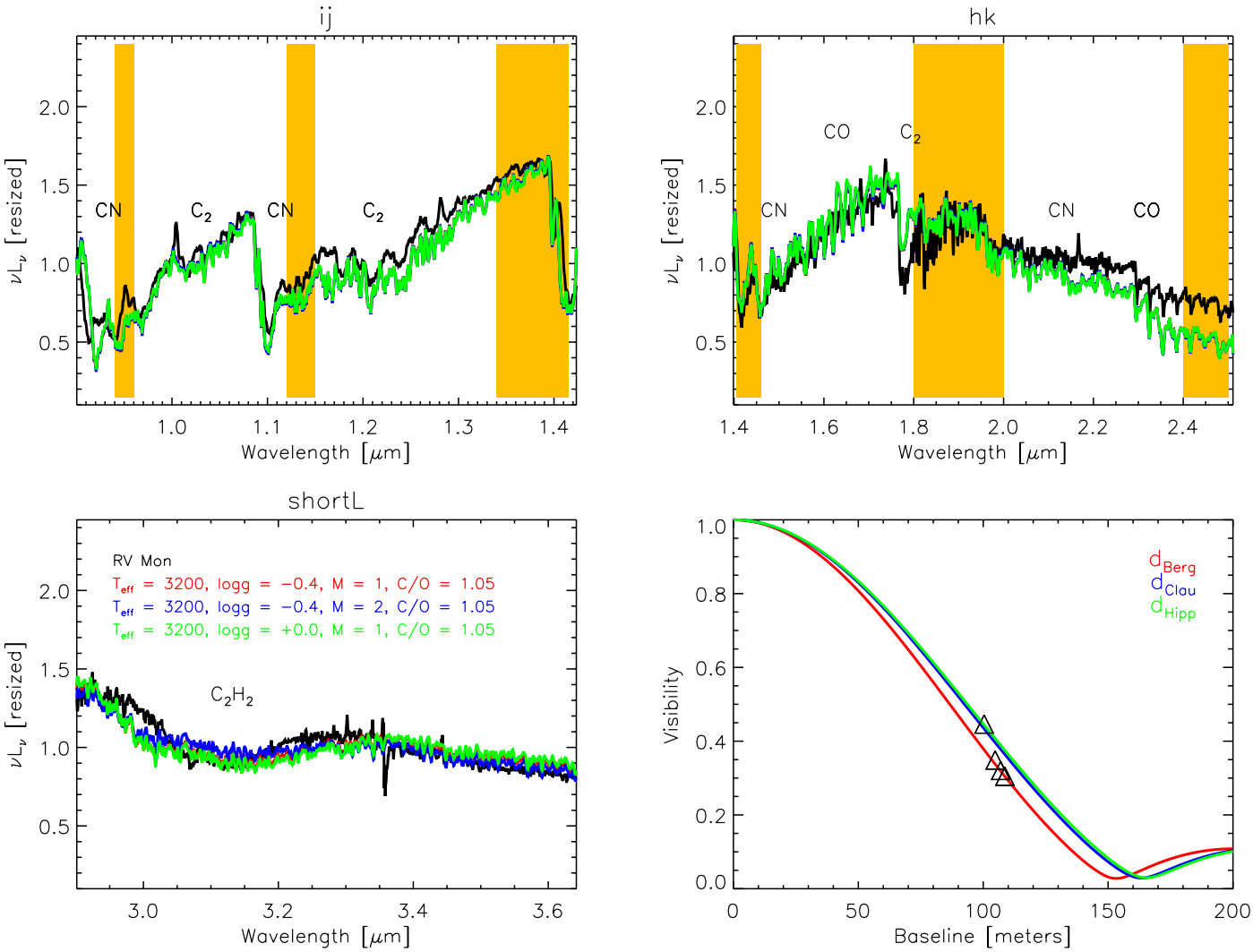

Fig. 8. Same as in Fig. 6 for RV Mon.

variability or possible asymmetries needs to be investigated in more detail, and the parameters derived for this object should be considered with caution.

6.4. Z Psc

Z Psc is an SRb variable with amplitude derived from photographic plates of 1.3 mag. The period in the GCVS is 144^{d}. The ASAS light curve has an amplitude of 0.52 mag in V band. The spectral classification from the GCVS (Samus+ 2007–2009) is C7,2(N0). Abia et al. (2002), and Boffin et al. (1993) determined a $^{12}C/^{13}C = 55$, moreover, they found enhancement of Tc, and no trace of Li in the spectrum. This implies that Z Psc is a standard low-mass TP-AGB star, and an intrinsic C-rich star.

Many temperature estimates were given for this star in the literature: Lambert et al. (1986) obtained 2870 K, Dyck et al. (1996) 3240 K, Ohnaka & Tsuji (1996) 3150 K, Bergeat & Chevallier (2005) 3095 K. All these values were obtained with different methods. Our measurement (see Table 3) is very close to the one given by Ohnaka & Tsuji (1996). The C/O = 1.05 we estimated agrees with the 1.014 of Lambert et al. (1986) and with the more recent 1.01 value of Abia et al. (2010). The match between models and observations is shown in Fig. 9. From spectroscopy a small disagreement is barely detectable in the C_2 band at 1.20 μm, while the 3 μm feature of the model is too deep to fit the data (the star is hotter than the model).

Z Psc is the only one among our targets with no PTI data. For this star we used an observation available from the literature (Dyck et al. 1996) taken in the K-broad band with IOTA (2.2 μm) as already described in Sect. 2.2. The fit of the interferometric IOTA data is presented in the lower right panel of Fig. 9. The best-fitting model for the Hipparcos distance has a mass $M = 1\,M_{\odot}$, $\log(g) = +0.0$, $L = 2300\,L_{\odot}$, and $R = 165\,R_{\odot}$. The distance determined by Bergeat & Chevallier (2005) gives a best-fitting model with the same $\log(g)$ obtained for Hipparcos distance fit but $M = 2\,M_{\odot}$, $L = 4500\,L_{\odot}$ and a radius $R = 230\,R_{\odot}$. In the case of the Claussen distance we have the best-fitting, which is the model with mass 1 $M_{\odot}$, $\log(g) = -0.5$, $L = 7150\,L_{\odot}$, and $R = 300\,R_{\odot}$.

6.5. DR Ser

According to the GCVS, DR Ser is an irregular variable Lb with an amplitude in the B-band of 2.99 mag. The ASAS light curve of this object is quite stable over the last 2000 days, it has a period of 196^{d}, and a V band amplitude of 0.3 mag. The spectral class is C6,4(N).

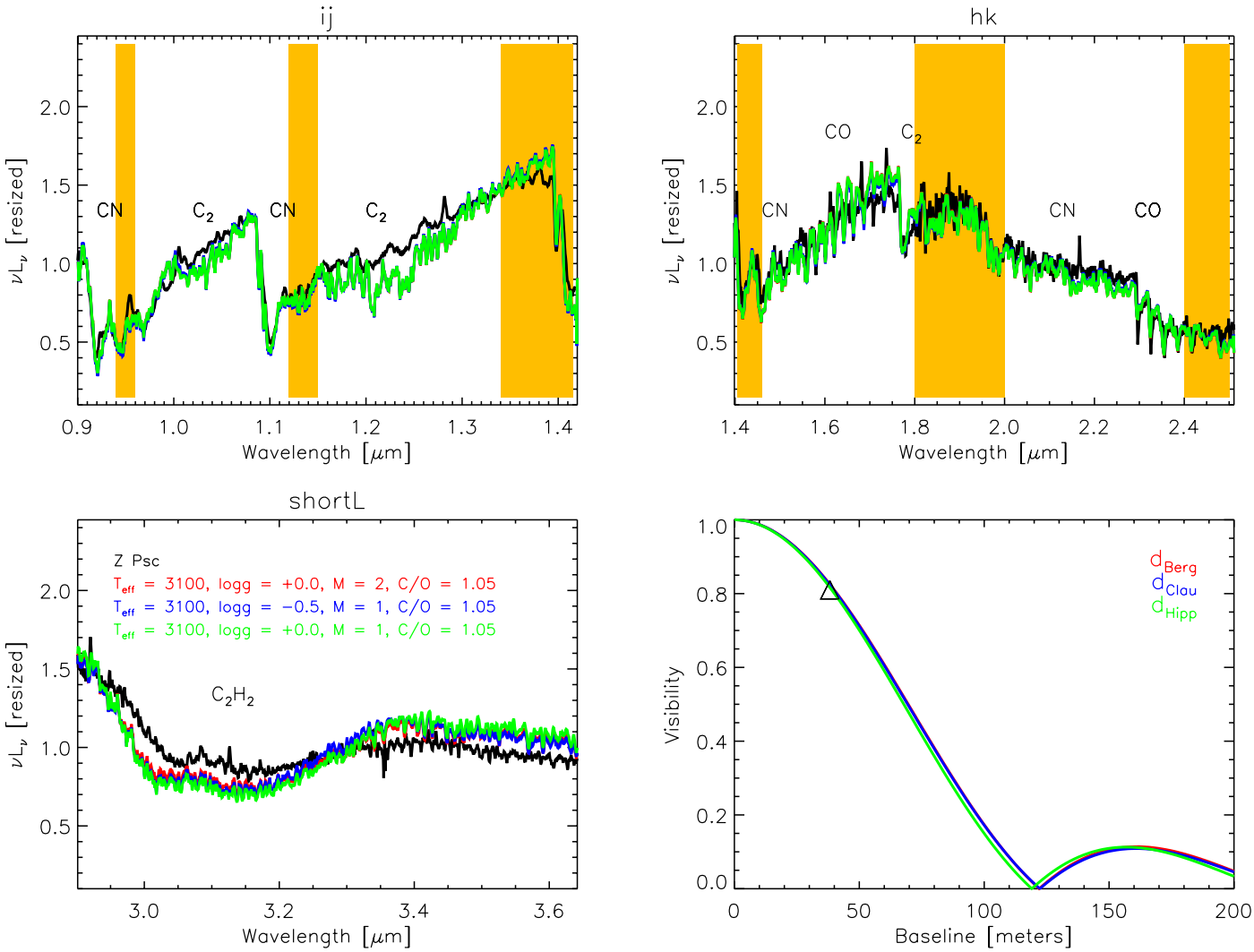

Fig. 9. Same as in Fig. 6 for Z Psc.

This object is the one in our sample with the highest value of interstellar reddening. Applying the reddening correction, we noted that the observed spectrum looks completely unrealistic. Remembering that reddening correction for single objects is always very uncertain, we decided to skip the step of the reddening correction for DR Ser. Further investigation and a detailed map of the ISM in the region of this star are needed.

We determined a temperature of 3080 K. In the literature the $T_{\rm eff}$ values associated to this object are usually lower (see Sect. 7): 2500 K (Abia & Isern 1997), 2570 K (Thompson et al. 2002), 2650 K (Schöier et al. 2005; Bergeat & Chevallier 2005). Abia & Isern (1997) estimated the isotopic ratio $^{12}C/^{13}C = 6$, which is also surprisingly low! The C/O we found, 1.05 is lower than the C/O = 1.26 obtained in literature by Eglitis & Eglite (1995).

There are 54 PTI points available for this object in the period between June 2000 and August 2001. The UD diameters determined agree with each other within a range of ±0.02 mas, therefore we considered for the model fitting all points together (Fig. 10). None of the profiles computed at the Hipparcos distance could fit the data points. The best-fitting models have a mass $M = 2\,M_{\odot}$, and $\log(g) = -0.4$ or -0.6 for $d_{\rm Clau}$ and $d_{\rm Berg}$ respectively. The first model has $L = 11\,400\,L_{\odot}$ and a radius of $370\,R_{\odot}$; the second one $L = 18\,000\,L_{\odot}$ and $R = 470\,R_{\odot}$. It is impressive to note how all the visibility points observed at different epochs and position angles fit the hydrostatic synthetic profile.

7. Discussion

Based on the fitting procedure described above, we can identify a sequence in effective temperature for our targets. The temperature increases, starting from CR Gem, DR Ser, HK Lyr, Z Psc, RV Mon. Our temperature determination is very precise thanks to the large grid of models available and to the use of the short L band spectrum. The $T_{\rm eff}$ here determined are always compatible within the error given in the literature.

The C/O ratio determination is not as accurate as the one of the temperature because of the very coarse spacing in the model grid, but mainly because of the low resolution of the spectra. Although the C/O values we determine have to be considered as indicative, they agree quite well with the ones estimated in the literature. We obtained the same C/O = 1.05 for all the stars except HK Lyr, which has C/O = 1.4. Those values agree with the range [1.01, 1.4] reported in the literature for classical C-stars (see Fig. 42 of Lambert et al. 1986; and Table 2 of Bergeat & Chevallier 2005).

In general there is a good agreement between synthetic and observed spectra. Small discrepancies are observed mainly in the

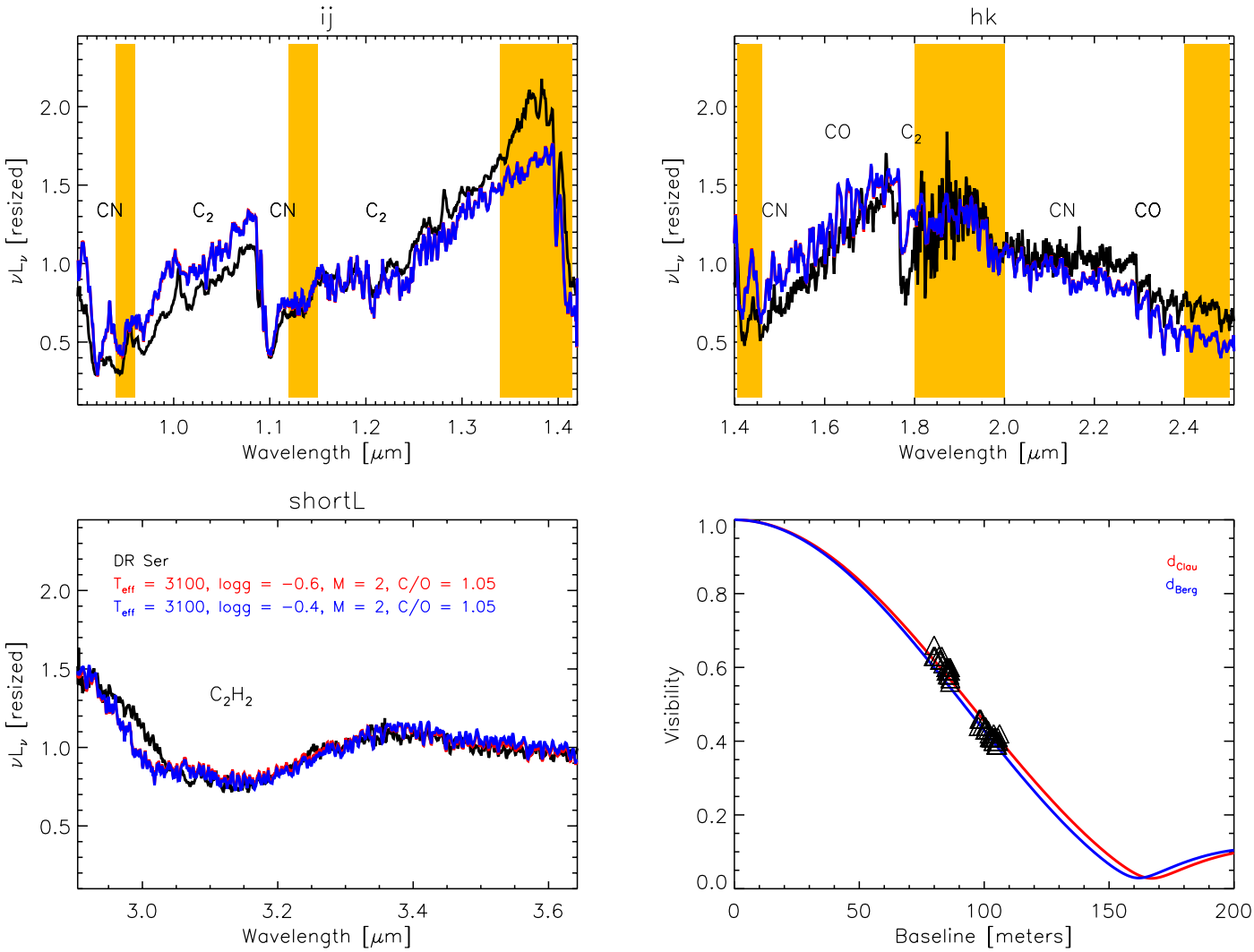

Fig. 10. Same as in Fig. 6 for DR Ser.

region between 1.2 and 1.4 μm, between 2.1 and 2.3 μm and on the left edge of the 3 μm feature. They can be attributed to small calibration problems, but also to a small amount of dust. This last point is supported by the fact that the differences detected in the IJ band between 1.2 and 1.4 μm are larger for the lower temperature stars (CR Gem, HK Lyr, DR Ser). We simulated the effect on the spectrum of a small amount of dust by using the DUSTY code (Ivezic & Eliztur 1997). Indeed, the IJ band of the spectrum fits slightly better for stars that have a high $J - K$ value (CR Gem, DR Ser). We also checked the effect of this small amount of dust on the stellar parameter determination. The effect on the temperature and on the interferometric observable was within the error bar we already took into account, therefore we proceed with the hydrostatic models. A detailed analysis of spectro-interferometric observations with a hydrostatic+dusty model atmosphere will be presented in a follow-up work.

From the fit of the interferometric observations with models at different distances we note that in three of five cases no model can fit the observations at the distance estimated from Hipparcos. This is not such a surprise considering the error associated to these distance measurements. Further consideration about the distance can be made by studying the position of the best-fitting models in the H-R diagram (Fig. 5).

Some of our hydrostatic models lie in a region of the H-R where larger masses are expected. If we consider the agreement between the two masses (from hydrostatic models and evolutionary calculations) as a criterion to select the correct distance of the objects, we have

- CR Gem. The point with lower luminosity is the one fitting the range of mass, therefore the distance determined by Claussen can be retained, and the one of Bergeat discarded.
- HK Lyr. Both models have the same mass and lie in a region in between 1 and 2.6 $M_{\odot}$. Considering an error on both distances of 20% (i.e. a factor 1.44 in luminosity), none of the values can be excluded.
- RV Mon. The Hipparcos distance is in the correct region of mass, but too far from the C-stars region, therefore it can be discarded. Both the other two distances correspond to a model that fits the region of masses, therefore they can be both retained.
- Z Psc. In this case the Bergeat distance can be discarded because the best-fitting model has 2 $M_{\odot}$, but falls in the range of 1 $M_{\odot}$. Considering the error on the luminosity, both the distances from Hipparcos and Claussen can be retained. Nevertheless, the position of the model at the Claussen distance is more probable because this is closer to the C-stars region.
- DR Ser. The distance estimated from Bergeat can be discarded because the model lies in the region of the stars with 3 $M_{\odot}$.

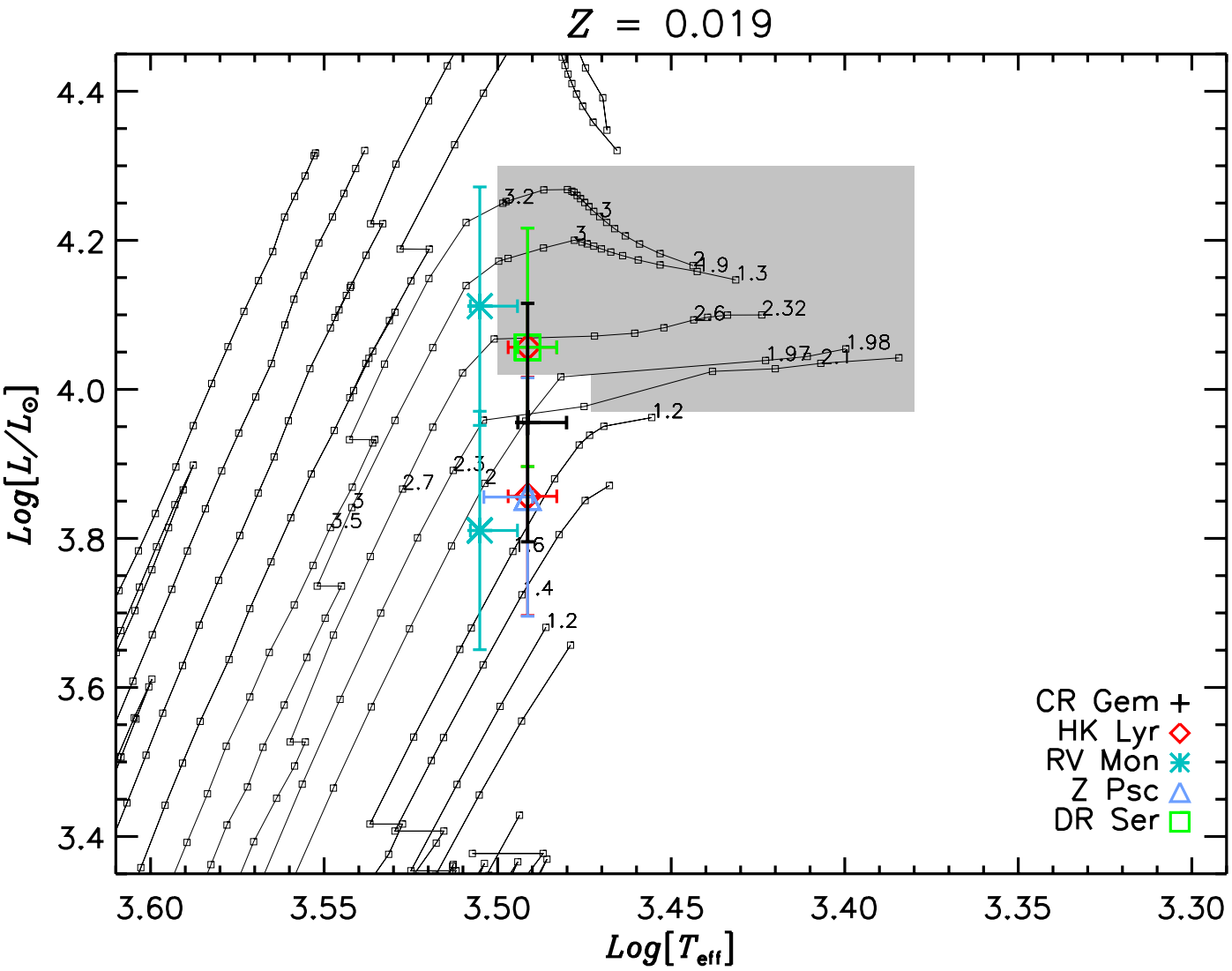

Fig. 11. Same as in Fig. 5, but this time only the parameters with most probable distances are plotted.

The parameters with the most probable distances, with associated errors in temperature and luminosity are shown in Fig. 11.

Taking into account the uncertainty associated to the transition phase M-C stars (see Sect. 5), all stars have at least one combination of parameters that lie in the region where the C-stars sequence starts. This agrees with the hydrostatic scenario for our targets: the objects are supposed to be hot C-stars, with relatively low mass-loss and low C/O. They "recently" turned into C-stars, and while moving on the evolutionary track, they will increase the production of carbon and will lose more and more mass because of the stellar wind. Our work is partially limited because that only model atmospheres with mass 1 and 2 are available.

Two objects of our sample show some peculiarity that deserves additional investigations. The interferometric observations of RV Mon show a possible non-hydrostatic nature. All visibility points acquired with PTI cannot be fitted with the same model. This might be caused by some instrumental effect, while the physical explanation would be an evidence of an asymmetry or (more probably) of a variability effect. According to the interferometric measurements, the star DR Ser is a hydrostatic object. We were able to fit with the same model 54 visibility points observed in different epochs and position angles. On the other hand, the fit of the IJ and HK band is not very good, and the reddening correction of the spectrum makes the fit even worse. A detailed ISM map for this region of the sky is needed.

8. Conclusions

More than a simple parameters determination, this work aims to identify which of the stellar parameters of C-stars can be constrained by using different techniques like spectroscopy and interferometry. Which limits appear by investigating only with one tool? Infrared interferometry is a relatively young field of research, but it can already give a significant contribution to the stellar parameter determinations.

We confirm that low-resolution infrared spectroscopy is not sensitive to $\log(g)$ and mass determinations of C-stars. We clearly show that a highly precise determination of the temperature can be achieved for C-stars with no significant dust contribution thanks to the use of the 3 μm feature (C_2H_2 + HCN). The determinations based only on the IJH bands tend to underestimate the temperature.

The hydrostatic model atmospheres adopted in this work were able for the first time to fit simultaneously spectroscopic and interferometric observations. This is a very important achievement considering that inaccuracies in model atmospheres reflect negatively on the check of the stellar evolution

calculations. On the other hand, the inaccuracy in the distance determination for this class of objects reflects negatively on the parameter determination, as already noted in Wittkowski et al. (2001). We considered a criterion to select the distance on the agreement between mass of the hydrostatic models and mass predicted by the isochrones. According to this, the distance estimated by Claussen et al. (1987) is the most probable among the three distances we used for this work. Taking into account the uncertainty in the transition phase from O-rich to C-rich star in the evolution models as well, we obtained that all the objects of our sample have at least one combination of observationally determined parameters that fits the C-stars region. We were able to associate temperature, C/O, mass, log(g) and a range of reasonable distances for all objects of our sample.

A grid of models with larger coverage of the mass range (at least from 1 to 4 $M_{\odot}$) as well as a more dense grid of points for the isochrones would significantly improve our estimations. The advent of a new dedicated mission (Gaia) might improve the distance problem for C-stars.

The synergy between different techniques of investigation and realistic theoretical atmospheric and stellar evolutionary models will be the key to determine precise characteristics for this class of objects, and to be able to understand clearly the physical processes that drive their evolution.

Acknowledgements. The authors acknowledge the anonymous referee for useful comments that helped improve the paper. This work is supported by the Projects P19503-N16 of the Austrian Science Fund (FWF). B.A. acknowledges funding by the contract ASI-INAF I/016/07/0, and ASI-INAF I/009/10/0. T.L. acknowledges support through the FWF-project P20046-N16. The United Kingdom Infrared Telescope is operated by the Joint Astronomy Centre on behalf of the Science and Technology Facilities Council of the UK Science operations with PTI were conducted through the efforts of the PTI Collaboration (http://pti.jpl.nasa.gov/ptimembers.html) and the National Aeronautics and Space Administration (NASA) Exoplanet Science Institute (NExScI), and we acknowledge the invaluable contributions of our PTI colleagues. We particularly thank Kevin Rykoski for his professional operation of PTI. PTI was constructed with funds from the Jet Propoulsion Laboratory, Caltech, as provided by NASA We acknowledge D. V. Shulyak for computing the models for the standard stars, P. Marigo and W. Nowotny for the useful discussions, A. Baier and S. Sacuto for helping with Dusty Code, L. Pavan for useful discussions on the reddening correction. The research leading to these results has received funding from the European Community's Seventh Framework Programme under Grant Agreement 226604.

References

Abia, C., & Isern, J. 1997, MNRAS, 289, 11
Abia, C., Domínguez, I., Gallino, R., et al. 2002, ApJ, 579, 817
Abia, C., Cunha, K., Cristallo, S., et al. 2010, ApJ, 715, 94
Amôres, E. B., & Lépine, J. R. D. 2005, AJ, 130, 659
Aringer, B. 2000, Ph.D. Thesis, University of Vienna
Aringer, B., Jørgensen, U. G., & Langhoff, S. R. 1997, A&A, 323, 202
Aringer, B., Girardi, L., Nowotny, W., Marigo, P., & Lederer, M. T. 2009, A&A, 503, 913
Aufdenberg, J., Ridgway, S., & White, R. 2009, in astro2010: The Astronomy and Astrophysics Decadal Survey, Science White Papers, astro2010S, 8
Bagnulo, S. 1996, Ph.D. Thesis, Belfast University
Beichman, C. A., Neugebauer, G., Habing, H. J., Clegg, P. E., & Chester, T. J. 1988, NASAR, 1190, 1
Bergeat, J., & Chevallier, L. 2005, A&A, 429, 235
Bergeat, J., Knapik, A., & Rutily, B. 2002, A&A, 390, 967
Boden, A. F., Colavita, M. M., van Belle, G. T., & Shao, M. 1998, Proc. SPIE, 3350, 872
Boden, A. F., Koresko, C. D., van Belle, G. T., et al. 1999, ApJ, 515, 356
Boffin, H. M. J., Abia, C., & Rebolo, R. 1993, A&AS, 102, 361
Cavanagh, B., Hirst, P., Jenness, T., et al. 2003, ASPC, 295, 237
Claussen, M. J., Kleinmann, S. G., Joyce, R. R., & Jura, M. 1987, ApJS, 65, 385
Colavita, M. M., Wallace, J. K., Hines, B. E., et al. 1999, ApJ, 510, 505
Cutri, R. M., Skrutskie, M. F., van Dyk, S., et al. 2003, in The IRSA 2MASS All-Sky Point Source Catalog, NASA/IPAC Infrared Science Archive
Dyck, H. M., van Belle, G. T., & Benson, J. A. 1996, AJ, 112, 294
Eglitis, I., & Eglite, M. 1995, Ap&SS, 229, 63
Epchtein, N., Le Bertre, T., & Lepine, J. R. D. 1990, A&A, 227, 82
Erspamer, D., & North, P. 2003, A&A, 398,1121
García-Hernández, D. A., García-Lario, P., Plez, B., et al. 2007, A&A, 462, 711
Gautschy-Loidl, R., Höfner, S., Jørgensen, U. G., & Hron, J. 2004, A&A, 422, 289
Goorvitch, D., & Chackerian, Jr. C. 1994, ApJS, 91, 483
Gustafsson, B., Bell, R. A., Eriksson, K., & Nordlund1975, A&A, 42, 407
Gustafsson, B., Edvardsson, B., Eriksson, K., et al. 2008, A&A, 486, 951
Harris, G. J., Tennyson, J., Kaminsky, B. M., Pavlenko, Y. V., & Jones, H. R. A. 2006, MNRAS, 367, 400
Hauschildt, P. H., Allard, F., Ferguson, J., Baron, E., & Alexander, D. R. 1999, ApJ, 525, 871
Houk, N. 1963, AJ, 68, 253
Iben, I., & Renzini, A. 1983, ARA&A, 21, 271
Ivezic, Z., & Elitzur, M. 1997, MNRAS, 287, 799
Jørgensen, U. G. 1997, in Molecules in Astrophysics: Probes and Processes, ed. E. F. van Dishoeck (Kluwer), IAU Symp., 178, 441
Jørgensen, U. G., Almlof, J., & Siegbahn, P. E. M. 1989, ApJ, 343, 554
Jørgensen, U. G., Johnson, H. R., & Nordlund 1992, A&A, 261, 263
Jørgensen, U. G., Hron, J., & Loidl, R. 2000, A&A, 356, 253
Kerschbaum, F., Lazaro, C., & Habison, P. 1996a, A&AS, 118, 397
Kerschbaum, F., Olofsson, H., & Hron, J. 1996b, A&A, 311, 273
Kervella, P., Thévenin, F., Ségransan, D., et al. 2003, A&A, 404, 1087
Kurucz, R. L. 1993, ASPC, 44, 87
Lambert, D. L., Gustafsson, B., Eriksson, K., & Hinkle, K. H. 1986, ApJS, 62, 373
Lederer, M. T., & Aringer, B. 2009, A&A, 494, 403
Lester, J., & Neilson, H. 2008, A&A, 491, 633
Loidl, R., Lancon, A., & Jorgensen, U. G. 2001, A&A, 371, 1065
Marigo, P., Girardi, L., Bressan, A., et al. 2008, A&A, 482, 883
Masana, E., Jordi, C., & Ribas, I. 2006, A&A, 450, 735
Mattsson, L., Wahlin, R., & Höfner, S. 2010, A&A, 509, 14
Mozurkewich, D., Johnston, K. J., Simon, R. S., et al. 1991, AJ, 101, 2207
Neilson, H. R., & Lester, J. B. 2008, A&A, 490, 807
Nowotny, W., Lebzelter, T., Hron, J., & Höfner, S. 2005, A&A, 437, 285
Nowotny, W., Höfner, S., & Aringer, B. 2010, A&A, 514, 35
Nowotny, W., Aringer, B., Höfner, S., & Lederer, M. T. 2011, A&A, 529, 129
Ohnaka, K., & Tsuji, T. 1996, A&A, 310, 933
Paladini, C., Aringer, B., Hron, J., et al. 2009, A&A, 501, 1073
Perryman, M. A. C., Lindegren, L., Kovalevsky, J., et al. 1997, A&A, 323, 49
Pojmanski, G. 2002, Acta Astron., 52, 397
Querci, F., Querci, M., & Tsuji, T. 1974, A&A, 31, 265
Ramsay Howat, S., Todd, S., Legget, S., et al. 2004, Proc. SPIE, 5492, 1160
Samus, N. N., Durlevich, O. V., et al. 2009, General Catalogue of Variable Stars, yCat, 102025S
Schöier, F. L., Lindqvist, M., & Olofsson, H. 2005, A&A, 436, 633, 646
Shulyak, D. V., Tsymbal, V., Ryabchikova, T., Stütz Ch., & Weiss, W. W. 2004, A&A, 428, 993
Sloan, G. C., Little-Marenin, I. R., & Price, S. D. 1998, AJ, 115, 809
Solano, E., & Fernley, J. 1997, A&AS, 122, 131
Tanaka, M., Letip, A., Nishimaki, Y., et al. 2007, PASJ, 59, 939
Thompson, R. R., Creech-Eakman, M. J., & van Belle, G. T. 2002, ApJ, 577, 447
Tsuji, T. 1986, ARA&A, 24, 89
Uttenthaler, S., & Lebzelter, T. 2010, A&A, 510, 62
van Belle, G. T., & van Belle, G. 2005, PASP, 117, 1263
van Belle, G. T., van Belle, G., Creech-Eakman, M. J., et al. 2008, ApJS, 176, 276
Vanture, A. D., Smith, V. V., Lutz, J., et al. 2007, PASP, 119, 147
Verhoelst, T. 2005, Ph.D. Thesis, University of Leuven
Wittkowski, M. 2004, Proc. of the 37th Liege International Astrophysical Colloquium, Science Case for Next Generation Optical/Infrared Interferometric Facilities (the post VLTI era)
Wittkowski, M., Hummel, C. A., Johnston, K. J., et al., 2001, A&A, 377, 981
Wittkowski, M., Aufdenberg, J. P., & Kervella, P. 2004, A&A, 413, 711
Wittkowski, M., Aufdenberg, J. P., Driebe, T., et al. 2006a, A&A, 460, 855
Wittkowski, M., Hummel, C. A., Aufderberg, J. P., & Roccatagliata, V. 2006b, A&A, 460, 843
Whitelock, P. A., Feast, M. W., & van Leeuwen, F. 2008, MNRAS, 386, 313

Pages 16 to 18 are available in the electronic edition of the journal at http://www.aanda.org

Appendix A: Statistical approach at temperature determination

In order to assign an observed spectrum to one out of a sample of available models, a statistical approach is employed: each model represents a Gaussian-shaped sandheap the width of which (in terms of standard deviation) is determined by the point-to-point scatter p of the spectrum. The height of the sandheaps can be adjusted by statistical weights. Thus, the shape of the nth sandheap is given by the Gaussian probability density function

$$G(d_n) = \exp\left(\frac{d_n^2}{2p^2}\right). \tag{A.1}$$

The "distance" d_n between the observed spectrum and the model is the rms deviation between the observed and the synthetic spectrum. The statistical analogy of the model assignment is to pick out a single grain of sand at the given distances from the synthetic spectra. Now the question is, how high is the probability of the picked grain to belong to the nth sandheap?

The total number of available grains at the selected position is determined by the sum of densities for all N models,

$$\nu = \sum_{n=1}^{N} G(d_n), \tag{A.2}$$

which represents our normalisation condition. Thus, the relative amount of grains belonging to model n – and hence the probability of the observed spectrum to represent this model – evaluates to

$$\mathrm{Pr}_n = \frac{G(d_n)}{\nu}. \tag{A.3}$$

In the context of our application, the only parameter of interest is the effective temperature, whence the temperature interval covered by the models is divided into a set of intervals I_t, $t = 1, ..., \tau$. Because the number of models belonging to such a temperature bin is not unique, the marginal probability density of temperature has to be corrected for this bias. In the sandheap metaphor, we would have to provide each temperature interval to be represented by a unique number of grains, and the probability of our spectrum to be assigned to the temperature interval I_t evaluates to the weighted sum of individual model assignment probabilities

$$\mathrm{Pr}(I_t) = \frac{m_t^{-1} \sum_{n=1}^{m_t} \mathrm{Pr}_n(I_t)}{\sum_{i=1}^{\tau} m_i^{-1} \sum_{k=1}^{m_i} \mathrm{Pr}_k(I_i)}, \tag{A.4}$$

m_t and denoting the number of models belonging to the interval I_t.

This normalisation is demonstrably valid, because the integral probability for all temperatures evaluates to

$$\sum_{t=1}^{\tau} \mathrm{Pr}(I_t) = \frac{\sum_{t=1}^{\tau} m_t^{-1} \sum_{n=1}^{m_t} \mathrm{Pr}_n(I_t)}{\sum_{i=1}^{\tau} m_i^{-1} \sum_{k=1}^{m_i} \mathrm{Pr}_k(I_i)} = 1. \tag{A.5}$$

Table A.1. Interferometric observations.

ID	UT Date	B [m]	PA [deg]	$V \pm \sigma_V$	Additional information
CR Gem	11/03/1999 Nov 3	101.49	80	0.324 ± 0.004	
HK Lyr	1999 May 20	109.79	71	0.277 ± 0.004	
	1999 May 21	109.78	78	0.277 ± 0.005	
	2000 May 22	109.29	63	0.258 ± 0.005	
	2000 May 22	109.33	64	0.265 ± 0.004	
	2000 May 22	109.76	71	0.238 ± 0.010	
	2000 May 22	109.77	72	0.244 ± 0.003	
	2000 May 22	109.73	80	0.249 ± 0.003	
	2000 May 22	109.72	81	0.242 ± 0.003	
RV Mon	1999 Nov 04	100.37	63	0.446 ± 0.015	
	2008 Sep 25	108.68	52	0.305 ± 0.005	
	2008 Sep 25	106.98	55	0.320 ± 0.004	
	2008 Sep 25	104.79	57	0.349 ± 0.006	
Z Psc	1995 Oct 08	38.21	–	0.810 ± 0.123	(1)
DR Ser	2000 Jun 03	106.29	55	0.387 ± 0.008	
	2000 Jun 19	107.05	54	0.535 ± 0.024	(2)
	2000 Jun 19	106.01	56	0.497 ± 0.035	(2)
	2000 Jun 19	105.45	56	0.487 ± 0.032	(2)
	2000 Jun 19	104.83	57	0.515 ± 0.024	(2)
	2000 Jun 20	103.33	59	0.435 ± 0.013	
	2000 Jun 20	102.19	60	0.429 ± 0.013	
	2001 Apr 18	104.41	57	0.407 ± 0.010	
	2001 Apr 18	104.20	58	0.415 ± 0.004	
	2001 Apr 18	103.23	59	0.407 ± 0.003	
	2001 Apr 18	103.06	59	0.413 ± 0.007	
	2001 Apr 18	102.13	60	0.410 ± 0.005	
	2001 Apr 23	106.14	55	0.418 ± 0.013	
	2001 Apr 23	103.56	58	0.410 ± 0.012	
	2001 Apr 23	100.63	62	0.429 ± 0.011	
	2001 Apr 23	99.18	64	0.435 ± 0.011	
	2001 Apr 23	97.73	66	0.440 ± 0.012	
	2001 Apr 29	105.27	56	0.389 ± 0.006	
	2001 Apr 29	105.01	57	0.391 ± 0.005	
	2001 Apr 29	103.67	58	0.396 ± 0.005	
	2001 Apr 29	102.84	59	0.406 ± 0.005	
	2001 Apr 29	102.68	59	0.407 ± 0.008	
	2001 May 03	86.43	15	0.587 ± 0.014	
	2001 May 03	86.40	15	0.597 ± 0.015	
	2001 May 03	85.92	15	0.591 ± 0.019	
	2001 May 03	84.84	16	0.593 ± 0.018	
	2001 May 03	83.03	17	0.626 ± 0.023	
	2001 May 04	86.07	15	0.583 ± 0.009	
	2001 May 04	85.98	15	0.580 ± 0.009	
	2001 May 04	84.76	16	0.599 ± 0.010	
	2001 May 04	82.50	17	0.615 ± 0.007	
	2001 May 04	82.24	17	0.621 ± 0.011	
	2001 May 05	86.31	15	0.589 ± 0.006	
	2001 May 05	85.79	15	0.598 ± 0.007	
	2001 May 05	84.85	16	0.605 ± 0.005	
	2001 May 05	83.54	17	0.613 ± 0.008	
	2001 May 05	81.86	17	0.626 ± 0.006	
	2001 May 23	104.92	57	0.402 ± 0.007	
	2001 May 23	103.80	58	0.416 ± 0.004	
	2001 Jun 21	103.71	58	0.404 ± 0.006	
	2001 Jun 21	102.06	60	0.420 ± 0.005	
	2001 Jun 21	100.30	63	0.433 ± 0.005	
	2001 Jun 21	98.60	65	0.460 ± 0.009	
	2001 Jul 16	79.72	14	0.627 ± 0.012	
	2001 Jul 22	105.69	56	0.402 ± 0.019	

Table A.1. continued.

ID	UT Date	B [m]	PA [deg]	$V \pm \sigma_V$	Additional informations
	2001 Jul 22	105.55	56	0.405 ± 0.019	
	2001 Jul 22	104.73	57	0.393 ± 0.015	
	2001 Jul 22	104.59	57	0.413 ± 0.016	
	2001 Jul 22	101.55	61	0.427 ± 0.016	
	2001 Jul 22	100.54	62	0.438 ± 0.014	
	2001 Aug 22	86.22	15	0.586 ± 0.022	
	2001 Aug 22	86.04	15	0.581 ± 0.020	
	2001 Aug 22	85.95	15	0.596 ± 0.022	
	2001 Aug 22	85.41	16	0.586 ± 0.026	
	2001 Aug 22	85.29	16	0.576 ± 0.020	
	2001 Aug 22	80.33	18	0.631 ± 0.028	
	2001 Aug 22	79.97	18	0.661 ± 0.055	
	2001 Aug 23	98.03	66	0.456 ± 0.011	
	2001 Aug 27	86.28	14	0.564 ± 0.005	
	2001 Aug 27	86.45	14	0.565 ± 0.003	
	2001 Aug 27	86.46	15	0.566 ± 0.004	

Notes. (1) Dyck et al. (1996); (2) spurious values, discarded from the computation.

A&A 525, A42 (2011)
DOI: 10.1051/0004-6361/200913786

Astronomy & Astrophysics

Observing and modeling the dynamic atmosphere of the low mass-loss C-star R Sculptoris at high angular resolution⋆

S. Sacuto[1], B. Aringer[2], J. Hron[1], W. Nowotny[1], C. Paladini[1], T. Verhoelst[3], and S. Höfner[4]

[1] University of Vienna, Department of Astronomy, Türkenschanzstraße 17, 1180 Vienna, Austria
e-mail: stephane.sacuto@univie.ac.at
[2] INAF-OAPD, Vicolo dell'Osservatorio 5, 35122 Padova, Italy
[3] Instituut voor Sterrenkunde, K. U. Leuven, Celestijnenlaan 200D, 3001 Leuven, Belgium
[4] Department of Physics & Astronomy, Division of Astronomy & Space Physics, Uppsala University, Box 515, 751 20 Uppsala, Sweden

Received 1 December 2009 / Accepted 8 September 2010

ABSTRACT

Context. We study the circumstellar environment of the carbon-rich star R Sculptoris using the near- and mid-infrared high spatial resolution observations from the ESO-VLTI focal instruments VINCI and MIDI, respectively.
Aims. These observations aim at increasing our knowledge of the dynamic processes in play within the very close circumstellar environment where the mass loss of AGB stars is initiated.
Methods. We first compare the spectro-interferometric measurements of the star at different epochs to detect the dynamic signatures of the circumstellar structures at different spatial and spectral scales. We then interpret these data using a self-consistent dynamic model atmosphere to discuss the dynamic picture deduced from the observations. Since the hydrodynamic computation needs stellar parameters as input, a considerable effort is first applied to determining these parameters.
Results. Interferometric observations do not show any significant variability effect at the 16 m baseline between phases 0.17 and 0.23 in the K band, and for both the 15 m baseline between phases 0.66 and 0.97 and the 31 m baseline between phases 0.90 and 0.97 in the N band. We find fairly good agreement between the dynamic model and the spectrophotometric data from 0.4 to 25 μm. The model agrees well with the time-dependent flux data at 8.5 μm, whereas it is too faint at 11.3 and 12.5 μm. The VINCI visibility measurements are reproduced well, meaning that the extension of the model is suitable in the K-band. In the mid-infrared, the model has the proper extension to reveal molecular structures of C_2H_2 and HCN located above the stellar photosphere. However, the windless model used is not able to reproduce the more extended and dense dusty environment.
Conclusions. Among the different explanations for the discrepancy between the model and the measurements, the strong nonequilibrium process of dust formation is one of the most probable. The transition from windless atmospheres to models with considerable mass-loss rates occurs in a very narrow range of stellar parameters, especially for the effective temperature, the C/O ratio, and the pulsation amplitude. A denser sampling of such critical regions of the parameter space with additional models might lead to a better representation of the extended structures of low mass-loss carbon stars like R Sculptoris. The complete dynamic coupling of gas and dust and the approximation of grain opacities with the small-particle limit in the dynamic calculation could also contribute to the difference between the model and the data.

Key words. techniques: interferometric – techniques: high angular resolution – stars: AGB and post-AGB – stars: atmospheres – circumstellar matter – stars: mass-loss

1. Introduction

AGB stars are complex objects where several physical processes are in play (nucleosynthesis, convective effects, stellar pulsation, shock waves, mass-loss, molecular and dust formation, etc.). Among these mechanisms, the mass loss is particularly important for the AGB phase by limiting the maximum luminosity of the object and controlling the overall stellar evolution. The general picture of the mass-loss process of carbon-rich AGB stars is quite well understood nowadays. The pulsation of the star creates shock waves pushing the matter to conditions where both temperature and pressure allow formation of dust grains. As the opacity of amorphous carbon dust is high, grains receive enough momentum through radiative pressure to be accelerated and to drag along the gas by collisions, causing a slow outflow from the star (e.g. Fleischer et al. 1992; Höfner & Dorfi 1997).

To investigate this dynamic process, it is necessary to compare predictions of hydrodynamic atmospheric models with observations. The code described by Höfner et al. (2003) solves the coupled equations of hydrodynamics, together with frequency-dependent radiative transfer, taking the time-dependent formation, growth, and evaporation of dust grains into account. Dynamic model atmospheres coming from this code have successfully reproduced line profile variations (Nowotny et al. 2005a,b) and time-dependent spectrometric data (Gautschy-Loidl et al. 2004) of carbon-rich stars.

Because of the large distance of the closest AGB stars (typically 100 to 1000 parsec), only the high angular resolution technique of long-baseline optical interferometry allows probing the

⋆ Based on observations made with the Very Large Telescope Interferometer at Paranal Observatory under programs 60.A-9220, 074.D-0601, 077.D-0294 (French Guaranteed Time Observation), 078.D-0112 (Belgian Guaranteed Time Observation), and 078.D-0122 (French Guaranteed Time Observation).

regions where the mass-loss process develops. Interferometric predictions based on the dynamic atmospheric models with and without mass loss are described in detail by Paladini et al. (2009). The aim of this paper is to extend the work comparing the dynamic models with near- and mid-infrared high angular resolution interferometric observations of a carbon-rich star.

R Sculptoris (R Scl) is a carbon-rich, semi-regular (SRa) variable star having a low mass-loss rate ($1-5 \times 10^{-7}$ $M_{\odot}$ yr^{-1}: Le Bertre 1997; Gustafsson et al. 1997; Wong et al. 2004). The mid-infrared emission between 10 and 12 μm observed in the ISO/SWS data indicates that the star is surrounded by a warm, carbon-rich dusty shell composed of amorphous carbon (AmC) and silicon carbide (SiC) (Hron et al. 1998). The pulsation period of the star is 374 days (Whitelock et al. 1997), and the cycle-to-cycle averaged visual magnitudes vary from 6.7 to 8.1. A second period of 1804 days (~5 times the stellar pulsation period) has also been detected by Whitelock et al. (1997); however, its origin is not yet understood.

Until now, all the interferometric studies of temporal evolution of carbon-rich stars have been based on sequences of geometric and hydrostatic models with varying stellar parameters (van Belle et al. 1997; Thompson et al. 2002; Ohnaka et al. 2007). However, as argued by Höfner et al. (2003), the only way to understand how the dynamic processes influence the atmospheric structure at different spatial scales is the use of time-dependent, self-consistent dynamic models.

In this paper, we thus present the first interpretation of spectrophotometric and interferometric data of a carbon-rich star in terms of a self-consistent dynamic model atmosphere. Near- and mid-infrared interferometric data at different baselines (15, 30, and 60 m) will allow probes of regions ranging from the stellar photosphere to the innermost region of its dusty environment where the dynamic processes of shock waves, stellar winds, and mass loss are all at work.

The outline of this paper is as follows. In Sect. 2, we present the VINCI and MIDI observations of R Scl and describe the calibration performed with the corresponding data-reduction software packages developed for these instruments. Section 3 is dedicated to the variability of the star obtained from previous visual photometric and polarimetric data. We investigate the mid-infrared spectrometric and near- and mid-infrared interferometric variability of the star by comparing measurements from cycle-to-cycle and phase-to-phase. In Sect. 4, we investigate the hydrodynamic modeling of R Scl. Since the hydrodynamic computation needs stellar parameters as input, a considerable effort is first applied to the determination of the corresponding stellar parameters. The last part of this section presents the results of the self-consistent hydrodynamic modeling of the spectrophotometric and of near- and mid-infrared interferometric data of the star. Finally, we conclude and give perspectives for future work in Sect. 5.

2. Observations

The Very Large Telescope Interferometer (VLTI) of ESO's Paranal Observatory was used with VINCI, the near-infrared (λ = 2.0–2.4 μm) interferometric recombiner (Kervella et al. 2000), and MIDI, the mid-infrared (λ = 8.0–13 μm) interferometric recombiner (Leinert et al. 2003). VINCI operates around 2 microns (K band), using single spatial mode interference by employing optical fibers for spatial filtering and beam combination. MIDI combines the light of two telescopes and provides spectrally resolved visibilities in the N band atmospheric window.

Table 1. Journal of all available VINCI observations of R Scl.

Star	UT date & Time	Phase	Config.	Base[m]	PA[deg]
β Cet	2001-11-15 01:30:15	...	–	...	...
β Cet	2001-11-15 01:54:23	...	–	...	...
β Cet	2001-11-15 02:01:16	...	–	...	...
R Scl	2001-11-15 02:15:27	0.17	E0-G0	16	69
R Scl	2001-11-15 02:29:56	0.17	E0-G0	16	71
R Scl	2001-11-15 02:35:41	0.17	E0-G0	16	71
R Scl	2001-11-15 02:40:42	0.17	E0-G0	16	72
β Cet	2001-11-15 03:50:07	...	–	...	...
β Cet	2001-11-15 03:58:02	...	–	...	...
β Cet	2001-11-15 04:05:08	...	–	...	...
R Scl	2001-11-15 04:18:11	0.17	E0-G0	15	84
R Scl	2001-11-15 04:34:41	0.17	E0-G0	14	86
R Scl	2001-11-15 04:39:59	0.17	E0-G0	14	87
β Cet	2001-11-15 05:32:55	...	–	...	...
β Cet	2001-11-15 05:39:46	...	–	...	...
β Cet	2001-11-15 05:46:41	...	–	...	...
R Scl	2001-11-15 06:03:45	0.17	E0-G0	11	99
R Scl	2001-11-15 06:09:24	0.17	E0-G0	11	100
R Scl	2001-11-15 06:14:57	0.17	E0-G0	11	101
α Cma	2001-11-15 06:30:06	...	–	...	...
α Cma	2001-11-15 06:34:52	...	–	...	...
α Cma	2001-11-15 06:46:09	...	–	...	...
α Cma	2001-11-15 06:52:23	...	–	...	...
R Scl	2001-12-08 00:57:37	0.23	E0-G0	16	70
R Scl†	2001-12-08 01:03:54	0.23	E0-G0	16	72
R Scl	2001-12-08 01:13:17	0.23	E0-G0	16	72
R Scl	2001-12-08 01:18:42	0.23	E0-G0	16	73
R Scl	2001-12-08 01:25:45	0.23	E0-G0	16	74
β Cet	2001-12-08 01:38:37	...	–	...	...
β Cet	2001-12-08 01:45:31	...	–	...	...
β Cet	2001-12-08 01:50:26	...	–	...	...
R Scl	2001-12-08 02:09:03	0.23	E0-G0	15	79
R Scl	2001-12-08 02:13:53	0.23	E0-G0	15	80
β Cet	2001-12-08 02:26:18	...	–	...	...
β Cet	2001-12-08 02:33:18	...	–	...	...

Notes. The calibrators used to calibrate the visibilities are given before or after the science target. The visual phase of the star during the observations is calculated from Eq. (1). The configuration used for the observations is given. The length and position angle of the projected baseline are also indicated. Same for Tables 2 and 3.
$^{(\dagger)}$ Means that the data were not exploitable (see text). Same for Tables 2 and 3.

Observations of R Scl were conducted in 2001, 2005, and 2006 with the VLT unit telescopes (UTs) UT2–UT4, and auxiliary telescopes (ATs) E0-G0, D0-G0, A0-G0, G0-K0, G0-H0, and D0-H0. This provides projected baselines and projected angles in the range of 11 to 64 m and 34° to 117°, respectively (see Tables 1–3, and Fig. 1). The seeing of all the VINCI observations is below 0.9″, whereas it is below 2.4″ in the case of the MIDI observations (see Tables 2 and 3).

Tables 1–3 present the journals of interferometric observations of R Scl with the VINCI and MIDI focal instruments. The calibrators, β Cet (G9II-III, angular diameter: $\oslash$ = 5.18 ± 0.06 mas), α CMa (A1V, $\oslash$ = 5.94 ± 0.02 mas) for VINCI and HD 12524 (K5III, $\oslash$ = 2.53 ± 0.07 mas), β Gru (M5III, $\oslash$ = 26.8 ± 1.3 mas), τ^4 Eri (M3/M4III, $\oslash$ = 10.6 ± 1.0 mas), HD 4128 (G9II-III, $\oslash$ = 5.04 ± 0.07 mas) for MIDI, were observed before or after the science target. Diameters of the VINCI calibrators were adopted from the `CHARM2` catalog (Richichi et al. 2005). Diameters of the MIDI calibrators HD 12524 and HD 4128 were taken from the ESO website through the `CalVin`

Table 2. Journal of all available MIDI Unit Telescopes observations of R Scl.

#	Star	UT date & Time	Phase	Config.	Base[m]	PA[deg]	Seeing[arcsec]	Mode	Spectral resolution
1	R Scl	2005-01-03 03:01:23	0.23	U2-U4	61	117	1.7	HIGH-SENS	230
Cal	HD 12524	2005-01-03 03:27:24	...	–	...	...	1.0	–	–
2	R Scl†	2005-01-03 04:05:54	0.23	U2-U4	47	136	0.9	HIGH-SENS	230
Cal	HD 12524	2005-01-03 04:45:32	...	–	...	...	0.8	–	–

Table 3. Journal of all available MIDI Auxiliary Telescopes observations of R Scl.

#	Star	UT date & Time	Phase	Config.	Base[m]	PA[deg]	Seeing[arcsec]	Mode	Spectral resolution
3	R Scl	2006-06-16 09:38:09	0.64	E0-G0	14	42	0.7	SCI-PHOT	30
Cal	β Gru	2006-06-16 10:23:60	...	–	...	...	0.6	–	–
4	R Scl	2006-06-22 09:29:58	0.66	D0-G0	29	46	0.8	SCI-PHOT	30
Cal	τ^4 Eri	2006-06-22 09:49:48	...	–	...	...	0.9	–	–
5	R Scl†	2006-06-23 09:23:50	0.66	E0-G0	14	45	1.0	SCI-PHOT	30
6	R Scl	2006-06-23 09:46:04	0.66	E0-G0	15	50	1.4	SCI-PHOT	30
Cal	τ^4 Eri	2006-06-23 10:04:33	...	–	...	...	1.1	–	–
7	R Scl	2006-08-08 09:52:10	0.79	A0-G0	62	77	1.1	SCI-PHOT	30
Cal	τ^4 Eri	2006-08-08 10:09:22	...	–	...	...	1.4	–	–
Cal	HD 4128	2006-09-17 04:56:51	...	–	...	...	2.0	–	–
8	R Scl†	2006-09-17 05:26:12	0.89	A0-G0	63	63	1.8	HIGH-SENS	30
Cal	HD 4128	2006-09-17 05:51:43	...	–	...	...	1.7	–	–
9	R Scl†	2006-09-17 06:20:53	0.89	A0-G0	64	71	2.4	HIGH-SENS	30
Cal	HD 4128	2006-09-17 06:42:41	...	–	...	...	2.0	–	–
10	R Scl†	2006-09-17 07:06:01	0.89	A0-G0	63	77	1.9	HIGH-SENS	30
Cal	HD 4128	2006-09-18 03:13:16	...	–	...	...	1.5	–	–
11	R Scl†	2006-09-18 03:55:48	0.89	A0-G0	59	48	1.6	HIGH-SENS	30
12	R Scl†	2006-09-18 04:19:15	0.89	A0-G0	60	53	1.5	HIGH-SENS	30
Cal	HD 4128	2006-09-18 04:39:39	...	–	...	...	1.7	–	–
13	R Scl†	2006-09-18 05:02:08	0.89	A0-G0	62	60	1.6	HIGH-SENS	30
Cal	HD 4128	2006-09-18 05:25:49	...	–	...	...	1.6	–	–
Cal	HD 4128	2006-09-18 07:05:14	...	–	...	...	1.5	–	–
14	R Scl†	2006-09-18 07:34:30	0.89	A0-G0	61	80	2.1	HIGH-SENS	30
Cal	HD 4128	2006-09-19 07:07:06	...	–	...	...	1.2	–	–
15	R Scl†	2006-09-19 07:32:00	0.90	D0-G0	30	81	1.3	HIGH-SENS	30
Cal	HD 4128	2006-09-19 07:56:01	...	–	...	...	1.2	–	–
16	R Scl†	2006-09-19 08:19:20	0.90	D0-G0	28	87	1.5	HIGH-SENS	30
Cal	HD 4128	2006-09-20 04:12:27	...	–	...	...	1.3	–	–
17	R Scl	2006-09-20 04:36:30	0.90	D0-G0	31	57	1.6	HIGH-SENS	30
18	R Scl	2006-09-21 02:40:17	0.90	G0-K0	54	34	1.7	HIGH-SENS	30
Cal	HD 4128	2006-09-21 03:03:59	...	–	...	...	1.1	–	–
19	R Scl	2006-10-16 03:05:26	0.97	G0-H0	31	59	0.6	SCI-PHOT	30
Cal	τ^4 Eri	2006-10-16 03:28:25	...	–	...	...	0.5	–	–
20	R Scl	2006-10-16 07:00:03	0.97	D0-H0	53	90	0.6	SCI-PHOT	30
Cal	τ^4 Eri	2006-10-16 07:24:05	...	–	...	...	0.5	–	–
21	R Scl	2006-10-17 02:05:02	0.97	D0-H0	59	49	1.4	SCI-PHOT	30
Cal	τ^4 Eri	2006-10-17 02:26:29	...	–	...	...	1.0	–	–
22	R Scl	2006-10-18 01:51:25	0.97	E0-G0	15	47	0.8	HIGH-SENS	30
Cal	HD 4128	2006-10-18 02:13:41	...	–	...	...	0.9	–	–
23	R Scl	2006-10-18 02:34:58	0.97	E0-G0	15	55	0.9	SCI-PHOT	30
Cal	τ^4 Eri	2006-10-18 02:59:24	...	–	...	...	0.8	–	–
24	R Scl	2006-10-18 04:51:15	0.97	E0-G0	16	75	1.0	HIGH-SENS	30
Cal	HD 4128	2006-10-18 05:22:11	...	–	...	...	1.1	–	–
25	R Scl†	2006-10-19 03:28:15	0.98	E0-G0	16	64	1.0	HIGH-SENS	30
Cal	HD 4128	2006-10-19 03:52:03	...	–	...	...	0.4	–	–
26	R Scl	2006-10-19 04:15:04	0.98	E0-G0	16	71	0.7	HIGH-SENS	30
Cal	HD 4128	2006-10-19 04:37:45	...	–	...	...	0.7	–	–
27	R Scl	2006-10-19 05:23:42	0.98	E0-G0	15	79	0.5	SCI-PHOT	30
Cal	τ^4 Eri	2006-10-19 05:49:48	...	–	...	...	0.4	–	–
Cal	τ^4 Eri	2006-12-16 02:57:16	...	–	...	...	1.7	–	–
28	R Scl	2006-12-16 03:19:24	0.13	G0-H0	25	93	1.4	SCI-PHOT	30
Cal	τ^4 Eri	2006-12-18 00:57:42	...	–	...	...	1.2	–	–
29	R Scl	2006-12-18 01:21:29	0.14	G0-H0	31	79	1.2	SCI-PHOT	30
Cal	τ^4 Eri	2006-12-21 01:27:43	...	–	...	...	0.9	–	–
30	R Scl	2006-12-21 02:06:31	0.15	G0-H0	29	86	1.7	SCI-PHOT	30

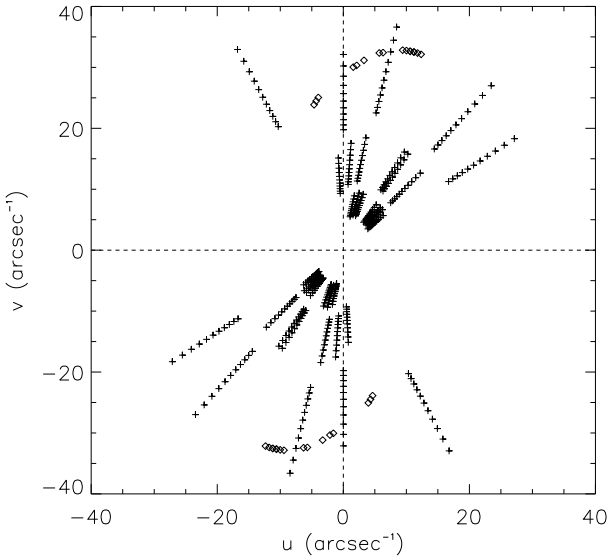

Fig. 1. *K*-band *uv* coverage of the VINCI observations (diamonds) and *N*-band spectrally-dispersed (from 8 to 13 μm) *uv* coverage of the MIDI observations (plus) (see Tables 1–3).

database[1]. The diameter of the MIDI calibrator τ^4 Eri was taken from the CHARM2 catalog (Richichi et al. 2005). Finally, the diameter of the MIDI calibrator β Gru was defined from the work of Sacuto et al. (2008).

The VINCI data (program 60.A-9220) were processed with the pipeline of data reduction based on the wavelet transform described in Kervella et al. (2004). After checking the stability of the transfer function (T_i) over the two nights of observations, the raw visibility measurements were calibrated using the weighted average of the estimated T_i^2.

The VINCI instrument has a bandpass corresponding to the *K*-band filter (2.0−2.4 μm) without spectral dispersion. It is thus necessary to compute an effective wavelength to determine the spatial frequency of the observation (Kervella et al. 2007). The effective wavelength of our observations was calculated from the relation given by Wittkowski et al. (2004) using the best-fitting hydrostatic model spectrum of R Scl described in Sect. 4.1. We obtained an effective wavelength of 2.253 μm.

Among the VINCI data, one observation (2001-12-08 01:03:54; see Table 1) led to an outlier showing an abnormally low level of amplitude as compared to the other visibility data at close base, PA, and phase. The corresponding visibility measurement was discarded.

In the case of MIDI, chopped acquisition images were recorded (f = 2 Hz, 2000 frames, 4 ms per frame) to ensure the accurate acquisition of the target. Photometry from the UT observations (program 074.D-0601) was obtained before and after the interferometric observations with the HIGH-SENS mode of MIDI, using the GRISM that provides a spectral resolution of about 230. Photometry from the AT observations were obtained with the HIGH-SENS mode (program 078.D-0112), and simultaneously with the interferometric observations with the SCI-PHOT mode of MIDI (programs 077.D-294 and 078.D-0122), using the PRISM that provides a spectral resolution of about 30. The acquisition images enabled us to confirm that the mid-IR source was unresolved by the single-dish UT. This implies that most of the mid-infrared flux originates in the inner 300 mas of the source, corresponding to the Airy pattern of the UTs and defining the Field Of View (FOV) of the interferometric observations. This also means that the flux detected within the 1.1″ FOV of the single-dish AT originates in this inner region. Therefore, measurements extracted from the ATs and the UTs are fully consistent with each other.

The data reduction software packages[2] MIA and EWS (Jaffe 2004) were used to derive the calibrated spectra and visibilities (Chesneau et al. 2005; Ratzka et al. 2007). MIA is based on a power spectrum analysis and uses a fast Fourier transformation (FFT) to calculate the Fourier amplitude of the fringe packets, while EWS uses a shift-and-add algorithm in the complex plane, averaging appropriately modified individual exposures (dispersed channeled spectra) to obtain the complex visibility.

To calibrate the MIDI visibility measurements of R Scl, we used the transfer functions derived from the closest calibrators in time from the source (see Tables 2 and 3). This allows a decrease in the bias due to the air mass difference between the source observation at a given sky location and the calibrator observation at another location. The main source of uncertainties on the calibrated visibility measurements comes from the time-dependent atmospheric transmission between the observation of the calibrator and the source and from the dimension and uncertainty on the calibrator angular diameter (Bordé et al. 2002; Cruzalebès et al. 2010). The rms of the transfer function deduced from all the calibrators of the night gives an upper estimate of the calibrated visibility error bar due the time-dependent atmospheric condition between the observations of the source and the calibrator. We assume a standard error bar of 10% on the calibrated visibilities corresponding to the upper limit on the error budget previously assigned. However, in the case of the HIGH-SENS mode, the photometry is performed about 5 to 10 min after the record of the fringe, i.e. correlated flux. As the atmospheric conditions change between both recordings, an additional error bar on the calibrated visibilities must be considered. Taking a similar error into account for both the SCI-PHOT and HIGH-SENS modes implicitly assumes that the variation in the transfer functions is *much* greater than the intrinsic error of one measurement due to the changing weather conditions. During good atmospheric conditions, this assumption is reasonable. During bad atmospheric conditions (i.e. up to a certain seeing threshold), the large fluctuation of the positions of the two beams reduces the beam overlap leading to strong variations in the fringe amplitude and the photometry. A solution to quantify the influence of the seeing on an individual measurement is to use the SCI-PHOT mode data with additional photometry (*pseudo HIGH-SENS* mode) taken under similar atmospheric conditions. Comparing calibrated visibilities reduced with the pure SCI-PHOT mode with those reduced with the pseudo HIGH-SENS mode gives a direct handle on the midterm (i.e. time span from fringe tracking to the photometry) influence of the seeing. Under bad conditions (i.e. seeing ≥1.5″), the pseudo HIGH-SENS mode gives systematic lower visibilities, up to a level of 4%, when comparing them to the ones deduced from the pure SCI-PHOT mode, while the difference falls to zero when the seeing is smaller than 1.1″. This is reasonable considering that the overlap of two beams is statistically reduced leading to systematically lower visibilities. We therefore consider an additional positive deviation of 4% (i.e. up to the 5% SCI-PHOT positive error) on the error bars associated to the calibrated visibilities recorded in HIGH-SENS mode under bad atmospheric conditions (i.e. seeing ≥1.5″). Finally, the error bar on the calibrated visibilities recorded in HIGH-SENS mode

[1] http://www.eso.org/observing/etc/

[2] http://www.mpia-hd.mpg.de/MIDISOFT/, http://www.strw.leidenuniv.nl/~nevec/MIDI/

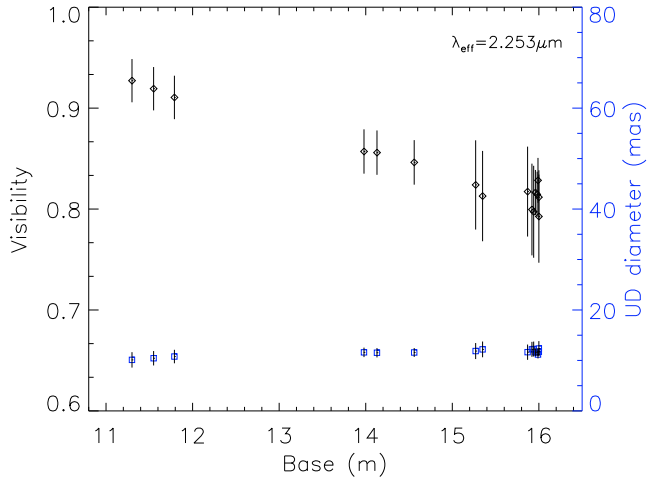

Fig. 2. Broadband VINCI visibilities of R Scl (black diamonds) as a function of the projected baselines observed over 2 nights between November and December 2001 (see Table 1). Uniform disk diameters (blue squares to be read from the scale on the right axis) are computed from each visibility measurement.

under better atmospheric conditions (i.e. seeing ≤1.1″) is similar to the standard 10% error bar assigned to the SCI-PHOT mode measurements.

The data quality has been checked using the *MIA Graphical User Interface*, and the software developed by Paris Observatory for MIDI[3]. Among the MIDI measurements, data sets #2, #5, #8, #15, and #25 (see Tables 2 and 3) led to outliers. Data sets #2, #15, and #25 show calibrated visibilities greater than unity, data set #5 shows an unusual spectral signature of the dispersed visibility, whereas data set #8 shows an abnormally high level of visibility amplitude compared to the other visibility data at close base, PA, and phase. Finally data sets #9, #10, #11, #12, #13, #14, and #16 show very broad dispersed power spectral densities (PSD) and/or fringe histograms (FH), especially from 8 to 10 μm since shorter wavelengths are more affected by the atmospheric conditions. If the PSD and FH are very broad, a very significant fraction of the fringe power is distributed outside the integration range, leading to a systematic underestimation of visibility. All the corresponding visibility measurements were discarded.

Figure 1 shows the K-band uv coverage of the VINCI observations (see Table 1) and the N-band spectrally-dispersed uv coverage of the MIDI observations (see Tables 2 and 3). The spatial coverage spreads over a large scale (from 15 to 60 m baselines), whereas the angular coverage is limited to 90°.

Figure 2 presents the VINCI calibrated visibilities observed over 2 nights between November and December 2001 (see Table 1). The angular diameters of the equivalent uniform disk are computed from each visibility measurement and show a stability from phase-to-phase at different position angles. Figure 3 shows the MIDI calibrated visibilities observed over 14 nights between January 2005 and December 2006 (see Tables 2 and 3). The diameters of the equivalent uniform disk were computed from the visibilities at each spectral channel. The dimension of those diameters regularly increases from 9 to 13 μm, indicating an extended circumstellar environment (Ohnaka et al. 2005).

[3] Software is available through the JMMC website: http://mariotti.ujf-grenoble.fr/

The phase shifts or differential phases correspond to the information extracted from the difference between the phase at a given wavelength and the mean phase determined in the full N-band region. It provides information about possible asymmetry of the source in the region covered by the different interferometric measurements. As an example, strong phase signals were detected in sources harboring dusty disks (Deroo et al. 2007; Ohnaka et al. 2008). Due to the low values (<±5°) of the calibrated differential phases for each projected baseline, the global centrosymmetry of the close circumstellar environment of the object is confirmed in the mid-infrared for the corresponding angular coverage.

3. Observed variability of R Scl

Sections 3.1–3.3 discuss the variability of the star derived from photometry, polarimetry, and spectroscopy. Finally, Sect. 3.4 is dedicated to the interferometric variability giving constraints on the dynamic process at work in the close circumstellar environment of R Scl.

3.1. Photometric variability

The K-band light curve of R Scl was discussed by Whitelock et al. (1997). The authors distinguish two main periods of 374 and 1804 days. The shorter period is identified to be the pulsation period of the star, whereas the longer one might be a beat period between two similar pulsation periods (Houk 1963). More recent polarimetric measurements (Yudin & Evans 2002, see Sect. 3.2) reveal a clumpy medium surrounding R Scl where orbiting dusty clump structures could also be the origin of the long period.

In the following, the phase of the star is established from the light curve according to

$$\phi = \frac{(t - T_0) \bmod P}{P}, \tag{1}$$

where t corresponds to the observing time in Julian day, T_0 = 2 451 044 is the Julian date of the selected phase-zero point corresponding to the maximum light of the star ($\phi_0 = 0$; see Fig. 4), and P = 374 days is the pulsation period of the star.

Besides the VINCI interferometric and MIDI spectro-interferometric observations of R Scl, polarimetric (Yudin & Evans 2002) and additional ISO/SWS spectrometric (Sloan et al. 2003) data of the star are available.

Figure 4 represents the visual lightcurve of R Scl where the polarimetric (Pola.), spectroscopic (ISO and MIDI), and interferometric (VINCI and MIDI) observing periods are marked.

3.2. Polarimetric variability

Wherever there is appreciable asymmetry in an astronomical situation, emitted light is likely to be polarized at some level. Yudin & Evans (2002) show that R Scl displays polarimetric variability in the VR_CI_C bands on different time scales from hours to one year. The authors argue that the polarimetric variations of the star are most probably not related to binarity, since these variations occur on timescales that are inferior to one pulsation period (~374 days). With a wavelength-dependence of polarization close to $P \propto \lambda^4$, consistent with Rayleigh scattering by small (≈0.01 μm) amorphous grains, the authors suggest that the polarimetric variation would be related to dusty clumps located in the inner zone of the warm dusty shell (i.e. from 2 to 4 $R_\star$) with a quasi-period of rotation in the range 470 to 1600 days.

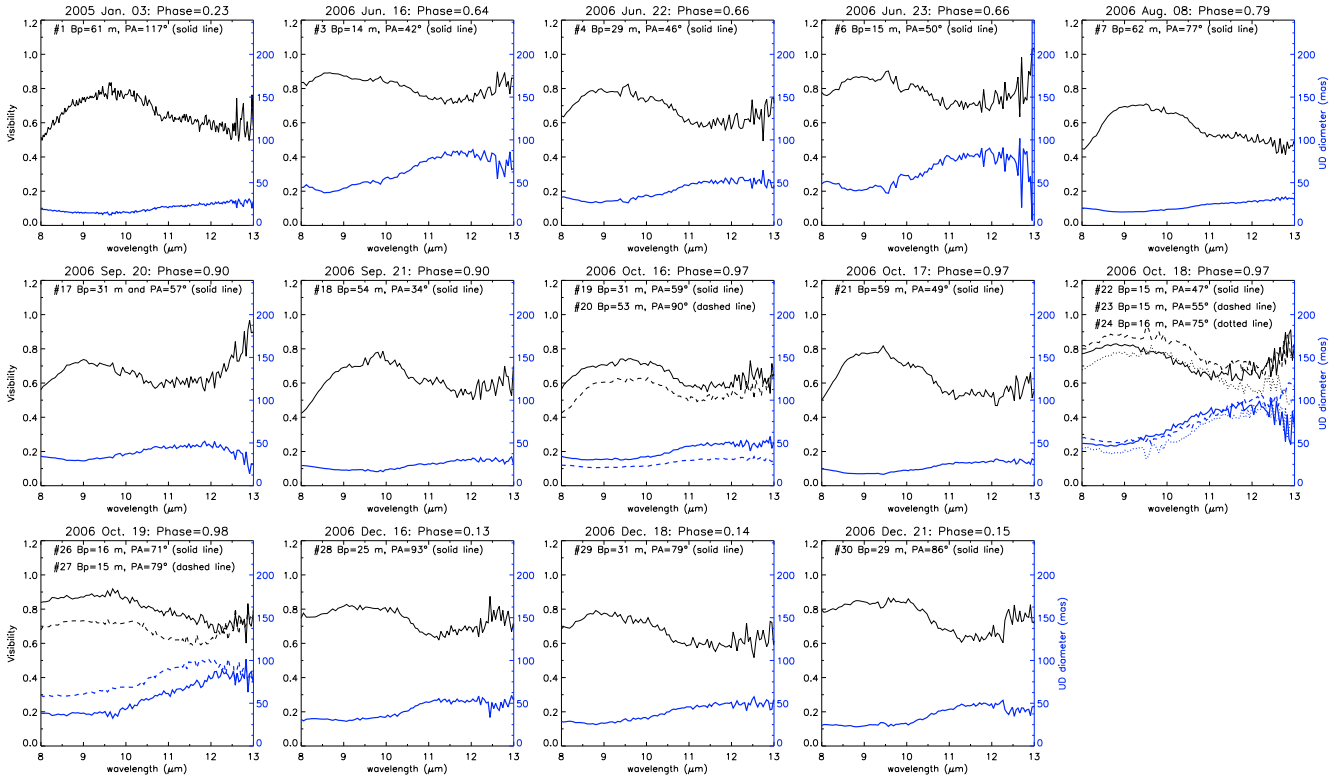

Fig. 3. Spectrally-dispersed MIDI visibilities of R Scl (black thin lines to be read from the scale on the left axis) observed over 14 nights between January 2005 and December 2006 (see Tables 2 and 3). Uniform disk diameters (blue thick lines to be read from the scale on the right axis) are computed from the visibilities at each spectral channel. Error bars are not included for clarity. The data set numbers are defined in Tables 2 and 3.

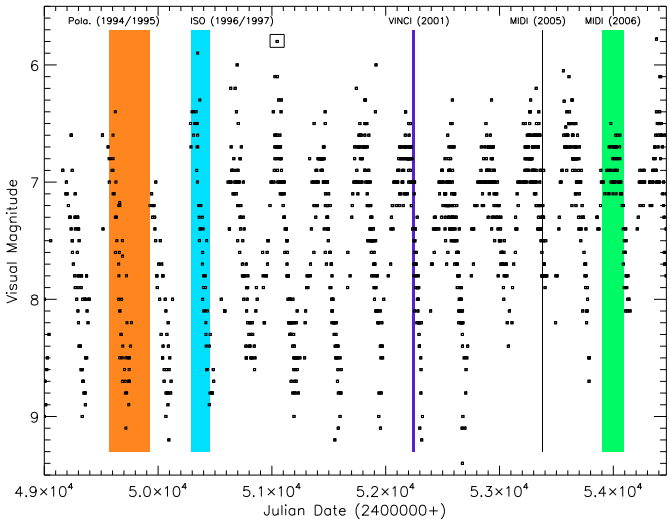

Fig. 4. AAVSO visual lightcurve of R Scl (Henden 2009). Colored zones indicate the observing period of Polarimetric measurements (orange) (Yudin & Evans 2002), ISO/SWS measurements (blue) (Sloan et al. 2003), VINCI measurements (violet), MIDI UT measurement (black), and MIDI AT measurements (green). The point surrounded by the open rectangle represents the chosen phase-zero point ($\phi_0 = 0$).

The constraints provided by the MIDI differential phases (see Sect. 2), which do not exhibit any asymmetries in the close vicinity of the source (from 2 to 10 $R_\star$), contradict the conclusions of Yudin & Evans (2002). Therefore, we are left with three possibilities.

(i) *The MIDI interfererometric angular coverage is outside the dusty clumps region.* It is difficult to determine the position of the clumps because of the large uncertainty on their rotational period found by Yudin & Evans (2002). As it is not possible to locate the clumps at the time of the MIDI observations, we cannot exclude that the clumpy region is situated out of the interferometric coverage, which only spreads over an angle of 90° (see Fig. 1).

(ii) *The dynamic range of MIDI is not high enough to separate the emission of the dusty clumps from the one coming from the circumstellar material.* We can investigate this point by an estimation of the constraints provided by the MIDI differential phase measurements. For that, we performed a perturbation of the intensity distribution of the best-fitting model (see Sect. 4.2) by a Gaussian-like dust cloud of 1.8 mas width (defined from the density structure found by Yudin & Evans 2002) varying its flux contrast, its distance (from 2 to 4 $R_\star$), and its position angle. Our tests allow any mid-IR dusty clump source representing more than about 4% of the total flux of the object (i.e. 4 to 8 Jy between 8 μm and 13 μm) to be discarded. Taking the condensation density ρ_c and the condensation mass derived by Yudin & Evans (2002) into account, and describing the dusty clump as a blackbody of 1000 to 1500 K at a distance ranging from 2 to 4 $R_\star$, we obtain a flux range between 2.0 and 3.5 Jy in the N-band. As these values are below 4% of the total flux of the object, this solution can be retained.

(iii) *The dusty clumps emission vanished from the N-band spectral window during the 10 years separation from the polarimetric to the MIDI interferometric observations.* Shock waves could push the dusty clumps observed by polarimetry to regions where its emission peak is outside the mid-infrared window. However, taking a shell expansion

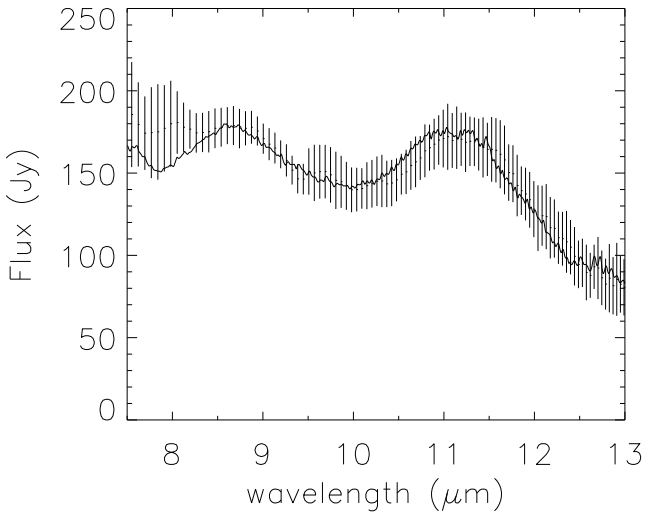

Fig. 5. Comparison of the ISO/SWS spectrum of R Scl at phase 0.97 (thick line), and the MIDI spectrum of R Scl at phase 0.98 (error bars).

velocity from 10.5 to 16.5 km s^{-1} into account for R Scl (Schöier & Olofsson 2001; Wong et al. 2004), the dusty clump would be located around 14.4 to 23.4 $R_\star$ (within the FOV of both AT and UT telescopes) at the end of the 10-year separation from the polarimetric to the MIDI observations. Assuming a Planckian radiation field geometrically diluted with distance from the star, the temperature of the clump reaches about 400 K corresponding to an emission peak well inside the mid-infrared window. Therefore this solution can be discarded.

3.3. Spectrometric variability

As discussed in Sect. 2, most of the mid-infrared flux originates in the inner 300 mas of the source. Therefore, the mid-infrared spectra obtained from the AT and UT single dishes are directly comparable to the ones produced by the ISO telescope (FOV = 33″ × 20″). To keep consistency in the comparison to the measurements, only ISO/SWS spectra using the AOT 1 template (Leech et al. 2003) are considered in the following. Figure 5 compares both calibrated MIDI and ISO/SWS spectra (Sloan et al. 2003) of R Scl around the maximum visual light ($\phi \sim 0$).

Figure 6 presents the calibrated MIDI and ISO/SWS flux of R Scl as a function of the phase at 8.5 μm (*pseudo-continuum*: defined where the blackbody continuum fits to the ISO/SWS spectrum of the star), 11.3 μm (SiC feature), and 12.5 μm (C_2H_2+HCN) spectral bands (Hron et al. 1998; Gautschy-Loidl et al. 2004; Zijlstra et al. 2006). Each monochromatic flux is determined by integration of the narrow-band filter fluxes over a bandwidth of $\Delta\lambda = 0.2$ μm. The MIDI error bars are estimated from the standard deviation of the N-band flux-calibrated spectra determined from each night and each telescope, i.e. typically 3 to 10 spectra, except at phases 0.23 and 0.79 where only one spectrum is available (see Tables 2 and 3).

From Figs. 5 and 6, we can argue that the level of flux received by MIDI is equivalent to the one of ISO. It means that the cycle-dependent flux level of the object in the N-band has probably not changed significantly from the ISO/SWS (1996/1997) to the MIDI (2005/2006) observations. From Fig. 6, it is rather difficult to determine a real trend in variability, keeping in mind typical errors in the absolute ISO/SWS flux level ranging from 10 to 12% (van der Bliek et al. 1998) and an error of about 20% for the MIDI flux.

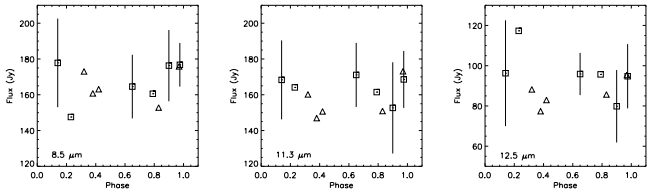

Fig. 6. MIDI (squares) and ISO/SWS (triangles) flux of R Scl as a function of the visual phase in the 8.5 (*left*), 11.3 (*middle*), and 12.5 μm (*right*) spectral band corresponding to the *pseudo-continuum*, the SiC feature, and the C_2H_2+HCN feature, respectively.

3.4. Interferometric variability

To study the interferometric variability of the star, we compare visibility measurements observed at the same projected baseline lengths for very close position angles (few degree differences) from one epoch to another one. The same projected baselines need to be used to probe the same spatial regions of the object, whereas very close projected angles are needed to avoid effect coming from potential deviation in the geometry of the object from spherical symmetry.

We first compare both sets of VINCI visibility measurements at $\phi = 0.17$ and $\phi = 0.23$ for the given 16 m projected baseline length through a range of 5° in position angle. This comparison does not display any significant (larger than 2σ) temporal variation. This fact is, however, not surprising given the short time interval at post-maximum brightness of the star and because the broadband measurements will average out the possible short term effects of shock fronts in CO or CN lines (e.g. Nowotny et al. 2005a; Paladini et al. 2009). As the VINCI data only probe the very low spatial frequency, what remains are thus only the slow variations due to stellar pulsation ($P = 374$ days).

In the case of the MIDI measurements, the lowest spectral resolution ($R = 30$) is high enough to resolve the broad features contained in the N-band spectral window (i.e. C_2H_2, HCN, C_3, and SiC). Therefore, we do not expect any effect that could possibly smear out the temporal variation coming from emission or absorption bands in that region. Figure 7 shows comparisons between the MIDI spectrally-dispersed visibilities from phase-to-phase at a given projected baseline length for very close position angles. The measurements do not show any significant variability effect for both 15 and 31 m baselines. Because those baselines probe the region located from ~17.5 to 100 mas (3.4 to 19.6 $R_\star$), this means that the stellar radiative pressure is not strong enough to reveal a significant movement of the warm mass dust shells detectable at the spatial resolution of the interferometer (from ~8 to 12 mas: 2.9 to 4.3 AU at 360 pc). Such behavior agrees with the amplitude of the mass shell of theoretical carbon-rich dynamic models, which does not exceed 3 AU over a full cycle in the mid-infrared (see Paladini et al. 2009).

4. Modeling the dynamic atmosphere of R Scl

The strategy of determining the best-fitting parameters for the dynamic model atmosphere of the C-rich star R Scl is the following:

Step 1: The hydrodynamic computation (see Sect. 4.3.1) starts with an initial hydrostatic structure mainly characterized

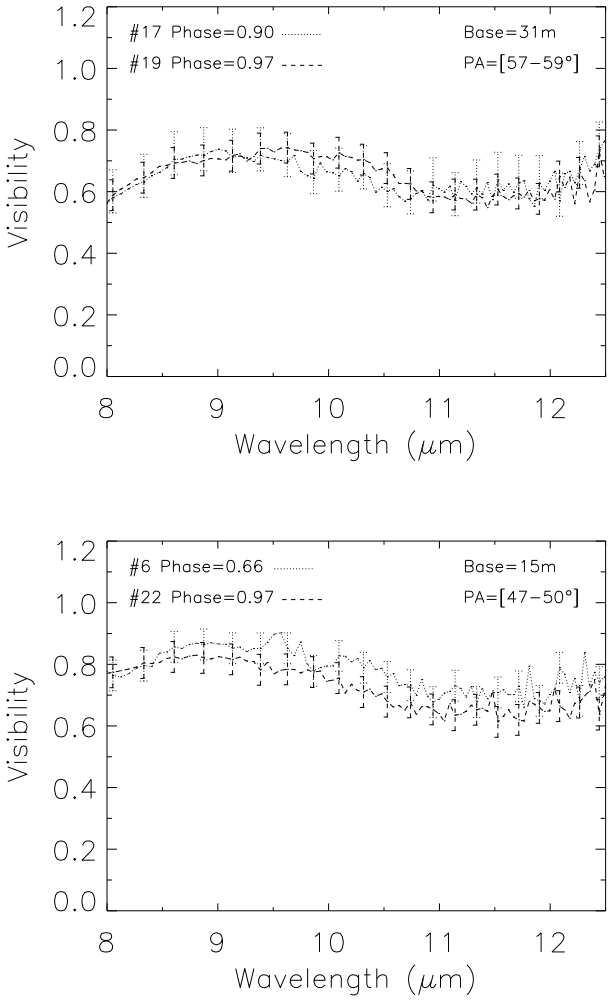

Fig. 7. Comparison between spectrally-dispersed MIDI visibilities from phase-to-phase (black thin dashed and dotted lines) at a given projected baseline length for very close position angles. The data set numbers are defined in Table 3.

Table 4. Broadband photometry of R Scl.

Band	Extinction coefficient	Dereddened magnitude	Phase	Reference
B	0.25	11.03 ± 0.3[1]	0.17	Bagnulo et al. (1998)
V	0.18	4.55 ± 0.7[1]	0.17	–
J	0.05	1.56 ± 0.05	0.12	–
H	0.03	0.46 ± 0.05	0.12	–
K	0.02	–0.24 ± 0.06	0.12	–
L′	0.01	–0.84 ± 0.28	0.12	–
J	0.05	1.97 ± 0.86	Whole cycle	Whitelock et al. (2006)
H	0.03	0.63 ± 0.64	–	–
K	0.02	–0.10 ± 0.36	–	–
L	0.01	–0.74 ± 0.28	–	–

Notes. [(1)] Uncertainties calculated from the measurements given in the Simbad database.

by the following parameters (Höfner et al. 2003): luminosity, mass, effective temperature, metallicity, C/O ratio, and micro-turbulent velocity (for line opacities). In order to derive these parameters, we first perform a hydrostatic modeling of the stellar atmosphere (Sect. 4.1) using a grid of COMARCS models (Aringer et al. 2009). By fitting synthetic spectra and visibilities based on such models to observed near-infrared spectro-interferometric measurements of R Scl, we find the best set of stellar atmospheric parameters for the initial hydrostatic structure of the dynamic model.

Step 2: The mid-infrared excess of R Scl shows an SiC feature around 11.2 μm (see Fig. 5). This component must therefore be considered in the spectral synthesis for the comparison with observational data. Since only AmC dust is treated in the hydrodynamic calculation (Höfner et al. 2003), opacities of SiC dust are added in the a posteriori radiative transfer computation (see Sect. 4.3.1). Those opacities are determined by finding the proper SiC optical constants, and the fractional abundance of SiC to AmC dust that has condensed. These two characteristics are determined in Sect. 4.2.1 by comparing observed mid-infrared spectro-interferometric measurements of R Scl with synthetic spectra and visibilities derived from the DUSTY numerical code (Ivezić & Elitzur 1997; Ivezić et al. 1999), which solves the radiative transfer equation through a dusty envelope.
In Sect. 4.2.2 we present the disagreement of the best-fitting model created by the combination of the hydrostatic COMARCS atmosphere and DUSTY circumstellar envelope (COMARCS+DUSTY model) with the observational data. This shows the necessity of using a self-consistent hydrodynamic model to understand how the time-dependent processes influence the atmospheric structures of the star.

Step 3: Finally, the self-consistent dynamic model used in Sect. 4.3.3 is chosen by the parameters deduced from the best hydrostatic fit of the stellar atmosphere (see Sect. 4.1) together with the SiC dust parameters derived from the DUSTY modeling (see Sect. 4.2.1). We then interpret the spectro-interferometric data of R Scl using this model to discuss the dynamic picture deduced from the observations.

4.1. Determination of the stellar parameters of R Scl with hydrostatic model atmospheres

Besides the ISO/SWS spectra (see Sect. 3.3), ground-based photometric measurements (Bagnulo et al. 1998; Whitelock et al. 2006) are available for R Scl (see Table 4). Using the relation of Milne & Aller (1980), also used by Bagnulo et al. (1998), a visual interstellar extinction value of 0.18 was derived. The ratio of total-to-selective extinction at V, 3.1, on average, allowed us to correct the other magnitudes using the absorption curve of Fitzpatrick (1999). The data of Whitelock et al. (2006) are dispersed over a wide range of 26.3 pulsation periods of the star, whereas the data of Bagnulo et al. (1998) are measured at post-maximum light of the object.

Because of all the absorption lines coming from strong molecular opacity sources (mainly species containing C, H, N, O; see Gautschy-Loidl et al. 2004), spectra of cool stars differ a lot from a blackbody continuum spectra as is highlighted in Fig. 8. The use of a more realistic synthetic carbon-rich spectrum is then required. The COMA code, developed by Aringer (2000), solves for the ionization and chemical equilibrium (using the method of Tsuji 1973) at a given temperature and density (or pressure) combination for a set of atomic abundances assuming LTE. Based on these results, atomic and molecular opacities are calculated. Details of computation and information on recent updates on the COMA code can be found

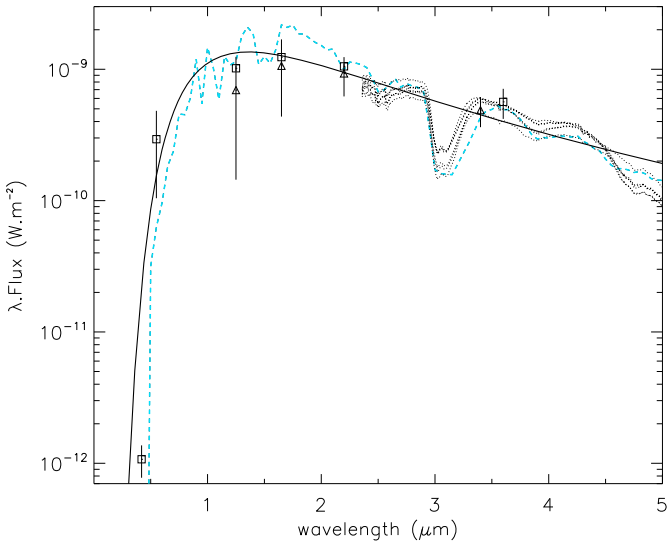

Fig. 8. Best-fitting hydrostatic model (blue dashed line) on the spectrophotometric measurements. Photometric measurements (squares: Bagnulo et al. 1998 + triangles: Whitelock et al. 2006; see Table 4) and ISO/SWS spectra of R Scl at different epochs (dotted lines) are shown. A blackbody continuum having the same temperature ($T_{\rm eff}$ = 2700 K) and angular diameter ($\oslash_\star$ = 10.2 mas) as the synthetic COMARCS spectrum is superimposed (black solid line).

in Lederer & Aringer (2009), and Aringer et al. (2009). These opacities are then introduced in a spherically symmetric radiative transfer code to calculate the emergent intensity distribution. This intensity distribution is then used to derive the synthetic spectrum and visibility profile, which are compared with observational data of the star.

The determination of the stellar parameters is done by comparing hydrostatic COMARCS models to the spectrophotometric data up to 5 μm. This limit is fixed because of the contribution of the dust becoming non negligible at longer wavelengths for optically thin, *warm dusty objects* like R Scl (Kraemer et al. 2002). This will be confirmed by the DUSTY modeling in Sect. 4.2.1. The hydrostatic model was chosen as best-fitting of the broadband photometric data (see Table 4) and the various features in the ISO/SWS spectra (see Fig. 8) averaged over all the phases. Furthermore, the best-fitting model should also agree with the K-broadband VINCI interferometric measurements (see Sect. 2).

A least-square fitting minimization was completed from the grid of models included in Aringer et al. (2009), varying the parameter values of effective temperature of the star from 2600 to 3000 K ($\Delta T_{\rm eff}$ = 100 K), the luminosity from 6000 to 8000 $L_\odot$ (ΔL = 200 $L_\odot$), the distance from 300 to 500 pc (Δd = 50 pc), the mass for values of 1 and 2 $M_\odot$, the metallicity for values of 1, 0.33, and 0.1 $Z_\odot$, and the C/O ratio for values of 1.1, 1.4, and 2.0. Finally, a value of 2.5 km s^{-1} for the microturbulent velocity (ζ), coming from the fit of very high spectral resolution data of carbon stars, is taken into account.

We obtained the best-fitting model to the ISO/SWS spectrometric data from 2.4 to 5 μm with a reduced χ^2 of 3.5 (see Table 5).

Figure 8 shows the best-fitting hydrostatic model on the spectrophotometric data of the star. As the VINCI data are integrated over the K-band (2.0–2.4 μm) defined by the corresponding filter curve, the synthetic broadband visibility results in a superposition of all the monochromatic profiles over the width of the band (Kervella et al. 2003). Figure 11 presents the best-fitting hydrostatic model superimposed on the VINCI visibility measurements.

Table 5. Stellar atmospheric parameters of R Scl deduced from best-fitting hydrostatic model of the spectrophotometric and near-infrared interferometric measurements.

Parameter	Value
Effective temperature: $T_{\rm eff}$ (K)	2700
Luminosity: L ($L_\odot$)	7000
Distance: D (pc)	350
Central star diameter: $\oslash_\star$ (mas)	10.2
Surface gravity: log g	–0.7
Micro-turbulent velocity: ζ (km s^{-1})	2.5
Stellar mass: M ($M_\odot$)	1
Metallicity: Z ($Z_\odot$)	1
Carbon over oxygen ratio: C/O	1.4

Table 5 summarizes the stellar atmospheric parameters of R Scl deduced from the best-fitting hydrostatic model of the spectrophotometric and near-infrared interferometric measurements.

The values found agree well with the ones found in the literature. The distance of 350 pc is relatively far from the Hipparcos distance of 474 pc but in very good agreement with the distance of 360 pc derived from the period-luminosity relation for carbon stars (Groenewegen & Whitelock 1996; Whitelock et al. 2008). The angular diameter of the central star is relatively close to the one coming from the bolometric luminosity of R Scl (from 11.8 to 13.8 mas; Yudin & Evans 2002). The C/O ratio of 1.34 derived by Lambert et al. (1986) agrees with the value that we found. The surface gravity, mass, metallicity, and C/O ratio are also in good agreement with those used by Hron et al. (1998) (log g = −0.5/−0.6, M = 1 $M_\odot$, Z = 1 $Z_\odot$, and C/O = 1.4, respectively).

4.2. Including of a dusty environment

4.2.1. Determination of the SiC dust parameters

The DUSTY code (Ivezić & Elitzur 1997; Ivezić et al. 1999) solves the problem of radiation transport in a circumstellar dusty environment by calculating the radiative transfer equation in plane-parallel or spherical geometry. The radiation from the star is scattered, absorbed, and re-emitted by dust grains. DUSTY has built-in optical properties for the most common types of astronomical dust. The stellar spectrum can be specified in a numerical form as a separate user-supplied input file. In our case, the best-fitting COMARCS stellar atmosphere model, defined in Sect. 4.1, is used as central source. The code can compute the wind structure by solving the hydrodynamic equations, including dust drift and the stars gravitational attraction, as a set coupled to radiative transfer (Ivezić et al. 1999). The calculation is performed for a typical wind in which the final expansion velocity exceeds 5 km s^{-1}, in agreement with the expansion velocity found for R Scl from 10.5 to 16.5 km s^{-1} (Schöier & Olofsson 2001; Wong et al. 2004). This allows derivation of the mass-loss rate of the object, fixing the dust grain bulk density $\rho_{\rm s}$ and the gas-to-dust mass ratio $r_{\rm gd}$.

The input parameters of DUSTY related to the dusty circumstellar environment are the optical constants and the fractional abundances of the relevant dust grains, the grain size distribution, the overall radial optical depth at a given wavelength, the geometrical thickness, and the dust temperature at the inner boundary. Different types of grains can have different

Table 6. Dusty circumstellar envelope parameters of R Scl deduced from the best-fitting COMARCS+DUSTY model on the spectrophotometric and the near- and mid-infrared interferometric measurements.

Parameter	Value
Shell inner radius: $\varepsilon_{\rm in}$ (mas)	22.4
Inner boundary temperature: $T_{\rm in}$ (K)	1200
Grain chemical composition[1]	90% AmC^r + 10% SiC^p
Grain size distribution[2]	MRN
Geometrical thickness: Y (inner radii)	1000
Visual optical depth: $\tau_{0.55\ \mu{\rm m}}$	0.40
1.0 μm optical depth: $\tau_{1.0\ \mu{\rm m}}$	0.18
11.2 μm optical depth: $\tau_{11.2\ \mu{\rm m}}$	7.6×10^{-3}
Mass-loss rate[3]: $\dot{M}$ ($M_\odot$ yr^{-1})	$(6.7 \pm 2) \times 10^{-7}$

Notes. [(1)] AmC^r stands for amorphous carbon of Rouleau & Martin (1991) and SiC^p for silicon carbide of Pégourié (1988); [(2)] grain size distribution as described by Mathis et al. (1977); [(3)] assuming a dust grain bulk density $\rho_{\rm s}$ = 1.85 g cm^{-3} (Rouleau & Martin 1991) and a gas-to-dust mass ratio $r_{\rm gd}$ = 590 (Schöier et al. 2005).

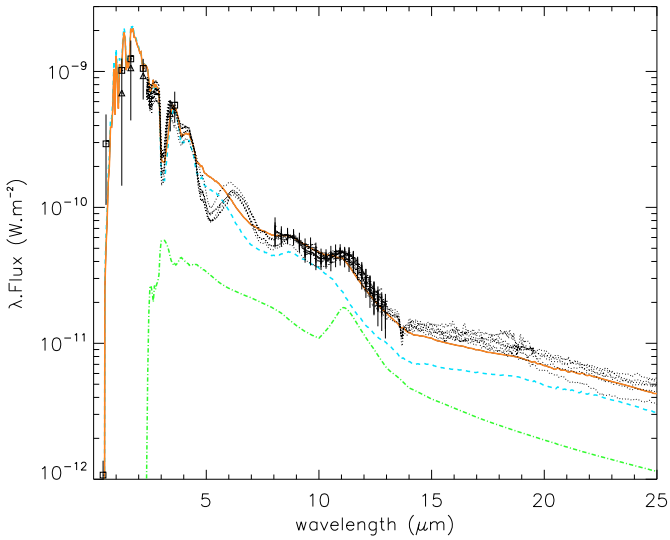

Fig. 9. Best-fitting COMARCS+DUSTY model (red solid line) on the ISO/SWS (dotted lines), MIDI (error bars) spectrometric measurements, and photometric (squares and triangles; see Table 4) measurements of R Scl. The stellar contribution (blue dashed line) and the dust shell contribution (green dashed-dotted line) are also shown.

temperatures at the same location. However, DUSTY currently treats mixtures as single-type grains whose properties average the actual mix, therefore only one temperature is specified.

The determination of the parameters is done by fitting the COMARCS+DUSTY model to the photometric measurements, the ISO/SWS spectrometric data from 0.4 to 25 μm, and the MIDI spectrometric measurements from 8 to 13 μm, averaged over all the phases. Furthermore, the best-fitting model should also agree with the K-band VINCI and N-band MIDI interferometric measurements. For that, a least-square fitting minimization was completed first by testing different sets of optical constants for AmC and SiC grains and by computing a large grid of models varying the fractional abundances of the relevant dust grains ranging from 100% AmC to 100% SiC grains in 10% increments, the 0.55 μm overall radial optical depth from 0.05 to 1 ($\Delta\tau_{0.55\ \mu{\rm m}}$ = 0.05), and the dust temperature at the inner boundary from 800 to 1500 K ($\Delta T_{\rm in}$ = 100 K). As the geometrical thickness does not have any significant impact on the model spectrum because of the very optically thin circumstellar environment ($\tau_{11.2\ \mu{\rm m}} = 7.6 \times 10^{-3}$, see Table 6), we fixed this parameter to 1000 dust shell inner boundary radii knowing that the result is similar for values between 100 to 10^4. The grain size distribution was also fixed to a standard MRN grain size distribution as described by Mathis et al. (1977)[4].

We obtained the best fit model to the ISO/SWS spectrometric data from 2.4 to 25 μm with a reduced χ^2 of 3.5 (see Table 6).

Figure 9 shows the best-fitting COMARCS+DUSTY model on the spectrophotometric data of the star. Figures 10 and 11 present the best-fitting COMARCS+DUSTY model superimposed on the MIDI and VINCI visibility data, respectively. Table 6 summarizes the parameters of the dusty envelope found from the best-fitting COMARCS+DUSTY model on the spectrophotometric and the near- and mid-infrared interferometric measurements. These parameters are complementary to the stellar atmospheric parameters (see Table 5).

The resulting values agree well with the ones found in the literature. The inner radius of the dust shell is close to 5 $R_\star$ (see Table 5) as determined by Lorenz-Martins et al. (2001). The optical constants of AmC from Rouleau & Martin (1991) and SiC from Pégourié (1988), together with the fractional abundance of SiC/AmC of 0.08 found by Lorenz-Martins et al. (2001), are also in good agreement with the values found in this work. These last two characteristics allow us to determine the opacities of SiC used to interpret the spectro-interferometric data of R Scl with the help of the dynamic model (see Sect. 4.3.3). The AmC dust grain optical constants from Rouleau & Martin (1991) are the same as adopted for the hydrodynamic calculation (Andersen et al. 2003; Höfner et al. 2003). Good agreement is also found with the works of Dehaes et al. (2007) and Lorenz-Martins et al. (2001), who determined a visual optical depth of $0.5^{+0.2}_{-0.3}$ and a 1.0 μm optical depth of 0.1, respectively. The dust shell inner boundary temperature of 1000^{+300}_{-200} K found by Dehaes et al. (2007) agrees well with the value determined in this work. Finally, the mass-loss rate of the star that we found also well agrees with the ones determined by Le Bertre (1997): $\dot{M} = 10^{-7}\ M_\odot$ yr^{-1}; Gustafsson et al. (1997): $\dot{M} = 4 \times 10^{-7}\ M_\odot$ yr^{-1}; and Wong et al. (2004): $\dot{M}$ = 2 to 5 $\times$ $10^{-7}\ M_\odot$ yr^{-1}. Such low values of mass-loss rate are consistent with the very optically thin circumstellar environment that we found from the fit ($\tau_{11.2\ \mu{\rm m}} = 7.6 \times 10^{-3}$).

4.2.2. Comparison of the COMARCS+DUSTY model with observations

While the best-fitting COMARCS+DUSTY model is able to reproduce the largest part of the ISO/SWS spectra (see Fig. 9), we can see a discrepancy from 5 to 7 μm, which could be linked to wrong or incomplete C_3 line list opacities in that spectral range[5]. Another discrepancy between the model and the ISO/SWS spectrometric data appears around the 13.7 μm C_2H_2 absorption feature. Gautschy-Loidl et al. (2004) argue that this weak and sharp 13.7 μm absorption would come from cool layers above the 500 K dust and gas layer proposed by Jørgensen et al. (2000) to explain the lack of the 14 μm photospheric band.

The model matches the observed near- and mid-infrared visibilities data rather well (see Figs. 10 and 11), except for few measurements in the mid-infrared. The first disagreement comes

[4] $n(a) \propto a^{-3.5}$ with minimum and maximum grain sizes of 0.005 μm and 0.25 μm, respectively.

[5] Since there is only one C_3 line list available, a cross check of different line lists is not possible.

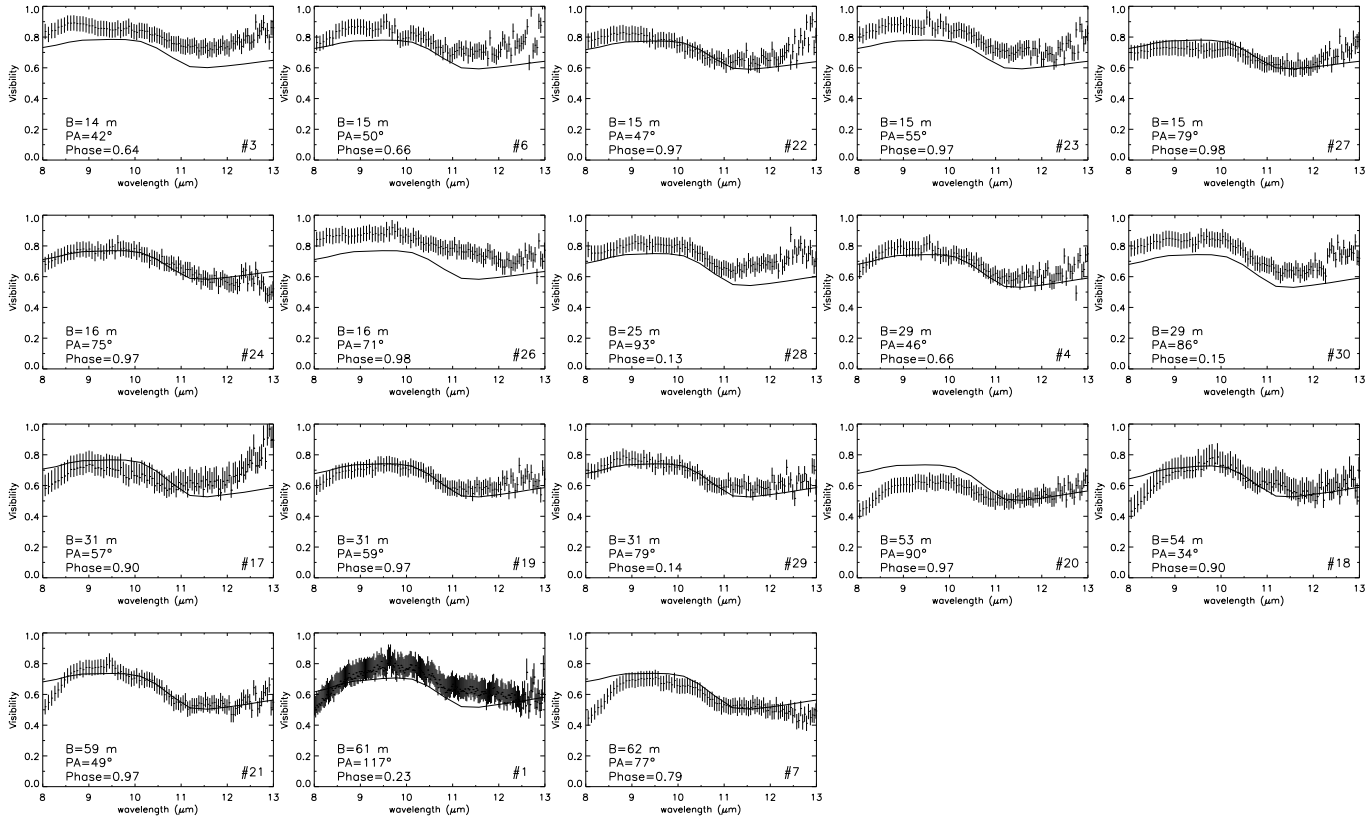

Fig. 10. Best-fitting COMARCS+DUSTY model (solid line) on the spectrally-dispersed MIDI visibilities of R Scl (error bars) from the smallest to the largest projected baselines. The data set numbers are defined in Tables 2 and 3.

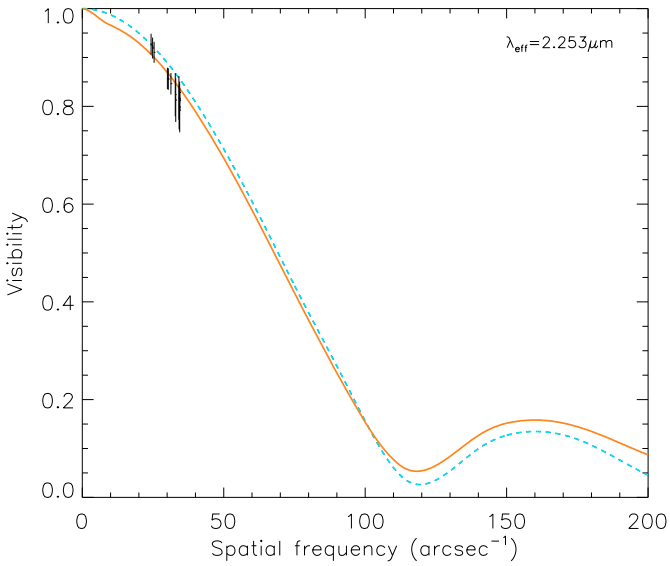

Fig. 11. Best-fitting hydrostatic model (blue dashed line) and best-fitting COMARCS+DUSTY model (red solid line) on the VINCI visibilities of R Scl (error bars).

from the amplitudes of the model visibilities, which are either higher or lower than the amplitudes of the visibility measurements at certain baselines. The most probable reasons for that follow.

(i) *The geometry of the object*: potential deviations from spherical symmetry (corresponding to the geometry of the COMARCS+DUSTY model) of the object at certain position angles could explain the disagreement. As the object subsequently appears more or less extended from one position angle to another, the corresponding amplitude of the visibility measurements decreases or increases, respectively, in contrast to the constant visibility amplitude of the COMARCS+DUSTY model.

(ii) *The variability of the object*: it has been shown that the motion of the dynamic model atmospheres without mass loss mainly follows the pulsation of the stellar interior, whereas in the case of mass-losing models, the dust formation may deform the corresponding sinusoidal pattern (see Fig. 2 of Höfner et al. 2003). As the object subsequently appears more or less extended from phase-to-phase, the corresponding amplitude of the visibility measurements decreases or increases (Paladini et al. 2009), respectively, in contrast to the constant visibility amplitude of the COMARCS+DUSTY model.

Another phenomenon that cannot be reproduced by the model is the slope in the *N*-band visibility data for the largest 60 m projected baselines in the 8−9 μm spectral range (see Fig. 10). As the model overestimates the visibility measurements, this reveals that the model is too optically thin. The regions probed at these baseline and spectral band are located between the photosphere of the star (~5 mas; see Table 5) and the dust shell inner radius (~22.4 mas; see Table 6). Because of the very low optical depth of the model in the 8−9 μm spectral range [$\bar{\tau}$(8−9 μm) = 4.6×10^{-3}], leading to domination of the stellar flux over the flux of the dust shell, the model is therefore close to the central star's intensity distribution. A way to reproduce the MIDI measurements is to increase the optical thickness of the model at the corresponding spatial frequencies. This can be done by adding

extended molecular layers of C_2H_2 and HCN emitting in that spectral range and located above the stellar photosphere.

Many works in interferometry revealed that diameters of Mira and non-Mira M- and S-type stars appear systematically larger than expected in the near-infrared (Mennesson et al. 2002; Ohnaka 2004; Perrin et al. 2004; Weiner 2004; Verhoelst et al. 2006) and in the mid-infrared (Weiner et al. 2000, 2003a,b; Weiner 2004; Ohnaka 2004; Ohnaka et al. 2005; Verhoelst et al. 2006; Sacuto et al. 2008). This increase cannot be attributed only to dust shell features, but also to the possible existence of extended gaseous shells above the stellar photosphere. Such a molecular shell, also called *MOLsphere* (Tsuji et al. 2000), is favored by the low surface gravity ($\log g = -0.7$) and the high luminosity ($\sim$7000 $L_\odot$) of the star, allowing the levitation of the upper layers by shock waves or other dynamic phenomena in an easiest way. The temperatures in this levitated matter are low enough that large amounts of polyatomic molecules can form (Hron et al. 1998; Woitke et al. 1999; Gautschy-Loidl et al. 2004; Verhoelst et al. 2006). Ohnaka et al. (2007) present their results on the modeling of the MIDI measurements of the carbon-rich Mira variable V Oph. The model consists of optically thick warm and cool C_2H_2 molecular layers and an optically thin AmC+SiC dust shell.

Although this *MOLsphere* is useful for increasing the optical thickness of the close circumstellar structure, it remains an inconsistent ad-hoc model. In the classical *MOLsphere* scenario, as is usually applied to interpreting interferometric or spectroscopic data, it is assumed that there are one or a few static layers with a certain concentration and temperature of a molecular species. The possible physical status and origin of such a layer is left unanswered, which is problematic for the following points.

(i) The radial temperature-density distribution of gas and dust around evolved objects is always a continuous and inconstant phenomenon.
(ii) The molecular (and dust) concentrations in a layer depend on each other, so it is impossible to freely choose the amount of certain species.
(iii) The radial structures are extremely time dependent.

As shown by Hron et al. (1998), Woitke et al. (1999), and Gautschy-Loidl et al. (2004), the hydrodynamic modeling leads to a self-consistent formation of extended molecular structures located between the photosphere and the dust formation zone. Finally, Höfner et al. (2003) argue that sequences of hydrostatic models with varying stellar parameters cannot reproduce the effects of shock waves, levitation, or winds. The only way to understand how the dynamic processes influence the atmospheric structure on different spatial scales is the use of time-dependent dynamic atmospheric modeling.

4.3. Dynamic model atmosphere for R Scl

The aim of this section is to show that a self-consistent hydrodynamic modeling forming a gaseous and dusty environment by itself is able to reproduce the time-dependent signature of the spectro-interferometric data of a carbon-rich, long-period variable star. Section 4.3.1 presents the dynamic model atmosphere used for the interpretation. Section 4.3.2 connects the bolometric phases given by the model with the visual phases of the observations which is needed to compare time-dependent models with real measurements of R Scl. Section 4.3.3 presents the specific dynamic atmospheric model that we chose for the comparison with the spectro-interferometric data of the star. Section 4.3.4 shows the ability of the dynamic model to form molecular layers located above the photosphere of the star in a self-consistent way. Finally, the last section (Sect. 4.3.5) compares the dynamic model with the time-dependent spectro-interferometric data.

4.3.1. Presentation of the hydrodynamic model atmospheres

The self-consistent hydrodynamic structures for dust-forming atmospheres and winds used here are taken from the models contained in Mattsson et al. (2008) and from additional models required for the present work (Mattsson, priv. comm.). The dynamic model atmosphere is based on the code described by Höfner et al. (2003) and Mattsson et al. (2010). The models were obtained by solving the coupled system of hydrodynamics and frequency-dependent radiative transfer in spherical symmetry, together with a set of equations describing the time-dependent formation and the growth and evaporation of dust grains. The formation of AmC dust is treated in a self-consistent way using the moment method described by Gail & Sedlmayr (1988) and Gauger et al. (1990). Optical properties of AmC grains were taken from Rouleau & Martin (1991). Each dynamic model starts from a hydrostatic initial structure, and the effects of stellar pulsation are simulated by a variable inner boundary just below the stellar photosphere (piston model). The dynamic code provides temporally varying temperature and density stratifications of the object. Based on such radial structures, at given instances of time, opacities are computed using the COMA code (see Sect. 4.1). The resulting opacities are used as input for a spherical radiative transfer code that computes the emergent intensity distribution for every frequency point of the calculation. This is used to calculate the synthetic spectra and visibility profiles, which are compared to the observational data of R Scl. Since only AmC dust is treated in the hydrodynamic calculation, opacities of SiC dust are added in the a posteriori radiative transfer computation. Those opacities are determined with COMA taking SiC optical constants into account and assuming that SiC dust is scaled with AmC dust. The scaling factor corresponds to the fractional abundance of SiC to AmC dust, which has condensed. Finally, SiC dust is assumed to follow the same temperature-density structure as AmC dust, derived from the full dynamic calculation.

4.3.2. Bolometric and visual phases

The phases of the dynamic model correspond to the bolometric phases derived from its bolometric lightcurve (Nowotny et al. 2005b). The phase-zero point was chosen at the maximum bolometric luminosity of the given dynamic model. As the radiation-hydrodynamic code stores atmospheric structures at more or less randomly distributed instances of time, the uncertainty in the choice of the phase-zero point amounts to a range of ± 0.03.

For O-rich Miras, a small shift between bolometric and visual lightcurves probably exists, such that bolometric phases lag behind visual ones by a value of ≈ 0.1 (Lockwood & Wing 1971; Nowotny et al. 2010). This phase shift is caused by the behavior of molecules occurring in atmospheres of red giants and their corresponding spectral features in the visual. Recently, Nowotny et al. (2010) have studied the photometric variation in the V-filter for similar dynamic model atmospheres as the ones used here. The authors find that, for models developing no wind such as their model W or the one used in this paper to represent R Scl (see Sect. 4.3.3), the visual lightcurves follow the bolometric light variation caused by the variable inner boundary

Table 7. Parameter values of the hydrostatic initial structure of the hydrodynamic model used in this work (first row) compared to the parameters derived from the best-fitting hydrostatic model determined in Sect. 4.1 (second row).

Model	$L_\star$ ($L_\odot$)	$M_\star$ ($M_\odot$)	$T_\star$ (K)	$Z_\star$ ($Z_\odot$)	ζ (km s^{-1})	C/O
Hydrodynamic	7080	1	2800	1	2.5	1.35
Hydrostatic	7000	1	2700	1	2.5	1.40

(piston) closely. Therefore, in the following, bolometric phases of the model within a range of ±0.03 around the observed visual phases of R Scl are used for comparisons between model and observations.

4.3.3. Choice of a specific dynamic model

The choice of the best dynamic model for R Scl comes from the stellar parameters and the distance derived from the previous hydrostatic modeling (see Sect. 4.1).

Among the dynamic models that we have, one model shows parameter values of the hydrostatic initial structure close to the ones we derived from the hydrostatic COMARCS modeling (see Table 5). Table 7 compares the stellar parameters of the hydrostatic model initiating the hydrodynamic computation with the stellar parameters derived from the best-fitting hydrostatic model determined in Sect. 4.1.

Opacities of SiC dust are added in the a posteriori radiative transfer calculation using the SiC optical constants of Pégourié (1988) and a fractional abundance of SiC to AmC dust of 10%, as derived from the COMARCS+DUSTY modeling (see Sect. 4.2.1).

Two other free parameters are required for the hydrodynamic computation (see Sect. 4.3.1):

$P_{\rm mod}$: *the pulsation period of the piston.* A pulsation period of $P_{\rm mod}$ = 390 days, the closest to the pulsation period of R Scl (374 days), was used.

$\Delta u_{\rm p}$: *the amplitude of the piston velocity.* Different amplitudes of the piston velocity were tested from a range of $\Delta u_{\rm p}$ = 2 to 6 km s^{-1}, with steps of 1 km s^{-1} (except for the $\Delta u_{\rm p}$ = 3 km s^{-1} model not at our disposal).

Determination of the best-fitting piston velocity amplitude is done by comparing the synthetic spectra based on these models to the spectrophotometric data. Increasing the amplitude of the piston moves the material to larger distances from the star, which favors dust formation and reduces the effective gravitation (e.g. Winters et al. 2000).

For a piston velocity lower than 4 km s^{-1} (i.e. model with $\Delta u_{\rm p}$ = 2 km s^{-1} in Fig. 12), it appears that the model shows too low a level of flux compared to the spectrometric data. Furthermore, as already discussed in Gautschy-Loidl et al. (2004), a broad and intense C_2H_2/HCN absorption band around 14 μm is present, in pronounced contrast to the observed ISO/SWS spectra which show a continuum-like infrared excess with a weak and narrow C_2H_2 feature at 13.7 μm (see Fig. 12). Finally, the variability amplitude of the model is smaller than 0.3 in the V magnitude, as compared with the 1.4 variability amplitude of the cycle-to-cycle averaged visual magnitudes of the star. Therefore, in the case of too low a piston velocity, the dynamic model corresponds to a dust-free pulsating atmosphere without any wind (no mass-loss), leading to a pure photospheric spectrum such as the one shown by the blue dashed line of Fig. 9.

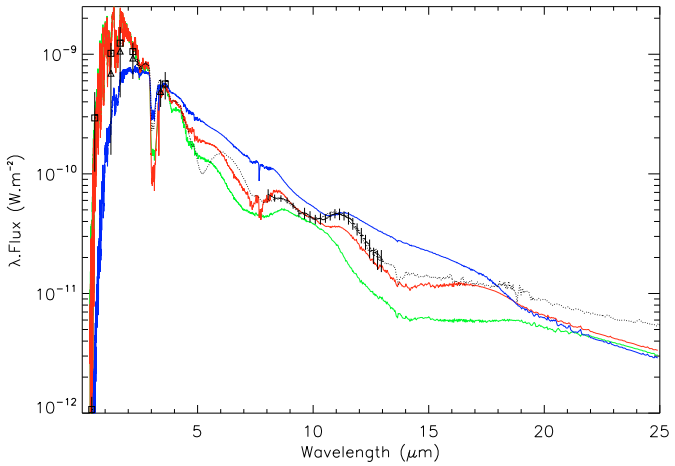

Fig. 12. Synthetic spectra based on the dynamic models at phase 0.98 with piston velocities of 2 (green line), 4 (red line), and 6 km s^{-1} (blue line), keeping the same parameter values as the ones contained in Table 7. The dotted line is the ISO/SWS spectrum of the star at phase 0.97, whereas the error bars in the N-band correspond to the MIDI fluxes at phase 0.98. Squares and triangles correspond to the photometric measurements of the star (see Table 4).

When the piston velocity amplitude exceeds 4 km s^{-1} (i.e. model with $\Delta u_{\rm p}$ = 6 km s^{-1} in Fig. 12), the dynamic model shows too high a level of flux compared to the spectrometric data and a filling up of the whole molecular features at wavelengths longwards of 3.5 μm. Furthermore, the variability amplitude of the model is greater than 5.5 in the V magnitude, as compared with the 1.4 variability amplitude of the cycle-to-cycle averaged visual magnitudes of the star. In that case, the dynamic model develops a strong wind ($\dot{M} > 10^{-6}$ $M_\odot$ yr^{-1}) where the large amount of formed gas and dust, located in the outer layers, obscures the innermost structures of the stellar atmosphere, although not significantly enough to fill up the 3.05 μm feature.

A dynamic model with a piston velocity of 4 km s^{-1} gives the best overall match of the spectrophotometric data from 0.4 to 25 μm, even if the emission is still lower than the [13–25 μm] infrared excess of the ISO/SWS spectrum (see Fig. 12). The variability amplitude of the model of about 1 in the V magnitude is relatively close to the 1.4 variability amplitude of the cycle-to-cycle averaged visual magnitudes of the star. In that case, the model is, in some sense, a transition case between a simple, periodically pulsating dust-free atmosphere and an object featuring a dusty wind. The kinetic energy supplied by the pulsation (piston) causes strong, quasi-periodic atmospheric dynamics and some intermittent dust formation, but is not sufficient to start a dust-driven outflow.

The possible reasons for the discrepancy in the 5 to 7 μm wavelengths regions are similar to the ones expressed in Sect. 4.2.2 suggesting wrong or incomplete C_3 line list opacities in that spectral range. The model is also unable to reproduce the weak observed 3.05 μm C_2H_2/HCN feature.

Possible explanations of the discrepancy between the model and the measurements are discussed in more detail in Sect. 4.3.5. This last model is, however, considered as the best dynamic model for R Scl, among the ones available, and will be used in the comparison to the observed spectro-interferometric measurements of the star in the following.

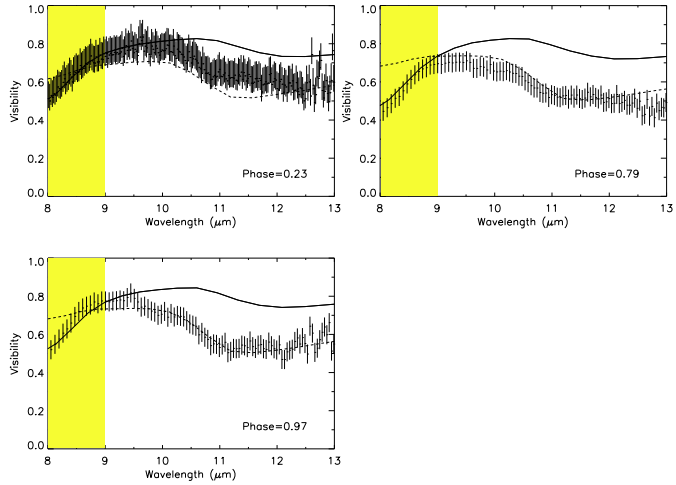

Fig. 13. Comparison of the visibility of the best dynamic model (solid line) with the best-fitting COMARCS+DUSTY model (dashed line; see Sect. 4.2.1) superimposed on the 60 m MIDI visibility data (error bars) at phases 0.23/0.79/0.97 (data sets #1, #7, and #21, respectively). The yellow zone corresponds to the region dominated by warm molecular layers.

4.3.4. Self-consistent formation of extended molecular structures

As discussed in Sect. 4.2.2, the *N*-band visibility data display a slope for the largest 60 m baseline in the 8−9 μm spectral range likely related to the emission of extended molecular structures of C_2H_2 and HCN. Figure 13 shows the comparison of the visibility of the best dynamic model for a given cycle with the best-fitting COMARCS+DUSTY model superimposed on the MIDI visibility data around 60 m for all the available phases: 0.23/079/0.97. From this figure, we can clearly see that the COMARCS+DUSTY model is too optically thin, showing a flat visibility profile in the 8−9 μm spectral range (see Sect. 4.2.2). On the contrary, the dynamic model is able to reproduce the slope of the MIDI visibilities well through this wavelength range. This means that the extension of the dynamic model is suitable for revealing the presence of the molecular structures of C_2H_2 and HCN, emitting in that spectral range and located above the stellar photosphere. However, the dynamic model is not optically thick enough to reproduce the measurements in the reddest part of the mid-infrared spectral band.

4.3.5. Comparison of the dynamic modeling results to the time-dependent spectro-interferometric data

In the following, we investigate 100 phases of the model randomly distributed over 56 cycles corresponding to a time sequence of 60 years. As there is no possibility to define the model cycle corresponding to the observations, we decide to follow a statistical approach and to represent all the available cycles for a phase range close to the observed one (see Sect. 4.3.2).

Figure 14 shows the time-dependent cycle-to-cycle averaged fluxes of the best dynamic model superimposed on the MIDI and ISO/SWS spectrometric data in the 8.5, 11.3, and 12.5 μm spectral bands. The figure shows that the model agrees relatively well with the time-dependent flux data at 8.5 μm, whereas the model is fainter than the measurements in the 11.3 and 12.5 μm spectral bands.

In compliance with the observations, the comparison of the cycle-to-cycle averaged visibilities of the best dynamic model from phase-to-phase, considering the same baselines and phases as the observations of R Scl (see Sect. 3.4), does not show any significant variability of the object in the *K* and *N* bands.

Figure 15 shows the cycle-to-cycle averaged visibility of the best dynamic model superimposed on the VINCI data at phases 0.17 and 0.23. The model shows good agreement with the data implying that the extension of the model is suitable in the *K*-band.

Figure 16 shows the time-dependent cycle-to-cycle averaged visibilities of the best dynamic model superimposed on the [14−16 m], [29−31 m], and [59−62 m] baselines MIDI data in the 8.5, 11.3, and 12.5 μm spectral bands. The figure only presents measurements showing a deviation from the best-fitting COMARCS+DUSTY model (see Fig. 10) smaller than the object variability scattering at 15 and 31 m baselines (see Fig. 7). This allows us to avoid comparing the spherically symmetric model with visibility measurements exhibiting a potential departure of the object from sphericity. As we do not have any information on the variability effect at the 60 m baseline, all the measurements are represented. From this figure, it is obvious that the model is not extended enough to reproduce the level of the mid-infrared interferometric data. Only the visibility measurements at the highest spatial frequencies (B = 60 m and λ = 8.0−9.5 μm), probing regions corresponding to the warm extended molecular layers (from 1.5 to 2 $R_\star$), are in good agreement with the model.

Besides the possibility of an inaccurate estimation of the parameter values of the hydrostatic initial structure, the most probable reasons for the discrepancy between the dynamic model and the spectro-interferometric measurements are the following ones.

(i) *The sparse sampling of the transition region from windless models to models with considerable outflows in certain critical stellar parameters*: the 100 K higher value of the dynamic model effective temperature compared to the hydrostatic model could be a reason for the discrepancy of the model to the MIDI interferometric measurements, given the closeness of the model to the mass-loss threshold defined by Mattsson et al. (2010). Another critical parameter for dynamic models, in particular for relatively weak winds, is the C/O ratio. After testing a model having a C/O ratio of 1.47, while all the other parameters are identical to the best dynamic model, we found that the model appears, in that case, too much extended compared to the 15 m baseline VINCI visibility data, whereas the levels of the 60, 30, and 15 m baselines MIDI visibility data are reproduced relatively well. The transition from windless models to models with considerable mass-loss rates occurs in a very narrow range of stellar parameters especially for the pulsation amplitude, the C/O ratio, and the effective temperature, as already pointed out by Gautschy-Loidl et al. (2004). In summary, a better sampling of parameter space beyond the models currently available (Mattsson et al. 2008, 2010), especially in effective temperature and C/O, could help reduce the discrepancies between models and observations. Such a study is, however, beyond the scope of this paper.

(ii) *The approximation of the stellar pulsation with the sinusoidal piston*: as the star is a semi-regular variable showing two main periods (374 and 1804 days) with harmonics in the smallest period (Whitelock et al. 1997), using the simple sinusoidal piston to describe the stellar pulsation could be a crude approximation for such a star. The overall wind properties are mostly affected by the pulsation

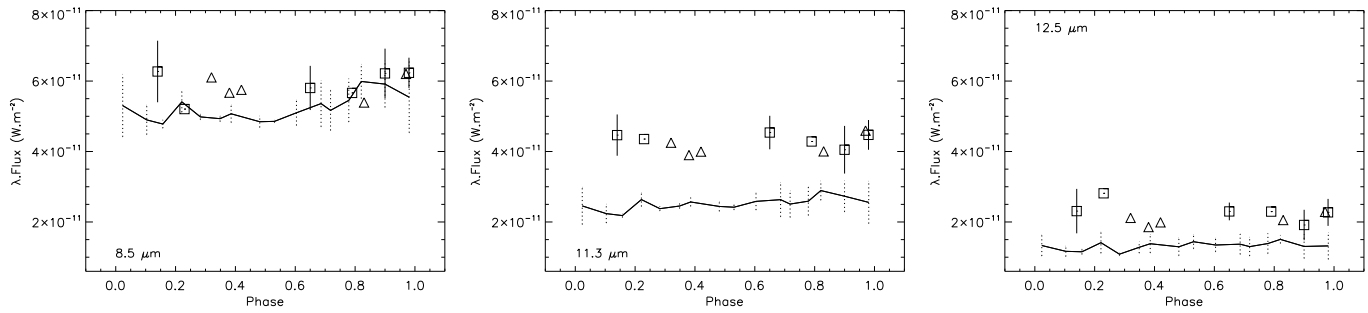

Fig. 14. Time-dependent cycle-to-cycle averaged fluxes of the best dynamic model (solid line) superimposed on the MIDI (squares) and ISO/SWS (triangles) spectrometric data in the 8.5 (*left*), 11.3 (*middle*), and 12.5 μm (*right*) spectral bands. Dotted error bars give the dispersion created by the cycle-to-cycle variation.

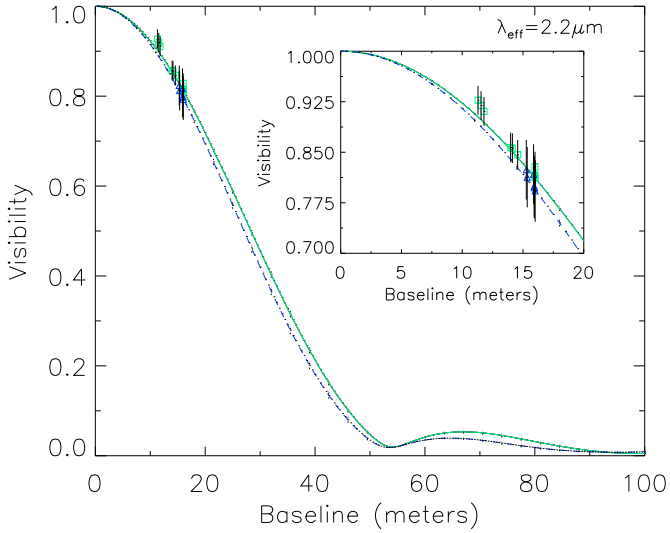

Fig. 15. Cycle-to-cycle averaged visibility profiles of the best dynamic model (green solid line: phase 0.17; blue dashed line: phase 0.23) superimposed on the VINCI data at phase 0.17 (green squares) and phase 0.23 (blue triangles). Dotted error bars give the dispersion created by the cycle-to-cycle variation. In the inset, a zoom of the relevant frequency region is represented.

amplitude and not so much by the actual form of the piston motion (see models based on different types of pulsation descriptions presented by Freytag & Höfner 2008). However, the particular phase coupling between dynamic and radiative properties of the models imposed by the sinusoidal piston might cause some of the discrepancies between models and observations encountered here.

(iii) *The approximation of a complete momentum and position coupling of gas and dust (i.e., absence of drift) and the approximation of the small-particle limit (or Rayleigh limit) in the determination of the dust grain opacity in the dynamic computations*: gas and dust decouple when the gas of the wind is diluted as is the case for low mass-loss rate stars like R Scl. Sandin & Höfner (2003, 2004) find that decoupling the dust and gas phase increases the dust formation, which could reconcile the dynamic model with the mid-infrared spectro-interferometric measurements. Similar arguments, regarding the difficulty of producing low mass-loss rate models, have also been pointed out by Mattsson et al. (2010).

It is found by Mattsson et al. (2010) that dust grains forming in slow wind atmospheres may grow beyond sizes where their opacities can be approximated by the small-particle limit. Moreover, it has been demonstrated by Höfner (2008) that radiation pressure on micron-sized silicate grains may play a key role in driving outflows in M-type AGB stars. Similar arguments could also apply to low mass-loss rate carbon-rich stars like R Scl.

5. Conclusions and perspectives

In this work, we have presented the first interpretation of combined photometric, spectrometric, and interferometric measurements of a carbon-rich star based on state-of-the-art, self-consistent dynamic atmospheric models.

Interferometric observations do not show any significant variability effect at the 16 m baseline between phases 0.17 and 0.23 in the *K* band. This is, however, not surprising given the short time interval and because the VINCI broadband measurements average out the short term effects of a shock front in CO or CN lines. No significant variability effect is found for both 15 m baseline between phases 0.66 and 0.97, and 31 m baselines between phases 0.90 and 0.97 in the *N* band. This means that the stellar radiative pressure is not strong enough to reveal a movement of the warm mass dust shells larger than 3 AU, in good agreement with the amplitude of the mass shell of theoretical carbon-rich dynamic models.

The spectro-interferometric predictions of the dynamic model atmosphere are in relatively good agreement with the dynamic picture that we deduced from observations. We find rather good agreement between the dynamic model and the spectrophotometric data from 0.4 to 25 μm. The model agrees relatively well with the time-dependent flux data at 8.5 μm, whereas the model is too faint compared to the measurements in the 11.3 and 12.5 μm spectral bands. The 15 m baseline VINCI visibilities are reproduced well for the two post-maximum brightness phases, meaning that the extension of the dynamic model is suitable in the *K*-band. In the mid-infrared, the slope of the 60 m baseline MIDI visibilities in the 8−9 μm spectral range is reproduced well for all the available phases. This means that the dynamic model has the proper extension to reveal the molecular structures of C_2H_2 and HCN located above the stellar photosphere, whereas the non consistent COMARCS+DUSTY model fails to do so.

The discrepancy between the dynamic model and the spectro-interferometric data could be related to inaccurate estimation of parameter values of the hydrostatic initial structure, a difference between the parameter values deduced from the hydrostatic modeling and the ones related to the hydrostatic initial structure of the dynamic model, the sinusoidal piston simulating the stellar pulsation, the inclusion of SiC opacities in the a

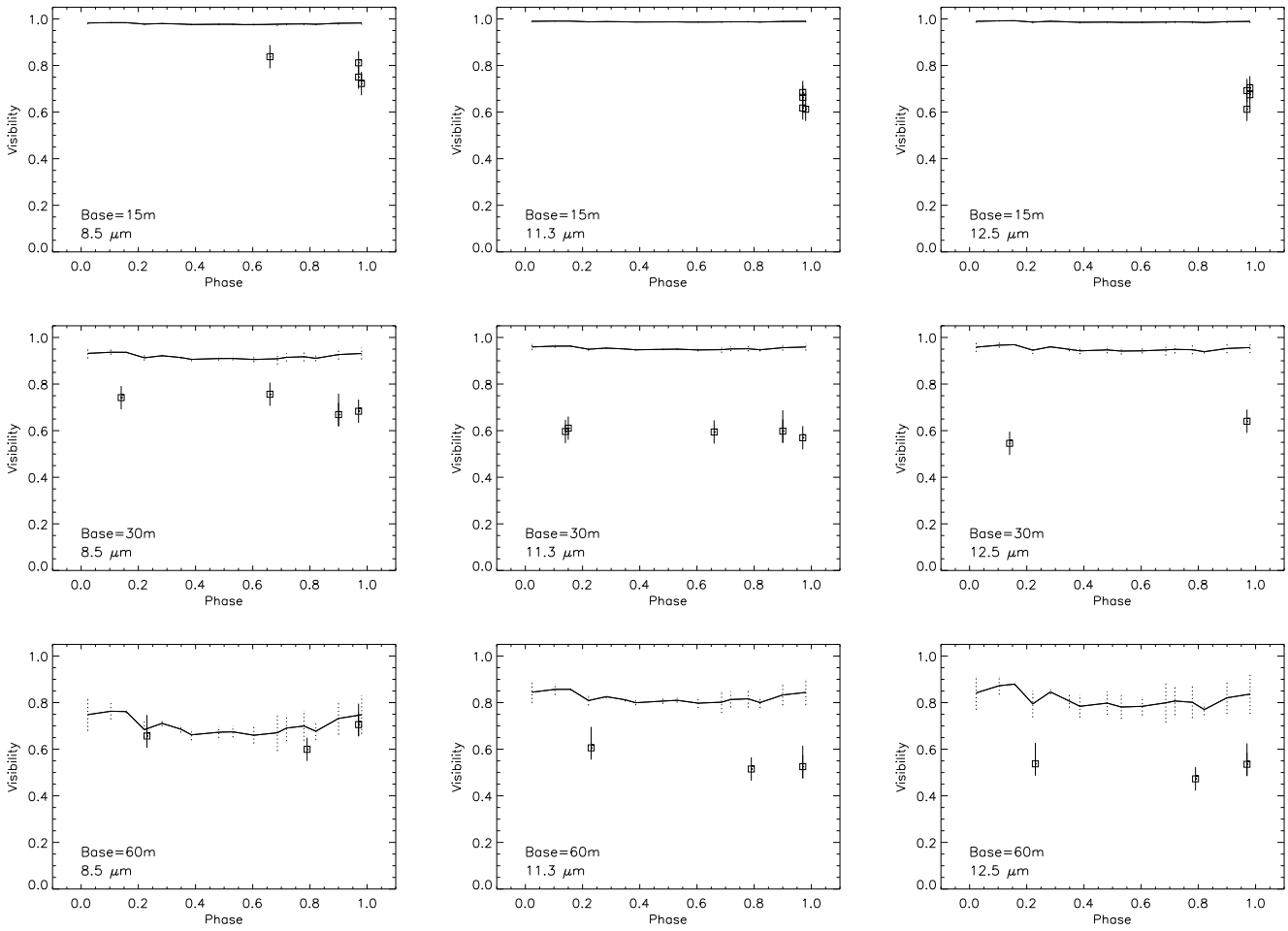

Fig. 16. Time-dependent cycle-to-cycle averaged visibilities of the best dynamic model (solid line) superimposed on the [14−16 m], [29−31 m], and [59−62 m] baselines MIDI data (squares) in the 8.5 (*left*), 11.3 (*middle*), and 12.5 μm (*right*) spectral bands. Dotted error bars give the dispersion created by the cycle-to-cycle variation.

posteriori radiative transfer, or a combination of all these effects. However, it seems that, owing to the strong nonequilibrium process of dust formation in AGB stars, the transition from models without wind to models with considerable mass-loss rates occurs in a very narrow parameter range. The most sensitive parameters allowing this sharp and strong transition between models with and without wind are the effective temperature, the amplitude of the piston velocity, and the C/O ratio. Therefore, it seems necessary to improve the sampling of critical regions in parameter space in the grid of hydrodynamic models for further investigations of the extended structures of low mass-loss carbon stars like R Scl.

Finally, the complete dynamic coupling of gas and dust, and the approximation of grain opacities with the small-particle limit in the dynamic calculation, both probably unsuitable for low mass-loss rate object like R Scl, could also contribute to the disagreement between the dynamic model and the spectro-interferometric data. First tests with C-star models based on opacities that take grain size into consideration (Mattsson & Höfner, in prep.) show that wind characteristics may be affected considerably in models close to a mass-loss threshold (Mattsson et al. 2010), such as the one used here to represent the low mass-loss C-star R Scl, resembling recent wind models for M-type AGB stars (Höfner 2008).

Acknowledgements. This work is supported by the Austrian Science Fund FWF under the projects P19503-N13, P18939-N16, and P21988-N16. Bernhard Aringer acknowledges funding by the contract ASI-INAF I/016/07/0. Tijl Verhoelst acknowledges support from the Flemish Fund for Scientific Research (FWO). Authors would like to acknowledge Lars Mattsson for computing and providing the dynamic atmospheric model structures. The authors would like to thank Thorsten Ratzka for helpful discussions on the MIDI reduction software. The authors would like to thank Harald Mutschke and Thomas Posch for providing optical constants of AmC from Rouleau & Martin (1991) in electronic form.

References

Andersen, A. C., Höfner, S., & Gautschy-Loidl, R. 2003, A&A, 400, 981
Aringer, B. 2000, Ph.D. Thesis, University of Vienna
Aringer, B., Girardi, L., Nowotny, W., et al. 2009, A&A, 503, 913
Bagnulo, S., Doyle, J. G., & Andretta, V. 1998, MNRAS, 296, 545
Bordé, P., Coudé du Foresto, V., Chagnon, G., & Perrin, G. 2002, A&A, 393, 183
Chesneau, O., Meilland, A., Rivinius, T., et al. 2005, A&A, 435, 275
Cruzalèbes, P., Jorissen, A., Sacuto, S., & Bonneau, D. 2010, A&A, 515, A6
Dehaes, S., Groenewegen, M. A. T., Decin, L., et al. 2007, MNRAS, 377, 931
Deroo, P., van Winckel, H., Verhoelst, T., et al. 2007, A&A, 467, 1093
Feuchtinger, M. U., Dorfi, E. A., & Höfner, S. 1993, A&A, 273, 513
Fleischer, A. J., Gauger, A., & Sedlmayr, E. 1992, A&A, 266, 321
Fitzpatrick, E. L. 1999, PASP, 111, 63
Freytag, B., & Höfner, S. 2008, A&A, 483, 571
Gail, H. P., & Sedlmayr, E. 1988, A&A, 206, 153
Gauger, A., Gail., H. P., & Sedlmayr, E. 1990, A&A, 235, 345
Gautschy-Loidl, R., Höfner, S., Jrgensen, U. G., & Hron, J. 2004, A&A, 422, 289
Groenewegen, M. A. T., & Whitelock, P. A. 1996, MNRAS, 281, 1347

Gustafsson, B., Eriksson, K., Kiselman, D., Olander, N., & Olofsson, H. 1997, A&A, 318, 535
Henden, A. A. 2009, Observations from the AAVSO International Database, private communication
Höfner, S. 1999, A&A, 346, 9
Höfner, S. 2008, A&A, 491, 1
Höfner, S., & Dorfi, E. A. 1997, A&A, 319, 648
Höfner, S., Feuchtinger, M. U., & Dorfi, E. A. 1995, A&A, 297, 815
Höfner, S., Gautschy-Loidl, R., Aringer, B., & Jrgensen, U. G. 2003, A&A, 399, 589
Houk, N. 1963, AJ, 68, 253
Hron, J., Loidl, R., Höfner, S., et al. 1998, A&A, 335, 69
Ivezić, Z., & Elitzur, M. 1997, MNRAS, 287, 799
Ivezić, Z., Nenkova, M., & Elitzur, M. 1999, User Manual for DUSTY
Jaffe, W. J. 2004, SPIE, 5491, 715
Jørgensen, U. G., Hron, J., & Loidl, R. 2000, A&A, 356, 253
Kervella, P. 2007, A&A, 464, 1045
Kervella, P., Coude du Foresto, V., Glindemann, A., & Hofmann, R. 2000, Proc. SPIE, 4006, 3142
Kervella, P., Thévenin, F., Ségransan, D., et al. 2003, A&A, 404, 1087
Kervella, P., Ségransan, D., & Coudé du Foresto, V. 2004, A&A, 425, 1161
Kraemer, K. E., Sloan, G. C., Price, S. D., & Walker, H. J. 2002, ApJS, 140, 389
Lambert, D. L., Gustafsson, B., Eriksson, K., & Hinkle, K. H. 1986, ApJS, 62, 373
Le Bertre, T. 1997, A&A, 324, 1059
Leech, K., Kester, D., Shipman, R., et al. 2003, The ISO Handbook', Volume V – SWS – The Short Wavelength Spectrometer Version 2.0.1, June 2003, ed. T. G. Mueller, J. A. D. L. Blommaert, & P. Garcia-Lario
Lederer, M. T., & Aringer, B. 2009, A&A, 494, 403
Leinert, C., Graser, U., Przygodda, F., et al. 2003, Ap&SS, 286, 73
Lockwood, G. W., & Wing, R. F. 1971, ApJ, 169, 63
Lorenz-Martins, S., de Araújo, F. X., Codina Landaberry, S. J., de Almeida, W. G., de Nader, R. V. 2001, A&A, 367, 189
Mathis, J. S., Rumpl, W., & Nordsieck, K. H. 1977, ApJ, 217, 425
Mattsson, L., Wahlin, R., Höfner, S., & Eriksson, K. 2008, A&A, 484, 5
Mattsson, L., Wahlin, R., & Höfner, S. 2010, A&A, 509, A14
Mennesson, B., Perrin, G., Chagnon, G., et al. 2002, ApJ, 579, 446
Milne, D. K., & Aller, L. H. 1980, AJ, 85, 17
Nowotny, W., Aringer, B., Höfner, S., Gautschy-Loidl, R., & Windsteig, W. 2005a, A&A, 437, 273
Nowotny, W., Lebzelter, T., Hron, J., & Höfner, S. 2005b, A&A, 437, 285
Nowotny, W., Höfner, S., & Aringer, B. 2010, A&A, 514, A35
Ohnaka, K. 2004, A&A, 424, 1011
Ohnaka, K., Bergeat, J., Driebe, T., et al. 2005, A&A, 429, 1057
Ohnaka, K., Driebe, T., Weigelt, G., & Wittkowski, M. 2007, A&A, 466, 1099
Ohnaka, K., Izumiura, H., Leinert, Ch., et al. 2008, A&A, 490, 173
Paladini, C., Aringer, B., Hron, J., et al. 2009, A&A, 501, 1013
Pégourié, B. 1988, A&A, 194, 335
Perrin, G., Ridgway, S. T., Mennesson, B., et al. 2004, A&A, 426, 279
Ratzka, T., Leinert, C., Henning, T., et al. 2007, A&A, 471, 173
Richichi, A., Percheron, I., & Khristoforova, M. 2005, A&A, 431, 773
Rouleau, F., & Martin, P. G. 1991, ApJ, 377, 526
Sacuto, S., & Chesneau, O. 2009, A&A, 493, 1043
Sacuto, S., Jorissen, A., Cruzalèbes, P., et al. 2008, A&A, 482, 561
Sandin, C., & Höfner, S. 2003, A&A, 404, 789
Sandin, C., & Höfner, S. 2004, A&A, 413, 789
Schöier, F. L., & Olofsson, H. 2001, A&A, 368, 969
Schöier, F. L., Lindqvist, M., & Olofsson, H. 2005, A&A, 436, 633
Sloan, G. C., Kraemer, K. E., Price, S. D., & Shipman, R. F. 2003, ApJS, 147, 379
Steffen, M., & Schönberner, D. 2000, A&A, 357, 180
Thompson, R. R., Creech-Eakman, M. J., & van Belle, G. T. 2002, ApJ, 577, 447
Tsuji, T. 1973, A&A, 23, 411
Tsuji, T. 2000, ApJ, 540, L99
van Belle, G. T., Dyck, H. M., Thompson, R. R., Benson, J. A., & Kannappan, S. J. 1997, AJ, 114, 2150
van der Bliek, N. S., Morris, P. W., Vandenbussche, B., et al. 1998, in Fundamental Stellar Properties: The Interaction between Observation and Theory, ed. T. R. Bedding, A. J. Booth, & J. Davis, IAU Symp., 189, 89
Verhoelst, T., Decin, L., van Malderen, R., et al. 2006, A&A, 447, 311
Weiner, J. 2004, ApJ, 611, L37
Weiner, J., Danchi, W. C., Hale, D. D. S., et al. 2000, ApJ, 544, 1097
Weiner, J., Hale, D. D. S., & Townes, C. H. 2003a, ApJ, 588, 1064
Weiner, J., Hale, D. D. S., & Townes, C. H. 2003b, ApJ, 589, 976
Whitelock, P. A., Feast, M. W., Marang, F., & Overbeek, M. D. 1997, MNRAS, 288, 512
Whitelock, P. A., Feast, M. W., Marang, F., & Groenewegen, M. A. T. 2006, MNRAS, 369, 751
Whitelock, P. A., Feast, M. W., & van Leeuwen, F. 2008, MNRAS, 386, 313
Winters, J. M., Fleischer, A. J., Gauger, A., & Sedlmayr, E. 1994, A&A, 290, 623
Winters, J. M., Le Bertre, T., Jeong, K. S., Helling, Ch., & Sedlmayr, E. 2000, A&A, 361, 641
Wittkowski, M., Aufdenberg, J. P., & Kervella, P. 2004, A&A, 413, 711
Woitke, P., Helling, C., Winters, J. M., & Jeong, K. S. 1999, A&A, 348, 17
Wong, T., Schöier, F. L., Lindqvist, M., & Olofsson, H. 2004, A&A, 413, 241
Yudin, R. V., & Evans, A. 2002, A&A, 391, 625
Zijlstra, A. A., Matsuura, M., Wood, P. R., et al. 2006, MNRAS, 370, 1961